Generation of an optimized model of iPSC-derived human intestinal organoids for the expression of an intestinal stem cell fluorescent reporter, and a preliminary assessment for its application in high-throughput screening

Christian Eduardo Wong Valencia

A thesis submitted in partial fulfilment of the requirements for the degree of Doctor of Philosophy

Department of Biomedical Sciences

January 2021

ACKNOWLEDGMENTS

ABSTRACT

The study of human diseases requires the development of modelling systems that accurately replicate both the normal physiology and the progression of the disease. However, commonly used cell culture models are unable to replicate key features of the tissue microenvironment such as the three-dimensional microarchitecture, organization, cellular diversity, and distribution. Organoid technology has overcome these limitations, generating better and more accurate models. The aim of this work was to generate a model of human intestinal organoids (HIOs) derived from induced pluripotent stem cells (iPSCs), expressing an LGR5-GFP reporter within the stem cell population, and implement it in high-throughput experiments for drug discovery studies. We have successfully generated an optimized protocol for the generation of HIOs from iPSCs. The organoids were comprised by an inner layer of columnar intestinal epithelium supported by an outer layer of mesenchymal cells. The gene expression profile revealed a differentiation bias towards the absorptive lineage. Our optimized protocol reduced the time and cost required for the production of the organoids, favouring its compatibility with high-throughput experiments. Excitingly, this protocol was implemented for the generation of intestinal epithelium tubules on an organ-on-a-chip format from *in situ* differentiated iPSC. Next, we attempted to generate an LGR5-GFP reporter iPS cell line to track the ISCs within the organoids; however, this task proved unsuccessful, and further comparisons with the literature suggested an inherent issue with the detection of human LGR5 using fluorescence-based techniques. Finally, in light of the results obtained from the LGR5-GFP reporter, and other technical limitations, we performed a preliminary high-throughput small-molecule screening on FUCCI-CaCo-2 cells, instead of LGR-GFP HIOs. The results of the screening identified a subset of compounds with an effect over the G1 phase of the cell cycle. Given the role of G1 in the self-renewal, differentiation, and malignant transformation of the ISCs, these compounds could potentially serve as regulators of the activity of the ISC population. Future work will focus on the validation of these results in HIOs.

TABLE OF CONTENTS

The gastrointestinal (GI) tract is a continuous hollow tube spanning from mouth to anus, responsible for the uptake of food, the absorption of nutrients, and the excretion of waste products. The GI tract is organized in 4 main layers: serosa, muscularis propria, submucosa, and mucosa. The serosa is the outer most layer made by squamous epithelium and connective tissue to support and protect the GI tract; the muscularis propria consists of longitudinal and circular muscle fibres to perform peristaltic movement; the submucosa provides with innervation and irrigation to the mucosal layer; and the mucosa is the functional component in charge of the absorptive and secretory functions of the GI tract. The mucosal wall on itself is divided in three layers: (i) the muscularis mucosa, two thin layers of muscle that creates foldings in the intestinal epithelium to increase the surface area available for nutrient absorption; (ii) the lamina propria comprised by lymph nodes and subepithelial connective tissue; and (iii) the intestinal epithelium, directly responsible for the absorption of water, nutrients, antigens and other compounds from the intestinal lumen (Van de Graaf, 1986; Jaladanki & Wang, 2010).

1.1 Microanatomy of the intestinal epithelium and the intestinal stem cell niche

The organogenesis of the GI tract consists of the patterning of 3 main compartments: fore-, mid- and hindgut. This is achieved through a gradient of differentiation factors along the GI primordium. The caudal type homeobox transcription factor 2 (**CDX2**) has been identified as the master regulator driving the intestinal differentiation program (Gao *et al.*, 2009). CDX2 is ubiquitously expressed across the crypt-villus axis (San Roman *et al.*, 2015). Studies have found the role of CDX2 consists on maintaining a transcription-permissive status on the chromatin allowing for the recruitment of other transcription factors (Verzi *et al.*, 2013). Knock-out experiments have found that the effects from the abrogation of *Cdx2* are stage dependent. In early endoderm it resulted in the aberrant expression of the foregut differentiation program replacing the intestinal epithelial cells with keratinocytes (Gao *et al.*, 2009). In mouse adult intestinal epithelium, the inactivation of Cdx2 did not affect the architecture of the intestinal crypts, although *Cdx2*- intestinal stem cells started to express gastric genes and appeared incapable of differentiating into any of the 4 main intestinal lineages (Stringer *et al.*, 2012). Moreover, *CDX2^{null}* LGR5$^+$ stem cells isolated from intestinal organoids (IOs) differentiated into gastric organoids (Simmini *et al.*, 2014).

The microarchitecture of the small-intestinal epithelium is characterized by two main features: the crypts of Lieberkühn and the villi. The crypt-villus axis regulates the cellular dynamics of the epithelium and is divided in three zones: crypts, transit amplifying zone, and villus (**Figure 1.1**) (Snoeck *et al.*, 2005; Barker *et al.*, 2012). In contrast, the microarchitecture of the colonic epithelium is defined by a

crypt-to-surface axis divided between crypts, transit amplifying zone, and a flat epithelium with no villi (**Figure 1.2**). In addition to this, the cellular composition of the small intestine and the colon is also different; **Table 1.1** summarizes these differences along with the main characteristics of the cellular components of the intestinal epithelium.

The proliferative intestinal stem cell (ISC) population resides at the bottom of the crypts, it divides every 24 hrs, and is responsible for the renewal and regeneration of the intestinal lining. Approximately 10 different crypts are required for the cell renewal of a single villus, which occurs every 2-3 days. In the small intestine, the ISC niche is comprised by 5-6 ISCs intercalated between a pool of Paneth cells, and surrounded by pericryptal intestinal subepithelial myofibroblasts. Together, these provide growth factors and signalling molecules that contribute to the homeostasis, self-renewal, and maintenance of the multipotency of the stem cell population (Barker *et al.*, 2010; Clevers, 2013; Gracz & Magness, 2014). In contrast, the colonic crypts lack Paneth cells, but a subpopulation of cKit$^+$/Reg4$^+$ deep crypt secretory cells have been identified to support the stem cell homeostasis. Deep crypt secretory cells, along with the intestinal subepithelial myofibroblasts, express ligands and growth factors that contribute to the self-renewal and stemness of the proliferative ISC population of the colonic epithelium (Rothenberg *et al.*, 2012; Sasaki *et al.*, 2016). Furthermore, in the position +4 of the small-intestinal crypts, right above the proliferative ISCs, resides a subset of quiescent ISCs. These cells have been reported to be inactive during homeostatic conditions; however, upon an external assault they can re-enter the division cycle, repopulate the proliferative ISC niche, and/or migrate towards the villus to undergo terminal differentiation (Barker *et al.*, 2010; Clevers, 2013; Gracz & Magness, 2014). Notably, this population was found in the crypts of the small intestine but is absent in the colonic crypts (Van Der Heijden & Vermeulen, 2019).

As part of the constant renewal and repopulation of the intestinal lining, proliferative ISCs migrate upward from the crypt and pre-commit towards the secretory or absorptive lineage. These cells are known as transit amplifying cells, they divide every 12-18 hrs and undergo between 4 to 6 division cycles prior to fully differentiating. Their terminal differentiation continue, exiting the crypt and incorporating into the villi as one of the four main cell types: enterocytes, goblet, Paneth or enteroendocrine cells (Clevers, 2013; Carulli *et al.*, 2014).

The function of differentiated cells will be discussed in more detail below. In brief, enterocytes/colonocytes are responsible for the absorption of water, nutrients, and drugs; these cells assemble as a tight impermeable monolayer, exerting a protective barrier against pathogens, antigens, and toxins. Goblet cells produce and secrete mucus as a defence mechanism against pathogens and mechanical shear stress from the flow of the luminar content. Enteroendocrine cells

mediate the communication with the nervous system by secreting peptide hormones in response to changes in the luminal content. Finally, Paneth cells can only be found in the crypts of the small intestine where they produce paracrine growth factors and antimicrobial peptides; as oppose to the previous three, Paneth cells migrate downward into the crypt, contributing to the ISC homeostasis (Trier, 1963; Madara, 1991).

As part of the turnover of the epithelial lining, old cells are shed from the tip of the villus in order to free space for younger cells to occupy. The process of programmed cell death in the intestinal epithelium is termed *anoikis*. The main purpose of this is to dispose of old cells without compromising the barrier integrity. First, the shedding cell detaches from the basement membrane, clinging from the intercellular junctions with neighbouring cells; next, the tight junctions of the surrounding cells rearrange and their cytoplasms stretch beneath the shedding cell; finally, their tight junctions re-join in a zipper motion towards the lumen, releasing the dying cell (Creamer *et al.*, 1961; Williams *et al.*, 2015).

Additionally, the microbiota has recently been acknowledged as an essential component of the intestinal microenvironment. It degrades insoluble dietary fibre, fermenting it into soluble products such as short chain fatty acids (Wong *et al.*, 2006). The microbiota and its metabolic products contribute to the overall homeostasis of the epithelium, provide compounds with protective properties against the onset of colorectal cancer, compete against the invasion of pathogenic bacteria, influence the maturation and differentiation of immunological components, and even regulate the behaviour of the host via the brain-gut-bacteria axis (Sommer & Bäckhed, 2013).
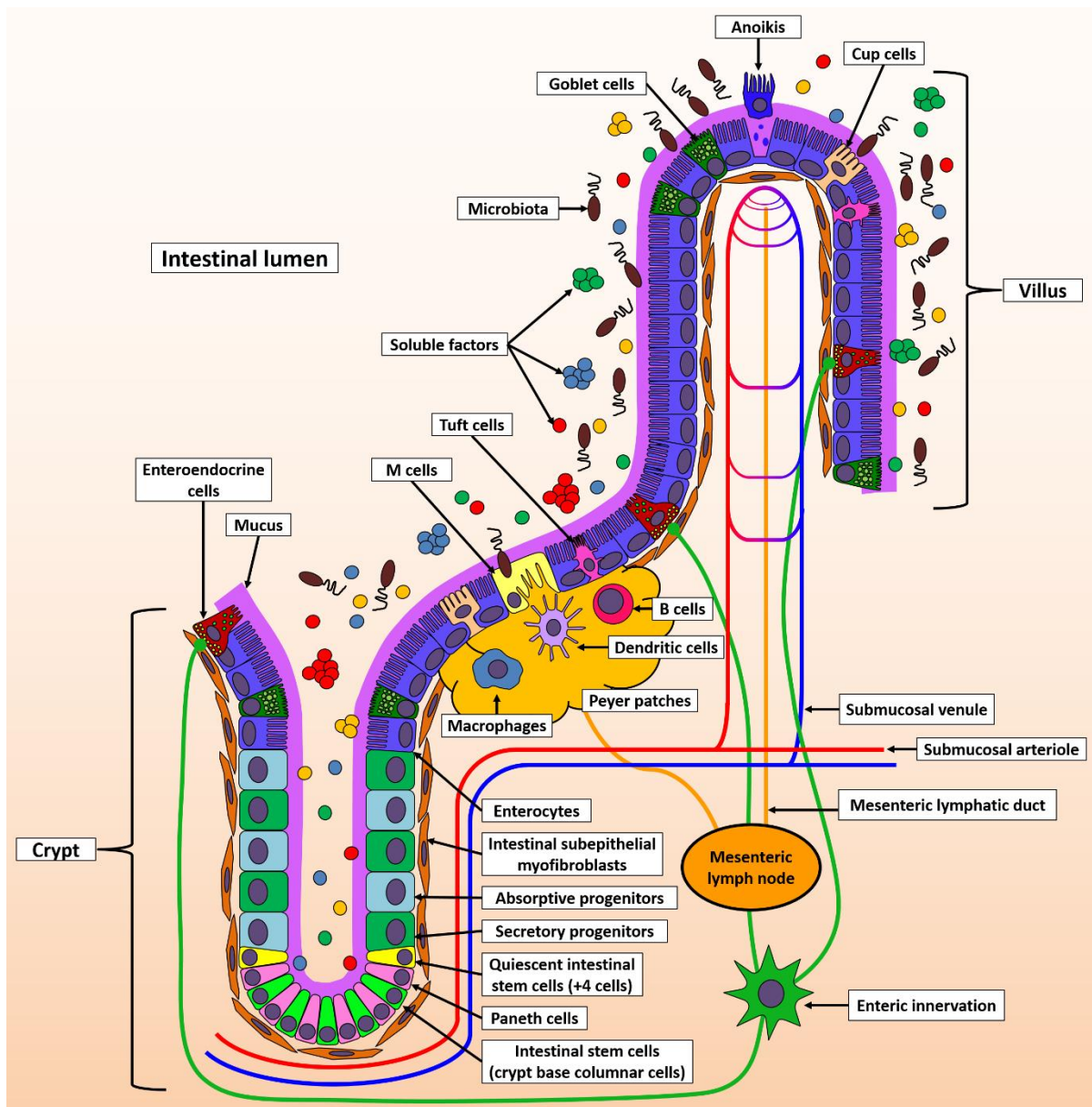
Figure 1.1 Microanatomy of the epithelium in the small intestine.

The dynamics of the intestinal epithelium is reliant on two major microstructures: the crypts of Lieberkühn and the villi. The crypts of Lieberkühn comprise the intestinal stem cell niche, at the bottom of these reside the crypt base columnar cells, which acts as actively dividing intestinal stems cells responsible for the renewal of the intestinal lining. During the early stages of differentiation, the stem cells migrate upward from the crypt and become transit amplifying cells, which are pre-committed towards a secretory or absorptive lineage.

Secretory and absorptive progenitor cells continue migrating up, towards the villi, while undergoing their final differentiation. Absorptive progenitors differentiate into enterocytes whereas the secretory progenitors generate goblet, enteroendocrine and Paneth cells. Furthermore, the intestinal epithelium is also populated by cells responsible for mediating the immune response, these are the M, tuft, and cup cells.

Additional components of the intestinal epithelium include the intestinal subepithelial myofibroblasts, the Peyer's patches, and the microbiota, all of which play a crucial role in regulating the maturation, homeostasis, and regeneration of the epithelial lining.
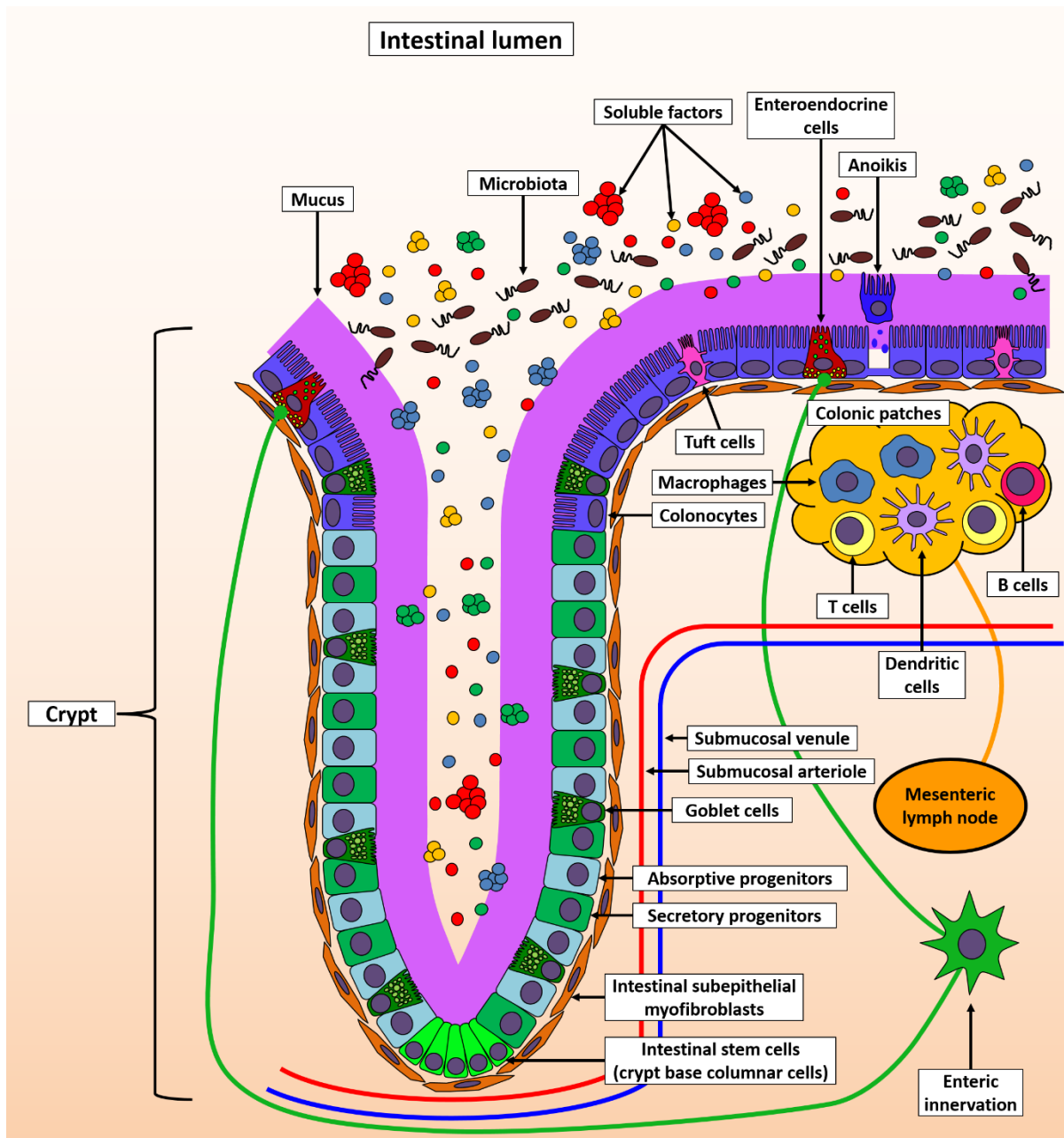
Figure 1.2 Microanatomy of the colonic epithelium.
The microarchitecture of the colonic epithelium is organized in a crypt-to-surface axis where the crypts are straight and deep, and the epithelium is flat and without villi.
The intestinal stem cell population is located at the bottom of the crypts, but it is not intercalated with Paneth cells, as these are absent in the colon. The differentiation process follows a pattern of upward migration along the crypt-to-surface axis. Right above the stem cell population are located the transit amplifying cells which undergo terminal differentiation into the absorptive or secretory lineage. The absorptive lineage gives rise to the colonocytes, and the secretory lineage generates goblet and enteroendocrine cells.
Notably, the population of goblet cells is considerably higher compared to the small intestine, creating a thicker layer of mucus responsible for containing a larger microbiota.
The immunological component of the colonic epithelium includes tuft cells but lacks M cells, and the lymphoid tissue of the colonic patches is considerably smaller compared to its counterpart in the small intestine.
Additionally, the intestinal stem cell niche is supported by pericryptal intestinal subepithelial myofibroblasts which contribute to the homeostasis and proliferation of the stem cell population.

15

Components	Small intestine	Colon	Function	Molecular markers	References
Proliferative stem cells (CBCs)	Yes	Yes	Regenerate the intestinal epithelium	LGR5, ASCL2	(Barker et al., 2007; van der Flier et al., 2009)
Quiescent stem cells (+4 cells)	Yes	No	Regenerate the ISC pool after injury	LRIG1, HOPX, TERT1 and BMI1	(Montgomery & Breault, 2008; Richmond et al., 2018)
Transit amplifying cells (absorptive and secretory)	Yes	Yes	Proliferate to expand the population of differentiated cells	NOTCH1/2 and HES1 (absorptive), and DLL1/4 and ATOH1 (secretory)	(VanDussen et al., 2012; Carulli et al., 2014)
Paneth cells	Yes	No*	Secretion of antimicrobial peptides and signalling molecules for the homeostasis of the ISC niche	DEFA5 and LYZ	(Sato et al., 2011; Clevers & Bevins, 2013)
Absorptive cells	Enterocytes	Colonocytes	Intestinal barrier, and absorption of water, nutrients, and other compounds	VIL1 and ALPI	(Madara, 1991; Snoeck et al., 2005)
Goblet cells	Yes	Yes	Innate immunity through secretion of mucus	MUC2	(Allaire et al., 2018)
Enteroendocrine cells	Yes	Yes	Hormone secretion and transduction of signals between brain and intestinal content	CHGA	(Latorre et al., 2016; Worthington et al., 2018)
Intestinal subepithelial myofibroblasts	Yes	Yes	Structural support and secretion of signalling molecules for the homeostasis of the ISC niche	ACTA2, VIM, and COL1A1	(Andoh et al., 2007; Date & Sato, 2015)
Lymphoid tissue	Peyer's patches	Colonic patches	Intestinal maturation, antigen processing, immunity, and inflammatory response	Variable depending on specific cell types	(Jung et al., 2010; Baptista et al., 2013)
Microfold cells	Yes	No*	Capture and internalization of antigens and microorganisms	VIM above Peyer's patches	(Fujimura & Iida, 2001; Dillon & Lo, 2019)
Tuft cells	Yes	Yes	Initiate innate immune response type 2	DCLK1, TRPM5, and POU2F3	(Gerbe et al., 2016; Howitt et al., 2016)
Cup cells	Yes	No	Unknown	VIM in villi	(Ramirez & Gebert, 2003)
Microbiota	~10^3-10^7 cells/gram of content	Up to 10^{12} cells/gram of content	Intestinal maturation, gut-brain communication, and production of metabolites for the regulation of intestinal homeostasis and inflammation	-	(Sommer & Bäckhed, 2013; Zeng et al., 2019)

Table 1.1 Summarized comparison between the cellular biology of the small and large intestine

*Small numbers have been detected in the cecum and/or in cases of metaplasia induced by inflammatory bowel disease.

1.2 Cellular biology of the intestinal epithelium

1.2.1 Proliferative intestinal stem cells

The crypt base columnar cells (CBCs) were first observed as a cell population adjacent to Paneth cells residing at the bottom of the crypts of Lieberkühn. Initially were described as 'slender undifferentiated cells which show frequent mitosis'. This work proposed that these cells were responsible for the renewal of the Paneth cell population (Cheng *et al.*, 1969). A later study confirmed that the CBCs are a population of multipotent intestinal stem cells responsible for the renewal and differentiation of the 4 main differentiated cell types (Cheng & Leblond, 1974).

Further work identified leucine-rich-repeat-containing G-protein-coupled receptor 5 (**LGR5**) as a molecular marker, exclusively expressed by CBCs in the small intestine and colon (Barker *et al.*, 2007). The first model of human intestinal organoids (HIOs) found that isolated individual Lgr5$^+$ ISCs embedded in a rich semisolid extracellular matrix were capable of self-organizing into three-dimensional (3D) structures that exhibit all major differentiated cell types of the intestinal epithelium (Sato *et al.*, 2009). However, later studies reported important constraints in the detection of LGR5 mRNA or protein due to the low levels of expression (van der Flier *et al.*, 2009*b*). Microarray profiling was used to identify the gene expression signature of LGR5$^+$ ISCs. The results of this study found 2 new candidates of molecular markers to identify the CBC population: the Achaete-scute-like 2 transcription factor (**Ascl2**) and olfactomedin (**Olfm4**) (Muñoz *et al.*, 2012; Barker, 2014).

Ascl2 was found to be directly regulated by the WNT signalling pathway, as opposed to other *Ascl* genes which are known targets of the Notch pathway. The experimental evidence demonstrated it is essential for the maintenance of the multipotency of LGR5$^+$ ISCs; furthermore, aberrant expression of *Ascl2* in non-stem cells led to crypt hyperplasia and disruption of the normal architecture of the villi (van der Flier *et al.*, 2009*a*).

Olfm4 on the other hand, is a WNT-independent marker identified through gene expression profiling of LGR5$^+$ ISCs. Its function has not been entirely characterized, however it has been found to be highly expressed in LGR5$^+$ ISCs from the small intestine and colon, and in a subset of cells within colorectal carcinoma samples (van der Flier *et al.*, 2009*b*).

1.2.2 Quiescent intestinal stem cells

After CBCs were proposed as the putative ISC population, further studies identified a subpopulation of putative quiescent ISCs, found only in the small intestine, at position +4 above the Paneth cells. These slow-cycling cells were characterized by the long-term retention of radiolabelled DNA (Potten, 1977; Van Der Heijden & Vermeulen, 2019). Later experiments used irradiation of the intestinal crypts,

which resulted in the identification of two stem cell subpopulations. The most radiosensitive population was eventually depleted; conversely, a different quiescent subpopulation was recruited from G0 back into the cell cycle and contributed to the partial repopulation of the crypts (Potten *et al.*, 1984). A recent study evaluated the functionality of proliferative and quiescent ISCs in a model of inflammation. Their results showed that proliferative ISCs were more sensitive to the inflammatory stress, while quiescent ISCs were more resistant and contributed to the regeneration of the tissue (Richmond *et al.*, 2018).

The study of quiescent ISCs has been limited due to the lack of a good molecular marker that allows the accurate identification of this subpopulation. Different molecular markers have been proposed: LRIG1, HOPX, SOX9, TERT1 and BMI1; though their accuracy is still in question due to reports of expression in unrelated cells (Montgomery & Breault, 2008).

The proto-oncogene polycomb complex protein, **B** cell-specific **M**oloney murine leukaemia virus **I**ntegration site 1 (**BMI1**) protein is one of the most accepted markers for quiescent ISCs. *Bmi1* was found expressed by the +4 stem cell population (Sangiorgi & Capecchi, 2008). Later it was confirmed that *Lgr5* and *Bmi1* marked 2 different ISC populations. The first one was found in Wnt-responsive, mitotically active cells. Whereas the latter, identified the quiescent population that were unresponsive to Wnt (Yan *et al.*, 2012).

Additionally, the mouse telomerase reverse transcriptase (**mTert**) is expressed by a subset of slow cycling cells. These cells reside at a similar position as the long-term label-retaining cells described by Potten *et al.* (1984). Moreover, mTert^{+} cells can differentiate into all intestinal cell types, and can regenerate the epithelium after injury (Montgomery *et al.*, 2011).

Notably, a recent study concluded that BMI1^{+} cells are not a dedicated population of quiescent stem cells, as it has been thought so far. This work indicated that BMI1^{+} is marking preterminal enteroendocrine cells. These secretory progenitor cells respond upon loss of the native LGR5^{+} ISCs, undergo a chromatin rearrangement which allows them to dedifferentiate and replenish the LGR5^{+} ISCs (Jadhav *et al.*, 2017).

1.2.3 Transit amplifying cells

The transit amplifying cells (TACs) are responsible for amplifying the reservoir of cells produced by the stem cells in both the small intestine and the colon. TACs are a specific subpopulation mostly found in tissues with high turnover such as the epidermis, hair follicles, cornea, prostate, mammary glands, and the GI tract. Due to the constant regeneration of these tissues, the stem cells are unable to cope with the workload. Consequently, TACs come into play by going through 4 to 6 division cycles prior to their

final differentiation, in order to maintain a pool of multipotent progenitors (Carulli *et al.*, 2014; Rangel-Huerta & Maldonado, 2017).

In the GI tract, TACs are located midway down the crypts and are contribute to the rapid reepithelialization of the intestinal lining. The cell fate is decided through the process of lateral inhibition orchestrated by the Notch signalling pathway. This determines whether a cell commits towards the absorptive or the secretory lineage (van Es *et al.*, 2012). The absorptive progenitors express NOTCH1 and 2, while the adjacent secretory progenitors express the Delta-like canonical NOTCH ligands 1 and 4 (**DLL1 and 4**). The activation of Notch signalling pathway in the absorptive progenitors leads to the expression of HES1 and the differentiation of enterocytes. Conversely, the secretory precursors lack of NOTCH receptors preventing the expression of HES1 and allowing the expression of ATOH1. Goblet, Paneth and enteroendocrine cells, derive from a common ATOH1^{+} precursor (VanDussen *et al.*, 2012; Noah & Shroyer, 2013; Demitrack & Samuelson, 2016).

The hairy and enhancer split of proteins, bHLH transcription factor 1 (**HES1**) is a transcriptional repressor of ATOH1, and has been associated with maintaining the self-renewal potential in LGR5^{+} ISCs (Goto *et al.*, 2017). It has been reported that loss-of-function mutation of *HES1* led to an increase in the proliferation of secretory cells (Zecchini *et al.*, 2005; VanDussen *et al.*, 2012). However, other reports have found that mutation in *HES1* alone is insufficient to alter the differentiation of TACs and other effectors such as *HES3 and HES5* may come into play to compensate for the loss of *HES1* (Ueo *et al.*, 2012).

The atonal homolog, bHLH transcription factor 1 (**ATOH1**) is a transcription factor commonly known for its proneural activity and is also involved in the differentiation of the secretory lineage of intestinal cells (Mulvaney & Dabdoub, 2012). Studies have found that the abrogation of ATOH1 leads to the depletion of goblet, enteroendocrine, and Paneth cells (Yang *et al.*, 2001; Shroyer *et al.*, 2007). Furthermore, overexpression of Math1, the mouse homolog of ATOH1, leads to the expansion of the secretory lineage, the depletion of the absorptive cells, and an overall inhibition in cell proliferation (VanDussen & Samuelson, 2010)

1.2.4 Absorptive cells

Enterocytes (small intestine) or colonocytes (colon) constitute the most abundant cell population on the intestinal epithelium. They are characterized for their columnar morphology and apical microvilli. Their main role is the absorption and transport of water, nutrients, and drugs into the basolateral compartment. These cells assemble as an intact monolayer interconnected by tight junctions, that

restrict the free flow of molecules into the cell, providing a protective barrier against harmful agents (Trier, 1963; Madara, 1991).

Enterocytes/colonocytes are characterized by the expression of villin 1 and 2 (**VIL1 and VIL2**), and a variety of brush border hydrolases such as intestinal alkaline phosphatase (**ALPI**), sucrase-isomaltase, lactase, aminopeptidase. Villin and ALPI are commonly used as molecular markers to identify the presence of functional differentiated absorptive cells in models of the intestinal epithelium (Hidalgo *et al.*, 1989; Madara, 1991).

Villin plays an essential role in reshaping the actin microfilaments of the cytoskeleton to assemble the microvilli of the brush border (Hodin *et al.*, 1997). Conventionally, the microvilli have only been considered as a mean to increase bioavailable surface area to uptake compounds from the lumen; however, novel insights into the structure and physiology of the microvilli have suggested these structures might play an active role as a vesicle-generating organelle. Proteomic analysis of the vesicular content found a mix of brush border hydrolases, particularly ALPI. It has been speculated the role of the catalytic vesicles might be related to nutrient processing or host defence (McConnell *et al.*, 2009).

The barrier function requires a fine balance in which nutrients and macromolecules must be assimilated without up taking pathogens, toxins, and antigens from the luminal milieu. The microvilli express apical mucin-like glycoproteins that create a glycocalyx over the brush border. The glycocalyx, prevents direct contact between the microvilli and pathogens, it also contributes to the digestion and degradation of nutrients. Furthermore, previous reports have suggested that enterocytes may act as antigen presenting cells. Harmful compounds are absorbed and degraded by lysosomes, then the processed antigen is presented to intra epithelial lymphocytes and T cells in the lamina propria through basolateral projections (Snoeck *et al.*, 2005).

The absorption of compounds from the intestinal lumen is performed by two different routes: transcellular and paracellular transport. The transcellular route requires the compounds to cross from the intestinal lumen through the epithelial barrier into the basolateral compartment. There are three different mechanisms for this: i) passive transcellular diffusion, which occurs when low-molecular-weight compounds are sufficiently lipophilic to rapidly cross through the cell membranes based on a concentration gradient; ii) carrier-mediated active transcellular transport, which uses energy to internalize specific substrates in spite of the concentration gradient; and iii) endocytosis, which consists on the internalization of proteins and other macromolecules through vesicle encapsulation. Alternatively, in the paracellular route, compounds are absorbed by passive diffusion through the

intercellular spaces between the tight junctions of the intestinal epithelium; this pathway operates mostly over hydrophilic compounds incapable of going through the lipid membrane (Watts & Fasano, 2000).

1.2.5 Goblet cells

Goblet cells are the second most abundant cell type, representing 10-15% of the cells in the small-intestinal epithelium, and up to 50% in the large intestine. These are vacuolated mucus-secreting cells mainly characterized by the expression of mucins **MUC2 and 5B** (Trier, 1963; Madara, 1991; Noah *et al.*, 2011). Mucins are gel-forming glycoproteins firmly attached to the epithelium that work as a decoy for bacterial adhesins and even carry antimicrobial molecules. The mucus layer is the first line of defence against antigens and microorganisms, preventing them from contacting the intestinal epithelium. Additionally, it has been proposed that the formation of a thicker layer of mucus in the colon is a consequence of the larger population of microorganisms residing in the large intestine (Pelaseyed *et al.*, 2014; Allaire *et al.*, 2018).

Goblet cells play a major role in the defence of the host against pathogenic compounds in the lumen. They have been reported to modulate the composition of the mucus layer in order to modulate the composition of the microbiota (Allaire *et al.*, 2018). Moreover, aside from the secretory functions, some studies have reported the uptake of luminal antigens by the goblet cells, to then present it to dendritic cells near the basolateral compartment (Birchenough *et al.*, 2015).

1.2.6 Enteroendocrine cells

Enteroendocrine cells (EECs) represent 1% of the cell population in the small-intestinal epithelium, and according to some reports up to 5% in the colonic epithelium. EECs act as neuroendocrine transducers to regulate food intake and intestinal motility. Morphologically they are granulated cells with apical microvilli that allows them to sense biochemical changes in the intestinal content to modulate the secretion of peptide hormones. At least 15 different types of EECs have been described, each one with different sensitivity to different macronutrients, leading to the secretion of more than 50 different peptides. This has resulted in the GI being referred as the largest endocrine organ in the body (Schonhoff *et al.*, 2004; Geibel, 2005; Gunawardene *et al.*, 2011; Latorre *et al.*, 2016; Worthington *et al.*, 2018).

EECs are an essential component of the brain-gut bidirectional communication system. The basolateral portion of the EECs is in close proximity with the afferent terminals of the vagus nerve, and communicate with it through the secretion of 4 peptides: cholecystokinin (CCK), ghrelin, peptide YY (PYY), and glucagon-like peptide (GLP1) (Latorre *et al.*, 2016; Martin *et al.*, 2018).

EECs are derived from an ATOH1^{+} precursor, however it has been reported that the expression of neurogenin 3 (NGN3) is also essential for the differentiation of EECs. NGN3 is a gene target from ATOH1 and studies have found that NGN3 is required for the proper development of endocrine cells, however these cells have been found with absent expression of NGN3. Two possibilities have been suggested, either EECs derive from a short-lived NGN3+ progenitor, or NGN3 is expressed by neighbouring cells that provide the conditions for the differentiation of EECs (Schonhoff *et al.*, 2004; Bjerknes & Cheng, 2006). Furthermore, transgenic overexpression of NGN3 has been used to induce the differentiation of EECs in models of IOs (Spence *et al.*, 2011).

The identification of EECs has been conducted through the expression of chromogranin A (**CHGA**), a protein associated with the formation of neuroendocrine secretory vesicles (Worthington *et al.*, 2018).

1.2.7 Paneth cells

Paneth cells are part of the innate immune system and an essential component for the maintenance of the cryptal homeostasis. These belong to the secretory lineage of the small-intestinal epithelium, but are absent in the colonic crypts, except for cases of Paneth cell metaplasia caused by inflammatory diseases (Elphick & Mahida, 2005). As oppose to the rest of the differentiated cells, Paneth cells migrate downward into the crypts where they survive for 6 to 8 weeks. They are characterized by the expression of antibacterial peptides such as α-Defensin 5 (**DEFA5**) and lysozyme (**LYZ**) (Clevers & Bevins, 2013).

Studies in IOs, found that the co-culture of Paneth cells with ISCs, considerably improved the organoid output. Also, abrogation of the Paneth population led to the loss of the LGR5^{+} ISCs (Sato *et al.*, 2011*a*). Furthermore, Paneth cells have shown to play an active role in epithelial regeneration upon tissue damage. This process is accompanied by a switch in the expression program, activating BMI1 and turning down the Paneth identity (Roth *et al.*, 2012)

1.2.8 Intestinal subepithelial myofibroblasts

Intestinal subepithelial myofibroblasts (ISEMFs) are a network of peri cryptal cells found in the extracellular matrix (ECM). They have been shown to interact with the intestinal stem cell niche through WNT, NOTCH, and BMP signalling. Previous studies have speculated about the source on WNT ligands in the intestinal crypt, the two major candidates being the Paneth cells and the ISEMFs. Double knockout experiments found neither of them are essential for the maintenance of the WNT induction, therefore remaining unclear where exactly is it coming from (San Roman *et al.*, 2014). However, ISEMFs have been implicated in the production of R-spondin 1, an enhancer of WNT activation essential for the maintenance of the crypt homeostasis (Date & Sato, 2015).

Furthermore, the secretion of ECM components by ISEMFs is regulated by proinflammatory factors. In Crohn's disease the abundance of proinflammatory signals induces the ISEMFs to secrete ECM component which modify the stiffness in the microenvironment leading to fibrosis of the tissue (Andoh *et al.*, 2007; de Bruyn *et al.*, 2018).

ISEMFs are cells from a mesenchymal origin, therefore have been found to express molecular markers such as: α – smooth muscle actin (**ACTA2**), vimentin (**VIM**), and collagen 1A1 (**COL1A1**) (Andoh *et al.*, 2007; Jabaji *et al.*, 2014).

1.2.9 Mucosa-associated lymphoid tissue

The mucosal-associated lymphoid tissue (MALT) is a secondary lymphoid organ and refers to the organized aggregates of lymphoid tissue responsible for mounting the immunological response on mucosal surfaces. Depending on its location MALT can also be referred as GALT (gut-), NALT (nasopharynx-), or BALT (bronchus-) (Elmore, 2006). This study is only concerned with the GALT, which in the small intestine is represented by the Peyer's patches, and in the large intestine by the colonic patches.

1.2.10 Peyer's patches

The Peyer's patches (PP) are multicellular tissue aggregates formed *in utero* but matured after birth, following the exposure with antigens from the microbiome. They are mostly found in the ileum, with ~46% being concentrated in the distal ileum, though they have also been detected in the duodenum and jejunum. PPs are mediate the interaction of the microbiome with the immune system and are responsible for the formation of the adaptive immune response, i.e., the maturation of B cells into antibody producing cells. Furthermore, early studies in human tissue have detected secreted forms of IgM and IgA, and all forms of cellular Ig, except for IgD (Spencer *et al.*, 1986; Jung *et al.*, 2010; Reboldi & Cyster, 2016).

The cellular composition of the PPs has been poorly studied in humans due to limited availability of endoscopy samples, however, in mouse the PPs have been properly characterized. In this case, it has been reported the PPs are comprised by 60% of B cells, 25% T cells, 10% dendritic cells, and 5% macrophages. The T cell population on itself is comprised by 45% T helper, 35% cytotoxic T, and 20% not defined (CD4$^-$/CD8$^-$) (Jung *et al.*, 2010).

Morphologically, the PPs are comprised by three compartments: the lymphoid follicle or follicular area, the interfollicular zone, and the follicle-associated epithelium. The lymphoid follicle is divided between the germinal centre, the corona, and the dome. The germinal centre (GC) contains lymphoid

follicle cores which are responsible for its protrusion into the lumen of the intestinal epithelium. Within the GC reside immature undifferentiated B cells, follicular dendritic cells, and some macrophages. The corona or subepithelial dome present a mix of macrophages, B, T, and dendritic cells. PP dendritic cells are highly specialized in the internalization, processing, and presentation of antigens to the immune cells. In this area, undifferentiated B cells are exposed to antigens sampled by M cells from the luminal milieu, and since the corona is connected by lymphatic vessels, it supplies the body with differentiated B cells. The interfollicular zone is mostly populated by T cells, and lysozyme-expressing dendritic cells and macrophages. The follicle-associated epithelium (FAE) consists of a monolayer of intestinal epithelium, mainly enterocytes and M cells, which separate the luminal microenvironment from the lymphoid tissue. In some instances, it has been observed the presence of macrophage, dendritic and/or lymphoid infiltrates. This particular section of epithelium does not contain subepithelial myofibroblasts and is in direct contact with the lymphoid tissue of the dome (Jung *et al.*, 2010; Williams & Owen, 2015; Reboldi & Cyster, 2016; Da Silva *et al.*, 2017).

1.2.11 Colonic patches

The colonic patches (CP) are the colonic homologue of the PP, similarly these are comprised by aggregates of lymphoid follicles divided into separate compartments of B and T cells. However, it has been noted that compared to PPs, CPs are smaller and present less follicles with smaller GCs. In addition to B and T cells, CPs contain dendritic and stromal cells; some works have reported the presence of M cells, but it is unclear if these just occur in significantly low numbers or arise in response to inflammatory induction (Owen *et al.*, 1991; Baptista *et al.*, 2013).

Previous works have suggested that a distinctive role of CPs is to drive the colonic inflammation in cases of ulcerative colitis. In this case the immune response elicited by T helper 2 cells triggers the release of pro inflammatory cytokines such as TNFα. Interestingly, it was reported that TNFα induced the development of M cells which in turn increased the access of luminal bacteria into the *lamina propria* of the colon. It is unclear if the bacterial infiltration serves a purpose in the regulation of the immune response, or it just worsens the inflammatory reaction (Dohi *et al.*, 2001; Bennett *et al.*, 2016).

1.2.12 M cells

Microfold cells or M cells are a key component in the immunosurveillance of the intestinal epithelium, and function as the gatekeepers that mediate the interaction of the microbiome with the enteric immune system. These cells are specialized in the phagocytosis and transcytosis of microorganisms and antigens from the luminal compartment into the underlying lymphoid tissue. They exhibit a

unique morphology in which the apical surface is irregularly shaped as a membrane or microfolding. In contrast, the basolateral compartment is invaginated, creating a pocket for the interaction with lymphoid and myeloid cells (Gebert *et al.*, 1996; Mabbott *et al.*, 2013; Ohno, 2016; Dillon & Lo, 2019).

M cells are part of the FAE and rest above the domes of the PPs in the small-intestinal epithelium (Gebert *et al.*, 1996; Mabbott *et al.*, 2013; Ohno, 2016). Previous studies have identified **VIM** as a molecular marker for the detection of M cells overlying the domes of the PPs (Gebert *et al.*, 1992; Jepson *et al.*, 1992; Fujimura & Iida, 2001). The presence of M cells in the large intestine has been reported only in the colonic patches, though it has seldomly been mentioned under normal conditions (Owen *et al.*, 1991; Lochner, 2011; Baptista *et al.*, 2013). In contrast, studies declaring to the presence of M cells in the colon usually refer to cases of inflammatory bowel disease and lymphoid hyperplasia (Fujimura *et al.*, 1992; Bennett *et al.*, 2016). However, this is the result of an aberrant differentiation and carries its own problematics given that the internalization of bacteria without the support of organized lymphoid tissue could contribute to the worsening of the inflammatory process (Dillon & Lo, 2019).

The origin of M cells has not been conclusively defined until now, the two main hypothesis suggest that M cells originate either from the trans differentiation of dome-associated mature enterocytes into M cells, or through the standard differentiation process of cryptal stem cells (Fujimura *et al.*, 1992; Corr *et al.*, 2008). Previous studies have reported the conversion of enterocytes into M cells following their interaction with lymphoid tissue (Kernéis *et al.*, 1997) or microbial exposure (Borghesi *et al.*, 1999). Following these works, other studies have disputed their conclusions; one of these studies traced the origin of the immunofluorescent signature of early immature M cells to the proliferative compartment of the intestinal crypts (Lelouard *et al.*, 2001). Another work generated intestinal stem cell cultures and achieved the differentiation of M cells using the receptor activator of NF-κB ligand (RANKL) (Rouch *et al.*, 2016). Alternatively, it is possible both mechanisms are valid and occur under different circumstances.

Currently, M cells are under study for their role in the maturation of IgA secreting B cells in the process of preserving the homeostasis of the intestinal microflora (Rios *et al.*, 2016); and as targets for the delivery of antigens in the development of new oral vaccines (Jia *et al.*, 2021).

1.2.13 Cup cells

The cup cells are a poorly understood intestinal subpopulation with no assigned function until now. The name derived from the slight cup-like indentation observed at the brush border created by their shorter microvilli, compared to adjacent enterocytes. Originally, cup cells were found in the villous

epithelium of the small intestine and represented ~6% of the cell population in samples of rabbit and guinea pig ileum, whereas in primates these were even more scarce (<2%). Further characterization described very low alkaline phosphatase activity at the brush border, poor lipid absorption, and no apparent transcellular permeability, although membrane-bound molecules were up taken through pinocytosis (Madara, 1982). A follow-up study found that, in guinea pigs, cup cells served as an adhesion point for certain bacilli, however this was not followed by internalization of the microbes or recruitment of inflammatory cells (Madara & Carlson, 1985).

Later, cup-like cells with similar features to the ones found in rabbit and guinea pig were reported in samples of human ileum. Notably, human cup cells were found more frequently in the jejunum, contrary to other mammals in which cup cells resided mostly in the ileum. According to the authors, human cup cells showed similar characteristics to immature M cells, although mature M cells had not been observed scattered in the villi, as oppose to the cup cells (Finzi *et al.*, 1993).

The first studies reporting the existence of the cup cells could only distinguish them through rough morphological features such as: the length and indentation of the microvilli at the brush border, slight staining differences using toluidine blue, and by the presence of linear arrays of intramembrane particles in the microvilli (Madara, 1982). A later study reported the expression of vimentin by cup and M cell, but not goblet and absorptive cells; thus, **VIM** was proposed as a potential molecular marker for the detection of cup cells. (Fujimura & Iida, 2001). Another work confirmed that the vimentin-positive cells at the villous epithelium were in fact cup cells, whereas the ones in the domes of Peyer's patches were M cells. Additionally, it was suggested that the linear intramembrane particle arrays in the microvilli could work as complementary glycoconjugate for the specific binding of **lectins LEA and STA**. Consequently, the function of these lectin-binding sites could be related to the aforementioned bacterial attachment, or to serve as receptors for regulatory function and/or luminal sensing. Overall, this study proposed three potential markers for the identification of cup cells: vimentin, and lectins LEA and STA (Ramirez & Gebert, 2003).

1.2.14 Tuft cells

Intestinal tuft cells, also known as caveolated or fibrillo-caveolated, have been described as bottle-shaped, highly vesiculated cells with large apical microvilli, and according to some reports also lateral microvilli. Cells with similar characteristics and functions have been found in different tissues under different denominations such as brush cells (airway and gall bladder), chemosensory cells (nasopharyngeal and thymus), and microvillous cells (olfactory). Tuft cells appear as isolated intraepithelial cells, representing 0.4-2% of the epithelium in the small intestine, cecum, and colon. Notably, the majority of the current knowledge on tuft cells is derived from mouse models (von

Moltke, 2018; Schneider *et al.*, 2019; Ting & von Moltke, 2019). In a previous correspondence it was emphasized that differentiated tuft cells were characterized by the expression of a highly specific marker, the doublecortin-like kinase 1 (**Dclk1**), also referred as doublecortin and calcium/ calmodulin-dependent protein kinase-like-1 (Dcamkl1) (Gerbe *et al.*, 2009). Two main functions have been explored in tuft cells: the establishment of a communication route between the luminal milieu and the nervous system, and its role in the regulation of type 2 immunity.

Earlier studies identified a chemosensory population of intestinal brush (tuft) cells expressing the transient receptor potential cation channel subfamily M member 5 (**Trpm5**), which is normally found in taste cells. Trpm5$^+$ cells were innervated suggesting some form of communication with the nervous system (central or enteric). Further analysis identified the expression of a large array of signalling components which would allow the cell to establish a bilateral feedback between the luminal content and the nervous system. (Bezençon *et al.*, 2008)

Another study the relationship between commensal and pathogenic microorganisms and tuft cells. Their findings indicated that the proportion of tuft cells in the intestinal epithelium is dependent on the composition of the microbiota. Additionally, given that previous works had identified the expression of chemosensory receptors in tuft cells, following experiments evaluated their role in the response toward parasitic infections. The results showed that the ablation of taste/chemosensory components such as gustducin and Trpm5 produced a significant reduction of tuft cells. Furthermore, *Trpm5$^{-/-}$* mice also failed to properly clear the parasitic infection, suggesting a link between the chemosensory components of tuft cells and the initiation of type 2 immune response mediated by these cells (Howitt *et al.*, 2016).

Another work studied the role of tuft cells in the orchestration of the immune response in the intestinal epithelium against helminth parasitic infections. It was observed that helminth infection resulted in a significant expansion of Dclk1$^+$ tuft cells. Also, using a *Pou2f3$^{-/-}$* mouse model, it was found that this transcription factor is critical for the development of tuft cells and other chemosensory cells in the tongue and olfactory epithelium. Furthermore, the anti-helminthic response and the secretion of interleukin 25 (IL-25) as part of the initiation of type 2 immunity was significantly lower and delayed in *Pou2f3$^{-/-}$* compared to *Pou2f3$^{+/+}$*. In conjunction, this study showed that *Pou2f3* knockout resulted in the ablation of the tuft population, and in consequence there was a significant delay in the initiation of the type 2 cell-mediated immune response. Notably, the expression of **Pou2f3** and **IL-25** was specific to tuft cells, and therefore have been proposed as potential molecular markers for this subpopulation (Gerbe *et al.*, 2016).

Overall, these studies have outlined the potential role of tuft cells in sensing changes in the microbiota, and in eliciting the type 2 cell-mediated immune response. Additionally, recent studies have implicated the participation of tuft cells in dampening the inflammatory response, contributing to the regenerative response of the epithelium after injury, and preserving the integrity of the epithelial barrier (May *et al.*, 2014; Steele *et al.*, 2016; Yi *et al.*, 2019)

1.2.15 Intestinal microbiota

The human intestinal microbiota is comprised by 10-100 trillion microorganisms between bacteria, archaea, protozoans, and viruses. It has been estimated that the human intestinal microbiota is comprised by 500-1000 species, mostly anaerobic and facultative anaerobic, from the phyla *Firmicutes*, *Bacteroidetes*, *Actinobacteria*, *Verrucomicrobia*, *Proteobacteria*, *Fusobacteria*, and *Cyanobacteria*. Formerly it was believed the microbiota first entered the organism through the birth canal, however recent studies have proposed intrauterine exposure from the placenta and amniotic liquid. The concentration of microorganisms has been reported to increase along the GI tract, starting with few scattered cells in the stomach, then a few thousand at the duodenum, and ultimately up to 10^{12} microorganisms per gram of intestinal content at the colon (Sommer & Bäckhed, 2013; Stiemsma & Michels, 2018).

Research into the exact composition and function of the microbiota has been limited, since ~80% of the microorganism cannot survive outside of the body and therefore cannot be cultured and studied. Most research on the microbiota is conducted through bulk experimental approaches e.g., metagenomic analysis, germ-free mouse models, microbiota/faecal transplant, antibiotic-induced dysbiosis, and probiotic stimulation. However, due to the high variability in the composition of the microbiota between individuals, and the even larger variability in the gene expression, current studies have reported significant limitations in reproducibility of the results. Also, this is even more troublesome when translating the results obtained in animal models, into human subjects (Mosca *et al.*, 2016; Martin *et al.*, 2018).

The microbiota communicates with its host through the release of secondary bile acids, SCFAs, and other metabolic by products. Secondary bile acids (deoxycholic acid (DA) and lithocholic acid (LA)) are produced by the microbiota following the metabolism of primary bile acids (cholic acid (CA), chenodeoxycholic acid (CDCA), and ursodeoxycholic acid (UDCA)) which are produced by the liver (Ridlon *et al.*, 2014). Short-chain fatty acids (SCFAs) are produced from the fermentation of dietary fibre into simple soluble compounds, mainly acetate, propionate, and butyrate (Wong *et al.*, 2006). Other bioactive metabolic products from the microbiota include vitamins, amino acid, lipids, and tryptophan secondary metabolites. Overall these compounds, and by extension the microbiota, have

been found to play a role in gut-brain communication, regulation of immune response and inflammation, and colorectal cancer (Zeng *et al.*, 2019).

The brain-gut-microbiota axis describes a line of bilateral communication encompassing the synthesis of neurotransmitters by the central nervous system, the intestinal motility and hormone secretion of the intestinal epithelium, and the population dynamics and gene expression changes of the microbiota. Metabolites from the microbiota are perceived by enteroendocrine cells resulting in the secretion of hormones responsible for the satiety sensation, glucose metabolism, and the synthesis of serotonin. These interactions describe the mechanism by which the intestinal microbiota can influence the food intake, obesity, metabolism, and behavioural changes. Furthermore, studies have reported the administration of probiotic bacteria *Lactobacillus* and *Bifidobacterium* produced significant improvements particularly in the reduction of stress-, anxiety-, and obsessive-compulsive-like behaviour, and even schizophrenia (Martin *et al.*, 2018; Mörkl *et al.*, 2020).

As mentioned before, GALT is in charge of sampling microorganisms from the lumen and induce the secretion of IgA, thereby maintaining the homeostasis between the microbial population and the intestinal epithelium. Disruption in the balance of the bacterial populations comprising the microbiota have been associated with the development of inflammatory bowel disease (IBD). An increase in the proportion of *Enterobacteriaceae* and/or a decrease in the population of *Bacteroidetes* and *Firmicutes* have been linked to the onset of IBD. This could be an effect of the depletion of butyrate-producing bacteria (*Bacteroidetes* and *Firmicutes*), which has been reported to supress NF-κB signalling (Wang *et al.*, 2020)

Moreover, previous works have studied the relationship between diet, microbiota, and the risk of colorectal carcinogenesis. The Western diet has been linked to the accumulation of secondary bile acids, such as DCA and LCA, produced by different species of *Clostridium*. Consequently, this has been associated with the activation of WNT pathway and NF-κB signalling, thereby triggering hyperproliferation, inflammatory response, oxidative damage, and deregulation of the cell cycle (Ridlon *et al.*, 2014; Zeng *et al.*, 2019). In contrast, SCFAs such as butyrate and propionate have shown anti-cancer properties by inhibiting histone deacetylases. Also, metabolites produced by *Lactobacillus casei* have shown to inhibit tumoral growth through the induction of apoptosis. Along with these findings, colorectal cancer (CRC) patients have shown depletion butyrate-producing bacterial populations, particularly *Bacteroidetes* and *Firmicutes* (Zitvogel *et al.*, 2015; Vivarelli *et al.*, 2019).

This evidence highlights the role of the microbiota in the development, maturation, and homeostasis of the gut. Consequently, it has justified the pursuit of integrating this component into current models of the intestinal epithelium.

1.3 Cellular dynamics and signalling pathways involved in the renewal and differentiation of the intestinal stem cell niche

1.3.1 Cell fate dynamics in the intestinal stem cell niche

The regeneration of the intestinal epithelium is maintained by the stem cell population at the bottom of the crypts of Lieberkühn. In homeostasis, the ISC population needs to preserve a balance between the self-renewal of the stem cell pool and the differentiation of cells to replenish the epithelium. Different hypotheses have speculated how the ISC population discern the fate decisions, while preserving a constant pool of stem cells in the niche. Originally it was suggested the cells in the crypt followed a hierarchical model. In this scenario an long-living stem cell divides asymmetrically, thereby releasing a cell into the differentiation pathway while maintaining a constant ISC population (Winton & Ponder, 1990; Quyn *et al.*, 2010). However, this notion ignored the phenomenon of monoclonal conversion, whereby ISCs within the crypt tend to become monophenotypic (clonal) after a period of time.

Later, Winton's group proposed a new model of neutral drift to explain the monoclonal conversion and the balance in the ISC pool. This study found that the stem cell pool in the small intestine and colon, behaves as a coordinated asymmetric population, in which some cells undergo asymmetric division, while others divide symmetrically either toward differentiation or proliferation. In this scenario, the proliferative cells compensate the imbalance left by the cells in differentiation. The monoclonal conversion and the cell fate decision process obeys a model of neutral drift, i.e., a stochastic phenomenon between equipotent stem cells, with no signs of competitive advantages. This results in monoclonal crypts that supply neighbouring villi with a stream of clonal cells migrating through the crypt-villus differentiation axis, and every villus is comprised by clones from several different crypts (Lopez-Garcia *et al.*, 2010). The neutral drift model was confirmed by Clevers' group using a multicolour reporter; additionally, this work suggested that symmetrical divisions were dominant in the crypt dynamic (Snippert *et al.*, 2010). However, a recent study disputed this last conclusion, and proposed the actual dominant division in the crypt is asymmetrical (Sei *et al.*, 2019).

The model of neutral drift has been accepted for the prediction of intestinal stem cell dynamics under homeostatic conditions; however, in disruptive scenarios such as the onset of colorectal cancer, this model does not fit anymore. The accumulation of oncogenic mutations such as *APC* loss, *KRAS* activation, and *TP53* mutations can confer clonal growth and survival advantages. Therefore, a biased drift model has been used to better describe the cellular dynamic in the early stages of colorectal carcinogenesis. To evaluate the effect of oncogenic mutations in the monoclonal conversion of the crypts, the bias drift model considers the number of stem cells, the turnover rate to replace each stem

cell per day, and the probability of replacement (P_R). The latter is disregarded in the neutral drift model since the P_R between two wild-type stem cells is equal (0.50). However, in the biased drift model, this parameter assigns a quantitative value to the "strength" of oncogenic mutations, i.e., their capacity to overtake a crypt and completely replace the wild-type population with pre-cancerous cells. Furthermore, the P_R is context-dependent, as it has been found that *TP53* mutations have a higher P_R in colitis-affected intestines, compared to healthy ones. However, in spite of the clonal advantages, the fixation of these mutations is an inefficient process, and mutated cells are often stochastically replaced by wild-type stem cells, likely due to tissue architecture constraints (Vermeulen *et al.*, 2013; Snippert *et al.*, 2014).

1.3.2 WNT signalling in crypt homeostasis

WNT signalling pathway (**Figure 1.3**) is essential in maintaining the homeostasis and self-renewal capacity of the ISC population at the bottom of the crypts of Lieberkühn (Gregorieff *et al.*, 2005). WNT ligands are produced and secreted by Paneth cells in the small intestine or pericryptal ISEMFs in the small intestine and colon; upon release, the signals are received by the LGR5$^+$ ISC population triggering the WNT signalling cascade. The activation of WNT signalling begins with the interaction of the ligand wingless-type MMTV integration site family, member 3A (**WNT3A**) with the frizzled (**FZD**) receptor and the low-density lipoprotein receptor-related protein 5/6 (**LRP5/6**). This heterotrimer recruits into the membrane the proteins from the destruction complex: adenomatous polyposis coli (**APC**), casein kinase 1 α (**CK1$_α$**), axis inhibition protein (**AXIN**), and glycogen synthase kinase 3 (**GSK3**). In the absence of the destruction complex, β-catenin remains unphosphorylated in the cytoplasm and translocates to the nucleus where it binds to members of the T cell factor/lymphoid enhancer factor (**TCF/LEF**) family and triggers the transcription of WNT target genes. In contrast, in the absence of WNT ligand activation, the destruction complex remains active in the cytoplasm, binding and phosphorylating β-catenin, thereby targeting it for proteasomal degradation and hindering the activation of WNT target genes. Additionally, the lack of WNT signalling can also lead to the recruitment of the co repressor Groucho, which contributes to the repression of WNT target genes (Krausova & Korinek, 2014).

Furthermore, recent studies have uncovered new components associated with the WNT pathway associated with regulating the strength of WNT signalling. The RING-type E3 ubiquitin ligase (**RNF43**) and its homologue the zinc and ring finger 3 (**ZNRF3**) are responsible for the turnover of WNT receptors by ubiquitinating FZD and targeting it for degradation. This reduces the presence of WNT receptors in the surface of the membrane and decreases its responsiveness to WNT activation (**Figure 1.4A-C**) (Koo *et al.*, 2012; Koo & Clevers, 2014). However, R-spondin (**RSPO**) ligands can form a heterotrimer with LGR5 and RNF43, triggering their removal from the membrane and thereby inhibiting the ligase activity of RNF43 (**Figure 1.4D-F**) (de Lau *et al.*, 2011, 2014; Hao *et al.*, 2012; Zebisch *et al.*, 2013). This has been described as a mechanism to enhance WNT signalling, and consequently the use of RSPO has been incorporated into all the current protocols used for the generation of HIOs (Antfolk & Jensen, 2020).

The output from WNT activation is the transcription of genes associated with cell proliferation, and the self-renewal and expansion of the ISC population. Some of the genes activated by WNT signalling include: *MYC* and *CCND1*, associated with cell cycle and proliferation; *TCF7*, for the control of self-renewal and differentiation; *LGR5*, *ASCL2*, *BMI1*, *TERT*, and *EPHB2*, which have been reported as intestinal stem cell markers and/or markers confined to cells within the crypts; *SOX9*, required for

Paneth cell differentiation; *AXIN2* and *DKK1* which function as WNT negative regulators; and *SATB1*, linked with promoting colorectal tumorigenesis (Krausova & Korinek, 2014; Bian *et al.*, 2020).
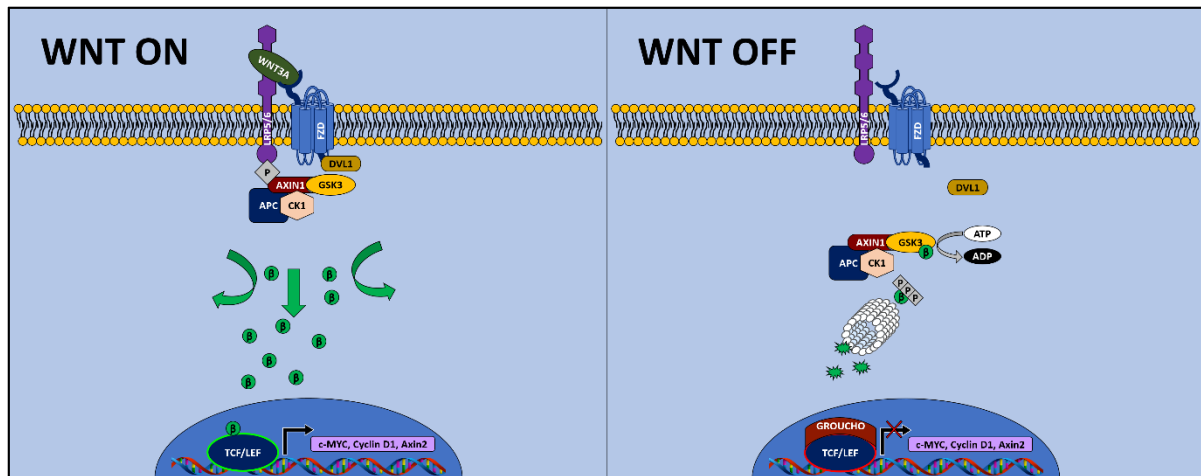
Figure 1.3 Canonical WNT signalling pathway.
The left panel presents the activation of WNT signalling; here the interaction of WNT ligands allows the accumulation of β-catenin in the cytoplasm, which then translocates to the nucleus to activate the WNT target genes. The right panel shows the inactive state of WNT signalling; in this case the absence of WNT ligand allows the degradation complex to phosphorylate β-catenin which leads to proteasomal degradation.
WNT3A (wingless-type MMTV integration site family, member 3A); **FZD** (frizzled receptor); **LRP5/6** (low-density lipoprotein receptor-related protein 5/6); **DVL1** (Dishevelled); **APC** (adenomatous polyposis coli); **CK1α** (casein kinase 1 α); **AXIN** (axis inhibition protein); **GSK3** (glycogen synthase kinase 3); **TCF** (T cell factor); **LEF** (lymphoid enhancer factor); **ATP** (Adenosine triphosphate); **ADP** (Adenosine diphosphate); **β** (β-catenin); **P**, phosphorylation.

Moreover, due to its role in the control of cell proliferation, disruptions in WNT signalling have been tightly linked to the onset of colorectal cancer. Mutations on negative regulators of WNT such as members of the destruction complex *APC,* and *AXIN1* and *2*, produce a state of constitutive transcription of the WNT target genes. Similarly, gain-of-function mutations in *CTNNB1* allow β-catenin to escape degradation, thereby accumulating in the cells and triggering the expression of WNT target genes. Additionally, loss-of-function mutations in RNF43/ZNRF3 or R-spondin overexpression have shown to enhance the sensitivity to WNT signalling induction, resulting in an increase in cell proliferation and crypt expansion. Consequently, WNT signalling has become an attractive target for cancer therapy, and some of the new therapeutic agents that have been developed include: (i) Nonsteroidal anti-inflammatory drugs (NSAIDs) used for their prophylactic effect on the regulation of catenin-responsive transcription; (ii) porcupine inhibitors to prevent the production of functional WNT ligands, by inhibiting the proteins involved with their post translational modifications; (iii) receptor-ligand disruptors such as monoclonal antibodies and peptides designed to block the interaction between the WNT ligand and the FZD receptor; (iv) Dishevelled inhibitors to disrupt the signalling cascade between the receptor proteins and the destruction complex; and (v) transcription complex

antagonists which act by destabilizing the β-catenin-TCF complex or its interaction with other co activator proteins. Nevertheless, the clinical applications of compounds targeting elements of the WNT signalling pathway are significantly troublesome, due to potential off-target cytotoxicity and disruption in the homeostasis of the ISC niche (Novellasdemunt *et al.*, 2015).
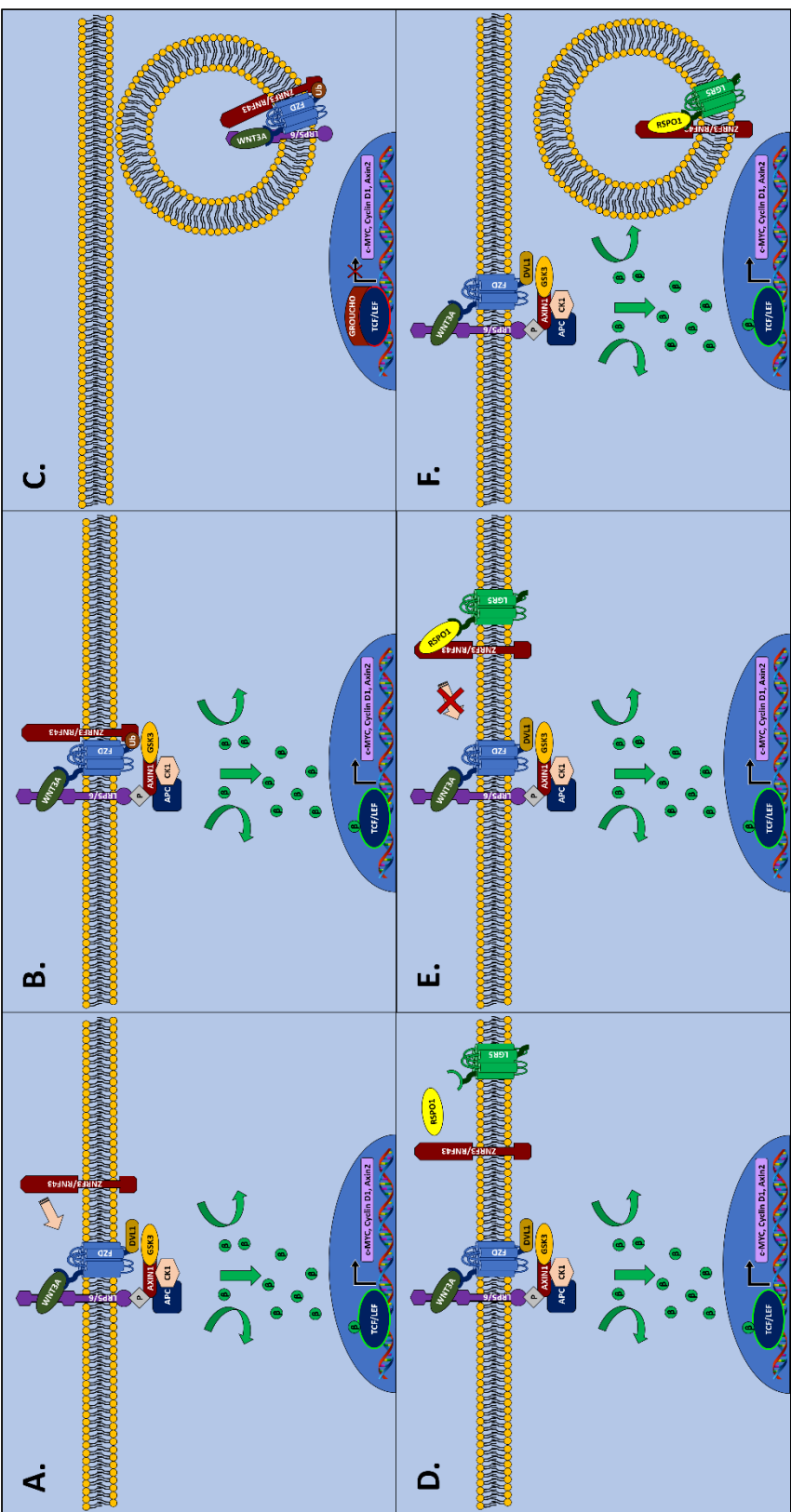
Figure 1.4 Role of RSPO1 in enhancing WNT signalling.

Upon WNT ligand activation and in the absence of RSPO1, FZD is targeted by the transmembrane protein RNF43 (A) which ubiquitinates the intracellular domain of FZD (B), leading to the recycling of the receptor (C). This eventually results in the attenuation of the signalling. In contrast, in the presence of RSPO1, it generates a trimeric complex RSPO1-RNF43-LGR5 (D), preventing it from targeting FZD (E) and causing the recycle and degradation of RNF43 (F). This allows the WNT receptors to be available for longer periods, thus enhancing the signalling effect.

WNT3A (wingless-type MMTV integration site family, member 3A); **FZD** (frizzled receptor); **LRP5/6** (low-density lipoprotein receptor-related protein 5/6); **DVL1** (Dishevelled); **APC** (adenomatous polyposis coli); **CK1α** (casein kinase 1 α); **AXIN** (axis inhibition protein); **GSK3** (glycogen synthase kinase 3); **TCF** (T cell factor); **LEF** (lymphoid enhancer factor); **RNF43** (RING-type E3 ubiquitin ligase); **ZNRF3** (zinc and ring finger 3); **LGR5** receptor (Leucine-rich repeat-containing G-protein coupled receptor 5); **RSPO1** (R-spondin 1); **β** (β-catenin); **P**, phosphorylation; **Ub**, ubiquitination.

1.3.3 NOTCH signalling in lineage differentiation

The NOTCH signalling pathway (**Figure 1.5**) is a highly conserved system responsible for a broad array of cellular functions, such as: cell proliferation, cell death, cell fate specification, early embryo morphogenesis, and the homeostasis of adult stem cell niches in different tissues. Its clinical relevance encompasses neurodegenerative diseases like Alzheimer, and different types of cancer (gut, prostate, breast, among others) (Hansson *et al.*, 2004; Lai, 2004).

In homeostasis, at the bottom of the intestinal crypts, NOTCH and WNT signalling collaborate in the proliferation and self-renewal of the ISC population. Above the ISC compartment, the transit amplifying cells undergo a cell fate specification process known as lateral inhibition, which is mediated by NOTCH signalling, and commits the cells towards the absorptive or the secretory lineage. Two cells participate in this process, a 'NOTCH OFF' and a 'NOTCH ON' cell. First, in a context of inactive NOTCH signalling, a repressor complex consisting of the nuclear receptor co repressor 2 (**NCOR2**), the silencing mediator for retinoid or thyroid-hormone receptors (**SMRT**) and the ski-interacting protein (**SKIP**), or histone deacetylase (**HDAC**), the CBF1 interaction co repressor (**CIR**) and the Sin3A-associated protein (**SAP30**), assembles around the bifunctional transcription factor **CSL** (human **C**BF1 (C promoter-binding factor), *Drosophila* **S**uppressor of Hairless, and *C. elegans* **L**ag-1)/**RBPJ** (Recombination signal binding protein for immunoglobulin kappa J region). This blocks the transcription of NOTCH target genes, particularly **HES1**. Consequently, the absence of HES1 allows **ATOH1** to trigger the expression of genes associated with the differentiation of the intestinal secretory lineage, and the expression of NOTCH ligands **DLL1 and 4**; the Jagged 1 and 2 (**JAG**) ligands are believed to be regulated by the WNT pathway. Next, DLL1/4 and JAG1/2 bind to the **NOTCH receptor 1 and 2** at the intercellular space, producing a conformational change in the receptors, followed by a sequential cleavage from the A disintigrin and metalloproteinase (**ADAM**) and the **γ-secretase complex**. This releases the NOTCH intracellular domain (**NICD**) into the cytoplasm, while the ligand-receptor conjugates are cleared from the membrane. NICD translocates into the nucleus and recruits other co activator proteins such as SKIP, histone acetylases (**HATs**), and the Mastermind-like transcriptional co activator 1 (**MAML**). The activator complex binds to CSL/RBPJ triggering the expression of NOTCH target genes, such as HES1. Finally, HES1 is responsible for inhibiting the activity of ATOH1, inducing the expression of the NOTCH receptors, and activating the differentiation program of the intestinal absorptive lineage (Pursglove & Mackay, 2005; Kazanjian & Shroyer, 2011; Noah & Shroyer, 2013).

NOTCH ON, i.e., NICD and HES1 target genes include: the NOTCH receptors 1 and 3, and *HES1,* which are involved in the autoregulation of NOTCH signalling, and the inhibition of ATOH1 and the secretory lineage; *MYC, CCND1,* and *P21/WAF1,* associated with cell cycle and proliferation of intestinal stem

cells; *IL2RA*, *GATA3* and *NF-κB*, related to maturation of T cells, and modulation inflammatory response (Borggrefe & Oswald, 2009). In contrast, NOTCH OFF, i.e., ATOH1 target genes include: *DLL1* and *4* NOTCH ligands; *CBFA2T2* and *CBFA2T3*, transcriptional co repressors of ATOH1, also linked to cancer; *GFI1*, which has been implicated in directing secretory cell commitment toward the differentiation of goblet and Paneth cells, rather than enteroendocrine cells; *SPDEF*, *CREB3L1*, *SPINK4*, *CLCA3*, and *MUC2*, linked to goblet cell differentiation, and Best2 associated exclusively with colonic goblet cells; *XBP1*, *EPHB3*, and *SOX9*, involved with Paneth cell differentiation; and *SCT*, a gene related to enteroendocrine cells (Lo *et al.*, 2017*b*).

Furthermore, previous studies have observed some association between NOTCH signalling and colorectal cancer. In some cases it has been reporter that NOTCH receptors and ligands were upregulated in up to 86% of the cases, while NOTCH target genes were found overexpressed in 33% of the samples (Shaik *et al.*, 2020). Due to the therapeutic implications of NOTCH signalling in cancer and other neurodegenerative diseases a broad array of compounds have been developed to modulate NOTCH activation, some of these are: (i) NOTCH decoys, anti NOTCH receptor and anti NOTCH ligand monoclonal antibodies to prevent the initial activation of NOTCH signalling cascade by blocking the interaction of the receptor with its corresponding ligand; (ii) ADAM and γ-secretase inhibitors, and nicastrin monoclonal antibodies to block the interaction of ADAM and γ-secretase with the cleavage sites at the NOTCH receptor; (iii) SERCA (sarcoplasmic/endoplasmic reticulum calcium ATPase) and POFUT1 (protein *O*-fucosyltransferase 1) inhibitors to disrupt the post translational modifications of the NOTCH receptors; and (iv) MAML stapled peptides and inhibitors of the NOTCH transcriptional complexes, which block the adequate formation of transcriptional complexes, thereby hindering the expression of NOTCH target genes. The specificity of these compounds vary depending on the nature of the specific target, additionally significant caveats are still under study, such as the delivery methods and the occurrence of gastrointestinal cytotoxicity (Purow, 2012; Majumder *et al.*, 2020).
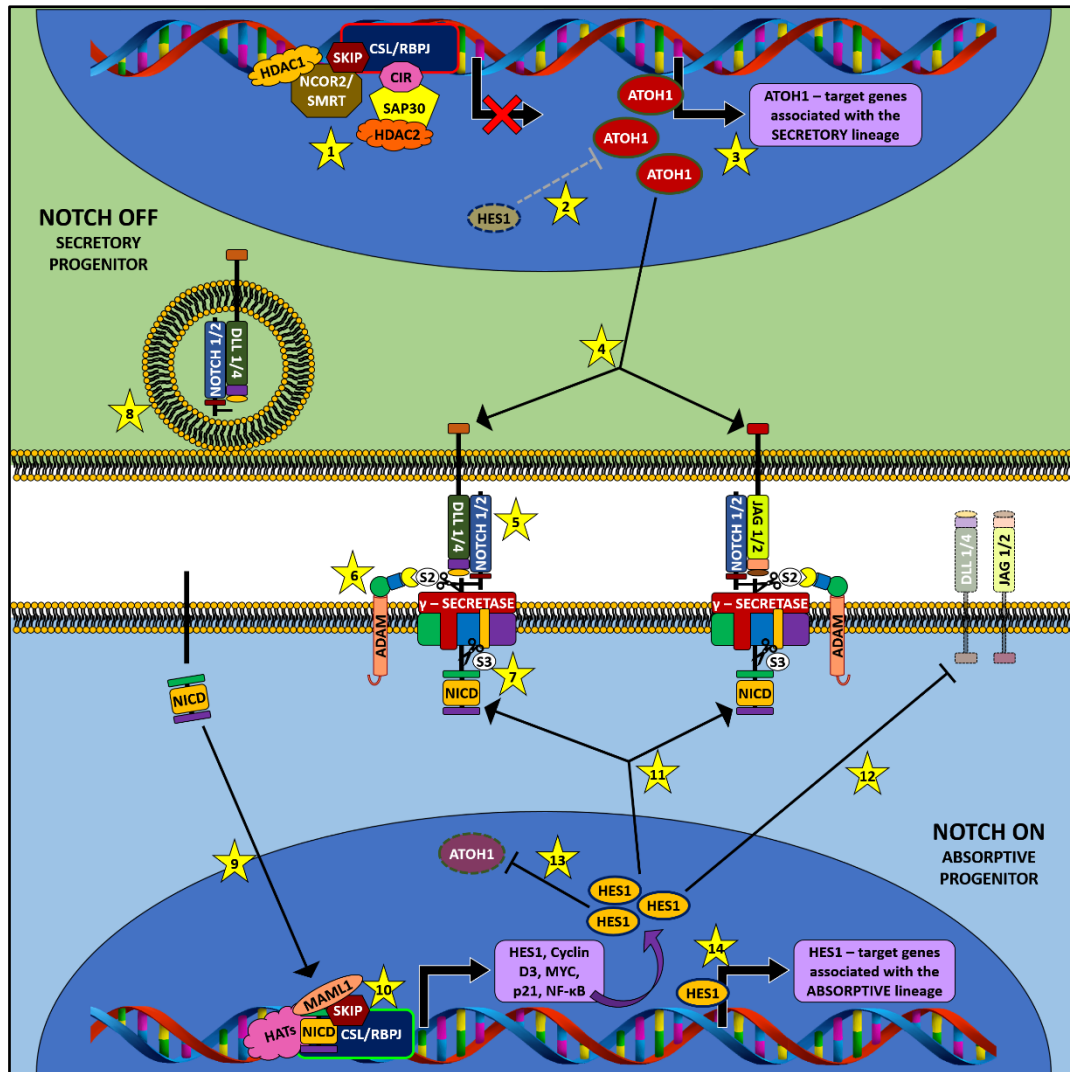
Figure 1.5 NOTCH signalling pathway in cell fate specification.
(1) In the absence of NOTCH signalling an array of co repressors such as NCOR2/SMRT, SKIP, HDAC 1/2, CIR, and SAP30 bind to the bifunctional transcription factor CSL to block the transcription of NOTCH target genes, such as *HES1*. (2) The absence of HES1 allows for the presence of the transcription factor ATOH1 which (3) triggers the expression of an array of genes associated with the differentiation of the intestinal secretory lineage (4) and the NOTCH ligands: DLL1, DLL4; JAG1 and JAG2 are speculated to be controlled through a different signalling pathway. (5) At the intercellular space, the NOTCH ligands interact with the extracellular domains of the NOTCH receptor from an adjacent cell, changing its conformation and exposing cleavage sites for (6) ADAM metallopeptidases (S2), (7) and gamma secretase (S3). (8) The fragment released by ADAM, remains attached to the NOTCH ligand and is internalized for recycling. (9) The NOTCH receptor intracellular domain (NICD) is released by gamma secretase and translocates into the nucleus. (10) NICD interacts with CSL and other co transcription factors, exposing a DNA binding domain that allows the expression of the NOTCH target genes, such as: *HES1*, *CYCLIN D3*, *P21*, *MYC*, and *NF-κB*. Subsequently, HES1 acts as a transcription factor that triggers the expression of the (11) NOTCH receptor, blocks the expression of (12) NOTCH ligands and (13) ATOH1, (14) and triggers the expression of genes associated with the intestinal absorptive lineage.
CSL (human **C**BF1 (C promoter-binding factor), *Drosophila* **S**uppressor of Hairless, and *C. elegans* **L**ag-1); **RBPJ** (Recombination signal binding protein for immunoglobulin kappa J region); **HDAC** (Histone deacetylase); **NCOR2** (Nuclear receptor co repressor 2); **SMRT** (Silencing mediator for retinoid or thyroid-hormone receptors); **SKIP** (Ski-interacting protein); **CIR** (CBF1 interaction co repressor); **SAP30** (Sin3A-associated protein); **HES1** (Hes (Hairy and enhancer split of proteins) family, bHLH transcription factor 1); **ATOH1** (Atonal homolog, bHLH transcription factor 1); **DLL** (Delta-like NOTCH ligand); **JAG** (Jagged); **ADAM** (A disintigrin and metalloproteinase); **NICD** (NOTCH intracellular domain); **HATs** (Histone acetylases); **MAML** (Mastermind-like transcriptional co activator 1); **MYC** (Myelocytomatosis proto-oncogene, bHLH transcription factor); **NF-κB** (Nuclear factor kappa B).

1.3.4 Balancing BMP signalling

The bone morphogenic protein (**BMP**) ligands are members of the transforming growth factor β (**TGF-β**) superfamily. BMP signalling was originally described for its role in osteogenesis and bone homeostasis (hence the name); however, further studies have linked BMP signalling with organogenesis, angiogenesis, cell differentiation, and as a negative regulator against the self-renewal of ISC (Wang *et al.*, 2014*b*).

Canonical BMP signalling starts with the association of BMP with the BMP receptors type I and II (**BMPR1 and 2**); next, BMPR2 phosphorylates BMPR1, which in turn phosphorylates SMAD1, 5, and 8. The SMAD heterotrimeric complex binds to SMAD4, and together translocate into the nucleus recruiting other co activators proteins, and finally triggering the expression of the BMP target genes. The specific functional output of BMP signalling is context-dependent, and may vary depending on the BMP ligand, tissue, and cellular context where the signalling cascade takes place (Ouahoud *et al.*, 2020).

In the intestinal epithelium, activation of BMP signalling is found as a gradient, where the highest concentrations are located among the differentiated cells, while the ISC niche is characterized by the presence of BMP antagonists (Takahashi & Shiraishi, 2020). Studies have found that loss of BMP signalling, outside the crypt compartment, repressed the differentiation of the intestinal secretory lineage (Auclair *et al.*, 2007). In contrast, within the ISC niche, BMP repression by Gremlin or Noggin has been associated with increased WNT activity and proliferation of the stem cell population (Takahashi & Shiraishi, 2020). Furthermore, previous works have found that as a consequence of BMP activation within the ISC niche, SMAD4 downregulated the expression of LGR5 signature genes associated with stemness and cell proliferation (Qi *et al.*, 2017).

The balance between BMP activation and repression within the ISC niche is responsible for restricting the expansion of pre-cancerous intestinal stem cells. In the context of colorectal cancer, BMP signalling has shown paradoxical properties, as some studies have reported that BMP2 may promote the proliferation of cancer stem cells (CSCs), while BMP4 can induce differentiation, apoptosis and repress the self-renewal of these cells (Zhang *et al.*, 2016). In contrast, other studies have shown evidence of the oncogenic effect of BMP4, and that its inhibition using LDN-193189 reduced tumoral growth (Yokoyama *et al.*, 2017). Yet, other works have reported that the use of LDN-193189 resulted in increased tumour growth and metastases (Whissell *et al.*, 2014; Vollaire *et al.*, 2019). These contradictions have not been resolved, though a possible explanation could be the high variability in the mutational background of colorectal cancer. Nevertheless, this highlights the need for extensive

validation on different models with different genetic backgrounds to reduce the risk of off-target adverse effects from any potential treatments targeting BMP signalling.

Aside from this, in the preparation of IOs, the BMP inhibitor Noggin is used to promote the formation of intestinal crypts. Alternatively, it has been proposed that the co culture with mesenchymal cells or the use of small-molecule BMP inhibitors such as LDN-193189 could achieve a similar effect (Kosinski *et al.*, 2007; Li *et al.*, 2018; Takahashi & Shiraishi, 2020).

1.4 Development of *in vitro* modelling systems for the intestinal epithelium

1.4.1 CaCo-2

CaCo-2 cells is a cell line derived from human colorectal adenocarcinoma originally established by Jørgen Fogh on 1964 (Fogh *et al.*, 1977*a*, 1977*b*). In early studies, Caco-2 cells were found to spontaneously differentiate into enterocyte-like cells. After 2-3 weeks in culture the cells displayed a columnar morphology with acentric nuclei and the ultrastructural analysis revealed the formation of a brush border with numerous microvilli. The cells expressed ALPI in a similar manner as differentiated small-intestinal enterocytes. Additionally, the transcellular absorption capacity was qualitatively similar to the small-intestinal villus cells (Hidalgo *et al.*, 1989). CaCo-2 assemble in monolayers characterized by the formation of intercellular tight junctions expressing ZO-1. These junctions contribute to the structural polarity of the cells and the establishment of the apical-basolateral axis (Anderson *et al.*, 1989).

Several studies have focused on evaluating the potential of CaCo-2 cultures as a model for drug absorption by the intestinal epithelium. The models for oral absorption have been evaluated by their capacity to transport compounds through two main routes: transcellular and paracellular transport. (Wilson *et al.*, 1990; Artursson *et al.*, 2001).

The first drug transport experiments with CaCo-2 cells used several compounds with different physicochemical characteristics to assess how these influenced their absorption and distribution. Even though CaCo-2 was derived from colon tissue, their findings revealed that the morphological and biochemical properties of CaCo-2 resembled the SI epithelium, and so far, it is the established model for small-intestinal enterocytes. The transcellular absorption rate of lipophilic drugs showed a good correlation when compared against previously reported values obtained from humans and *in situ* models of rat ileum. However, hydrophilic compounds which relied on paracellular absorption showed low permeability coefficients. This was explained due to a more constrained assembly of the tight junctions in the CaCo-2 monolayers, restricting the intercellular space. Therefore, hydrophilic compounds that were excluded from the transcellular pathway were found to be incompletely or not at all internalized through the paracellular pathway. Overall, the evidence collected support the use of CaCo-2 cells as a model for transcellular absorption, given that the permeability coefficients remain constant along the whole intestine. Additionally, since the paracellular permeability resembled more accurately colonic epithelium rather than the SI, it has been proposed to implement this model for predicting compounds that can be absorbed by the SI but not the colonic epithelium (Artursson, 1990; Artursson & Karlsson, 1991; Lennernäs *et al.*, 1996).

Because of the importance of CaCo-2 as a model of the intestinal epithelium in the early phases of drug discovery, several studies have focused on optimizing the culture conditions in order to make them cost effective and less time consuming. The standard culture conditions require 2-3 weeks for CaCo-2 to develop complete tight junctions across the monolayer with low paracellular permeability and functional features of differentiated enterocytes. A previous work reported the use of puromycin in the culture medium to reduce the culture time to 6 days, with arguably comparable results in the generation of low-permeability differentiated CaCo-2 monolayers. However, drug permeability is merely one of several parameters that are assessed in early drug discovery. Therefore, features such as the intracellular metabolism and the enzymatic activity might also be affected by the presence of puromycin, and these effects remain to be evaluated. Furthermore, the use of puromycin in the culture medium can lead to the selection of resistant cells with additional spontaneous mutations or growth advantages, which can compromise the results obtained from studies using this culture method (Sevin *et al.*, 2013).

Drug transport experiments originally used CaCo-2 cells seeded over collagen-coated nitrocellulose microporous filters. This system created a permeable separation between the apical and the basolateral compartment which allowed the transport of solutes across the intestinal epithelium and their quantification (Wilson *et al.*, 1990). Later it was found that CaCo-2 cells could attach to the polycarbonate surface of the Transwell diffusion cell system, even without a collagen coating. Further characterization revealed the cells still developed as a tight monolayer of columnar epithelial cells with low paracellular permeability and functional features of differentiated enterocytes (Hilgers *et al.*, 1990).

The combined advantages of CaCo-2 monolayers seeded over Transwell inserts are considered the gold standard for modelling and quantifying the transport of compounds across the intestinal epithelium, and have been extensively used by pharmaceutical companies to perform drug screenings (Artursson *et al.*, 2001; Hubatsch *et al.*, 2007; Tan *et al.*, 2018).

CaCo-2 cells been mostly used in pharmacodynamic studies to evaluate drug absorption, intracellular transport, metabolism, and oral toxicity (Yang *et al.*, 2017). Nevertheless, due to its mutational spectrum, it has also been used as a model for testing novel antineoplastic agents, which could later be incorporated into standard chemotherapy regimens for the treatment of colorectal cancer.

Previous characterization studies on CaCo-2 cells have identified it as microsatellite-stable with chromosome instability and hypertetraploidy (96 chromosomes) (Ahmed *et al.*, 2013). According to the canSAR database an approximate of 198 mutations have been identified in CaCo-2 cells, these

include: frame shifts (7.3%), missense (61%), nonsense (3.4%), silent (23.9), and splice shift mutations (4.4%) (Coker *et al.*, 2019). Perhaps the most relevant mutations are those found on critical cancer genes involved in the regulation of cell proliferation and apoptotic control. CaCo-2 has been reported to carry nonsense mutations in the tumour suppressor genes *TP53* and *APC*, missense mutations in *SMAD4*, but no alterations in the proto-oncogenes *BRAF*, *KRAS*, or *PIK3CA* (Ahmed *et al.*, 2013).

Loss of *TP53* has been found in a >50% cancer cases, in CaCo-2 cells is the result of a G-to-T nonsense transversion in codon 610. Under normal circumstances p53 is responsible for inducing G1 or G2 cell cycle arrest, in response to DNA damage. However, due to the loss of functional p53, cancer cells such as CaCo-2 continue with the cell cycle regardless of the accumulation of other mutations (Liu & Bodmer, 2006). Furthermore, studies conducted in CaCo-2 cells have found *TP53* mutation conferred a resistance against antineoplastic agents (Thant *et al.*, 2008; Wang *et al.*, 2013). Therefore, CaCo-2 cells could be used to evaluate combination therapies that counteract TP53-associated resistance against chemotherapy.

SMAD4 is a transducer of TGF-β signalling and has been established as a tumour suppressor which operates by regulating the antiproliferative signals triggered by TGF-β stimulation. CaCo-2 cells express a mutated version of this gene, SMAD4 D351H, which is unable to bind to SMAD2 or SMAD3, thereby hindering its translocation into the nucleus, and preventing the transcription of TGF-β target genes (De Bosscher *et al.*, 2004). Interestingly, this process has shown to be reversible upon the addition of lithium chloride, a GSK3 inhibitor capable of restoring the responsiveness of the cell to TGF-β signalling (Demagny & De Robertis, 2016). This opens the possibility of using CaCo-2 cells as a model for the evaluation of antiproliferative compounds targeting TGF-β and/or the restoration of SMAD4 functionality.

CaCo-2 cells have been reported to carry mutations in at least two genes involved in the canonical WNT signalling pathway: *CTNNB1* and *APC*. *CTNNB1* encodes for the expression of β-catenin, a signal transducer of WNT, that ultimately facilitates the expression of WNT target genes involved in cell proliferation. In contrast, in the absence of WNT stimulation, the APC protein serves as a scaffold that binds to β-catenin and other proteins responsible for tagging it for degradation, thereby controlling the activation of cell proliferation genes. An earlier work found a G-to-C missense transversion in codon 245 of the *CTNNB1* gene. This mutation has been suggested to prevent β-catenin from being recognized by tyrosine kinases, thereby escaping degradation (Ilyas *et al.*, 1997). In addition to this, in CaCo-2 cells a C-to-T nonsense transition in the *APC* gene has resulted in the production of truncated proteins, which retain their capacity to bind β-catenin, but are unable to target it for degradation. Notably, APC inactivation has been reported as the initial step in colorectal carcinogenesis, and it has

been found in 80-90% of the cases (Mariadason *et al.*, 2001). Both of these mutations have been proposed to generate a state of constitutive WNT activation in CaCo-2 cells, which in part can explain its fast proliferation rate. Therefore, the CaCo-2 cell line represents a suitable model for the study of compounds which may restore the function of *APC* in the early stages of colorectal cancer and/or counteract the constitutive activation of WNT.

Moreover, due to the aberrantly high proliferation rate of CaCo-2 cells, these have been used as a model to assess the efficacy of new antiproliferative agents, and to study the mechanisms of chemoresistance developed by CRC cells. For example, a previous study reported the overexpression of the EGF receptor in CaCo-2 cells, taking advantage of this feature, the authors assessed the chemosensitivity of CaCo-2 cells against 5-fluorouracil upon stimulation with EGF. The results suggested a synergistic effect, in which EGF triggered the cells into exiting G0 and re-enter the cell cycle, making them more vulnerable to treatment with 5-fluorouracil, thereby inducing cell cycle arrest in S and G2/M (Ye *et al.*, 2010).

Another work used CaCo-2 cells to evaluate the anti-tumour effect of insulin pre-treatment in combination with the antineoplastic agents 5-fluorouracil or irinotecan. Their results found a significant decrease in cell viability of CaCo-2 cells, increased apoptosis, and reduced the expression of cell proliferation regulators *PIK3CA* and *GRB2* (Agrawal *et al.*, 2019).

In another study, the authors evaluated the chemoresistance of different subpopulations of CaCo-2 cells against the chemotherapeutic agent camptothecin. This work isolated a subpopulation of putative CSCs (CD44^{+}) from CaCo-2 cultures and found it to be less sensitive to camptothecin treatment compared to non-CSCs (CD44^{-}). The results from this study could provide a deeper insight into the mechanisms of chemoresistance of the CSC population, which has been found responsible for tumoral regrowth (Roy *et al.*, 2014).

1.4.2 HT-29

HT-29 is a colonic adenocarcinoma cell line originally established by Jørgen Fogh in 1964. Early observations described it as epithelial-like cells capable of producing tumours in nude mice (Fogh & Trempe, 1975; Fogh *et al.*, 1977*a*, 1977*b*). HT-29 has been used as a model for the secretory lineage. It has been reported that HT-29 cells undergo a process of emergent differentiation into absorptive and mucus-secreting populations, as an adaptive response against methotrexate-induced metabolic stress (Lesuffleur *et al.*, 1990). Another study showed that using MTX-selected HT29 cells and mechanical stimulation, cells were able to generate a polarized intestinal epithelium with an apical compartment secreting different types of mucins (Navabi *et al.*, 2013). Comparative studies have found that due to the mucus production, HT-29-MTX outperformed CaCo-2 and HT-29 as a model to study the attachment and invasion of *Salmonella* (Gagnon *et al.*, 2013). Furthermore, some works have used co cultures of CaCo-2 (enterocytes) and HT-29-MTX (goblet cells) to generate more physiologically relevant models of the intestinal epithelium (Chen *et al.*, 2010).

Genetic characterization of HT-29 cells identified it as microsatellite stable, with numerous chromosomal aberrations and hypertriploid karyotype (68-72 chromosomes) (Kawai *et al.*, 2002). Epigenetic analysis found HT-29 exhibit a CpG island methylator phenotype (CIMP), i.e., promoter hypermethylation of multiple genes. This does not point to a specific gene set, but it is indicative of extensive gene expression abnormalities (Ahmed *et al.*, 2013).

The canSAR database has registered an approximate of 542 mutations in HT-29 cells, including: frame shifts (3.7%), missense (60.3%), nonsense (5.4%), silent (26.2%), splice shift (3.9%), and other mutations (0.6%) (Coker *et al.*, 2019). Particularly, HT-29 cells have been reported to carry missense mutations in the proto-oncogenes *BRAF*, *PIK3CA*, and the tumour suppressor gene *TP53* (Ahmed *et al.*, 2013).

The *BRAF* V600E mutation found in HT-29 cells, has also been found in 10-15% of colorectal cancer cases, and it has been linked to a poor prognosis for the patients. BRAF is a protein kinase involved in the MAPK signalling cascade, which is responsible for cell proliferation. However, the mutated variant V600E generates a constitutive MAPK activation, resulting in uncontrolled proliferation (Bond & Whitehall, 2018). The use of BRAF inhibitors to treat BRAF-mutant CRC has proved insufficient due to the development of resistance mechanisms. Consequently, studies have used HT-29 cells to evaluate the efficiency of new combinatorial therapies with BRAF and EGFR inhibitors to re sensitize the cells and halt the proliferation of cancerous cells (Herr *et al.*, 2018; Kikuchi & Hoshino, 2020). This highlights the importance of HT-29 cells as a model for the development of new therapies targeting BRAF-mutant CRC. In addition to this, other applications for the HT-29 cell line include its use as a reference sample

in studies screening for the *BRAF* V600E mutation in CRC patient samples (Benlloch *et al.*, 2006; Roma *et al.*, 2016).

Mutations in *PIK3CA* have shown to confer resistance to apoptosis to cancer cells, through different mechanisms such as the disruption of the tumour suppressor gene *PTEN* and activation of AKT (Samuels *et al.*, 2005). Other studies have found that the mutant variant *PIK3CA* P449T, found in HT-29 cells, generate a glutamine dependency on CRC cells. This suggests that glutamine metabolism could be exploited as a therapeutic target, and HT-29 cells could be a suitable model for this studies (Hao *et al.*, 2016).

HT-29 cells carry the mutated *TP53* R273H gene which has been reported to facilitate cell proliferation and survival by activating c-Myc and Bcl-XL (Li *et al.*, 2019). Also, studies have proposed *TP53* R273H regulates the transcription of long non coding RNAs (lncRNAs) associated with tumour growth, chemoresistance, and the self-renewal of colorectal CSCs (Zhao *et al.*, 2019). Moreover, HT-29 has been used as a model to evaluate the effect of gold small molecules as a potential new therapy against CRC. The results from this study showed this particular mutation was more resilient to the treatment than cell lines carrying other mutational variants of *TP53* (Dabiri *et al.*, 2019). In spite of these results, HT-29 has proved to be a representative model of an alternative CRC genotype, thereby highlighting its value as a reference in drug discovery studies which target the effects of *TP53* mutations.

Similar to CaCo-2, a nonsense mutation in the *APC* gene of HT-29 cells, results in the expression of an inactive truncated APC protein, which in consequence leads to an increase in cell proliferation. The absence of functional APC in HT-29 cells has been used to develop a model with inducible expression of wild type APC and evaluate the effect of its restoration. Using this model studies have found that exogenous expression of wild type APC led to an increase in apoptosis, which could not be attributed to TP53 activity since this is inactive in this cell line (Morin *et al.*, 1996). Other works have found that functional APC leads to the downregulation of *COX2*, a gene associated with poly formation in colorectal cancer (Hsi *et al.*, 1999). These works highlight the applications of HT-29 as a model for the study of gene mutations responsible for colorectal carcinogenesis.

Furthermore, the model of APC-mutant HT-29 was used in a drug screening study which sought to identify compounds with an inhibitory effect on the transcriptional activity of β-catenin. The results showed three candidate inhibitors of catenin-responsive transcription induced G0/G1 arrest, along with a dramatic reduction in the total cell number (Gonsalves *et al.*, 2011). Similar studies have taken advantage of the constitutive WNT activity of APC-mutant HT-29, and have employed it in the identification of small molecules which may disrupt the interaction of β-catenin with the TCF/LEF

promoter, thereby regaining control of the cell proliferation (Lepourcelet *et al.*, 2004; Badder *et al.*, 2020).

Aside from this, HT-29 has proved to be a suitable model for high-throughput experiments in drug discovery studies. A previous study sought to identify compounds which may enhance the chemosensitivity of cisplatin-resistant cancer cells; HT-29 was selected due to its low sensitivity towards cisplatin treatment (Sun *et al.*, 2018). Another study used RNAi high-throughput screening (HTS) to identify a synthetic lethal gene combination interacting with mutated TP53; the results revealed some gene combinations which accelerated cell cycle arrest in the presence of TP53 R175H, however no combination interacted with the mutational variant R273H found in HT-29 cells (Imai *et al.*, 2014). Nevertheless, these experiments suggest that the specific mutational spectrum of HT-29 cells could be exploited to identify new therapies against CRC.

Overall, these studies highlight the potential of CaCo-2 and HT-29, not only as models of the small-intestinal epithelium in pharmacodynamic studies but to model and study the behaviour of colorectal cancer cells. The evidence presented indicate that CaCo-2 and HT-29 cells have provided an outstanding insight toward the effect of mutation in key genes associated with colorectal carcinogenesis. Furthermore, these cell lines have proved to be a suitable model to evaluate the antineoplastic effect of new compounds in drug discovery studies. Nevertheless, it is important to notice that cell lines derived from colonic adenocarcinoma samples present important limitations to accurately represent the normal epithelium of the intestine.

1.4.3 FHs-74

FHs-74 is one of the first normal foetal human intestinal cell lines isolated (Owens *et al.*, 1976). Initial characterization confirmed FHs-74 did not exhibit classic neoplasia markers (colony formation and tumorigenicity) (Smith, 1979). Further studies compared this and other non-malignant cell lines against cancerous cell lines, finding consistent differences in the nuclear ultrastructure (Smith *et al.*, 1979). Considering FHs-74 derives from normal foetal tissue, and according to the databases, there are no reported mutations for this cell line.

FHs-74 exhibits similar features to that of normal foetal intact immature mucosa. For this reason it has been used to investigate the intracellular mechanisms of the proliferative effects of human breast milk on the neonatal gastrointestinal maturation (Ichiba *et al.*, 1992; Takeda *et al.*, 2004). Also, given the higher risk of Salmonella infections in infants, these cells were a suitable model to evaluate the protective effect of human milk mucins against Salmonella invasion (Liu *et al.*, 2012). Furthermore, FHs-74 has been used to study the proinflammatory effect of tocopherols in a foetal system to understand the effect of vitamin E intake on infants (Elisia & Kitts, 2013).

Other studies have used FHs-74 as a model of enterocytes to evaluate the expression of transporters responsible for the absorption of fatty acids and other lipidic compounds. Although CaCo-2 is widely used as the model for intestinal absorption, it was hypothesized that FHs-74 may offer some advantages, given that it was derived from normal small intestine, whereas CaCo-2 was isolated from colon adenocarcinoma (Jesch *et al.*, 2009; Ku *et al.*, 2011).

Moreover, toxicogenomic studies have found tumour cell lines to be unreliable models due to their abnormal gene expression profile and genetic instability. In consequence, to overcome these artifacts FHs-74 has been used as a model for non-transformed human intestinal epithelium in genotoxicity assays (Attene-Ramos *et al.*, 2010).

In addition to this, some models of HIOs have been found to exhibit a foetal phenotype (Finkbeiner *et al.*, 2015*b*); therefore a potential field of application for FHs-74 could be to provide a cheap and simple model to screen for compounds with an effect in the maturation of the intestinal epithelium.

1.5 Organoids: A novel modelling system

In spite of their considerable advantages and applications, *in vitro* monolayer models of the intestinal epithelium using CaCo-2, HT-29, or even FHs-74, are still significantly limited. The Transwell inserts allowed for a separation between the luminal and the basolateral compartment of the intestinal epithelium, allowing to study the effects of drug absorption, transport, and metabolism. However, this still consisted of a single cell type, and even with the co culture of CaCo-2 (enterocytes) and MTX-HT-29 (goblet cells), it still lacked other relevant cell types from the intestinal epithelium. Furthermore, monolayer models cannot replicate three-dimensional features present in the intestinal epithelium, such as: crypt-villus axis, cellular organization and distributions, heterotypic multicellular interactions, and the formation of an intestinal stem cell niche with epithelial and stromal cells (Gamboa & Leong, 2013; Liu & Chen, 2018).

The model of gut-on-a-chip represented a significant advance and incorporated additional features, such as: (i) formation of three-dimensional tubular structures similar to the intestinal tract; (ii) peristaltic-like stimulation and mechanical stress from the perfusion of medium; (iii) formation of the crypt-villus axis; and (iv) some studies reported the differentiation of four major cell types: enterocytes, goblet, Paneth, and enteroendocrine cells. Nevertheless, this model was generated from CaCo-2 cells, and in spite of these advantages it still derived from a cancer cell line; consequently, the mutational background could exert an impact in studies addressing the physiology of the normal intestinal epithelium, and/or could be affected by the genetic abnormalities from this cell line (Kim *et al.*, 2012; Trietsch *et al.*, 2017).

This precedent highlighted the need for a better model to study the intestinal epithelium, and such model should: (i) incorporate the major microarchitectural features previously described, in a three-dimensional format; (ii) develop all major cell types in the intestinal epithelium; (iii) accurately represent the physiology and genetic background of the normal intestine; (iv) could integrate multisystemic interactions with the mesenchyme, microbiota, vascular, immune and nervous system; (v) low cost and easy to prepare; and (vi) compatible with high-throughput experiments.

1.5.1 Clevers' model of intestinal organoids

The first protocol reporting the generation of IOs, defined them as self-organising three-dimensional structures that exhibit the major structural and functional anatomical and cellular features to accurately resemble a specific organ or tissue. Clevers and Sato reported the use of single Lgr5$^+$ stem cells isolated from mouse intestinal crypts which, when embedded in a rich semisolid ECM such as

Matrigel, were able to generate crypt-villus 3D structures that exhibit the main features of the small intestine (Sato *et al.*, 2009).

Following works focused on establishing the culture conditions to generate LGR5^{+}-derived HIOs. It was found that the main effectors driving the growth, differentiation, and long-term survival of HIOs were WNT, R-Spondin 1, Noggin, and EGF. Additionally the use of N-acetylcysteine, nicotinamide and p38 inhibitors, contributed in the maintenance and expansion of the stem cell niche and the overall long-term survival of the organoids (Sato *et al.*, 2011*a*, 2011*b*).

Further studies conducted in mouse IOs aimed to generate homogeneous cultures of Lgr5^{+} cells by enhancing self-renewal, using a combination of CHIR99021 and valproic acid. Additionally, the expression of WNT and NOTCH were modulated in order to improve and control the differentiation of the cell lineages in the organoids (Yin *et al.*, 2014). Recently, new modifications have been proposed to the culture conditions of IOs. In this study the use of IGF1 and FGF2 was found to promote crypt expansion and regeneration, while allowing differentiation of most of the *in vivo* cell types (Fujii *et al*., 2018).

1.5.2 Wells' model of intestinal organoids

In 2011, Wells and Spence proposed a different approach for the production of HIOs derived from pluripotent stem cells. This intended to overcome a disadvantage from Clevers' model: the limited availability of human crypt biopsies required as the source material for the generation of IOs. Starting with pluripotent stem cells (PSCs) the protocol aimed to recreate the events that occur during embryogenesis. First, activin A and low concentrations of serum trigger the differentiation of the definitive endoderm; next FGF and WNT signalling promote the patterning of the hindgut. Finally, the physical cues exerted by the ECM and the confluency of the culture, in combination with the signalling of the growth factors in the medium, lead to the release of spheroids containing a mix of CDX2^{+} hindgut cells, along with mesoderm-derived cells. These spheroids were embedded in Matrigel and fed with R-spondin 1, Noggin and EGF allowing the formation of cyst-like organoids comprised by intestinal epithelial cells surrounded with a layer of mesenchymal cells. The epithelium is mainly enterocytes and absorptive progenitors, with a small population of secretory and stem cells (Spence *et al.*, 2011; McCracken *et al*., 2011).

Transcriptomic analysis performed on HIOs derived from induced pluripotent stem cells (iPSCs), revealed that the phenotype exhibited by this model resembles that of a foetal stage rather than and adult intestine. This issue was overcame by transplanting the immature organoids into the kidney capsule of immunocompromised mice; after 16 weeks the expression profile change significantly and

several functional and cellular markers resemble an adult-like phenotype (Finkbeiner *et al.*, 2015*b*). However, it is important to mention this procedure defeats the purpose of using a 3D *in vitro* model as a substitute for animal models.

The initial protocols developed by Clevers and Wells for the generation of HIOs are summarized in **Figure 1.6**. They differ in the initial cell type, the composition of the growth and differentiation media, and the timing of each differentiation stage. Clever protocol is overall simpler, although is limited by the availability of the source material, i.e., crypt biopsies, and the complexity of the differentiation medium used at each stage. Additionally, the outcome of this protocol is a 3D structure with a single layer of intestinal epithelium. This is despite numerous publications highlighting the relevance of the extracellular matrix and the mesenchymal compartment, in the basolateral portion of the intestinal epithelium, in performing signalling and structural functions (Ishizuya-Oka, 2005; Powell *et al.*, 2005; Date & Sato, 2015). This model is referred to as 'enteroids' rather than organoids (Sinagoga & Wells, 2015).

In contrast, Wells' model produces organoids comprised by an inner layer of intestinal epithelium and an outer mesenchymal compartment; however, it requires additional differentiation steps to transition the pluripotent cells into intestinal progenitors, and as mentioned before, the transcriptomic profile resembles a foetal intestine rather than an adult one.
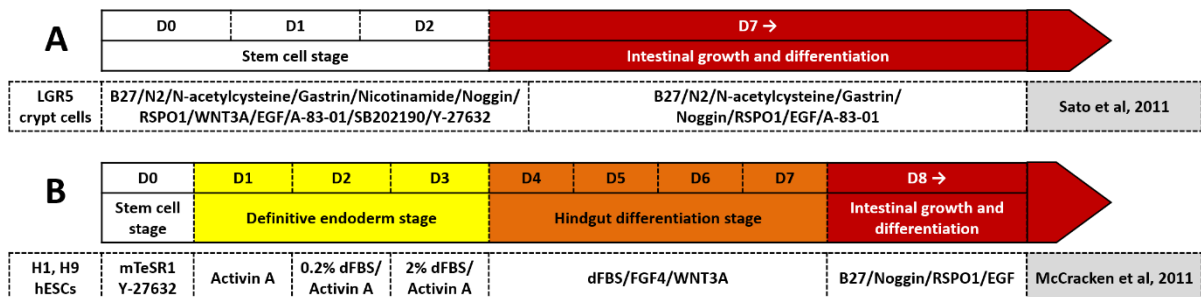
Figure 1.6 First protocols published for the generation of human intestinal organoids.
(A) The protocol developed by Clevers and Sato requires single LGR5^{+} ISC isolated from crypt biopsies. The cells are embedded in Matrigel and fed with a complex differentiation media. The differentiation process is divided in two stages resulting in the generation of intestinal 'enteroids'. These are comprised by a single layer of intestinal epithelium and are reported to develop structures resembling the crypts and villi. (B) The protocol developed by Wells and Spence starts from pluripotent cells and requires the sequential transition into definitive endoderm and hindgut. The spheroids obtained from the hindgut stage are a mix of endodermal and mesodermal cells. These are embedded in Matrigel and the resulting organoids develop as cyst-like structures with an inner layer of intestinal epithelium and an outer layer of mesenchymal support cells.

1.5.3 Other protocols for the generation of intestinal organoids

Following the works from Clevers and Wells, Jensen's group developed an alternative approach for the generation of IOs. In this case the starting material consisted of a population of foetal intestinal progenitor cells (FIPCs) at gestational week 10. These FIPCs were dissociated, seeded into Matrigel, and fed with EGF, Noggin, R-spondin 1 and prostaglandin E2, which led to the formation of foetal enterospheres (FEnS). This model offered few advantages over the previous ones: it allows for the study of a foetal stage of the intestine as opposed to the adult phenotype exhibited by Clevers' model of IOs; and it does not require the sequential differentiation process described by Wells' model. In contrast, obtaining and processing the source material is more complicated than the *in vitro* culture of PSCs. Also, a brief characterization of their gene expression profile indicated that the FEnS present an immature phenotype and do not express markers for all relevant cells types (Fordham *et al.*, 2013; Senger *et al.*, 2018; Antfolk & Jensen, 2020).

A different study reprogrammed human umbilical vein endothelial cells (HUVECs) into induced foetal intestine-derived progenitor cells (iFIPCs) by exogenous expression of transcription factors HNF4α, FOXA3, GATA6, and CDX2. These iFIPCs were differentiated into spherical organoids (SO) using similar conditions as the ones established by Sato *et al.* (2011a, 2011b). The SOs were able to reconstitute the epithelium when transplanted into injured mouse colon (Miura & Suzuki, 2017). This model provides an alternative strategy for the generation of IOs from different sources, however it does not appear to contribute to any significant advantage compared to Clevers' and Wells' model. Conversely, it requires additionally genetic manipulation to reprogram the cells into progenitors.

1.5.4 Incorporating multisystemic interactions into intestinal organoids

In spite of the incorporation of three-dimensional features and multicellular interactions into the existing models of the intestinal epithelium, integrating them with a vascular, immune and/or nervous system remains a great challenge.

After the generation of PSC-derived HIOs, following works achieved the maturation of the organoids by transplanting them into the kidney capsule of mice (Watson *et al.*, 2014; Finkbeiner *et al.*, 2015*b*). However, this was not sustainable for high-throughput applications, and by using animal models it disregarded the main advantage of the organoids. A recent study identified a subpopulation of endothelial cells within PSC-derived HIOs; these cells appeared during the early growth stages and disappeared over time. Similar to the mesenchymal component in these organoids, it was speculated the endothelial cells derived from mesodermal cells produced during the formation of the definitive endoderm. Using a combination of VEGF (vascular endothelial growth factor) and other growth

factors, the authors managed to successfully expand and preserve the endothelial subpopulation in the HIOs. This is a promising start, though it is still necessary to properly characterize these cells and their functionality (Holloway *et al.*, 2020). Another study presented the first evidence of HIOs developing a primitive enteric nervous system. This was accomplished by co culturing aggregates of mid- and hindgut spheroids with PSC-derived neural crest cells; these were embedded into Matrigel and generated HIOs with intercalated neuroglial cells. However, this protocol still required for the organoids to be transplanted into mice to develop functional features (Workman *et al.*, 2017).

Regarding the incorporation of immune cells into models of the intestinal epithelium, previous works have attempted to co culture organoids or organoid-derived intestinal epithelium along with immune cells. A study co cultured Lgr5$^+$ ISCs with lymphocytes capable of producing interleukin 22 (IL-22). The results showed that IL-22 induced the proliferation of the Lgr5$^+$ ISC population through a mechanism independent of Wnt and Notch, this was accompanied by an increment in the size of the organoids (Lindemans *et al.*, 2015). Another work used Transwell inserts to co culture PSC-derived HIOs with Jurkat T cells; the results showed that the secretion of interleukin 2 (IL-2) by Jurkat T cells induced in the activation of STAT3 in the HIOs. Consequently, IL-2 boosted organoid growth and budding, but more importantly it triggered the expression of maturation markers, thereby rescinding the need for transplantation into mice. Also, this evidence highlights the importance of the immunological components in the maturation of the intestinal epithelium (Jung *et al.*, 2018).

In addition to this, new models have integrated the intestinal epithelium from the organoids, cells from the immune system, and the microbiota. A previous study used a model of enteroids co cultured with lymphocytes and *Lactobacillus reuteri* D8, to study the protective effects of the microbiota over the intestinal epithelium. The results found that *L. reuteri* D8 contributed to the regeneration of organoid-intestinal epithelium following damage by the pro inflammatory cytokine TNFα (Hou *et al.*, 2018). In contrast, an infection model used HIOs co cultured with neutrophils and commensal or enteropathogenic *Escherichia coli*. Commensal bacteria were restrained by the natural defences of the organoid, whereas pathogenic *E. coli* disrupted the epithelial barrier and triggered the expression of interleukins associated with neutrophil recruitment (Karve *et al.*, 2017). Alternatively, a study developed a model of enteroid-derived monolayers co cultured with human macrophages, to study the interaction of intestinal epithelial cells with the immune cells. In contrast to the Clevers' enteroid model, this system provides access to the apical compartment. Additionally, the co culture with the macrophages resulted in the production of cytokines and chemokines revealing an interplay between both systems. Furthermore, macrophages and intestinal epithelial cells exhibited morphological changes following infection with enteropathogenic bacteria, suggesting a functional interaction

between the three components: gut, immune system, and microbiota (Noel *et al.,* 2017). The enteroid monolayer model offers an alternative to integrate organoid-derived epithelium with access to the apical compartment, components of the immune system, and microbiota. Previous studies have used microinjection to study the interaction of commensal and pathogenic microbiota with the intestinal epithelium. However, this method is more disruptive and can compromise the structural integrity of the organoids.

1.5.5 Applications of intestinal organoids

After the development of protocols for the derivation of HIOs, several studies focused on assessing their functional relevance and potential applications in different areas. For example, as models of infection, in inflammatory diseases, genetic conditions, regenerative medicine and CRC (Sinagoga & Wells, 2015). iPSC-derived HIOs have been used as a model to study intestinal infections such as *Salmonella enterica* (Forbester *et al*., 2015), *Clostridium difficile* (Leslie *et al.*, 2015; Liu *et al.*, 2019*b*), *E. coli* (Karve *et al.*, 2017; Pradhan *et al.*, 2020), and rotavirus (Finkbeiner *et al.*, 2012).

As a model for inflammatory diseases, HIOs have proven to be useful in the study of intestinal fibrosis in Crohn's disease. Current *in vitro* models are unable to replicate the microarchitecture of the intestine, *in vivo* models are expensive and cannot accurately replicate all the aspects of the human disease. A recent study used iPSC-derived HIOs to model intestinal fibrosis, due to their capacity of developing a mesenchymal layer with myofibroblasts. The results indicated that myofibroblasts responded to fibrogenic stimulation, and the fibrosis could be reversed with anti-fibrotic drugs. The results support the use of HIOs as a viable model to study intestinal fibrosis, and in drug screening studies (Rodansky *et al.*, 2015).

The model of HIOs developed by Clevers and Sato has been used for the study of the four main mutations associated with CRC (*APC*, *KRAS*, *SMAD4* and *P53*). Mutant organoids were engineered with CRISPR-Cas9 gene editing and the selection was performed by removal of specific growth factors: WNT and R-spondin 1 for APC, EGF for KRAS, Noggin for SMAD4, and nutlin-3 was added to select for P53 mutants. The results showed that quadruple mutants were able to survive independently of any growth factor and when transplanted into nude mice were able to form tumours with invasive carcinoma features. This highlights the feasibility of HIOs as a model for the study of mutations that contribute to the progression of colorectal cancer (Drost *et al*., 2015). Furthermore, these studies prompted the formation of a biobank with patient-derived organoids. In the long term it is expected this initiative will increase the general understanding of rare mutations among the population, but also to be used for HTS (Van De Wetering *et al*., 2015).

1.5.6 Other three-dimensional models of the intestinal epithelium

Organoids technology is a groundbreaking development which has allowed the modelling of the 3D microarchitecture of the intestinal epithelium. However, the access to the lumen is an important limitation that hinders the study of important physiological aspects of the intestine.

Organ-on-a-chip technology has been developing since before the emergence of organoid models. Previous works have prepared gut-on-a-chip cultures seeding CaCo-2 cells over a porous membrane polydimethylsiloxane (PDMS). This system uses a microfluidics device with a double chamber, where the cells and the medium are located. Additionally two adjacent vacuum chambers on the sides provide mechanical strain simulating the peristaltic movement (Kim *et al.*, 2012). It was reported that this mechanical stimulation induces the differentiation of the cells and the formation of intestinal villi (Kim & Ingber, 2013). This system provided a platform to study the gut epithelium, and in addition to the mechanical cues, further work has assessed the interaction with the microbiome and inflammatory cells in order to generate a comprehensive model of the intestinal microenvironment (Kim *et al.*, 2016).

The development of phaseguide technology represented a breakthrough in microfluidics technology, providing a better control on the filling and emptying of microfluidic chips. It consists of a line of material extending along a channel of a moving liquid-air interface. The geometrical change provided by the material, induces the formation of a liquid-air meniscus aligned with the boundary between two adjacent channels. This "bump" creates a barrier effect due to the "meniscus-pinning effect", preventing the liquid from overfilling and crossing into the next channel (Vulto *et al.*, 2011).

Phaseguide technology was printed in chips in cell culture plates, now known as OrganoPlates. This system has been implemented for the 3D culture of dopaminergic neurons (Moreno *et al.*, 2015), endothelial vasculature (van Duinen *et al.*, 2015), and kidney proximal tubules (Wilmer *et al.*, 2016). Notably, OrganoPlates seeded with CaCo-2 cells developed as 3D polarized intestinal tubules expressing markers for differentiated enterocytes and tight junctions. The barrier function of these tubules was tested based on the permeability of fluorescent dextran, and the results indicated the formation of leak-tight intestinal tubules (Trietsch *et al.*, 2017).

In light of the development of organoid cultures and microengineering technology, a recent study attempted to merge these modelling systems to overcome their limitations and capitalize of their advantages. In this study iPSC-derived HIOs were dissociated and seeded over a PDMS scaffold in a microfluidics chip. The epithelial cells from the organoid were sorted from the mesenchyme based on the expression of CD236/EpCAM. After 7 days of culture with a constant media flow, the cultures

developed as crenulated monolayers, exhibiting differentiation markers for epithelial subtypes. However, this system did not form a 3D tubular structure as oppose to cultures prepared with the OrganoPlate chips (Workman *et al.*, 2018).

1.5.7 Assessment of high-throughput applications for intestinal organoids

After the development and optimization of the original protocols for the generation of IOs, following works explored their potential for high-throughput applications and began the generation of a biobank of patient-derived tumour organoids (PDTOs) (Van De Wetering *et al.*, 2015). However, so far enteroids, HIOs and colorectal PDTOs have mostly been used in low-throughput experiments (<1000 compounds), and just recently a study reported a protocol for the generation of miniaturized colonic organoids and their application in a high-throughput assays (>1000 compounds). This protocol proposed an alternative to generate the organoids embedded in Matrigel in 384-well plates, thereby reducing the costs and volume of medium (Du *et al.*, 2020). Other studies have opted for dissociating the organoid to generate monolayers of normal intestinal epithelium, thereby overcoming the limitations of CaCo-2 cells. Although, this neglects the need for three-dimensional organization (Yoshida *et al.*, 2020). Nevertheless, there are still significant limitations for the routine implementation of intestinal organoids in high-throughput studies. The main caveats of this technology are: (i) production requires long time and elevated cost; (ii) difficult to prepare since the source material requires isolation, purification, and/or differentiation prior to the growth of the organoids; (iii) difficult to handle due to the Matrigel matrix; and (iv) lack of automation for the sorting, imaging, and analysis of the organoids. Therefore, the use of organoid models in large-scale screening studies is still significantly limited (Arora *et al.*, 2017; Takahashi *et al.*, 2018; Liu & Chen, 2018; Zanoni *et al.*, 2020; Kim *et al.*, 2020).

Alternatively, other models have been developed for drug screening purposes, such as monolayer cultures, spheroids, and gut-on-a-chip. As mentioned before, monolayer cultures of intestinal cells such as CaCo-2, HT-29, and CaCo-2/MTX-HT-29 represent an oversimplification of the actual anatomy and physiology of the tissue. Still, they can still provide useful information and help to sieve successful candidates from a large array of compounds (Gamboa & Leong, 2013; Liu & Chen, 2018). Spheroid models are three-dimensional, avascular, and disarrayed aggregates generated from cancer cell lines. This model is relatively easy to prepare and has been used in high-throughput experiments to study the cytotoxicity, permeation, and distribution of antineoplastic agents within solid tumours. However, it lacks tissue organization and cannot be used to study the physiology of pre cancerous intestinal epithelium undergoing malignant transformation and its response to drug treatments (Mehta *et al.*, 2012; Katt *et al.*, 2016; Nunes *et al.*, 2019; Gilazieva *et al.*, 2020). The model of gut-on-a-chip is suitable

to evaluate the intestinal epithelium in a three-dimensional environment. As oppose to the organoids, this model has open access to the luminal and basolateral compartment, thereby facilitating the study of drug absorption and metabolism. Currently, there are high-throughput formats of gut-on-a-chip, however this are relatively expensive and require additional equipment to incorporate the perfusion of medium (Kim *et al.*, 2012; Kim & Ingber, 2013; Trietsch *et al.*, 2017). Finally, an alternative approach is to perform preliminary screening experiments in economic models such as monolayer cultures or spheroids. This will reduce the number of candidates, which then can be validated in more sophisticated model such as organoids or gut-on-a-chip. Ultimately, the selection of suitable models for high-throughput experiments depends on the specific aims and applications, the strategy to obtain and analyze the output, and the time and budget available.

2.1 Extraction of genomic DNA

Genomic DNA was either extracted from confluent T75 flasks (CaCo-2, HepG2, HeLa, and NT2) or confluent wells (9 cm^2) from a 6-well plate of miFF1 cells. Cells were harvested using trypsin or EDTA, and centrifuged at 800 x g for 5 min. The medium was discarded, and the pellet was resuspended in 600 µL nuclei lysis buffer and 107 mAU of protease (Qiagen). The reaction was incubated at 55°C for 30 min. After incubation, 200 µL of protein precipitation solution (Promega) was added, and mixed by vortexing for 20 s. The reaction was centrifuged for 5 min at 10,000 g. The supernatant was transferred into a 1.5 mL Eppendorf tube containing 600 µL of isopropanol. The solution was mixed by inversion until fine white threads of DNA appeared. The solution was centrifuged for 5 min at 10,000 x g. The supernatant was discarded, and the DNA pellet was washed with 600 µL of 70% ethanol. The sample was centrifuged for 5 min at 10,000 g, and the pellet was resuspended in 50 – 100 µL Tris-EDTA buffer, pH 7.4.

2.2 Quantification of nucleic acids

All nucleic acid samples were quantified using a NanoDrop ND-1000 Spectrophotometer (Thermo Scientific). The measurements were taken following the instructions from the device. First, the lens of the machine was cleaned with 2 µL dH$_2$O, and the constant settings were adjusted to 'DNA-50' or 'RNA-40', depending on the sample. A control solution (typically TE for DNA or nuclease-free H$_2$O for RNA) was used to blank the device, and then 2 µL of sample was used for the measurements. The concentration values were presented in ng/µL and the quality of the sample was evaluated based on the 260/280 and 260/230 absorbance ratios. For DNA samples the expected 260/280 and 260/230 absorbance ratios were >1.8 and >2.0, respectively; and for RNA, the values were > 2.1 and > 2.0, respectively.

2.3 Polymerase Chain Reaction (PCR)

All primers were purchased from Integrated DNA Technologies, and except for the case of qPCR primers, all primer designs were performed as follows:

First, the target gene sequence was obtained from the National Center for Biotechnology Information (NCBI) database (https://www.ncbi.nlm.nih.gov/). Next, suitable primer candidates were selected from the sequence using Primer3Plus (http://www.bioinformatics.nl/cgi-bin/primer3plus/primer3plus.cgi).

The formation of secondary structures (hairpin and primer dimers) was verified using OligoAnalyzer 3.1 from Integrated DNA Technologies (https://eu.idtdna.com/calc/analyzer). The primers sequences were modified until the thermodynamic parameters were optimal using the following selection criteria: hairpin ΔG > -3 Kcal/mol; hairpin T_m < 40°C; homodimer ΔG > -7 Kcal/mol; heterodimer ΔG > -6.5 Kcal/mol. The results from the primer design and optimization are summarized in Table 2.1 below. Also, in the characterization of the final reporter construct, M13, Clon-NeoR and the Seq series of primers were not used coupled with a specific primer, therefore the heterodimer ΔG and amplicon size varied and were not included in the table.

Gene	Primer sequence 5' -> 3'	Size (nt)	Sense	% GC	T_m (°C)	Hairpin ΔG (Kcal/mol)	Hairpin T_m (°C)	Homo dimer ΔG (Kcal/mol)	Hetero dimer ΔG (Kcal/mol)	Amplicon (bp)
LGR5-LHA-	TGGTTGCCATGTCATTGG	18	Fwd	50	59.9	-0.5	31.4	-5.38	-5.09	1031
	TAGCTGAACAAATTATACAAAGCAGC	26	Rev	34.6	60.2	-1.63	40.3	-6.69		
LGR5-RHA-	CTTGATACTTGAGAGTGAATATAAGTC	27	Fwd	33.3	54.3	-0.97	36.5	-4.88	-3.42	1089
	CTAACAGCCATTTGGTTTG	19	Rev	42.1	54.3	-0.65	33.4	-5.02		
IGK	CCAAATACGGCACACTG	17	Fwd	52.9	54.1	0.92	8.7	-3.61	-5.02	3868
	TGAGTAACCTGAGGCTATGG	20	Rev	50	55.4	0.31	20.3	-4.67		
M13	GTAAAACGACGGCCAG	16	Rev*	56.2	53.2	1.89	-19.4	-9.28	-	-
	CAGGAAACAGCTATGAC	17	Fwd§	47.1	46.1	-0.52	33.0	-6.34		
Clon-NeoR	CCTGAGGCGGAAAGAAC	17	Fwd	58.8	56.7	0.6	12.1	-4.67	-	-
Seq-LIR1	TGGGCACTGTGTGTTATTAGG	21	Fwd	47.6	58.6	-0.48	31.1	-3.3	-	-
Seq-LIR2	CGAGTTTCACCTCAGCTCTTC	21	Rev	52.4	59.2	-0.44	29.7	-6.34		
Seq-LIR3	AAGAGCTGAGGTGAAACTCG	20	Fwd	50.0	57.3	-0.33	28.9	-6.34	-	-
Seq-LIR4	GCCATGATATAGACGTTGTGG	21	Rev	47.6	58.0	-0.06	25.8	-6.3		
Seq-LIR5	TGCCATAGCCTCAGGTTACTC	21	Fwd	52.4	59.4	-0.55	33.5	-4.67	-	-
Seq-LIR6	CAAATCCAAGTTAAAACATCTGATC	25	Rev	32.0	58.2	-0.37	29.8	-4.85		
Seq-EGFP	TTTCCTTTGAAAAACACGATG	21	Fwd	33.3	57.8	-0.38	29.8	-5.46	-	-
	GGACAAACCACAACTAGAATGC	22	Rev	45.5	58.6	-0.62	34.6	-4.16		
Seq-NeoR	ATCAAGAGACAGGATGAGGATC	22	Fwd	45.5	57.2	-0.7	38.9	-4.62	-	-
	CTTCCGTGTTTCAGTTAGCC	20	Rev	50	57.5	1.9	-19.3	-3.61		

Table 2.1 Optimized primer design for the amplification and characterization of the LGR5-GFP expression cassette.
M13, Clon-NeoR and all the primers from the Seq series were not coupled with a specific primer but rather in different pair combinations during the characterization of the final construct. Therefore, the heterodimer ΔG and amplicon size varied, and were not included in the table.
*Rev primer used as forward; §Fwd primer used as Rev.

Unless otherwise stated, all routine PCR reactions were prepared using BioMix Red PCR Master Mix (BioLine). This mixture is an economic solution ideal for the amplification of DNA fragments below 1.5 Kb. It contains standard DNA *Taq* polymerase, *Taq* buffer, dNTPs, and magnesium chloride. Due to the

lack of proofreading capacity, BioMix Red PCR Master Mix was specifically used to detect the presence of target genes and/or constructs.

PCR reactions were prepared in a final volume of 10 µL, mixing 1x BioMix Red PCR Master Mix (BioLine), 0.5 µM of each primer, and 30-100 ng DNA template.

Step	Temp (°C)	Time	Cycles
Initial denature	95	3:00 min	1
Denature	95	30 s	
Annealing	variable	30 s	35
Elongation	72	30 s/kb	
Final elongation	72	5:00 min	1

Table 2.2 Standard PCR conditions.

Regardless of the size, fragments intended for cloning applications (e.g., homology arms and reporter cassette) were amplified using Platinum Superfi DNA polymerase, a high-fidelity polymerase. The reaction mix was prepared in a final volume of 10 µL, containing 1x Superfi buffer, 0.5 U Platinum SuperFi DNA polymerase (Invitrogen), 200 µM dNTPs (New England Biolabs), 0.5 µM of each primer, and 30-50 ng DNA template.

Step	Temp (°C)	Time	Cycles
Initial denature	98	1:00 min	1
Denature	98	10 s	
Annealing	variable	10-15 s	35
Elongation	72	30 s/kb	
Final elongation	72	5:00 min	1

Table 2.3 PCR conditions used for amplification with high fidelity Platinum SuperFi DNA polymerase

Primer3Plus conditions were used to carry out the PCR reactions. In the cases where the PCR reaction did not lead to an amplicon, a temperature gradient was used to determine the optimal annealing temperature. The reactions were run in a Bio-Rad T100 Thermal Cycler.

Molecular Biology and cloning		
Product	Supplier	Cat. No.
100 bp DNA ladder	New England Biolabs	N3231
1kb DNA ladder	New England Biolabs	N3232
ATP solution [10 mM]	Invitrogen	PV3227
BioMix Red	BioLine	BIO-25006
Deoxynucleotide (dNTP) solution mix [10 mM each nt]	New England BioLabs	N0447
Dithiothreitol [0.1 M]	New England BioLabs	B1034
FastStart Universal Probe Master (ROX)	Sigma-Aldrich	4913957001
GelRed Nucleic Acid Gel Stain	Biotium	41003
One Shot OmniMAX 2 T1R Chemically Competent *E. coli*	Invitrogen	C8540
PfuTurbo DNA Polymerase	Stratagene/ Agilent Technologies	600250
Platinum SuperFi DNA Polymerase	Invitrogen	12351
Protease, 7.5 Anson units	Qiagen	19155
Protein precipitation solution	Promega	A7953
ProtoScript II Reverse Transcriptase [200,000 U/mL]	New England BioLabs	M0368
PureLink Quick Gel Extraction and PCR purification combo kit	Invitrogen	K2200
QuantiTect SYBR green PCR kits	Qiagen	204143
Quick Dephosphorylation Kit	New England Biolabs	M0508
Quick-Load Purple 50 bp DNA Ladder	New England Biolabs	N0556
RNase inhibitor, human placenta [40,000 U/mL]	New England BioLabs	M0307
RNeasy mini kit	Qiagen	74104
Subcloning Efficiency DH5α Competent Cells	Invitrogen	18265
T4 DNA Ligase [1 U/μL]	Invitrogen	15224
TOPO XL-2 Complete PCR Cloning Kit	Invitrogen	K8050
TRIzol reagent	Invitrogen	15596
Universal Probe Library probe 017	Sigma-Aldrich	4686900001
Universal Probe Library probe 034	Sigma-Aldrich	4688015001
Universal Probe Library probe 042	Sigma-Aldrich	4688589001
Universal Probe Library probe 060	Sigma-Aldrich	4687671001
Universal Probe Library probe 061	Sigma-Aldrich	4688597001
Universal Probe Library probe 063	Sigma-Aldrich	4688627001
Universal Probe Library probe 068	Sigma-Aldrich	4688678001
Universal Probe Library probe 070	Sigma-Aldrich	4688937001
Universal Probe Library probe 073	Sigma-Aldrich	4688961001
Universal Probe Library probe 078	Sigma-Aldrich	4689011001
Universal Probe Library probe 087	Sigma-Aldrich	4689127001
Zero Blunt TOPO PCR Cloning Kit	Invitrogen	450245

Table 2.4 Molecular biology reagents and probes.

Standard laboratory reagents		
Product	**Supplier**	**Cat. No.**
2-Mercaptoethanol	Sigma-Aldrich	M3148
Acetic acid	Fisher Chemical	A/0400/PB17
Agarose	Fisher Bioreagents	BP160
Ammonium acetate solution [5 M]	Sigma-Aldrich	09691
Ammonium sulfate	Sigma-Aldrich	A4418
Boric acid	Sigma-Aldrich	B6768
Chloroform	Sigma-Aldrich	34854
D-glucose anhydrous	Fisher Chemical	G/0500/60
Dimethyl sulfoxide	Fisher Bioreagents	BP231
Ethanol [96%]	Fisher Bioreagents	BP8202
Ethylenediaminetetraacetic acid	AppliChem	A1103
Formaldehyde [37%]	AlfaAesar	33314
Glycerol	Sigma-Aldrich	G5516
Glycine	Fisher Bioreagents	BP381
HEPES	Sigma-Aldrich	H3375
Hoechst 33342, trihydrochloride, trihydrate - [10 mg/mL] solution	Invitrogen	H3570
Hydrochloric acid [37%]	Fisher Chemical	H/1200/PB15
Isopropanol	Fisher Chemical	P/7490/17
Phenol – chloroform – isoamyl alcohol mixture	Sigma-Aldrich	77619
Potassium acetate	Sigma-Aldrich	60035
Potassium chloride	Sigma-Aldrich	P9541
Potassium phosphate monobasic	Sigma-Aldrich	P5655
Sodium bicarbonate	Sigma-Aldrich	S5761
Sodium chloride	Fisher Chemical	S/3161/60
Sodium citrate tribasic dihydrate	Sigma-Aldrich	C8532
Sodium dodecyl sulfate	Sigma-Aldrich	L4390
Sodium hydroxide	Sigma-Aldrich	S8045
Sodium phosphate dibasic	Sigma-Aldrich	71636
Sodium phosphate monobasic dihydrate	Sigma-Aldrich	71500
Tris base	Fisher Bioreagents	BP152
Tris-EDTA buffer solution, pH 7.4	Sigma-Aldrich	93302
Triton X-100	Sigma-Aldrich	T8787

Table 2.5 Molecular biology laboratory reagents.

2.4 Agarose gel electrophoresis

The gels were prepared using 1% (w/v) multipurpose agarose in 0.5x TBE buffer, and precast stained with 0.000075x GelRed. GelRed is an economic and safer alternative to ethidium bromide for routine visualization of nucleic acids in electrophoresis gels.

Gels were run at 100 volts for 30-60 min, to allow for a clear separation of different molecular weight species. Depending on the expected size of the DNA fragment, three different standards were used to compare the molecular weight of the DNA fragment: 50 bp, 100 bp, and 1 kb DNA ladders. All gels were imaged using U:Genius[3] Gel Documentation System (Syngene).

2.5 TOPO cloning

PCR products from Platinum SuperFi DNA polymerase were cloned into TOPO vectors: pCR-Blunt II-TOPO or pCR-XL-2-TOPO vectors (**Figure 2.1**). The first was used for routine subcloning of amplicons below 1.5 Kb, while the latter was used for longer fragments of up to 10 Kb. The constructs were cloned into the vectors following the instructions of the manufacturer. In brief, the TOPO cloning reaction was carried out in a final volume of 3 µL, containing 0.5 µL TOPO vector, 0.5 µL of salt solution and 2 µL of PCR product. The reaction was incubated for 30 min at room temperature, after which 2 µL of the reaction was used for the transformation of competent cells.
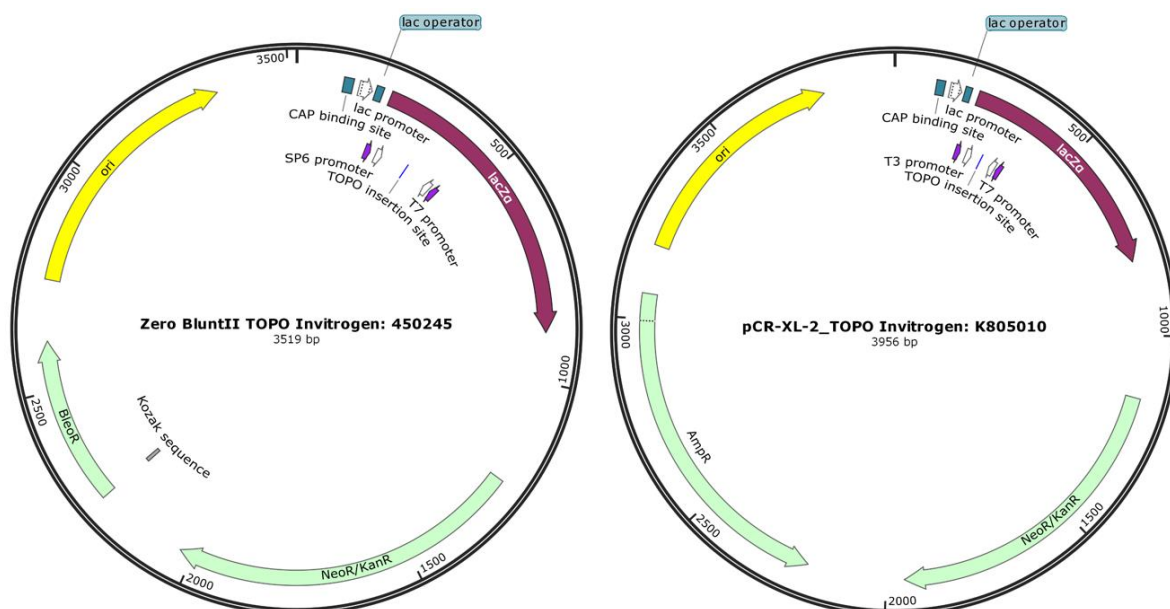
Figure 2.1 TOPO cloning plasmids.
pCR-Blunt II-TOPO vector (left) was used for routine sub cloning of PCR products <4 kb in length, e.g., homology arms and the GFP expression cassette; pCR-XL-2-TOPO vector (right) was used for subcloning gel-purified constructs >4 kb, e.g., LGR5-GFP expression cassette.

2.6 Growth and storage of bacterial cultures of competent cells

E. coli (DH5α) colonies were grown on Luria-Bertani (LB) agar plates with the appropriate antibiotics and incubated overnight at 37°C. Bacterial colonies were selected from a clonal population and a stab inoculated into broth for plasmid amplification. Bacteria were grown overnight in LB broth with antibiotics in suspension culture shaken at 225 rpm. The concentrations for antibiotics were 100 µg/mL for ampicillin and 50 µg/mL for kanamycin.

The frozen stock of bacterial cultures was prepared by mixing 0.5 mL of bacterial suspension in LB broth with 0.5 mL of a solution of 50% glycerol (sterilized with a 0.22 µm filter). The aliquots were kept in cryovials at -80°C.

Bacterial culture		
Product	**Supplier**	**Cat. No.**
Ampicillin	AlfaAesar	J60977
G418 disulfate [50 mg/mL] solution	AlfaAesar	J63871
Kanamycin A	Cayman Chemical	16140
Luria Bertani broth	Sigma-Aldrich	L3022
Luria Bertani broth with agar	Sigma-Aldrich	L2897
Puromycin dihydrochloride [10 mg/mL]	Gibco	A11138
Super Optimal broth with Catabolite repression medium	Invitrogen	15544
Zeocin [100 mg/mL] solution in HEPES	AlfaAesar	J67140

Table 2.6 Bacterial growth reagents.

2.7 Transformation of competent *E. coli* cells

Two different strains of competent cells were used for plasmid transformation: Subcloning efficiency DH5α competent cells and One Shot OmniMAX 2 T1^R chemically competent cells. Subcloning Efficiency DH5α is an economic and robust strain of competent cells with a reported transformation efficiency of >1x10^6 cfu/µg of pUC DNA, thus ideal for routine cloning. Alternatively, One Shot® OmniMAX™ 2 T1R is a strain of chemically competent cells capable of producing >5x10^9 cfu/µg of pUC DNA. This strain was used for recalcitrant constructs which did not yield colonies upon transformation on standard Subcloning Efficiency DH5α competent cells.

Competent cells were transformed by heat-shock following the specifications from the manufacturer for each type. In brief, 25 µL of competent cells were mixed with a suitable amount of plasmid DNA (1-10 ng in a volume no larger than 2 µL) and incubated on ice for 30 min. Next, the transformation reaction was briefly incubated at 42°C to apply the heat-shock, and immediately placed on ice for 2-5 min. Then, 130 µL of LB broth or SOC medium was added to the cells and incubated for 1 hr at 37°C

and shaken at 225 rpm. Finally, 100 μL cells were spread on LB agar plates containing the appropriate selection antibiotic and incubated at 37°C overnight for colonies to appear.

2.8 Extraction of plasmid DNA from *E. coli*

Plasmid DNA was extracted from 25 mL liquid cultures using alkaline lysis, following the protocol from Sambrook *et al.* (1989) with some slight modifications. Briefly, bacteria cells were harvested by centrifugation at 6,000 x *g* for 30 min, the supernatant was discarded, and the pellet was resuspended in 4 mL of Alkaline Lysis Solution I. After thoroughly mixing the bacterial suspension, 4 mL of Alkaline Lysis Solution II was added. The solution was gently mixed by inversion and the solution was incubated for 5 min at room temperature. Next, 4 mL of Alkaline Lysis Solution III was added and incubated for 20 min on ice. After the incubation, the solution was centrifuged twice at 6,000 x *g* for 30 min, each time the supernatant was transferred into a clean Falcon tube and the pellet was discarded. The plasmid DNA was precipitated with 0.7 volumes of isopropanol followed by a 70% ethanol wash. Finally, the pellet was resuspended in 1 mL Tris-EDTA buffer (pH 7.4).

Plasmids	
Name	**Supplier/Cat. No.**
AIO-Puro	Kindly provided by Dr Joanne Lacey, Centre for Stem Cell Biology, University of Sheffield.
FUCCI reporter	Kindly provided by Dr Ivana Barbaric, Centre for Stem Cell Biology, University of Sheffield.
pCAGMKOSiE	Addgene plasmid #20865
pCR-Blunt II-TOPO	Invitrogen Cat. No. 450245
pCR-XL-2-TOPO	Invitrogen Cat. No. K805010

Table 2.7 Plasmids used in this study.

2.9 Restriction enzyme digest

The digestion of DNA templates with restriction enzymes was performed using 1 μg of plasmid in a final volume of 20 μL, with appropriate buffers, unless otherwise stated, for 1 hr at 37°C. The outcome was confirmed by agarose gel electrophoresis.

2.10 Gel purification

Purification of DNA fragments from agarose gels was performed using PureLink Quick Gel Extraction Kit (Invitrogen), according to the manufacturer's protocol.

2.11 Ligation of DNA

Depending on the cloning strategy to assemble the reporter construct, some fragments were left with incompatible sticky ends. Therefore, prior to proceeding with the ligation of DNA, *PfuTurbo* DNA polymerase was used to fill in these incompatible sticky ends and generate blunt-end fragments. Briefly, the entire volume obtained after the gel purification protocol (~50 μL) was supplemented with 1x Cloned *Pfu* reaction buffer, 200 μM dNTPs, and 1 μL (2.5 U) of *PfuTurbo* DNA polymerase. The reaction was incubated for 1 hr at 68°C.

The ligation of DNA inserts into plasmid vectors were carried out in a final volume of 20 μL. The reaction mixed was prepared with T4 ligase buffer [50 mM Tris-HCl, pH 7.6 + 10 mM $MgCl_2$ + 1 mM ATP + 1 mM DTT + 5% (w/v) polyethylene glycol-8000], 5 U of T4 DNA ligase (Thermo Scientific), 1 mM ATP, DNA insert, and linearized vector. A ratio of 3:1 or 5:1, insert to vector, was typically used. The ligation reaction was then incubated at room temperature for 1-3 hrs. The ligation product was diluted 1/10, and from this dilution, the volume used for transformation was kept below 10% of the total volume of competent cells used.

2.12 Design of CRISPR/Cas9 guide RNAs

The design of suitable guide RNAs (gRNAs), for CRISPR/Cas9 editing, was conducted using the algorithm from the Zhang Lab (http://crispr.mit.edu).

2.13 Site-directed mutagenesis

Site-directed mutagenesis was performed using overlapping mutagenic primers with 3'- overhangs. Mutagenic primers were designed to cover a 15 to 20 nt of 5'- complementary region, and a 3'- non-complementary overhang of at least 8 nt. The targeted mutation was positioned in the middle of the primers and is highlighted in red on the table below.

Gene	Primer sequence 5' -> 3'	Size	Sense	% GC	T_m (°C)
MUT/LGR5/LHA	CTGAAAAC**A**TCTTGATACTTGAGAGTG	27	Fwd	37.0	**59.8**
	GTATCAAGA**T**GTTTTCAGCCTTTTCTTAC	29	Rev	34.5	**61.9**
MUT/LGR5/RHA	CAGCTAA**A**GGATAGATCGATCACAC	25	Fwd	44.0	**60.5**
	GATCTATCC**T**TTAGCTGAACAAATTATAC	29	Rev	31.0	**57.8**

Table 2.8 Primers used for site-directed mutagenesis in LGR5-GFP construct.

The target template was amplified using the mutagenic primers and Platinum SuperFi DNA polymerase, following the indications previously described, with one exception, the amount of template was reduced to 0.1 ng. The amplification was confirmed by agarose gel electrophoresis.

The PCR product was digested with *DpnI*, a methylation-sensitive restriction enzyme, to eliminate any leftover non-mutagenic template. The reaction was carried out in a final volume of 20 μL, containing 7 μL mutagenic PCR product, 5 U *DpnI*, and 1x reaction buffer. The digestion was incubated for 1 hr at 37°C, after which the product was introduced into competent cells.

2.14 Cell culture growth and storage

Cell lines		
Name	**Description**	**Supplier/Cat. No.**
CaCo-2	Colorectal adenocarcinoma	ECACC, Cat. No. 86010202.
Cultrex R-spondin 1 (Rspo1) cells	293T cell line stably transfected to express murine Rspo1 with an N-terminal HA epitope tag and fused to a C-terminal murine IgG2α Fc fragment. Stable clones were selected in medium containing 300 μg/mL zeocin.	Amsbio, Cat. No. 3710-001-01.
ShiPS-miFF1 (Sheffield human induced pluripotent stem mRNA-induced foreskin fibroblasts 1)	Human induced pluripotent stem cells	Kindly provided by Dr Christian Unger, Centre for Stem Cell Biology, University of Sheffield (https://hpscreg.eu/cell-line/UOSi001-A).

Table 2.9 Cell lines used in this study.

Non-iPSC lines (CaCo-2, HT-29, HepG2, HeLa) were cultured in full media (DMEM + 1% P/S + 10% FBS) and incubated at 37°C in 5% CO_2, while NT2 cells were incubated at 37°C with 10% CO_2.

Cell cultures were routinely passaged every 5-7 days. In brief, the medium was removed, and the monolayer was washed with PBS. The cells were harvested using trypsin-EDTA, and incubated for 3-5 min at 37°C, 5% CO_2. The trypsinization was stopped with 2 volumes of full medium. The cell suspension was then used to seed a new vessel (T75 flask for routine maintenance), which was then topped up with full medium.

To prepare a frozen stock of the cell lines, the cultures were harvested as stated before. After inhibition of trypsinization, the cell suspension was centrifuged 5 min at 800 *g*. The supernatant was discarded, and the cell pellet was resuspended in a final concentration of $1-2x10^6$ cell/mL with standard freezing medium (full medium + 10% DMSO). The aliquots were stored at -80°C in a Mr. Frosty freezing box, containing isopropanol. For long-term storage, samples were transferred into liquid nitrogen the next day. Batch numbers and dates were recorded on the laboratory database.

Cell culture reagents		
Product	**Supplier**	**Cat. No.**
Basement membrane Matrigel	Corning	354234
CD293 medium	Gibco	11913019
Cultrex 3D Culture Matrix Rat Collagen I	R&D Systems	3447-020-01
Dispase II powder	Sigma-Aldrich	D4693
Dulbecco's Modified Eagle Medium, high glucose, with L-glutamine and pyruvate	Gibco	41966
Dulbecco's Modified Eagle Medium/Ham's F-12	Gibco	12634
Essential 8 basal medium + Supplements [50x]	Gibco	A1517001
Fetal Bovine Serum (FBS)	Gibco	10270
HyClone defined Fetal Bovine Serum	GE Healthcare Life Science	16777-002
KnockOut DMEM	Gibco	10829
KnockOut Serum Replacement	Gibco	10828
L-Glutamine [200 mM]	Gibco	25030
Minimum Essential Medium non-essential Amino Acids [100x]	Gibco	11140
mTeSR1 basal medium + Supplements [5x]	STEMCELL Technologies	5850
Penicillin [10,000 U/mL] / Streptomycin [10,000 U/mL] solution (P/S)	Lonza	DE17602E
Phosphate-buffered saline, pH 7.2 [1x]	Gibco	20012
Recombinant human laminin-521 [100 µg/mL]	Gibco	A29248
Roswell Park Memorial Institute 1640 Medium	Gibco	11875
Trypsin-EDTA [0.05%], with phenol red	Gibco	25300
UltraPure [0.5 M] EDTA, pH 8.0	Invitrogen	15575020
Vitronectin (VTN-N) [500 µg/mL]	Gibco	A14700

Table 2.10 Cell culture media components.

2.15 Culture and storage of induced pluripotent stem cells

The cell line miFF1, an induced pluripotent stem cell line, was a gift from Dr Christian Unger (Prof Peter Andrews' group at the Centre for Stem Cell Biology), was seeded over feeder cells (mitomycin-inactivated mouse embryonic fibroblasts) and fed with human embryonic stem cell (hESC) medium.

Human Embryonic Stem Cell (hESC) medium	
Component	**Final concentration**
KnockOut DMEM	
bFGF	4 ng/mL
KnockOut Serum Replacement	20%
L-Glutamine	2 mM
NEAA	1x
β-mercaptoethanol	0.1 mM

Table 2.11 Composition of human embryonic stem cells growth media.

Cells were maintained on this medium for one day after initial seeding. The following day, cells were fed with a mix of hESC medium and E8 medium. E8 medium was developed as a chemically defined economic alternative to mTeSR1 medium for the culture of PSCs under feeder-free conditions.

For the next 5 days, the proportion of E8 medium was increased 20%, until the iPSCs were in 100 % E8 medium. After 6-7 days of culture, iPSCs were split into feeder-free conditions.

Prior to the passage, tissue culture plates were coated with 0.5 µg/cm^2 of laminin-521 (LN-521) diluted in basal DMEM. The plates were incubated at 37°C, 5% CO_2 for 2 hrs. LN-521 is a defined extracellular matrix suited for the culture of PSCs. It is an economic alternative to Matrigel, capable of maintaining the stemness of the cells, minimize cell death, and promoting cell proliferation. LN-521 was used for cells transitioning from feeder into feeder-free conditions, and for differentiation protocols.

Next, cells were harvested with 0.5 mM EDTA in PBS and incubated for 5-6 min at room temperature. The cells were flushed from the layer of feeders using E8 medium, trying to lift medium sized colonies, rather than single cells. The colonies were transferred into LN-coated wells, containing 10 µM Y-27632, and incubated at 37°C, 5% CO_2. Y-27632 is an inhibitor of Rho-associated, coiled-coil containing protein kinase (ROCK) and has been reported to improve the adhesion and survival of PSCs upon passaging.

The medium was replenished every day with fresh E8 medium without Y-27632. The cultures were passaged every 4-6 days or when they reached 80-90% confluence.

For routine passage, LN-521 was substituted by vitronectin, a cheaper alternative than LN-521. The tissue culture plates were coated with 0.5 µg/cm^2 of vitronectin diluted in PBS without calcium and magnesium, and were incubated at room temperature for 1 hr. The passaging and maintenance procedures were the same as described for the cultures grown over LN-coated wells.

To prepare a frozen stock of miFF1, the cells were harvested and stored in stem cell freezing medium (E8 medium + 10% DMSO). The aliquots were stored at -80°C in a Mr. Frosty freezing box, containing isopropanol. For long-term storage, samples were transferred into liquid nitrogen the next day. Batch numbers and dates were recorded on the laboratory database.

Recombinant proteins and growth factors		
Product	Supplier	Cat. No.
Activin A	R&D Systems; Peprotech	338-AC; 120-14
B-27 Supplement [50x], serum free	Gibco	17504
Bovine Fibroblast Growth Factor	R&D Systems	233-FB
Epidermal Growth Factor	Sigma-Aldrich	E9644
Fibroblast Growth Factor 4	R&D Systems; Peprotech	235-F4; 100-31
Noggin	R&D Systems; Peprotech	6057-NG; 120-10
R-spondin 1	R&D Systems	4645-RS
WNT-3A	R&D Systems	5036-WN

Table 2.12 Recombinant proteins and growth factors for the generation of iPSC-derived HIOs.

2.16 Cell transfection

Transfections/Nucleofections were performed using a 4D-Nucleofector System X Unit (Lonza) in a 20-µL nucleocuvette strip format. The transfection master mix was prepared by mixing SE nucleofection solution for CaCo-2 cells or P3 for iPSCs, with its corresponding supplements and 1 µg of DNA substrate.

Cells were harvested and distributed in aliquots containing $2x10^5$ cells. The cells were centrifuged at 500 g for 5 min, the medium was discarded, and the pellet resuspended in the master mix solution. The reaction cocktail was transferred into a nucleocuvette and the nucleofection was set up using the custom program DS 150 (CaCo-2) or CB 150 (iPSCs). Finally, cells were transferred into a 24-well plate and topped up with the appropriate medium.

To generate a stable recombinant cell line, the transfected cells were subcultured for 14 days with selection medium supplemented with either 3.5 µg/mL of puromycin for FUCCI-CaCo-2 cells, or 180 µg/mL of G418 for LGR-GFP miFF1 cells. After the selection process, the cells were returned to their respective routine growth medium.

2.17 Generation of intestinal organoids

The protocol for the generation of intestinal organoids derived from iPSCs was originally described by McCracken *et al.* (2011). This procedure was modified to increase the efficiency of organoid formation with miFF1 cells.

The cultures were grown in a 24-well plate format, seeded at $1.8x10^5$ miFF1 cells per LN-coated well. The cells were fed with 500 µL mTeSR1 medium containing 10 µM Y-27632, and incubated overnight at 37°C, 5% CO_2.

The following day, the medium was replaced with the definitive endoderm differentiation medium 1 (DE1). After 24 hrs, DE1 was removed and the cells were fed with DE2 for another 24 hrs. Upon differentiation of the definitive endoderm, the cultures were started on mid- and hindgut differentiation medium (MHDM), likewise, the medium was renewed every day. Under these conditions, the monolayer started to release mid- and hindgut spheroids into the medium on the third day. The spheroids were aspirated with the medium, transferred into an Eppendorf tube, and allowed to settle to the bottom. The medium was discarded, and the spheroids mixed with 50 µL basement-membrane Matrigel (BMM). The mid- and hindgut monolayer was fed again with HDM, and more spheroids were collected and transferred into BMM on the fourth day.

On the day of collection, each 50-μL aliquot of spheroids in BMM was carefully transferred into a 24-well plate; this was done slowly to allow the formation of a dome with BMM. The plates were incubated at 37°C for 15 min to allow the domes to become rigid within the matrix. Once they were steady and fixed in position, the wells were topped up with 400 μL intestinal growth medium.

The medium was changed every 3-4 days, depending on the acidification of the medium, due to the size of the developing organoids. Likewise, depending on the density of each dome, the organoids were split around day 20 to provide them space to continue their growth. Finally, around day 27, the organoids were transferred into agarose-coated 96-well plates to continue their culture in suspension.

Samples of the organoids were taken at different time points to evaluate the gene expression profile during their development.

Definitive Endoderm Differentiation Medium (DE1)		Definitive Endoderm Differentiation Medium (DE2)	
Component	Final concentration	Component	Final concentration
RPMI-1640 basal medium		RPMI-1640 basal medium	
B27	1x	B27	1x
CHIR99021	3 μM	L-Glutamine	2 mM
L-Glutamine	2 mM	NEAA	1x
NEAA	1x	P/S	1%
P/S	1%		

Table 2.13 Composition of DE1 and DE2 media for the generation of definitive endoderm (modified from Siller *et al.*, 2015).

Mid- and Hindgut differentiation medium (MHDM)	
Component	Final concentration
RPMI-1640 basal medium	
CHIR99021	2 μM
Defined FBS	2%
FGF4	500 ng/mL
L-Glutamine	2 mM
NEAA	1x
NOG	100 ng/ mL
P/S	1%

Table 2.14 Composition of mid- and hindgut differentiation medium (modified from McCracken *et al.*, 2011).

Intestinal organoids growth medium	
Component	Final concentration
Advanced DMEM/F-12 basal medium	
B27	1x
EGF	100 ng/ mL
HEPES buffer	15 mM
L-Glutamine	2 mM
NOG	100 ng/mL
P/S	1%
rmRSPO1	500 ng/mL
*Decrease EGF to 10 ng/mL after 30 days of culture.	

Table 2.15 Intestinal organoids growth medium.

Basement membrane Matrigel (BMM)	
Component	Final concentration
Basement membrane Matrigel	
B27	1x
EGF	100 ng/ mL
NOG	100 ng/mL
rmRSPO1	500 ng/mL

Table 2.16 Composition of basement membrane Matrigel.

2.18 Organ-on-a-chip culture: Generation of CDX2^{+} cultures on 3-lane OrganoPlate

*Work performed in collaboration with Ms Elena Naumovska (Mimetas) and Dr Kai Erdmann (Department of Biomedical Science, University of Sheffield).

Cell culture on the OrganoPlates was performed following the indication from the supplier, and additional expertise was provided by Ms Naumovska.

In brief, following the timeline presented on **Figure 2.2A**, on day -1, 1.6 µL of ECM solution (4 mg/mL Collagen I, 100 mM HEPES and 3.7 mg/mL NaHCO$_3$) was loaded into the middle/gel inlet of the OrganoPlate chips. The plates were incubated for 15 min in a cell culture incubator (37°C, 5% CO$_2$) to allow the polymerization of the Collagen I; next, 50 µL of Hank's Balanced Salt Solution (HBSS) was added into the gel inlet and outlet to prevent the gel from drying out, after which the plates were returned into the incubator.

After 24 hrs of incubation the top channel was coated with 2 µL vitronectin diluted in basal DMEM to a final concentration of 10 µg/mL, plates were incubated for 1 hr at 37°C. Next, the plates were seeded with 4x10^4 miFF1 cells per chip. The cells were fed with 30 µL mTeSR1 medium containing 10 µM Y-

73

27632 (**Figure 2.2B and C**), and incubated overnight at 37°C, 5% CO_2. Plates were incubated while placed on a resting position at 75° angle, to facilitate the attachment of the cells to the ECM. After 24 hrs, the medium was changed with fresh mTeSR1 and the cultures were continued for another 24 hrs before starting the differentiation conditions.
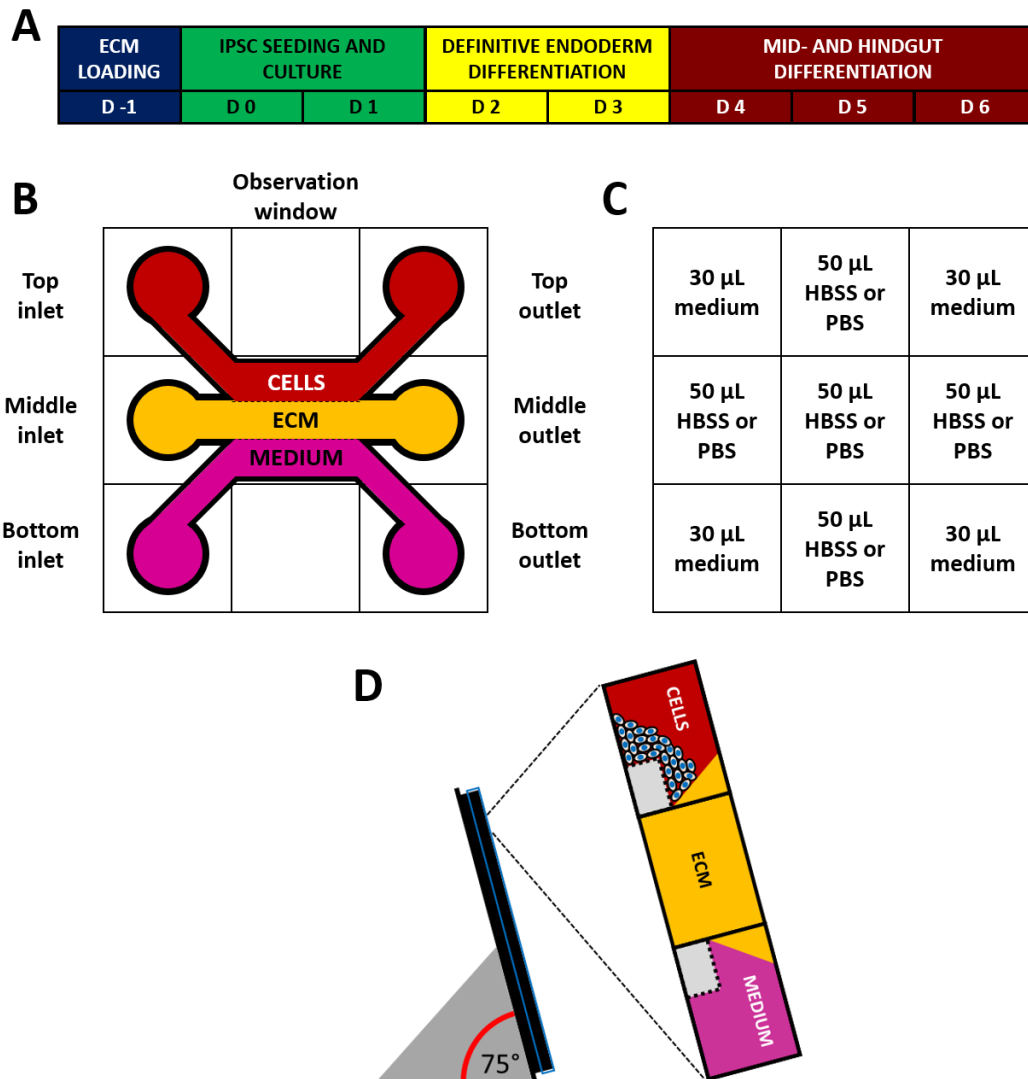
Figure 2.2 Generation of organ-on-a-chip intestinal cultures using OrganoPlate technology.
(A) Schematic timeline for the generation of CDX2$^+$ 3D cultures in an OrganoPlate chip; (B) Configuration of the cell culture components in an OrganoPlate chip; (C) Feeding layout; (D) Effect of the inclination when pre incubating the cells on the OrganoPlate chips. Cells aggregate around the phase guide and the ECM meniscus, allowing the cells to spread and form tubular structures.

After 48 hrs on mTeSR1 medium, the cells were started on differentiation conditions to generate definitive endoderm. The medium was changed with DE1 for 24 hrs, followed by 24 hrs on DE2.

Once the differentiation of the definitive endoderm was completed, the cultures were started on mid- and hindgut differentiation medium. These conditions were maintained for 72 hrs, with medium

changes every 24 hrs. After the mid- and hindgut differentiation stage, the cultures were processed for immunostaining.

2.19 Production of recombinant murine R-spondin 1

Protein purification and analysis		
Product	**Supplier**	**Cat. No.**
4–20% Mini-PROTEAN TGX Precast Protein Gels, 10-well, 30 µl	Bio-Rad	4561093
Bradford Protein Assay Kit II	Bio-Rad	5000002
Coomassie Blue R250	Fisher Chemical	C/P540/46
Pierce ECL Western Blotting Substrate	Thermo Scientific	32209
Prism Ultra Protein Ladder (10-245 kDa)	Abcam	ab116028
Protein A Agarose Kit	KPL	553-50-00
Sample Buffer, Laemmli [2x]	Sigma-Aldrich	S3401
SnakeSkin Dialysis Tubing, 10K MWCO, 22 mm	Thermo Scientific	68100
Trans-Blot Turbo Mini PVDF Transfer Packs	Bio-Rad	1704156

Table 2.17 Protein purification reagents.

A cell line of 293T was transfected with an expression cassette for recombinant murine R-spondin 1 (rmRSPO1). The rmRSPO1 expression cassette (**Figure 2.3**) was generated by Kuo Lab (Ootani *et al.*, 2009) and is now commercially available as Cultrex R-spondin 1 (Rspo1) cells (Amsbio).
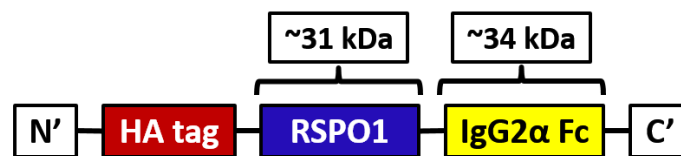
Figure 2.3 rmRSPO1 fusion protein structure.
An expression cassette was designed for the generation of recombinant murine R-spondin 1 (blue), labelled with a hemagglutinin A tag (red) for antibody characterization and the Fc fragment of murine IgG2a (yellow) for further purification with protein A agarose columns.

An aliquot of approximately 1.3×10^3 RSPO1 cells were seeded into a T75 flask, fed with full medium, and incubated at 37°C, 5% CO_2. After 48 hrs, the medium was removed and changed with selection growth medium (full medium + 300 µg/mL of zeocin). The selective conditions were kept for 3 to 5 days, replenishing the medium every 3 days. Once the cells reached a confluence of 80-90%, they were split into a 3-layer flask (525 cm²).

After the cells achieved 80% confluency, the medium was changed with 75 mL CD293 containing 2 mM glutamine. This medium was formulated for the growth of 293 cells on serum free conditions to facilitate the purification of rmRSPO1 from the supernatant and prevent carryover of serum proteins.

The culture was continued for approximately 8 more days, and the cells eventually started to detach and continued growing in suspension. The pH of the media was monitored, and when it started to turn yellow (approximately after 4 days), the media was collected and replaced with 75 mL of fresh media. The collected media was centrifuged at 3,000 rpm for 15 min to remove cells and debris, and then stored at 4°C. The culture was continued for another 4 days, after which the new batch of medium was collected and centrifuged in the same way as before, and the flask was discarded.

Both batches of supernatant were pooled together and filtered through a 0.22 µm filter at 4°C. The supernatants were processed for the purification of rmRSPO1 or stored at 4°C until needed.

2.20 Purification of rmRSPO1

The supernatant, approximately 150 mL per 3-layer flask, was transferred into SnakeSkin dialysis tubing (Thermo Scientific) with a 10K molecular weight cut-off. The supernatant was dialyzed overnight in 5 L of 1x PBS, the next day the PBS was changed, and the dialysis continued for another 8-16 hrs.

Protein A agarose columns were packed and prepared following manufacturer's instructions and equilibrated with 10 volumes of wash/binding buffer. The dialyzed supernatant was equilibrated 1:1 with wash/binding buffer. Next, the supernatant was passed through the protein A columns and the rmRSPO1 was recovered by adding ~20 mL elution buffer. The rmRSPO was collected in 1 mL aliquots and the pH was adjusted adding 240 µL of 5x wash/binding buffer. The concentration of rmRSPO1 was quantified using BSA as a control, and the aliquots were stored at -20°C until needed.

2.21 SDS-PAGE and Western blot analysis

SDS-PAGE was prepared to confirm the success of the purification protocol of rmRSPO1 from the CD293 culture medium.

First, 10 µL of protein sample was mixed with 10 µL of 2x laemmli buffer containing 10% β-mercaptoethanol, the sample was heated at 95°C for 5 min to fully denature all proteins. Denatured protein was carefully loaded into a well of a 4–20% Mini-PROTEAN TGX precast protein gel (Bio Rad). Additionally, 3 µL of Prism Ultra protein ladder (10-245 kDa) (Abcam) was ran in parallel, as a molecular weight standard. A second set of samples and control were loaded in the same gel, each set will be used for Coomassie blue staining and western blot, respectively. The gel was run on 1x SDS-PAGE running buffer at 150 volts for approximately 1 hr.

The gel was cut with a scalpel blade. The first gel was placed in a 90 mm petri dish and covered with ~20 mL of Coomassie blue staining solution followed by 3 hrs incubation on a shaker. After the incubation period, the stain was discarded, and the gel was gently rinsed with tap water. Next, the gel was covered with ~20 mL of destaining solution and kept on a shaker for 1hr. This process was repeated several times until the background of the gel was clear.

The second half of the gel was transferred into a Trans-Blot Turbo mini PVDF transfer membrane (Bio Rad), using the default settings in a Trans-Blot Turbo Transfer System (Bio Rad). Prior to antibody labelling, the membrane was incubated for 2 hrs in a blocking solution of 1x TBST + 5% BSA. Next, the blocking solution was discarded, and the membrane was covered with primary antibody diluted in blocking solution, followed by 2 hrs incubation at room temperature or overnight at 4°C.

Primary antibody				
Product	Stock [µg/mL]	Final [µg/mL]	Supplier	Cat. No.
Goat anti mouse RSPO1	200	0.1	R&D Systems	AF3474

Table 2.18 Primary antibodies for western blot.

The membrane was subsequently washed 3 times with a solution of 1x TBST. Then, the secondary antibody diluted in blocking buffer was added into the membrane, followed by 1 hr incubation at room temperature. After incubation, the membrane was washed 3 times with a solution of 1x TBST.

Secondary antibody				
Product	Stock [µg/mL]	Final [µg/mL]	Supplier	Cat. No.
Rabbit anti goat IgG-HRP	-	1:1000	R&D Systems	HAF017

Table 2.19 Secondary antibodies for western blot.

To reveal the protein bands, the membrane was incubated for 1 min with Pierce ECL western blotting substrate (Thermo Scientific). After incubation, the excess reagent was drained, and the membrane was imaged. Both, the Coomassie-stained gel, and the western blot membrane were imaged with a ChemiDoc XRS+ system – Molecular imager (Bio-Rad).

2.22 Extraction of total RNA using the RNeasy mini kit (Qiagen)

For cultures grown on T75 flasks, the cells were harvested as done for routine passaging, and the trypsinized cell suspension was centrifuged at 800 x g for 5 min. The supernatant was discarded, and the pellet was lysed.

For cultures grown in 24-well plates, the medium was discarded, and the lysis reagent was added directly to the well.

The cells were lysed using 650 μL of RLT buffer for T75 cultures and 350 μL per well in 24-well plates. The lysate was homogenized by repeated pipetting, after which 650 μL of 70% ethanol was added to the samples. Next, the full volume of lysate was loaded into a RNeasy spin column set over a 2 mL collection tube. The column was centrifuged for 30 s at 8,000 g, and the waste flow-through was discarded. The column was washed by adding 700 μL RW buffer, followed by centrifugation for 30 s at 8,000 g, while the flow-through was discarded. The column was washed twice with 500 μL RPE buffer, each time followed by centrifugation at 8,000 g for 30 s and 2 min, respectively. Finally, the sample was eluted into a clean tube by adding 30 – 50 μL of RNase-free water into the column and centrifugation for 1 min at 8,000 g.

2.23 Total RNA extraction using TRIzol

For cultures grown on T75 flasks, first the cells were harvested as done for routine passaging, and the trypsinized cell suspension was centrifuged at 800 x g for 5 min. The supernatant was discarded, and the pellet was lysed. For cultures grown in 24-well plates, the medium was discarded, and the lysis reagent was added directly to the well.

The cells were lysed using 400 μL of TRIzol reagent for T75 cultures and 200 μL per well in 24-well plates. The lysate was transferred into clean RNase free Eppendorf tubes, and incubated for 5 min at room temperature, to allow the complete dissociation of nucleoprotein complexes. Next, 0.2 mL of chloroform per 1 mL of TRIzol were added into the lysate, followed by 3 min incubation. The sample was centrifuged 15 min at 12,000 x g, and the upper aqueous phase, containing the total RNA, was recovered in a clean tube. This solution was mixed with 10 μg of RNase-free glycogen and 0.5 mL of isopropanol per 1 mL of TRIzol and incubated for 10 min at RT. Glycogen was used as a carrier agent to improve the yield of RNA collected upon precipitation with isopropanol. The sample was centrifuged for 10 min at 12,000 x g. The RNA precipitated as a white pellet, and the supernatant was discarded with a micropipette. The RNA pellet was resuspended in 30 μL of RNase free water, followed by the addition of ammonium acetate to a final concentration of 2M, and 2.5 volumes of ice-cold absolute ethanol. The solution was incubated for 30 min at -20°C, after which it was centrifuged for 30 min at 10,000 x g. The supernatant was discarded, and the pellet was resuspended in 200 μL of 70% ethanol. The sample was vortexed briefly, and centrifuged for 15 min at 10,000 x g. The supernatant was carefully removed with a micropipette and the pellet was air-dried. Finally, the sample was resuspended in 20 – 50 μL RNase free water.

After extraction, the samples were quantified in the NanoDrop, and stored at -80°C until needed.

2.24 Synthesis of first-strand cDNA

The samples were first treated with DNase to remove any residual genomic or mitochondrial DNA. Briefly, DNase treatments were done in a final volume of 20 µL, containing 1 µg of total RNA, 1x TURBO DNase buffer, and 2 U TURBO DNase (Ambion). The reaction was incubated at 37°C for 1 hr. Next, the reaction was stopped using 5 mM EDTA, and incubated at 70°C for 10 min to inactivate the DNase.

First, the mRNA was denatured in a final volume of 15 µL containing: 5 µM **Oligo d(T)$_{23}$VN***, 5 µM **random hexamers***, 500 nM dNTPs, and 1 µg of DNA-free RNA for 5 min at 65°C, and immediately placed on ice. Secondly, the cDNA synthesis reaction was carried out in a final volume of 30 µL containing 1x ProtoScript II buffer, 2 U ProtoScript II Reverse Transcriptase (New England Biolabs), 10 mM DTT, and 12 U Placental RNase inhibitor. The final reaction was incubated at 42°C for 1.5 hr, followed by heat inactivation at 65°C for 20 min. The cDNA was stored at -20°C until required.

*A combination of Oligo d(T)$_{23}$VN and random hexamers was used for the synthesis of first-strand cDNA, as the following amplification results were more consistent than when used either of them separately.

2.25 Real time PCR

Quantitative/real time reverse transcriptase PCR (RT-qPCR) was performed using two systems: SYBR Green and Taqman. SYBR Green is an intercalating agent used for the quantification of amplicons in real time PCR. It binds to the major groove of double stranded DNA, and upon denaturing it releases a fluorescent signal. However, this makes SYBR Green prone to the emission of unspecific signal given that it has no specificity to the target gene. Conversely, Taqman has a lower risk of unspecific signal emission, but it is more expensive, and the initial calibration was considerably troublesome due to its high sensitivity to the amount of template cDNA.

SYBR Green primers were designed to amplify intron spanning fragments between 70 and 250 bp, following the same general guidelines as previously described for standard PCR primers. The table summarising the results of the analysis is presented in the Appendix section 2. RT-qPCR reactions were prepared in a final volume of 10 µL containing: 1x QuantiTect SYBR Green PCR Master Mix, 300 nm of each primer, and 50 ng of cDNA.

Taqman probes and primers were obtained from Roche's Universal Probe Library (UPL). The selection of UPL probes and the primer design for each specific gene, was performed using the Probe Finder

Assay Design Software from Roche (https://lifescience.roche.com/en_gb/brands/universal-probe-library.html#assay-design-center). The table summarising the results of the analysis is presented in the Appendix section 3. RT-qPCR reactions were prepared in a final volume of 25 μL containing: 1x FastStart TaqMan Probe Master (ROX), 200 nM UPL probe, 900 nm of each primer, and 50 ng of cDNA. The reactions were prepared with 3 technical replicates in a 384 well plate format.

SYBR Green system				
Step	Temp (°C)	Time	Ramp rate (°C/s)	Cycles
UNG prevention	50	2 min	1.5	1
Activation	95	15 min		1
Denaturation	94	15 s		40
Annealing	55-60	30 s	-	
Elongation	72	30 s		
Dissociation curve and detection	95	15 s		
	60	1 min		
	Raise to 95°C		0.5	
Taqman system				
Step	Temp (°C)	Time	Ramp rate (°C/s)	Cycles
UNG prevention	50	2 min	1.5	1
Activation	95	10 min		1
Amplification and detection	95	10 s	1.5	40
	60	1 min		

Table 2.20 qPCR cycling conditions.

2.26 Immunostaining of cells

The medium from the wells was discarded and the cultures were washed twice with 1x PBS. Then the cell cultures were incubated with fixing solution for 20 min at room temperature, followed by 2 washes with 1x PBS. Specifically for organoids, the fixing solution was prepared with 3.7% formaldehyde in HCE buffer, and samples were washed once with IF buffer.

For intracellular epitopes, cells were incubated with **permeabilization solution*** for 15 min at room temperature, followed by 2 **washing steps*** with 1x PBS. After permeabilization, to prevent nonspecific binding of the antibodies, the samples were incubated for 1 hr in **blocking buffer***. If the protein was a cell surface marker, the permeabilization and blocking steps were omitted. Next, the cells were incubated with primary antibody diluted in **washing buffer***, the incubation continued for 1 hr at room temperature or overnight at 4°C.

Primary antibodies				
Product	**Stock [µg/mL]**	**Final [µg/mL]**	**Supplier**	**Cat. No.**
Goat anti-human CDX2	200	10	R&D Systems	AF3665
Goat anti-human HNF-3β/FOXA2	200	10	R&D Systems	AF2400
Mouse anti-human BSG/CD147 clone TRA-1-85	-	1:50	In house (provided by CSCB)	
Mouse anti-human LGR5 clone OTI2A2	1000	10	Invitrogen	MA5-25644
Mouse anti-human SOX17 clone 614013	200	10	R&D Systems	MAB19241
Mouse anti-human SSEA1 clone MC480	-	1:20	In house (provided by CSCB)	
Rat anti-human SSEA3 clone MC631	-	1:20	In house (provided by CSCB)	

Table 2.21 Primary antibodies for immunofluorescence.

The sample was washed twice with wash buffer, followed by 1 hr incubation with secondary antibody diluted in wash buffer and containing 1.5 µg/mL Hoechst 33342. The cells were washed 3 times with 1x PBS, and imaged, or stored a 4°C until needed.

*Appendix section 1 describes the preparation of these solutions and alternative versions specific for the immunostaining of organoids. Particularly, IF buffer was used in all washing steps and in substitution of washing buffer.

Secondary Antibodies				
Product	**Stock [µg/mL]**	**Final [µg/mL]**	**Supplier**	**Cat. No.**
Donkey anti goat IgG-NL557	1000	5	R&D Systems	NL001
Donkey anti mouse IgG-NL493	1000	5	R&D Systems	NL009
Donkey anti rabbit IgG-NL637	1000	5	R&D Systems	NL005
Goat anti mouse IgG$_1$-Alexa Fluor 633	2000	2	Invitrogen	A21126
Goat anti rat IgG-Cy5	2000	10	Invitrogen	A10525

Table 2.22 Secondary antibodies for immunofluorescence.

2.27 Microscopy

Bright field images were taken with an Olympus CKX41 inverted microscope attached to a PixeLINK PL-A686 camera.

An EVOS FL inverted epifluorescence microscope (AMG) was used for *ad hoc* fluorescence microscopy.

High-throughput imaging was performed with an IN Cell Analyzer 2200 Cell Imaging System – High Content Analysis/High Content Screening Microscope (GE Healthcare Life Sciences).

Confocal imaging was performed with a Nikon A1 confocal laser microscope (Light Microscopy Facility (LMF)).

Organoids were imaged with a ZEISS Lightsheet Z.1 light sheet fluorescence microscope (LMF).

2.28 High-throughput small-molecule screening

FUCCI-CaCo-2 cells were seeded at a density of 3500 cells per well on 384 well-plates using a MultiDrop™ Combi Reagent Dispenser (Thermo Scientific). Cells were fed with full medium and incubated overnight. The next day, the medium was replaced with fresh full medium and the cells were treated with the Tocriscreen Total Compound Library and a plate with a subset of handpicked small molecules, hereafter referred as CW.

The Tocriscreen Total Compound Library consists of 14 plates with 1120 different compounds active in GPCRs, kinases, ion channels, nuclear receptors, and transporters. A detailed list with all the compounds is presented in the Appendix section. These compounds came in 10 mM DMSO solutions and were used to prepare 'mother plates' where they were pre dissolved in full medium to a concentration of 100 µM (equivalent to 1% DMSO). Finally, for the cellular assay the small molecules were added to a final concentration of 5 µM on full medium (equivalent to 0.05% DMSO).

The CW plate consists of 9 compounds at 3 different concentrations each (listed in the table below). The compounds and concentrations were handpicked based on reports from the literature regarding their activity on signalling pathways involved in the self-renewal and proliferation of stem cells or the differentiation of the intestinal secretory lineage. This plate also contained a set of controls with the solvents of these 9 compounds: water, 2 and 1% ethanol, 0.4 and 0.05% DMSO.

The mother plates and cellular assays were prepared using a Microlab STAR Liquid Handling System (Hamilton Company). Each 384 well plate, containing 4 plates from the small-molecule libraries, was prepared in triplicates.

Cells were incubated for 72 hrs with the small-molecule library, after which the cells were fixed with fixing solution and stained with 1.5 µg/mL of Hoechst 33342. The plates were processed using a MultiDrop™ 384 Reagent Dispenser (Thermo Scientific) and an ELx405 Select CW Microplate Washer (Bio-Tek Instruments).

High-throughput imaging was performed with an ImageXpress Micro Imaging System (Molecular Devices). Further analysis was conducted using MetaXpress – High-Content Image Analysis Software (Molecular Devices) with a Multi-Wavelength Cell Scoring algorithm, to identify positive cells on different wavelengths.

Small molecules			
Product	Final [µM]	Supplier	Cat. No.
CHIR99021	2, 3, 4	Cayman Chemical	CAY13122-1
DAPT (GSI-IX)	5, 10, 20	Generon	A10288-5
Dasatinib	5, 10, 20	Santa Cruz Biotechnology	sc-358114
Methotrexate	0.1, 1, 10	Cayman Chemical	13960-50
N-Acetyl-L-cysteine	1, 500, 1000	Sigma-Aldrich	A9165
Nicotinamide	5000, 10000, 20000	Sigma-Aldrich	N0636
Taurodeoxycholic acid, sodium salt hydrate	0.1, 10, 25	Fisher Scientific (ACROS Organics)	10716822
Tocriscreen Total compound library collection	5	Tocris	2284
Valproic acid (sodium salt)	500, 1000, 2000	Cayman Chemical	13033-10
Y-27632	10, 20, 30	Cell Guidance Systems	SM02-1

Table 2.23 Small molecules used on high-throughput screening.

CHAPTER 3. ESTABLISHMENT AND OPTIMIZATION OF A PROTOCOL FOR GENERATION OF iPSC-DERIVED HUMAN INTESTINAL ORGANOIDS.

3.1 Introduction

Spence *et al.* (2011) and McCracken *et al.* (2011) described the first protocol for the formation of human intestinal organoids derived from pluripotent stem cells. Along with the work from Sato *et al*. (2009), these groundbreaking studies led to the development of a new stream of works exploring novel applications for these outstanding modelling systems. Nonetheless, the model of intesinal organoids is not without limitations, particularly: (i) the high cost required for the production of large quantities of organoids, essential for their implementation in high-throughput experiments (Zanoni *et al.*, 2020); (ii) the maturation of the tissue, along with the expression of all representative cell types found in the intestinal epithelium (Finkbeiner *et al.*, 2015*b*); and (iii) the generation of complex models by incorporating vasculature, microbiome, and multi systemic interaction with the immune and nervous system (Min *et al.*, 2020).

Therefore, the aim of this chapter was to optimize the protocol established by McCracken *et al.* (2011) to reduce the time and cost required for the differentiation process, and improve the organoid production output. For this task, we have identified critical steps to introduce modifications into the culture conditions, improving the final outcome of the differentiation process. Based on our analysis of the differentiation protocol, we identified three key aspects to focus our experiments: (i) the general differentiation conditons for the definitive endoderm stage; (ii) the replacement of commercial growth factors for small molecules and recombinant proteins produced in-house; and (iii) the ECM composition.

3.1.1 Importance of the definitive endoderm differentiation stage in the generation of HIOs

The endoderm is the inner layer of cells generated after the gastrulation of the epiblast in the early stages of embryogenesis. Gastrulation starts with the formation of the primitive streak (PS) at the posterior epiblast. The cells migrating through the PS acquire a mesendodermal identity and eventually diverge their commitment into either a mesoderm or definitive endoderm (DE) lineage. The DE is the germinal layer responsible for deriving the gastrointestinal tract (oesophagus, stomach, small and large intestine), the associated glands (liver, pancreas and gall bladder), and other organs (thyroid, thymus and lungs) (Wells & Melton, 1999; Grapin-Botton & Melton, 2000; Lewis & Tam, 2006). During the differentiation events that give rise to the DE, two transcription factors are upregulated (*SOX17* and *FOXA2),* which have been widely used as markers to characterize DE differentiation (Tam *et al.*, 1993; Wang *et al.*, 2012).

As mentioned before in Chapter 1, every differentiation process relies on the interplay of intracellular factors and the crosstalk of different signalling pathways. In the case of DE differentiation, the main pathways involved are: Activin/Nodal, PI3K-Akt, FGF, BMP and WNT, all of which have been targeted in different studies in order to optimize the outcome of the differentiation protocols (Sulzbacher *et al.*, 2009; Mathew *et al.*, 2012, 2015).

Early studies in *Xenopus* have shown that ectodermal explants submerged in activin A (AA) solution led to differentiation into yolk-rich endodermal cells (Ninomiya *et al.*, 1999). AA is a member of the TGF-β family, and has been found to be the common denominator in all the differentiation protocols for DE (Mathew *et al.*, 2012).

Initial reports describing the successful differentiation of hESCs into DE relied on the addition of AA at increasing yet low concentrations of serum over the course of three days (0%, 0.2%, and 2%) (D'Amour *et al.*, 2005). Notably, this served as the basis to assemble the protocol for the generation of HIOs (McCracken *et al.*, 2011, 2014).

Likewise, bone morphogenetic protein-4 (BMP4) has been studied in DE differentiation. BMP4, a member of the TGF-β family, is capable of triggering signalling events that emulate the formation of the primitive streak (Wiles & Johansson, 1999). This induces pluripotent cells to acquire a mesendodermal identity (Taha *et al.*, 2016). Previous studies have found that BMP4 acts synergistically with AA. The first one has been shown to contribute in accelerating the downregulation of pluripotency genes, while the latter leads the transition into the DE identity (Teo *et al.*, 2012).

Wells and Spence first described the generation of HIOs derived from pluripotent cells. This required recreating the transition of cells from a pluripotent state into definitive endoderm. Their conclusions highlighted the importance of the DE differentiation stage to accomplish the production of intestinal organoids (McCracken *et al.*, 2011). Additional modifications to the DE stage of this protocol included adding BMP4 on the first day of differentiation to optimize the production of gastric organoids (McCracken *et al.*, 2014).

Several studies have reported the generation of definitive endoderm using defined growth factor, serum-free conditions and supplementation with B27. (Yu *et al.*, 2015; Qu *et al.*, 2017). The use of B27 supplements has been reported to provide a substantial improvement in the differentiation of hESCs and iPSCs into DE. This is mostly due to an increase in cell survival and by facilitating the transition into the DE stage (Wang *et al.*, 2015).

A study described the use of B27, AA, and WNT induction to obtain DE. After 3 days under differentiation conditions, 60-80% of the cells exhibited DE markers, although there was still a considerable population expressing OCT4. Additionally, it was found that extending the differentiation time to 5 or 7 days reduced the undifferentiated population, but compromised the capacity of DE cells to undergo further differentiation (Toivonen *et al.*, 2013). This highlights the importance of the length and timing of the differentiation conditions.

Interestingly, although OCT4 is a marker of pluripotency, it acts in collaboration with WNT on an epigenetic level to prime endodermal promoters. Therefore, the synergy between OCT4 and WNT signalling is essential for the cells to transition into mesendoderm (Ying *et al.*, 2015). Additionally, another study found that WNT induction during DE differentiation activates CDX2, facilitating the transition into intestinal cells (Sherwood *et al.*, 2011).

The combination of AA and WNT3A has shown to be generally successful in differentiating pluripotent cells into DE. However, cost-effective alternatives have been developed to substitute the use of WNT3A. The most commonly used is CHIR99021, a GSK3β inhibitor which has proven to be just as effective as the recombinant protein (Teo *et al.*, 2014; Takeuchi *et al.*, 2015).

Siller *et al.* described a small-molecule-driven differentiation protocol to generate hepatocyte progenitors. As opposed to previous works, the DE differentiation was performed in 2 days and did not require the use of AA. Their protocol required one day with B27 supplementation and a relatively high dose (3 µM) of CHIR99021 to induce WNT activation, and a second day just with B27 supplementation. The expression of SOX17 and FOXA2 was reported in ~80% of the cell population. This protocol appears to provide a more efficient approach in terms of timing and medium composition (Siller *et al.*, 2015).

3.1.2 Influence of the extracellular matrix composition in the generation of HIOs

As part of this project, one of the objectives was to develop a protocol compatible with HTS and scalable for clinical applications. The latter requires it to be in accordance with good-manufacturing process (GMP) guidelines, which strictly control the use of animal derivatives.

The protocol presented by McCracken *et al.* (2011), described the use of hESC-qualified Matrigel for seeding the pluripotent stem cells. However, Matrigel is an undefined ECM derived from mouse sarcoma tumours with significant batch-to-batch variability. To overcome this issue, we sought a defined ECM that could allow the culture of iPSCs without compromising their differentiation potential into DE.

The stiffness and elasticity of the ECM is known to provide mechanical stimulation to the cell, which triggers an array of cellular responses such as proliferation, apoptosis, and differentiation. The exact molecular mechanism is still not fully understood, but it is known to be associated with WNT and Hippo-YAP/TAZ pathways (Du *et al.*, 2016). In particular, pluripotent stem cells (PSCs) have been reported to exert a low traction force yet switch into a highly contractile state during DE differentiation. Moreover, fibronectin and laminin-111 can regulate DE differentiation by triggering integrin-mediated signalling pathways (Taylor-Weiner *et al.*, 2013, 2015). This indicates that differentiation protocols can be optimized by co-regulating the ECM alongside the soluble factors in the medium and highlights the importance of identifying the most appropriate ECM composition.

The human intestinal epithelium is supported mostly by LNs α2-, α3-, and α5 (Teller *et al.*, 2007). It has been found that LN α5 plays a crucial role in building and supporting the crypt-villus microarchitecture of the intestinal mucosa in mice. Additionally, LNs provide positional information, and can influence cell proliferation, migration, apoptosis and differentiation by interacting with integrins (Mahoney *et al.*, 2008).

A previous work compared the effect of Matrigel, laminin-521, and laminin-511 in the differentiation of hESC-derived hepatocytes. The characterization of the DE showed a similar percentage of FOXA2$^+$ cells between the 3 matrixes, though the proportion of SOX17$^+$ cells with laminin-521 was considerably higher compared to Matrigel. Also their results found that cultures seeded over LN matrixes exhibited a more efficient suppression of unwanted pluripotency genes (Cameron *et al.*, 2015). Later, a different study evaluated the effect of laminin-521, laminin-511, and fibronectin in the differentiation of hPSCs into hepatocyte-like cells. Fibronectin did not show a relevant effect in the differentiation process. In contrast, LN 521 and 511 appeared to improve the hepatic specification of hPSC-derived DE cells (Kanninen *et al.*, 2016).

Matrigel has been used as a feeder-free alternative for the culture of PSCs, although as mentioned before, it is still an undefined matrix. Vitronectin was proven to be a reliable, defined, xeno-free alternative which supported the self-renewal and pluripotency of hESCs (Braam *et al.*, 2008). Further studies found that fibronectin and vitronectin promote endodermal differentiation of hESCs, through the interactions with integrin α5 (ITGA5) and integrin αV (ITGAV), respectively. Additionally, it was found that compared to Matrigel, the combination of fibronectin and vitronectin improved the differentiation of DE, based on qPCR analysis of *SOX17*, *FOXA2* and *CXCR4* (Brafman *et al.*, 2013).

The aforementioned evidence highlights the relevance of the composition of the medium and the ECM in the process of the DE differentiation, and hence the generation of HIOs. Therefore, in accordance

with the core aim of this project, we assessed different modifications to these factors which could improve the outcome of the differentiation protocol.

3.2 Results

The aim of this chapter consisted in developing a cost-effective optimized protocol for the differentiation of hPSC-derived intestinal organoids, compatible with HTS. The first step of the experimental work covered the validation of in-house recombinant proteins and the standard culture conditions for the growth of miFF1-iPSCs. Next, we implemented the protocol for the production of HIOs described by McCracken *et al*. (2011). Alongside this, we tested modifications in the composition of the ECM and the DE differentiation medium to improve the organoid output and reduce both time and cost for their production. Finally, the resulting protocol was applied to the direct differentiation of iPSCs in an OrganoPlate format, resulting in the generation of a novel model of gut-on-a-chip (organoid-on-a-chip).

3.2.1 Validation of reagents: Production of recombinant R-spondin 1

During the final stage of organoid differentiation, the constant replenishment of media required the use of commercial purified recombinant human R-spondin 1, which was exceptionally costly. To overcome this issue, Ootani *et al.* (2009) described the development of a transgenic cell line for the production of recombinant murine R-spondin1 fused with the Fc fragment of IgG2a (**Figure 2.3**).

Our protocol SRSF v.2 incorporated the use of rmRspo1 in the production and maintenance of HIOs. The protein was produced following the conditions provided by Ootani et al. (2009) and Amsbio. In brief, Cultrex Rspo1-293T cells were cultured in selection growth medium; upon reaching confluency they were changed into CD293 protein-free medium for ~14 days. The medium was collected and the rmRspo1 was purified by dialysis and protein A agarose columns.

The elution of the agarose columns was processed using SDS-PAGE under reducing conditions. Coomassie staining showed a single band with a molecular weight between 63 and 75 kDa (**Figure 3.1A**). Each lane corresponds to a different loaded dilution in order to determine the minimum amount that could be detected. This suggests either the presence of a single protein of the right size, or a cluster of proteins with similar molecular weight. Western blot of a similar gel also showed a single band after incubation with an anti-mouse Rspo1 antibody (**Figure 3.1B**).

No functional analysis or quantification of the activity of rmRspo1 was performed using TopFlash luciferase reporter assay. Alternatively, we attempted to assess the activity of rmRspo1 using the reporter SuperTop-DsRed.T4, a modified version of SuperTopFlash. The original design for the

SuperTopFlash reporter was developed by Moore's Lab to assess the activity of WNT signalling and consisted of eight TCF/LEF binding sites upstream from a luciferase reporter (Veeman *et al.*, 2003). SuperTop-DsRed.T4 and its cerulean version SuperTop-Cerulean.T4 were designed by substituting the luciferase reporter in SuperTopFlash, with a dsRed and cerulean fluorescent protein, respectively. We then transfected SuperTop-DsRed.T4 into CaCo-2 cells. However, the activity of the reporter was not consistently detected across the culture, even after using CHIR99021 as a positive control to measure WNT signalling activation. After contacting the authors, they have indicated that only 5% of successful expression of the reporter was achieved with SuperTop-Cerulean.T4, which was consistent with our observations. Therefore, we could not obtain a functional or quantitative readout of the activity of rmRspo1.
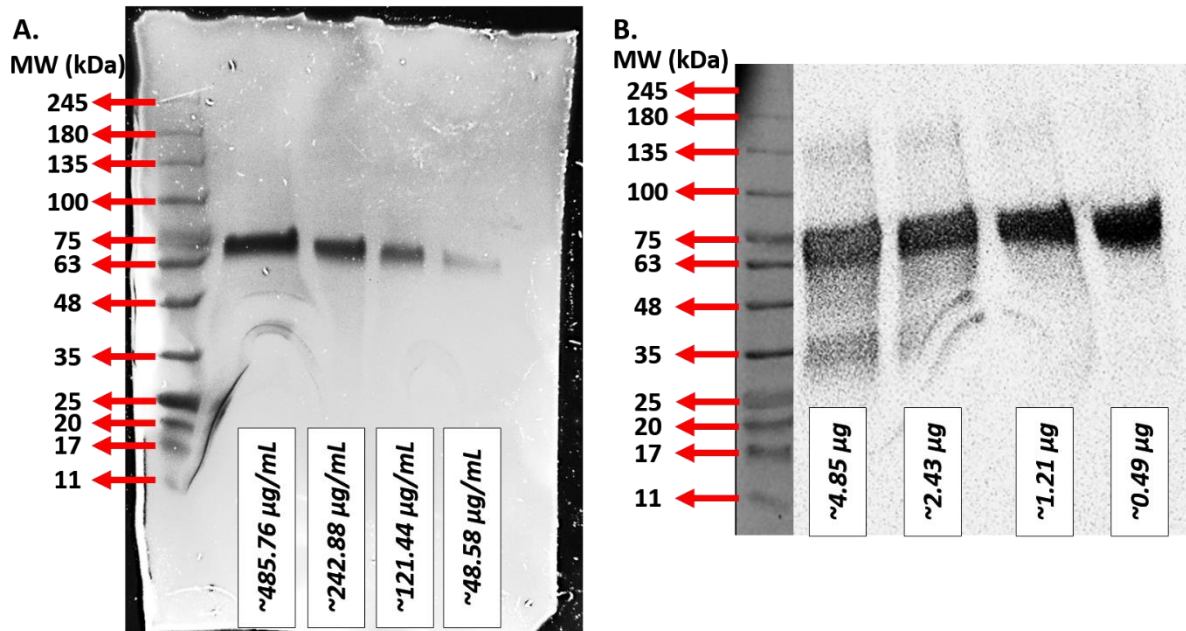
Figure 3.1 Recombinant murine Rspo1 purification.
Cells were grown and proteins were extracted according to the materials methods chapter, sections 2.23 and 2.24. (A) SDS-PAGE of the purified Rspo1 –Fc fusion protein under reducing conditions, stained with Coomassie blue (>60 kDa), purified using Protein A agarose columns. Proteins were quantified according to the Bradford assay. (B) A Western blot of purified rmRspo1-Fc protein.

3.2.2 Validation of reagents: Cell culture of iPSCs, miFF1 cell line

The original protocol, reported by McCracken *et al.* (2011), started from H9 hESCs seeded over hESC-qualified Matrigel and fed with mTeSR1 for 24 hrs prior to starting the differentiation conditions. However, Matrigel is derived from dissociated animal tissue and has an undefined composition with batch-to-batch variability. Therefore, our modified version of the differentiation protocol (SRSF v.1) incorporated laminin-521, an economic, xeno-free, defined matrix, which is widely used in the routine culture of PSCs.

For the selection of the cell line, we opted for iPSCs as these do not require the approval of an ethics committee or otherwise. The ShiPS-miFF1 (Sheffield human induced pluripotent stem mRNA-induced foreskin fibroblasts 1) cell line was produced by the Centre of Stem Cell Biology (CSCB), at The University of Sheffield. The cell line was readily available thanks to previous collaborations between the CSCB and the Sheffield RNAi Screening Facility (SRSF). Additionally, the CSCB counted with extensive documentation regarding the background of the cell line, reprogramming method, and characterization tests. In brief, the source of the tissue sample consisted of foreskin fibroblasts from a healthy neonate male with no diagnosed diseases. The reprogramming strategy used the mRNA of POU5F1, SOX2, KLF4, MYC, and LIN28. Karyotypic analysis confirmed lack of chromosomal abnormalities and the stemness of the cell line was validated by immunostaining against the pluripotency markers POU5F1 (OCT4), SSEA3, and TRA-1-81. The differentiation potential of miFF1 was verified using *in vivo* teratoma formation assay and results confirmed the derivation of all three germinal layers. Also, *in vitro* cell culture found evidence of spontaneous differentiation into ectoderm, mesoderm, and endoderm.

In our study, we ensured the quality of the starting material by labelling cells for the expression of pluripotency marker (SSEA3) and a marker for cells in early stages of differentiation (SSEA1). The results presented in **Figure 3.2** show all cells expressing SSEA3 and null expression of SSEA1. Therefore, miFF1 cells cultured over laminin-521 [0.5 µg/cm^2] display a pluripotent identity and are suitable for continuing with further differentiation.
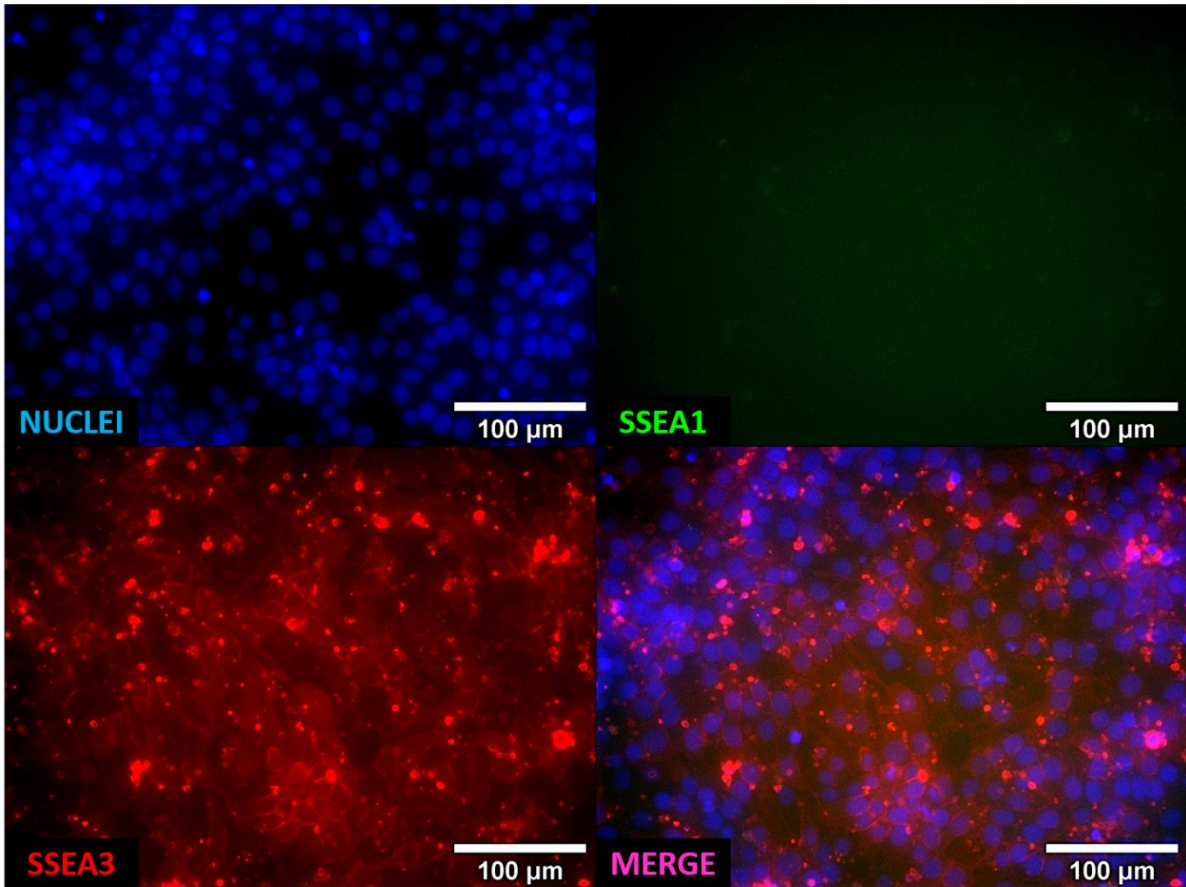
Figure 3.2 Expression of pluripotency markers on miFF1 cells.
Immunostaining of miFF1 cells seeded on laminin-521 [0.5 µg/cm^2] and incubated overnight. On the next day, the cells were fixed and stained to confirm the expression of the pluripotency marker SSEA3 (red), and absent expression of SSEA1 (green), a marker for early stages of differentiation; nuclei were stained with Hoechst 33342 (blue). Scale bars represent 100 µm.

3.2.2 Effect of extracellular matrix composition on iPSC culture

To continue with the optimization of the differentiation protocol, we evaluated the influence of the ECM in the output of mid- and hindgut spheroids. First, we assessed the effect of different coating proteins in the pluripotency of iPSC. Previously, we have explained the rationale behind the use of laminin-521. However, vitronectin as an alternative matrix is also used in the routine culture of PSC and possesses the same advantages as laminin-521 but at a fifth of its cost. Therefore, three different ECM compositions were tested: laminin-521 [0.5 µg/cm^2] (LAM), vitronectin [0.5 µg/cm^2] (VTN), and a mix of 50% laminin-521 [0.25 µg/cm^2] + 50% vitronectin [0.25 µg/cm^2] (L/V).

miFF1-iPSC were cultured for 48 hrs using these coating conditions. After the culture period, the assay was evaluated based on the expression of the pluripotency surface antigen SSEA3 (red) and the early differentiation surface antigen SSEA1 (green). At this stage, we expected all three matrixes could support the culture of iPSCs without affecting their stemness. In accordance with this, results showed ubiquitous expression of the SSEA3 independent of the ECM composition. SSEA1 was not detected under any condition (**Figure 3.3**). Interestingly, ECM composition appeared to have an effect in the confluency of the cultures, suggesting that the combination of L/V led to a high cell density (>90% confluency), whereas VTN cultures were sparser (70-80% confluency). This might be due to increased attachment after seeding, higher survival rates, or enhanced proliferation. Laminin-521 cultures seemed more adequate (80-90% confluency) since too low or high confluency might affect the efficiency of the following differentiation steps.
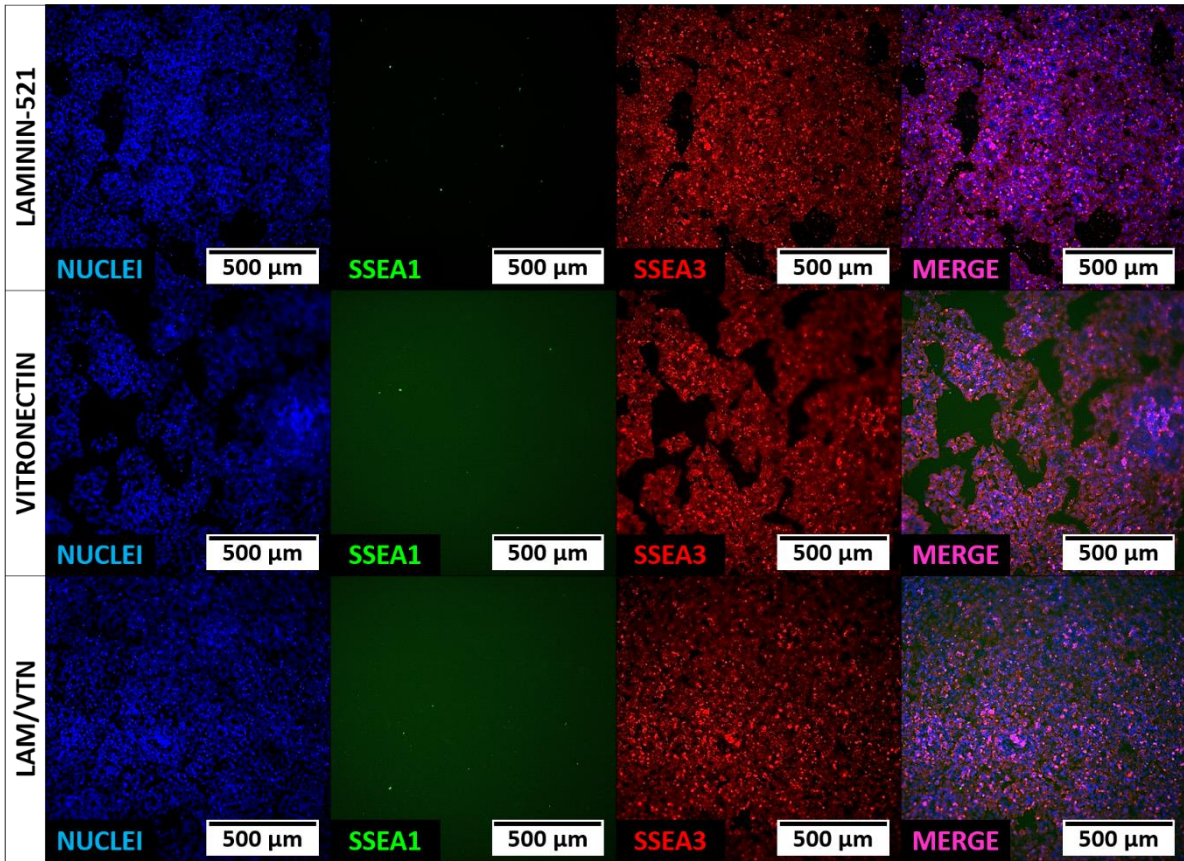
Figure 3.3 miFF1 cells cultured under different coating proteins.
The effect of the ECM on the differentiation of miFF1 cells was evaluated using three different coating treatments: laminin-521, vitronectin, and a combination of 50% laminin-521 and 50% vitronectin. After 48 hrs of culture, the laminin samples showed a confluency of 80-90%, vitronectin 70-80%, and the combination of both resulted in >90% cell confluency. Expression of the pluripotency marker SSEA3 (red) was ubiquitous, and the marker for early differentiation SSEA1 (green) was absent. Nuclei were stained with Hoechst 33342 (blue). Scale bars indicate 500 µm.

3.2.3 Definitive endoderm differentiation

Initially, we tested the culture conditions originally reported by McCracken *et al*. (2011), using AA and defined FBS (dFBS) as the main drivers for the differentiation of miFF1 into DE (**Figure 3.4**). The cells were seeded over a laminin-521 ECM, and after overnight incubation (D0) were able to attach and survive. After 24 hrs (D1) under DE differentiation conditions (AA [100 ng/mL]), a considerable amount of cellular debris was found floating on the supernatant of the cultures. The next day (D2), the medium was replenished (AA [100 ng/mL] + 0.2% dFBS) though the remaining cells attached to the surface of the well continued decreasing. By the end of the DE differentiation stage (D3) and following the corresponding change of medium (AA [100 ng/mL] + 2% dFBS), only few sparse cell clusters remained. These were deemed insufficient to continue for the mid- and hindgut differentiation stage, considering that formation of mid- and hindgut spheroids is highly dependent on the confluency of the monolayer.
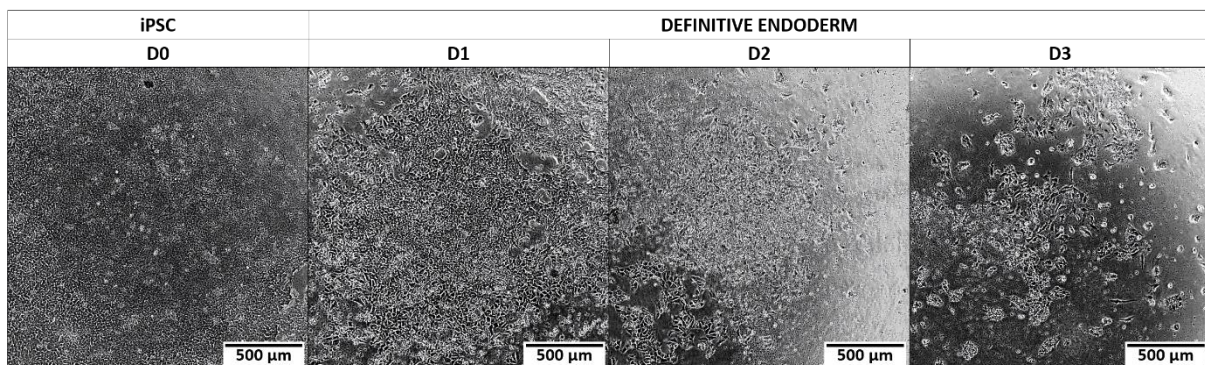
Figure 3.4 Definitive endoderm differentiation based on McCracken *et al*, 2011.
Bright-field images of iPS cells after being treated with the definitive endoderm differentiation medium proposed by McCracken *et al*. (2011). Day 0 (DO), (iPSC), Day 1-3 (D1, D2, D3) defined as definitive endoderm. Note the change in confluency from D1 to D3, due to the lifting of cells from the matrix. Scale bars indicate 500 µm.

Failure to generate DE cultures with the protocol from McCracken *et al*. led us to modify the composition of the DE differentiation medium. AA [100 ng/mL] remained as the key effector driving the differentiation, though the use of dFBS was replaced by B27 supplements [1x]. B27 is a chemically-defined mixture of enzymes and growth factors which has been shown to facilitate DE differentiation. Additionally, we induced the activation of canonical WNT signalling during DE differentiation, opting for the use CHIR99021 [2 µM] rather than purified recombinant WNT3A since this option was more economic. CHIR99021 is a small-molecule WNT agonist that inhibits the activity of GSK3, preventing the phosphorylation of β-catenin and allowing it to activate WNT target genes. The sum of these modifications was expected to support the adhesion and survival of the cells, along with their transition into DE and the corresponding expression of stage-specific molecular markers.

On the first day of DE induction (D1), the entire culture showed a high density (>90% confluency), and the cells within the monolayer exhibited a cobblestone-and-petal morphology. Furthermore, as reported by the original protocol, there was a considerable amount of cell death and debris being released into the supernatant alongside with the differentiation of iPSC into DE. Next, on day 2 (D2) the cells appeared smaller and more packed within the colony (>95% confluency), though by day 3 (D3) these have clustered in localized regions, opening spaces within the colony. As a distinctive feature, the cells bordering these openings exhibited a stretched and elongated morphology (**Figure 3.5, arrowheads**).
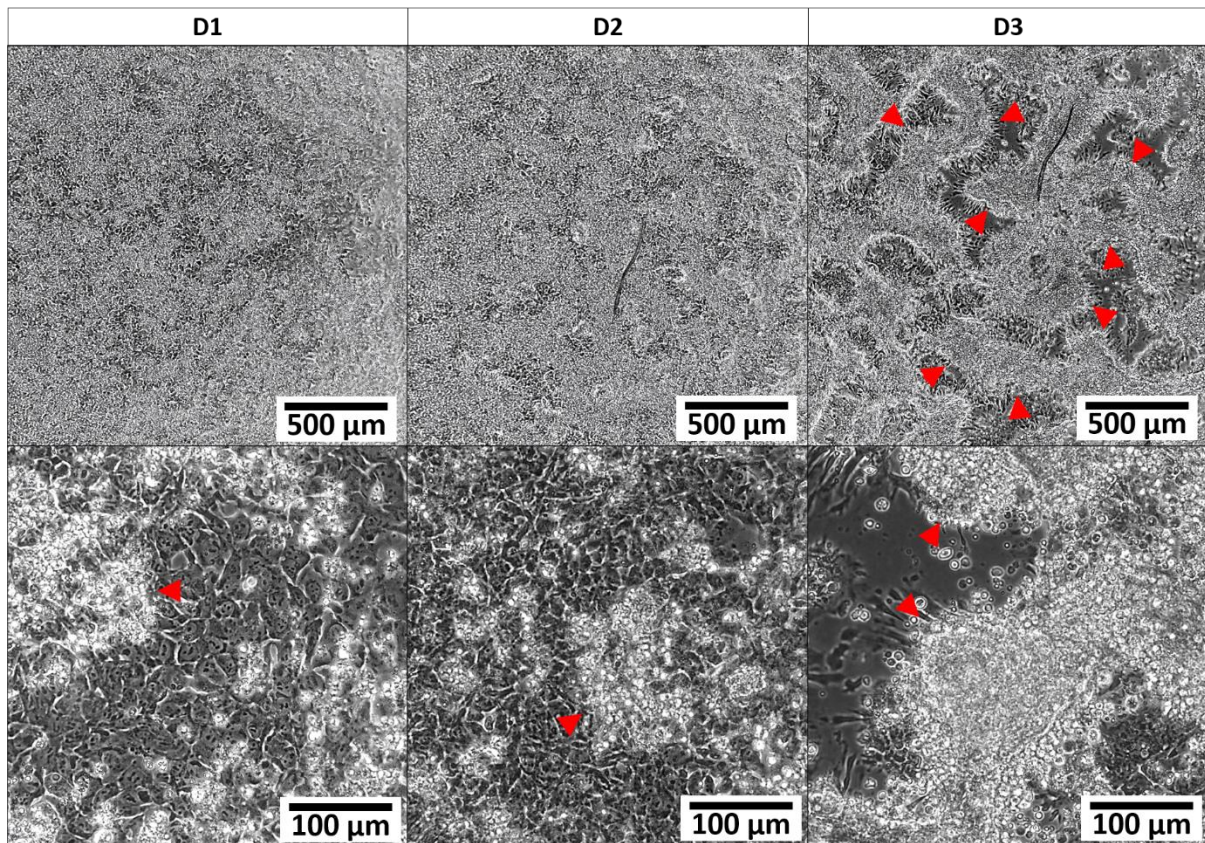
Definitive Endoderm morphological changes

Cobblestone morphology

Petal morphology

Stretched and elongated morphology
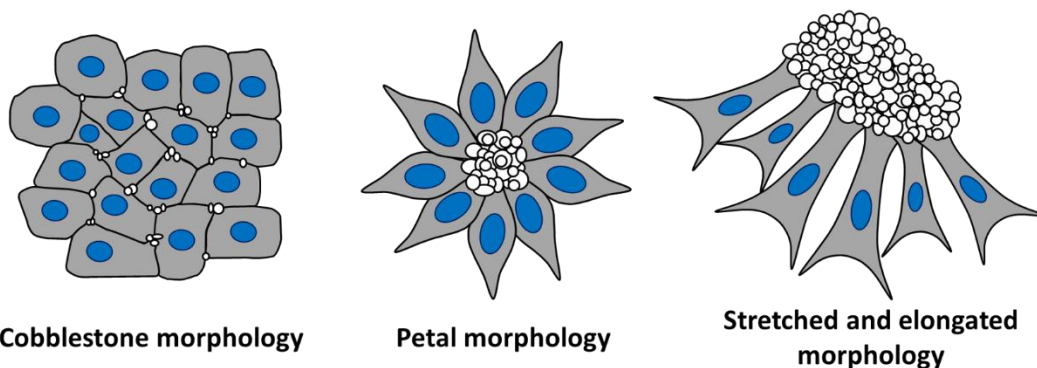
Figure 3.5 Timeline progression of the definitive endoderm differentiation stage using protocol SRSF v.1.
Bright-field images of miFF1 cultures undergoing endodermal differentiation using SRSF v.1 protocol. The transition into differentiation conditions provoked considerable cell death as observed by the amount debris discarded each day of the protocol. Low magnification images (4x, upper panels) showed a cloud of cellular debris which did not allow to distinguish morphological changes in the colony on D1. However, over the course of D2 and 3, the differentiation progressed, and the cells started clustering (arrowheads). High magnification images (20x, middle panels) revealed a cobblestone-and-petal morphology of individual cells (D1). On the following days (D2 and 3), the cells exhibited morphological changes, shrinking and clustering in localized regions of the culture (arrowheads). The lower panels illustrate the main morphological changes observed in the cultures. Cobble and petal morphologies were detected scattered in the middle of the colonies. In contrast, the shrinking and clustering of cells caused the formation of open spaces within the colony, in which the cells appeared stretched and elongated. Scale bars represent 500 µm (upper panels) and 100 µm (lower panels).

We conducted a molecular characterization of the resulting cultures to test whether the DE was induced from the iPSCs and to confirm the differentiated identity prior to continuing with the mid- and hindgut differentiation stage. We used two methods for characterization: immunocytochemistry, and RT-qPCR. According to the immunocytochemistry characterization, the differentiated cells expressed FOXA2, a marker of late endodermal differentiation (**Figure 3.6A**).

Further analysis with RT-qPCR assessed the expression of two extensively used DE markers: *SOX17* and *FOXA2*. Additionally, we tested the expression of *LGR5*, a marker for proliferative ISC that has recently been identified to be part of the DE gene signature, and *BMI1*, a marker for quiescent ISC. The expression of the housekeeping gene *HPRT1* (hypoxanthine phosphoribosyl transferase 1) was used to normalize quantification. Additionally, the gene expression of DE samples was compared against a control cell line (CaCo-2), representing the expression of genes from the intestinal epithelium. This control was used to compare whether the gene expression profile of our differentiated samples could match that of *bona fide* intestinal cells. However, following extensive consideration, the parental cell line miFF1 could have provided a more suitable reference baseline to assess changes in the gene expression in response to the differentiation treatment. This issue has been considered in the interpretation of the results and could be resolved in future work.

Figure 3.6B presents the RT-qPCR results as dot plots indicating each data point from 3 biological and 3 technical replicates (9 data points) for DE samples, and 1 biological with 3 technical replicates (3 data points) for CaCo-2. The graphs are presented in logarithmic scale and for the cases where the samples did not express the gene, the value was 0 and therefore presented as NOT DETECTED. Statistical analysis of the results was conducted under a significance level of 95% ($p≤0.0500$), using non-parametric Mann-Whitney test pairwise comparison as the low number of replicates could not fit a normal distribution.

Mann-Whitney test found a significant expression of *SOX17* ($p=0.0091$) and *FOXA2* ($p=0.0091$) in DE samples compared to CaCo-2. These results are consistent with our expectations in which the expression profile of the sample treated for DE differentiation indicated an evident upregulation of DE-specific markers *SOX17* and *FOXA2*. Additionally, the expression of *FOXA2*, detected by RT-qPCR, is consistent with our observations using immunostaining.

Aside from the DE markers, the expression of ISC markers *LGR5 and BMI1* was assessed to investigate whether these populations could be detected at this early stage of the process of intestinal differentiation. In DE samples the expression of *LGR5* was detected barely above the levels of the normalising gene, however statistical analysis found it to be significantly higher compared to CaCo-2

(*p=0.0091*). The expression of *BMI1* was detected below the baseline of *HPRT1* with no significant difference between DE samples and CaCo-2 cells (*p=0.2091*). Overall, these results suggest the potential development of a *LGR5⁺* ISC population in DE samples, yet the BMI1 population remains absent. Nevertheless, it is important to recognize that the lack of a comparison against the parental cell line miFF1 remains an important shortcoming of the results.
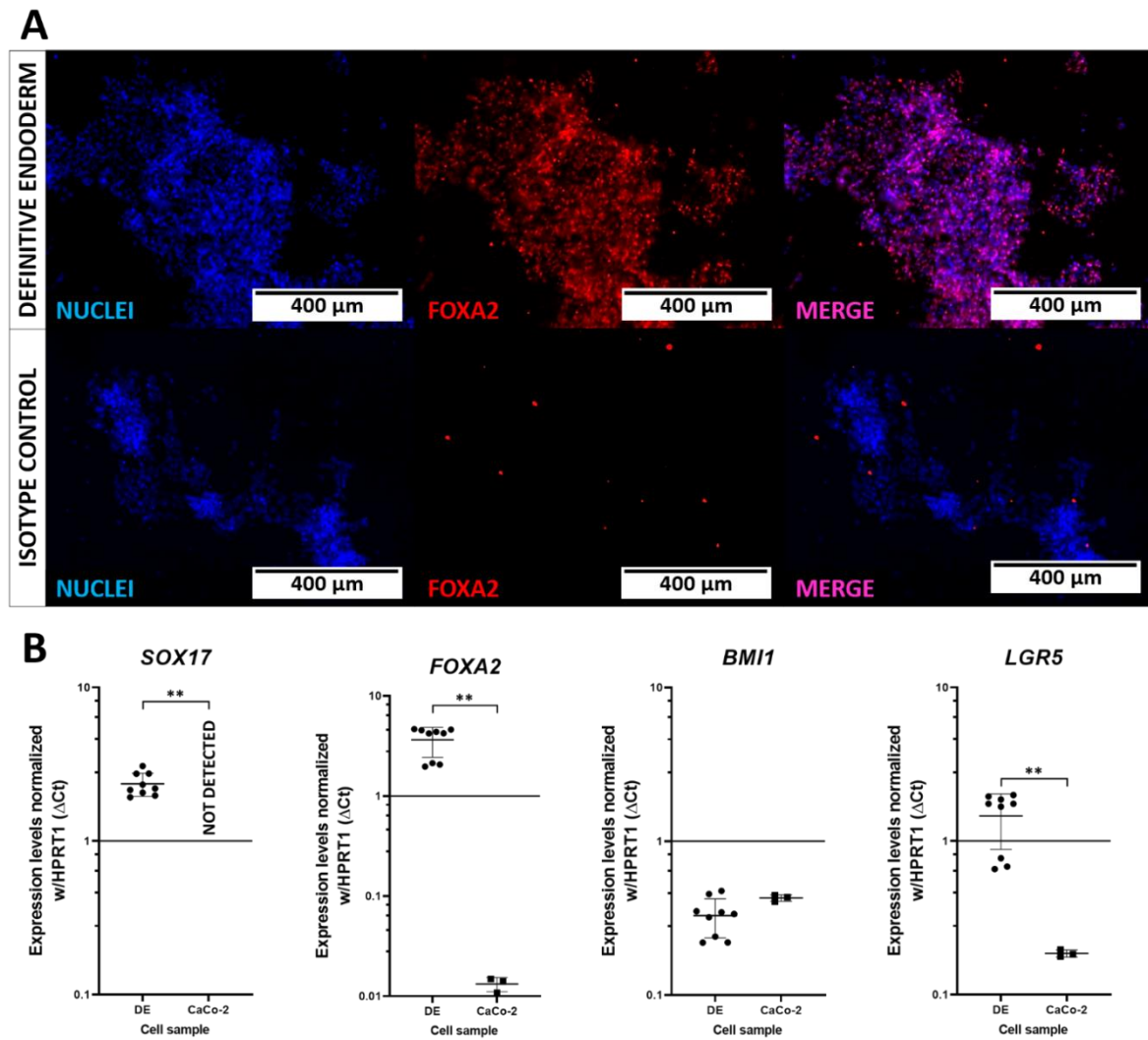
Figure 3.6 Characterization of the DE differentiation stage.
(A) Immunostaining of miFF1 cells after definitive endoderm induction revealed positive expression of FOXA2, as defined by immunostaining with an anti-FOXA2 antibody (red), compared to the isotype control. Nuclei were stained with Hoechst 33342 (blue) and scale bars indicate 400 μm. (B) RT-qPCR analysis showing fold change of definitive endoderm (*SOX17, FOXA2*) and intestinal stem cell genes (*BMI1, LGR5*) in differentiated samples. The results are presented as the fold change of ΔC_t normalized against the housekeeping gene *HPRT1*, additionally, the same genes were tested on a control intestinal cell line (CaCo-2). The data showed a significant increase in the expression of *SOX17* (*p=0.0091*) and *FOXA2* (*p=0.0091*) in samples of DE, compared to CaCo-2. Dot plots present the mean and standard deviation of 3 biological and 3 technical replicates (9 data points) from the DE dataset, and 1 biological with 3 technical replicates (3 data points) for CaCo-2 cells. Statistical analysis was conducted using non-parametric Mann-Whitney pairwise comparison under a significance level of 95%, where: *$p \leq 0.0500$; **$p < 0.0100$; ***$p < 0.0010$; ****$p < 0.0001$.

3.2.4 Mid- and hindgut differentiation

After DE differentiation, the medium was replaced with mid- and hindgut differentiation medium containing: FGF4 [500 ng/mL] to block foregut morphogenesis, favouring the formation of mid- and hindgut; dFBS [2%], a complex mix of growth factors, hormones, and co factors usually associated with cell survival and proliferation; CHIR99021 [2 µM] instead of WNT3A, to promote cell proliferation and drive differentiation via WNT signalling; and Noggin [100 ng/mL] to facilitate WNT signalling by inhibiting BMP inhibition of WNT. Based on the description from the original protocol, these culture conditions were expected to: (i) downregulate the expression of DE genes; (ii) induce the patterning of the posterior gut, characterized by the expression of the intestinal marker CDX2; and (iii) promote further cell proliferation along with the formation of spheroid structures which presumably can develop into organoids.

The progression of the mid- and hindgut differentiation stage was recorded in **Figure 3.7**. Also, **Tables 3.1** and **3.2** outline classification guidelines to evaluate the outcome of the differentiation protocol based on the number of organoid-forming units (OFUs) and their morphological characteristics. As observed during the DE stage, cells continued proliferating in specific regions across the monolayer. The cells within the monolayer appeared tightly packed and at the edge of the colony some cells showed an irregular stretched and elongated morphology. Tight cell packing appeared as a dark cluster, where small spheroidal outgrowths were detected around D2 of the mid- and hindgut stage (**Figure 3.7, arrowheads**). At D3, mid (++) levels of type II and III structures were observed floating in the supernatant of the cultures (**Figure 3.7, red dashed lines**). These putative OFUs were recovered and replated in BMM Matrigel beads to continue with the intestinal growth stage. It was observed that if not recovered promptly, the spheroids were able to attach to the well and generate colonies. On day 4 (D4), high (+++) levels of type II and type III structures were observed and transferred into Matrigel beads. The rest of the monolayer culture was processed for further characterization.

The outcome of the differentiation protocol during the mid- and hindgut stage was analyzed by immunostaining (**Figure 3.8**) and RT-qPCR (**Figure 3.9**). The patterning of the DE into mid- and hindgut led to the commitment towards the intestinal lineage, which is characterized by the expression of the transcription factor CDX2. Our analysis of the cultures treated with mid- and hindgut differentiation medium revealed that only a small amount of the entire colony was actually CDX2$^+$; the majority was focused on regions of high confluency where small aggregates started protruding from the monolayer. McCracken *et al.* (2011) showed these aggregates are primordia of the mid- and hindgut spheroids, released into the supernatant. The colonies derived from the reattachment of the spheroids exhibited

a ubiquitous expression of CDX2 similar to the CaCo-2 monolayers used as a positive control. Predictably, the isotype control had null expression of CDX2 (**Figure 3.8**).

Classification		Number of OFUs/well
Null	-	0*
Low	+	1 – 100
Mid	++	101 – 200
High	+++	201 – 300

Table 3.1 Semi quantitative classification of differentiation conditions based on the number of OFUs produced.
*Including type 0 structures where the spheroids remained attached to the colony
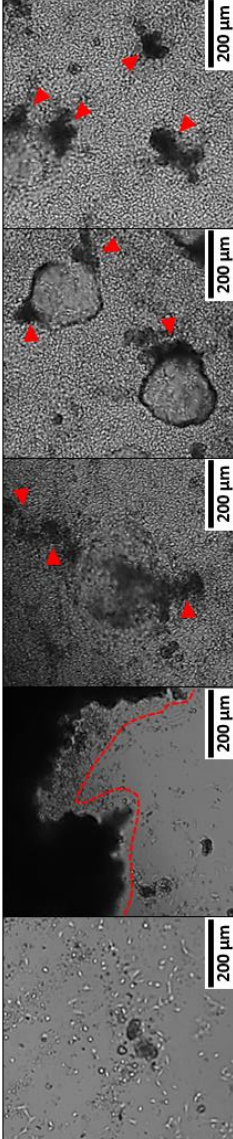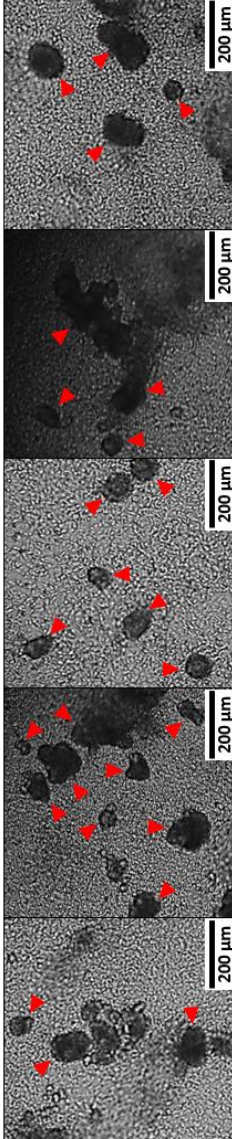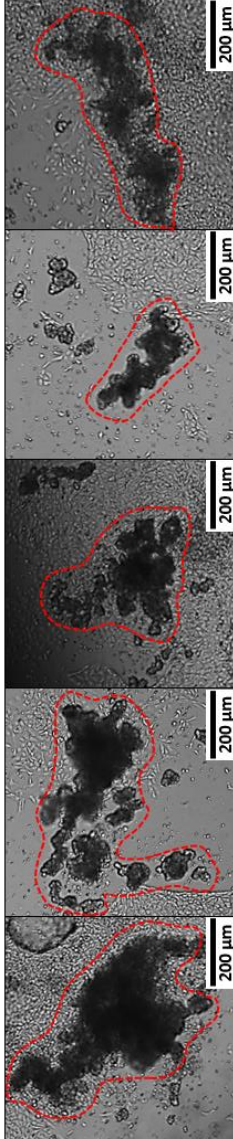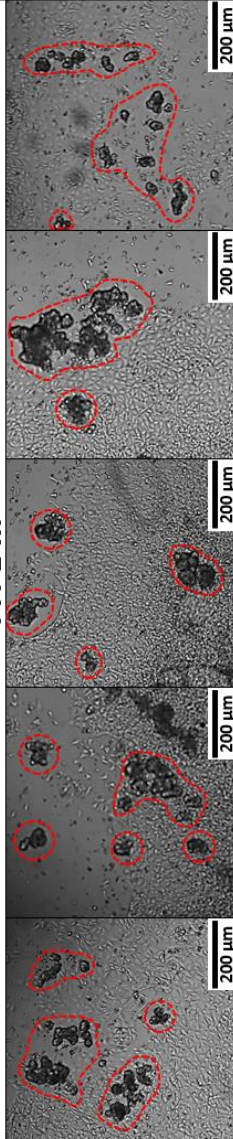
TYPE 0

Type 0 structures do not share common morphological characteristics. These structures do not develop into organoids, but rather represent confluency foci where the spheroids are formed. Depending on the culture conditions, in some instances the spheroid primordia do not fully develop and remain attached into the main colony.

TYPE I

Type I structures show a spheroidal or ellipsoidal morphology, with a size between 100 – 300 μm length. In contrast to type III structures, type I appeared black or dark grey under a bright field microscope. This suggests a tighter aggregation of cells, perhaps compromising their viability and potential for differentiation. Also, in some cases it exhibited branching buds sprouting out of the main structure.

TYPE II

Type II structures are generally comprised of large aggregates of type III structures (>500 μm length). They do not have a distinctive shape, although in general all have loosely attached spheroids at the borders and a condensed dark core of spheroid aggregates and mesenchyme. In some cases, these could be broken apart into smaller type III structures.

TYPE III

Type III structures appeared as irregularly shaped spheroids. Individual structures had a size of 70 – 150 μm length, though small (~220 μm length) and medium sized (~300 μm length) aggregates could also be detected. In general, type III structures could be detected around type 0 confluency foci, although they tend to float and gather around the edges of the well.

Table 3.2 Criteria guide for the classification of organoid-forming units
Red arrow heads and dashed lines indicate putative organoid-forming units. Scale bars represent 200 μm.

101
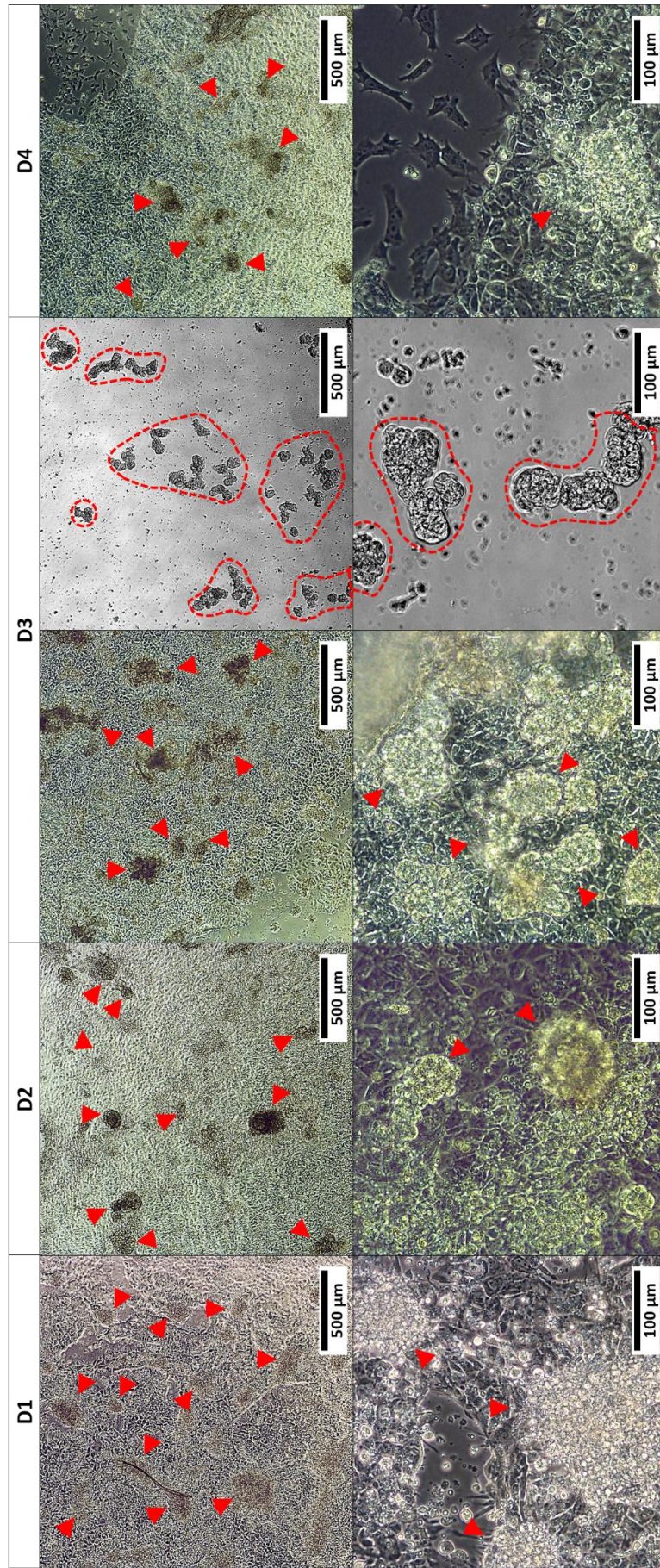
Figure 3.7 Timeline progression of the mid- and hindgut differentiation stage using protocol SRSF v.1.
Bright-field images of the process of mid- and hindgut differentiation. After the DE stage, the focalized clusters of cells continued growing, developing spheroid-like outgrowths (arrowheads); between days 3 and 4 several of these structures were released into the supernatant (dashed line). These mid- and hindgut spheroids were harvested and plated in Matrigel beads for the final step of differentiation, the generation of 3D intestinal tissue. Scale bars represent 500 µm (upper panels) and 100 µm (lower panels).
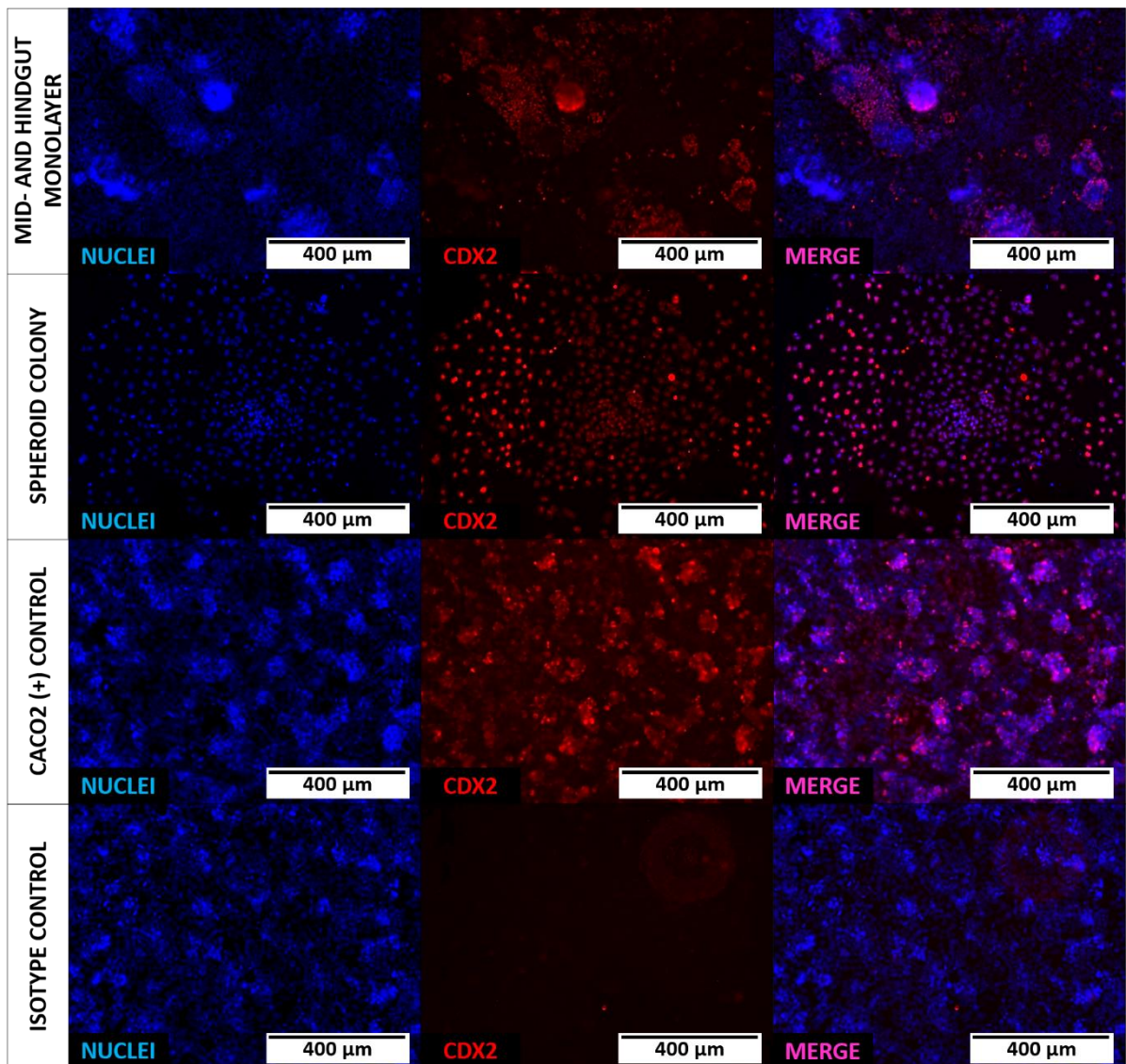
Figure 3.8 Characterization of the mid- and hindgut differentiation stage.
The expression of the intestinal marker CDX2, stained with anti-CDX2 antibody (red) on four different samples: mid- and hindgut monolayer, mid-and-hindgut-spheroid-derived colonies, CaCo-2 monolayers (positive control), isotype/negative control. In mid- and hindgut cultures the expression of the intestinal marker was particularly focused on regions of high cell density, suggesting that confluency played a role in the differentiation and formation of spheroids. Furthermore, spheroid colonies showed ubiquitous expression of CDX2, demonstrating these are comprised of intestinal cells and therefore are suitable for the generation of organoids. Nuclei were stained with Hoechst 33342 (blue), and scale bars indicate 400 μm.

Additionally, we performed RT-qPCR analysis to assess the gene expression profile of key molecular markers on samples treated with mid- and hindgut differentiation medium. The results were normalized with the housekeeping gene *HPRT1* and compared against a control intestinal cell line (CaCo-2) and a cell line of mesenchymal origin (HDFs). The purpose of using these cell lines was to examine if the gene expression profile of differentiated mid- and hindgut samples approached the levels shown by control intestinal and mesenchymal cells. Nevertheless, it is acknowledged that the parental cell line miFF1 could have provided a more relevant comparison to evaluate the activation of stage/lineage-specific genes in response to the differentiation treatment.

The dot plots presented in **Figure 3.9** reflect the results of 3 biological and 3 technical replicates (9 data points) in mid- and hindgut samples, and 1 biological with 3 technical replicates (3 data points) in the control cell lines CaCo-2 and HDFs. The graphs are presented in logarithmic scale, thus genes which were not expressed by a cell line have a value of 0 and are shown as NOT DETECTED. All statistical analysis was performed under a significance level of 95% ($p \leq 0.0500$) using non-parametric Mann-Whitney test since the low number of replicates could not fit a normal distribution.

Statistical analysis found the expression of pluripotency genes *OCT4* ($p=0.0091$) and *NANOG* ($p=0.0227$) to be significantly higher in mid- and hindgut samples compared to CaCo-2. This suggests the presence of cells which might have not undergone the differentiation program. The expression of the DE marker *FOXA2* ($p=0.9091$) was statistically similar in mid- and hindgut differentiated cells and CaCo-2 cells. However, *SOX17* ($p=0.0091$) was still significantly expressed, suggesting the prevalence of DE cells which may have not acquired a mid- and hindgut identity.

Next, we tested *MKI67,* a marker for proliferative cells, which has often been used in conjunction with *LGR5* to detect the presence of proliferative ISCs. Additionally, we evaluated the expression of the quiescent ISC marker *BMI1*. The expression of *MKI67* ($p=0.0091$), *LGR5* ($p=0.0091$), and *BMI1* ($p=0.0091$) was significantly higher in CaCo-2 compared to mid- and hindgut differentiated cells. The presence of *MKI67* along with the low levels detected for *LGR5* might indicate the presence of a proliferative population that does not belong to the ISC subset, though it can also be explained due to endogenous low levels of *LGR5* expression. Interestingly, expression of *BMI1* was increased during mid- and hindgut differentiation compared to the DE stage.

HES1 and *ATOH1* are markers for TACs from the absorptive and secretory lineage, respectively. *ATOH1* was examined and shown to be minimally expressed in our mid- and hindgut cultures. However, statistical analysis found it to be significantly higher compared to CaCo-2 ($p=0.0182$). In contrast, *HES1* was considerably upregulated, indicating the prevalence of cells from the absorptive lineage. *HES1*

expression was significantly lower than on CaCo-2 cells (*p=0.0091*), suggesting just a small population has entered the early stages of terminal differentiation.

CDH1 and *VIL1* were examined to test for markers of the intestinal epithelium. Both were highly upregulated in mid- and hindgut samples, although at a significantly lower level compared to CaCo-2 cells (*p=0.0091* for both genes). The expression of *CDH1* and *VIL1* by mid- and hindgut cells suggests the development of enterocyte-like cells, though not at the level of a fully developed intestinal epithelium.

VIM presence was examined as it is used as a marker of mesenchymal-derived cells. Statistical analysis indicated the expression of *VIM* in HDFs was significantly higher than in mid- and hindgut cultures (*p=0.0091*). However, *VIM* expression in mid- and hindgut samples is indicative of the presence of cells from a mesenchymal origin within the spheroids released into the supernatant. This is consistent with the results described in the original protocol from McCracken *et al.* (2011). Their results found that 85-90% of the cells undergo endoderm differentiation. In contrast, only a limited sub population (10-15%) continue through the mesodermal lineage, which is responsible for the development of mesenchymal cells.
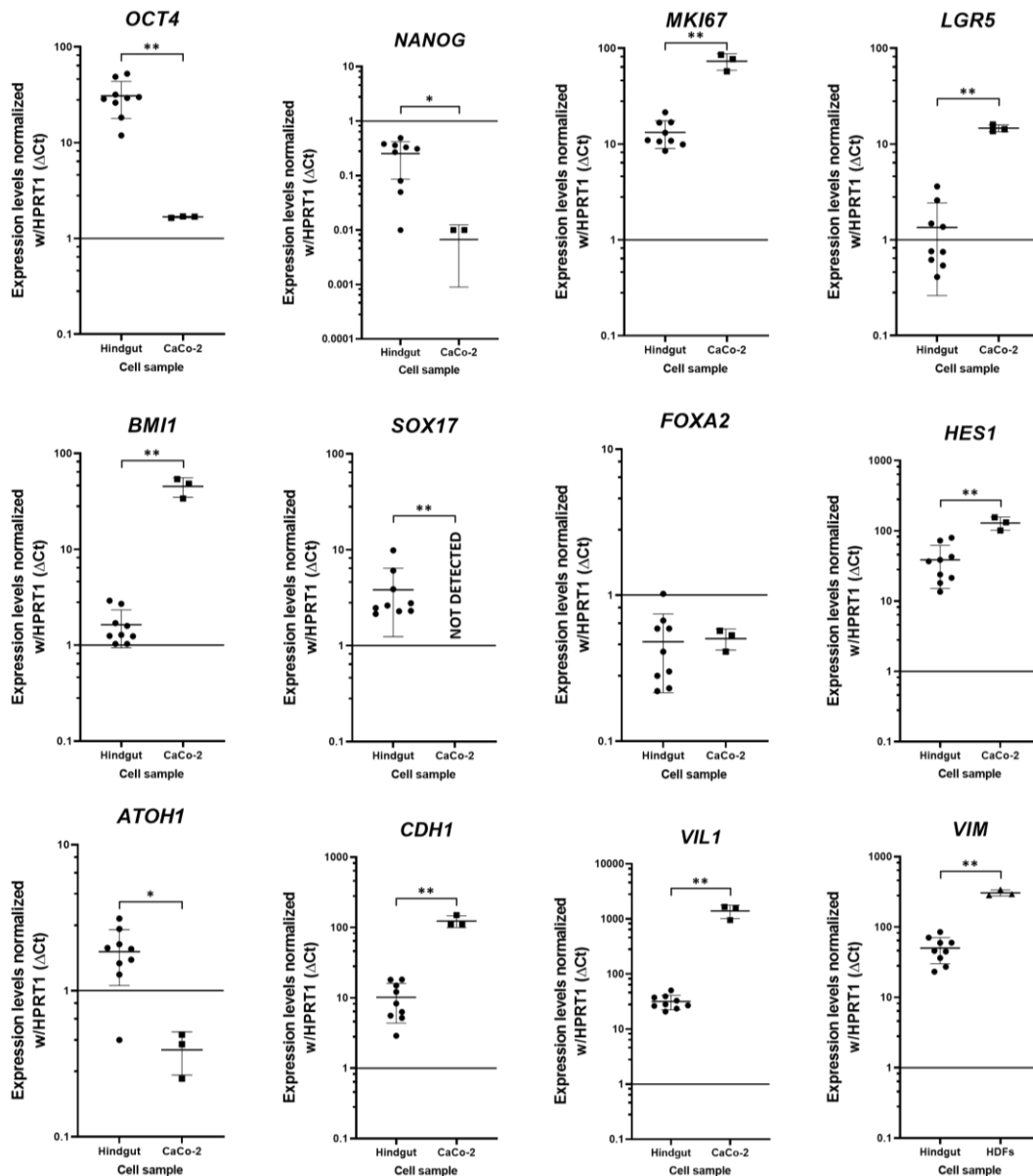
Figure 3.9 RT-qPCR analysis of the mid- and hindgut differentiation stage.
RT-qPCR analysis evaluated an array of different genes in the mid- and hindgut monolayer assessing different properties of the sample: pluripotency (*OCT4, NANOG*), ISCs (*MKI67, LGR5, and BMI1*), DE (*SOX17, FOXA2*), TACs (*HES, ATOH1*), intestinal epithelium (*CDH1, VIL1*) and mesenchyme (*VIM*). The same genes were tested for their expression on CaCo-2 and HDFs control cells. The results are presented as the fold change of ΔC_t normalized against the housekeeping gene *HPRT1*. Mid- and hindgut samples showed persistent expression of pluripotency markers *OCT4* (*p=0.0091*) and *NANOG* (*p=0.0227*), and the DE marker *SOX17* (*p=0.0091*). The expression of the proliferation marker *MKI67* (*p=0.0091*), and the ISC markers *LGR5* (*p=0.0091*) and *BMI1* (*p=0.0091*), was significantly lower in mid- and hindgut samples compared to CaCo-2. The expression of *ATOH1* (*p=0.0182*) in mid- and hindgut cells was significantly higher than in CaCo-2 cells, suggesting the presence of putative secretory TACs. Also, compared to CaCo-2, the expression of *HES1* (*p=0.0091*), *VIL1* (*p=0.0091*), *CDH1* (*p=0.0091*) was significantly lower in mid- and hindgut cells. Nevertheless, it is still indicative of the development of cells from the intestinal epithelium and the absorptive lineage. Finally, mid- and hindgut cells showed a significantly lower expression of the mesenchymal marker *VIM* (*p=0.0091*) compared to HDFs. Still, the expression of this marker pointed to the presence of a relevant population of mesenchymal cells. Dot plots present the mean and standard deviation of 3 biological and 3 technical replicates (9 data points) from the mid- and hindgut dataset, and 1 biological with 3 technical replicates (3 data points) for CaCo-2. Statistical analysis was conducted using non-parametric Mann-Whitney test under a significance level of 95%, where: **p≤0.0500*; ***p<0.0100*; ****p<0.0010*; *****p<0.0001*.

3.2.5 Effect of ECM composition and BMP4 in the production of mid- and hindgut spheroids

McCracken *et al*. (2011) described the endodermal differentiation using a combination of AA [100 ng/mL] and increasing concentrations of dFBS. However, a later work by McCracken *et al*. (2014) presented a similar protocol for the production of gastric organoids using BMP4 [50 ng/mL] during the first day of DE differentiation. Aside from these, numerous other studies have mentioned the combined effect of AA and BMP4 in the initial transition towards a mesendodermal lineage. In this section, we tested the effect of incorporating BMP4 [50 ng/mL] in the first day of the endodermal differentiation step. The expectation was that the addition of BMP4 would improve the differentiation efficiency toward the DE, facilitate the posterior gut patterning, and lead to the generation of a higher production of OFUs.

Additionally, we assessed the effect of three different ECM compositions: laminin-521 [0.5 µg/cm^2] (LAM), vitronectin [0.5 µg/cm^2] (VTN), and a mix of 50% laminin-521 [0.25 µg/cm^2] + 50% vitronectin [0.25 µg/cm^2] (L/V). In a previous experiment we had confirmed that these modifications in the ECM compositions did not alter the stemness of iPSCs. We sought to validate the use of vitronectin in the differentiation protocol, as this is an economic option. Alternatively, the combination of L/V could benefit the differentiation process, resulting in a higher output of OFUs. However, both of these conditions produced important alterations in the confluency of the cultures. According to previous observations by McCracken *et al.* (2011), the effect of the confluency is fundamental for the optimal differentiation and formation of OFUs. Therefore, we were uncertain to whether these conditions could derive in a substantial improvement to the differentiation protocol.

The results from these modifications were evaluated based on the production of mid- and hindgut spheroids (**Figure 3.10**), the downregulation of the DE identity following treatment with mid- and hindgut differentiation medium (**Figure 3.11 and 3.13A**), and the upregulation of the intestinal marker CDX2 and posterior gut genes (**Figure 3.12 and 3,13B**).

LAM+BMP4 (upper left) mid (++) levels of type II and III structures. VTN+BMP4 (upper middle), showed null (-) production of OFUs, and the outcome consisted of type 0 structures. The colony collapsed detaching from the well and folding over itself, while the remnant cells that remained attached did not produce spheroids. L/V+BMP4 (upper right) low (+) levels of type III structures, but most of the colony remained as a confluent monolayer (type 0), without showing the typical outgrowths that indicate the formation of mid- and hindgut spheroids. LAM (lower left) released high (+++) levels of type III structures. VTN (lower middle) released high (+++) levels of type II structures. L/V (lower right) produced low (+) levels of type II structures, however most of them remained attached to the monolayer (type 0) (**Figure 3.10A, red dashed lines**).

The production of OFUs was quantified in 4 independently differentiated mid- and hindgut cultures for each condition, and 8 field per replicate (**Figure 3.10B**). The results from the quantification of OFUs were analyzed using Kolmogorov-Smirnov (KS) test to assess the normal distribution of the data ($p≥0.0500$). KS analysis showed that the results from LAM ($p>0.1000$), VTN ($p>0.1000$) and L/V+BMP4 ($p>0.1000$) fit within the Gaussian distribution. However, L/V ($p=0.0393$), LAM+BMP4 ($p=0.0002$), and VTN+BMP4 ($p<0.0001$) did not exhibit a normal distribution of the data. Therefore, statistical analysis of the results was conducted using non-parametric Kruskal Wallis test, followed by *post hoc* pairwise comparison with Dunn's test. Both were assessed under a significance level of 95%. The Kruskal Wallis test found significant differences between the treatments ($H=145.2, p<0.0001$). Subsequent pairwise comparison considered LAM cultures as the parental conditions and serve as reference for the statistical analysis. VTN ($p>0.9999$) and LAM+BMP4 ($p>0.9999$) did not showed a significant difference in the number of OFUs generated compared to LAM. However, VTN+BMP4 ($p<0.0001$), L/V ($p<0.0001$), and L/V+BMP4 ($p<0.0001$) produced a significantly lower number of OFUs. Based on these observations, exclusively in terms of the production of spheroids, the most promising conditions seemed to be LAM, VTN, and LAM+BMP4.
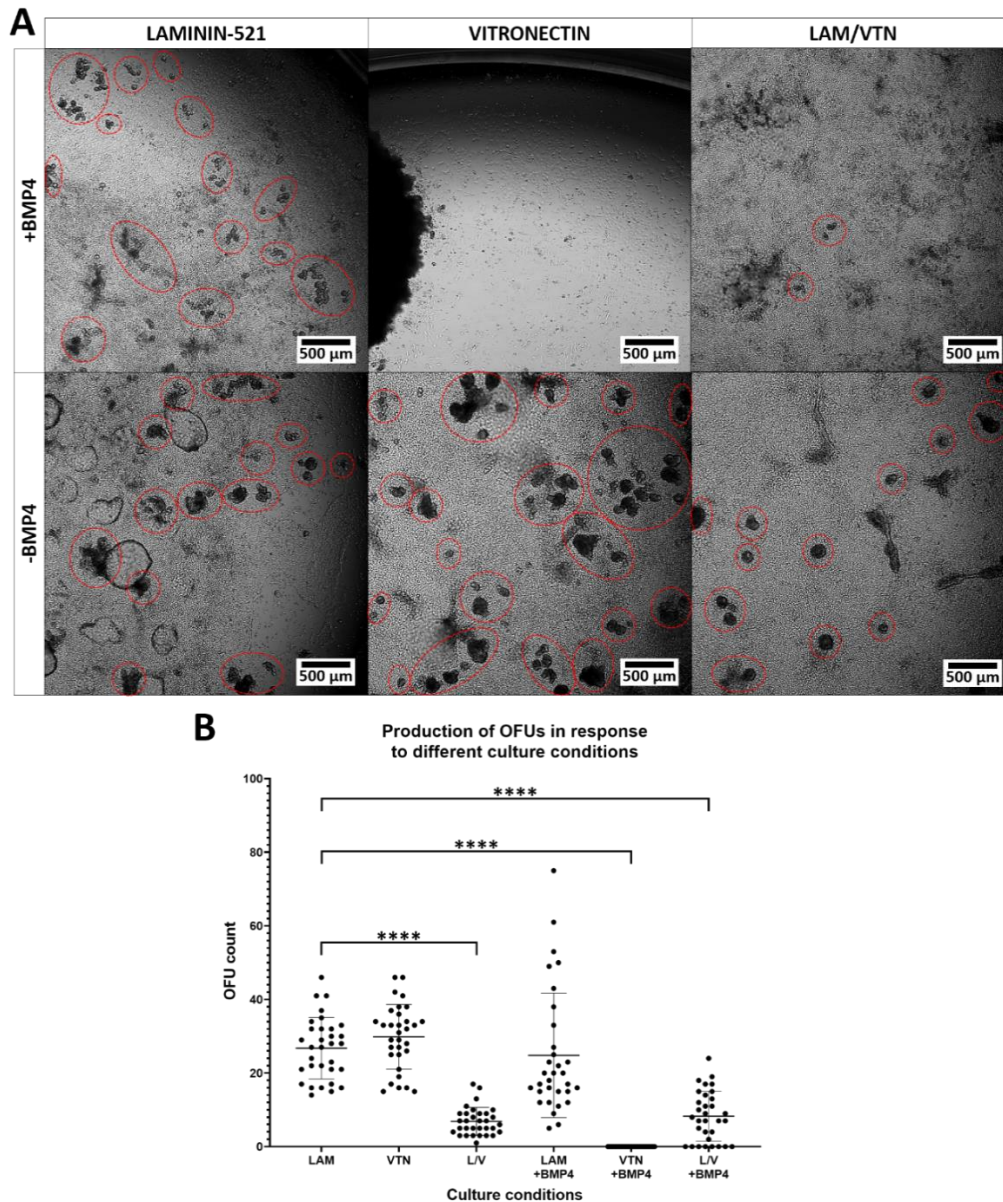
Figure 3.10 Generation of mid- and hindgut spheroids.
(A) Bright-field images from mid- and hindgut monolayers differentiated over 3 different ECMs (LAM, VTN and L/V) with and without the use of BMP4 (upper and lower panels respectively) during DE differentiation. Newly formed spheroids are indicated by a red dotted ring (----). The morphology, size and number of spheroids varied between the different culture conditions. LAM and LAM+BMP4 produced OFUs with similar morphological characteristics, and likewise with VTN and L/V. L/V+BMP4 produced scares OFUs, and VTN+BMP4 led to the detachment of the entire colony, no OFUs were recorded. Scale bars indicate 500 μm. (B) Quantification of OFUs produced by differentiated mid- and hindgut cultures, grown with different ECMs and media composition. No significant difference was found between the parental culture condition (LAM) and the use of VTN (*p>0.9999*) or LAM+BMP4 (*p>0.9999*). A significant decrease in the production of OFUs was observed in cultures prepared with L/V (*p<0.0001*), VTN+BMP4 (*p<0.0001*), and L/V+BMP4 (*p<0.0001*). The results presented correspond to the quantification of 4 independently differentiated mid- and hindgut cultures and 8 fields per replicate (32 data points). Since some of the datasets did not fit a normal distribution, statistical analysis was conducted using non-parametric Kruskal-Wallis and post hoc pairwise comparison with Dunn's test. Both were assessed under a significance level of 95%, where: **p≤0.0500; **p<0.0100; ***p<0.0010; ****p<0.0001*.

3.2.6 Effect of ECM composition and BMP4 in mid- and hindgut differentiation

Mid- and hindgut differentiation was evaluated with immunostaining against FOXA2 (**Figure 3.11**), and CDX2 (**Figure 3.12**). The quantification of normalized relative fluorescence intensity (RFI) for both markers revealed a higher expression of CDX2 compared to FOXA2, in all culture conditions (**Figure 3.13**). These suggest that a great majority of the cells across the monolayer have transitioned from definitive endoderm into a mid- and hindgut identity.

In LAM+BMP4, FOXA2 was expressed in most of the monolayer except for foci of high confluency, whereas in LAM the fluorescence intensity across the monolayer was lower but increased in the overgrowth found in the most confluent regions (**Figure 3.11, arrowheads**). In both conditions, LAM+BMP4 and LAM, the expression of CDX2 was clustered in patches of high confluency spread side to side of the monolayer (**Figure 3.12, arrowheads**). VTN+BMP4 samples could not be detected.

The expression of FOXA2 in VTN samples, was evenly distributed across the monolayer with a decrease in its intensity in highly confluent regions, as seen by the increase in the fluorescence intensity of the blue channel. In contrast, the expression of CDX2 is more intense in these specific regions. These support the idea that highly confluent regions have progressed more into the differentiation program, leading to the outgrowth of mid- and hindgut spheroids.

L/V+BMP4 and L/V grew mostly as monolayers with few regions of high confluency, and poor production of spheroids. The expression of FOXA2 in L/V+BMP4 seems to be homogeneous across the monolayer, whereas in L/V patches without expression of FOXA2 were detected. The regions absent of FOXA2 match with the most confluent regions of the culture. In the case of CDX2, the expression is in most of the cells, with peaks of intensity in the scattered regions of high confluency. Interestingly, the intensity of FOXA2 in L/V+BMP4 is slightly lower when compared against L/V. Conversely, in the case of CDX2 is the opposite L/V+BMP4 is slightly higher compared to L/V.
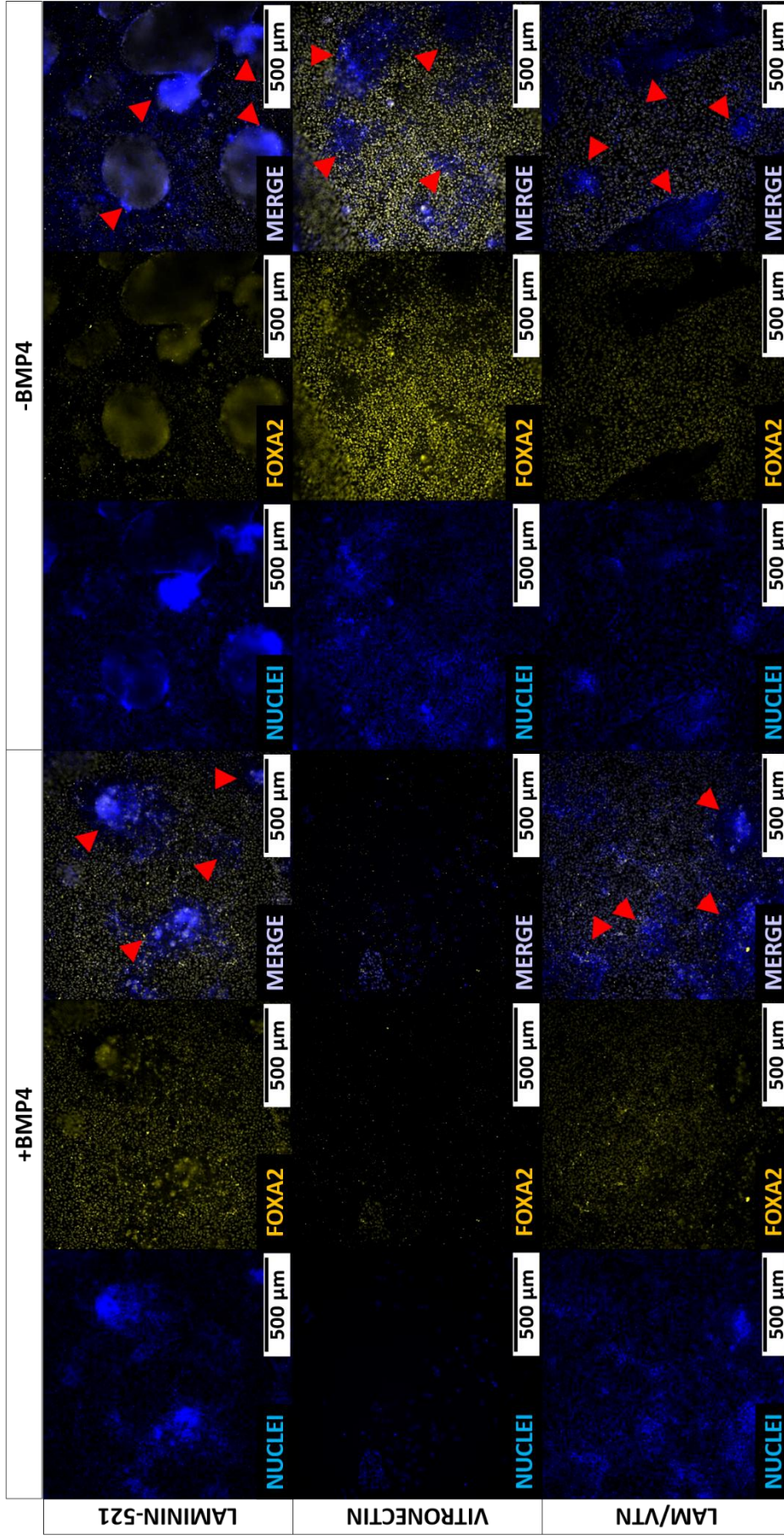
Figure 3.11 Expression of definitive endoderm marker FOXA2 after mid- and hindgut differentiation treatment.

Further modifications to the differentiation protocol evaluated the effect of BMP4 and ECM composition. After the mid- and hindgut differentiation stage, the cells were fixed and stained with Hoechst 33342 (blue) and the DE marker FOXA2 (yellow). Immunostaining results indicated the prevalent expression of FOXA2 in putative mid- and hindgut cultures, with varying intensities between the different culture conditions. The fluorescence was particularly reduced on scattered regions of high confluence (arrowheads). Scale bars indicate 500 µm.
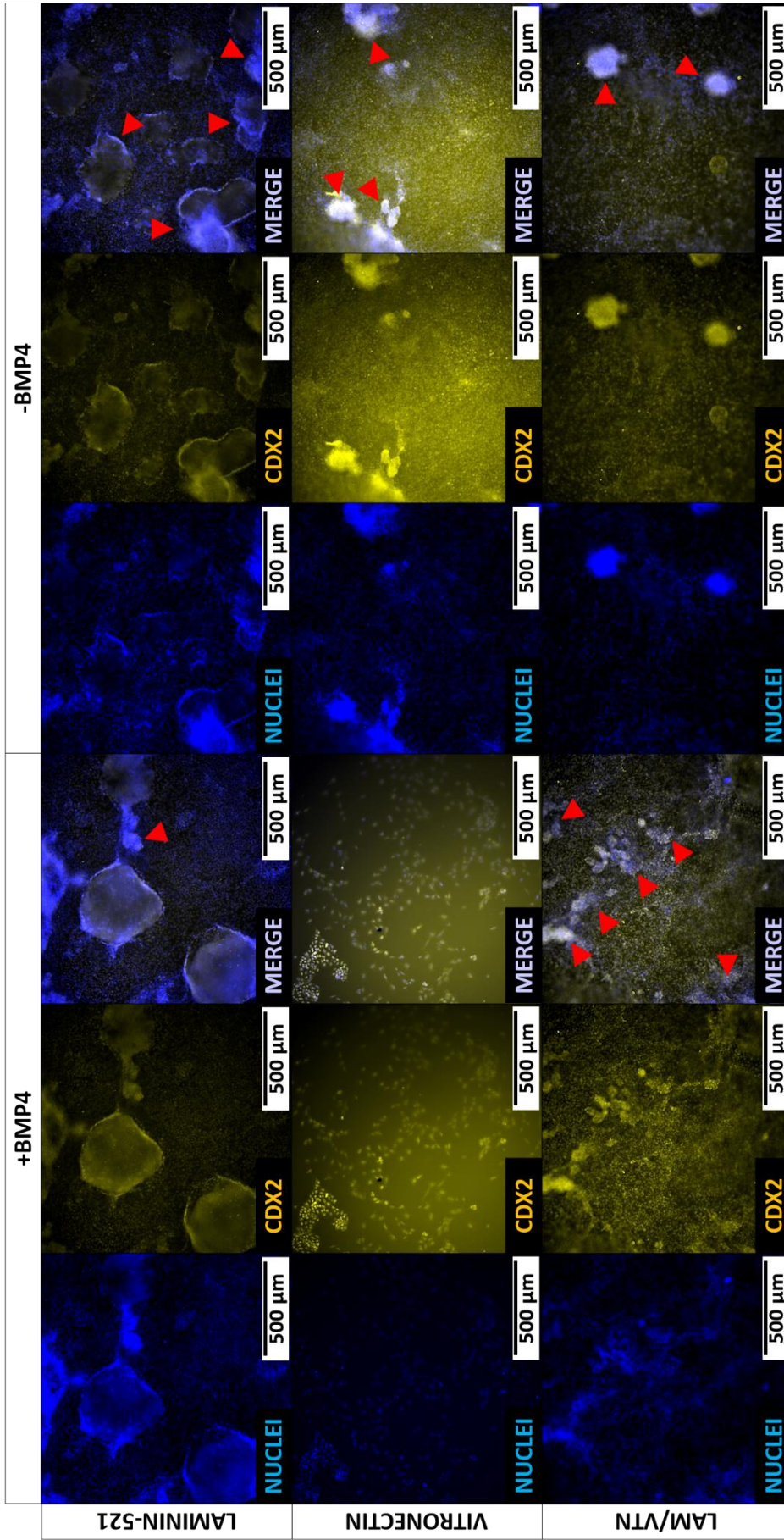
Figure 3.12 Expression of CDX2 intestinal marker after mid- and hindgut differentiation treatment.
Further modifications to the differentiation protocol evaluated the effect of BMP4 and ECM composition. After the mid- and hindgut differentiation stage, the cells were fixed and stained with Hoechst 33342 (blue) and the intestinal marker CDX2 (yellow). Immunostaining results showed varying expression levels of CDX2 between the different culture conditions in putative mid- and hindgut cultures. The fluorescence was particularly accentuated on scattered regions of high confluence (arrowheads). Scale bars indicate 500 μm.

Relative Fluorescent Intensity (RFI) was quantified using the Fiji distribution of plugins within ImageJ to measure integrated fluorescence intensity above the background threshold. Next, the data was analyzed with Kolmogorov-Smirnov test to assess its normal distribution ($p≥0.0500$). After analysing the measurements obtained from FOXA2 staining, four of the culture conditions, LAM ($p>0.1000$), VTN ($p>0.1000$), L/V ($p>0.1000$), and L/V+BMP4 ($p>0.1000$), were found to be normally distributed, though two conditions, LAM+BMP4 ($p=0.0450$) and VTN+BMP4 ($p<0.0001$), did not follow a normal distribution according to the test. Similarly, KS analysis of the results obtained from CDX2 staining found four culture conditions, LAM ($p>0.1000$), VTN ($p>0.1000$), L/V ($p>0.1000$), and LAM+BMP4 ($p>0.1000$), fit the Gaussian distribution and two conditions, VTN+BMP4 ($p=0.0058$) and LAM+BMP4 ($p=0.0432$) were not normally distributed. Therefore, given that some datasets did not follow a normal distribution, the results were analyzed using non-parametric statistical analysis. Kruskal Wallis test was used to evaluate whether modifications in the ECM and composition of the differentiation media produced a significant difference in the expression of the differentiation markers FOXA2 and CDX2. LAM was used as the basal culture conditions and serve as the reference baseline for *post hoc* pairwise comparisons using Dunn's test. All statistical analysis was conducted with a significance level of 95%.

Kruskal Wallis analysis of the data obtained from FOXA2 staining (**Figure 3.13A)** found a statistical difference between the datasets ($H=72.18$, $p<0.0001$). Pairwise comparison showed that compared to LAM, only VTN+BMP4 ($p<0.0001$) exhibited a significant decrease in the expression of FOXA2. This was expected since most of the colony detached from the well and was lost during the differentiation protocol. Conversely, VTN ($p=0.1099$), L/V ($p>0.9999$), LAM+BMP4 ($p>0.9999$), and L/V+BMP4 ($p>0.9999$) did not show a statistical difference compared to the control conditions. These results suggested that BMP4 did not improve the expression of differentiation markers. However, it did have a negative effect in the cell adhesion when combined with a VTN coating matrix.

The expression of CDX2 (**Figure 3.13B**) highlighted the overall impact of the ECM composition in a pre-terminal checkpoint of the differentiation protocol. Overall, in spite of the persistent expression of FOXA2, the RFI of CDX2 was considerably higher. KW statistical analysis of the expression of CDX2, revealed a statistical difference ($H=31.64$, $p<0.0001$) within the datasets of samples cultured under different conditions. Subsequent analysis found that only VTN+BMP4 ($p<0.0001$) showed a significant reduction in the RFI of the mid- and hindgut marker, although this can be explained due to the detachment of most of the cells from the well. Aside from this condition, VTN ($p=0.8284$), L/V ($p=0.0668$), LAM+BMP4 ($p>0.9999$), and L/V+BMP4 ($p=0.8747$) did not have a significant effect in the expression of CDX2.

Overall, with the exception of VTN+BMP4, the evidence did not indicate that the addition of BMP4 or the use of different ECMs has an effect on the expression pattern of DE and/or mid- and hindgut differentiation markers.
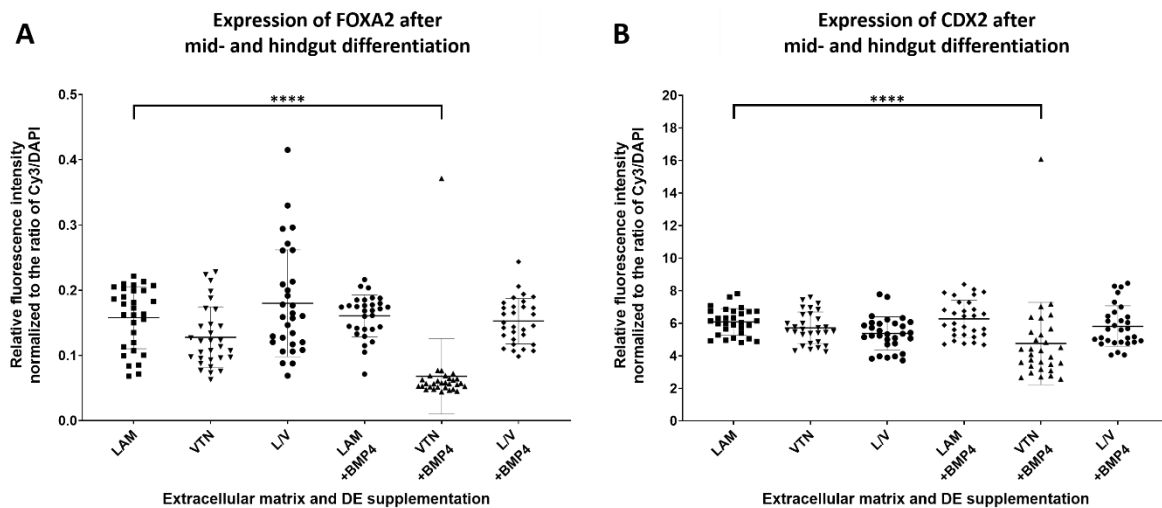
Figure 3.13 Expression of FOXA2 and CDX2 markers after mid- and hindgut differentiation treatment.
Quantification of the RFI emitted by the expression of differentiation markers FOXA2 and CDX2, for DE (A) and mid- and hindgut (B), respectively. The data presents a comparison between the basal culture conditions (LAM) against the modifications in the ECM and media composition, and their impact on the expression of differentiation markers. The expression of FOXA2 was not significantly different on the samples cultured with VTN (*p=0.1099*), L/V (*p>0.9999*), LAM+BMP4 (*p>0.9999*), or L/V+BMP4 (*p>0.9999*). Likewise, the expression of CDX2 did not change significantly on cells cultured with VTN (*p=0.8284*), L/V (*p=0.0668*), LAM+BMP4 (*p>0.9999*), or L/V+BMP4 (*p=0.8747*). Statistical analysis showed only VTN+BMP4 produced a significant decrease in the expression of FOXA2 (*p<0.0001*) and CDX2 (*p<0.0001*). Experiments were performed by duplicate and the fluorescence output was measured in 15 different fields per replicate (30 data points). Since some of the data sets did not fit a normal distribution statistical analysis was performed using non-parametric tests. The data was processed using Kruskal-Wallis' test with *post hoc* pairwise comparison using Dunn's test. Both were assessed under a significance level of 95%, where: **p≤0.0500*; ***p<0.0100*; ****p<0.0010*; *****p<0.0001*.

3.2.7 Comparison of the outcome from SRSF differentiation protocols

Originally, we attempted to implement the protocol established by McCracken *et al.* (2011), though the DE differentiation was unsuccessful. Nevertheless, this protocol was the backbone for further optimization. After testing modification in the composition of the ECM and the DE differentiation medium, we have identified 3 culture conditions which provided an optimal amount of OFUs: (i) LAM, the first iteration of our differentiation protocol, in which iPSCs were initially seeded on a laminin-521 ECM, and the main driver of DE differentiation was AA; (ii) VTN, where the cells were cultured on a vitronectin matrix and DE differentiation was also driven by AA; and (iii) LAM+BMP4, in this instance iPSCs were seeded over laminin-521, but the main driver of DE differentiation was a combination of AA and BMP4. LAM produced a high (+++) amount of type II and type III OFUs, whereas LAM+BMP4 only generated mid (++) levels of these type of OFUs. In contrast, VTN generated a high (+++) number of type I putative OFUs. After embedding the OFUs into Matrigel, type I structures generated with VTN ECM could not develop into a full size HIOs, but rather disaggregated over time. Only type II and III structures generated with LAM and LAM+BMP4 survived and led to the development of intestinal organoids.

Figure 3.14 outlines the modifications we have tested in the different version of our SRSF protocol for the generation of iPSC-derived HIOs. In brief, **SRSF v.1** incorporated the use of laminin-521 instead of Matrigel as a support matrix for the culture of miFF1-iPSCs; it also implemented a new set of conditions for the generation of DE, maintaining AA [100 ng/mL] as the main effector, and including the induction of WNT signalling at this stage using the small molecule CHIR99021 [2 µM]. **SRSF v.2** incorporated the use of recombinant R-spondin 1 produced in-house [500 ng/mL] in order to reduce the cost of using commercial purified recombinant R-spondin 1. **SRSF v.3** tested the use of BMP4 [50 ng/mL] and different ECMs to improve the differentiation of the DE. Among these conditions, only LAM+BMP4 showed potential in the generation of HIOs. Finally, we have developed protocol SRSF v.4, which incorporated the use of small-molecule-driven DE differentiation as proposed by Siller *et al.* (2015), using B27 [1x] and a high concentration of CHIR99021 [3 µM].

		D0	D1	D2	D3	D4	D5	D6	D7	D8 →	
		Stem cell stage	Definitive endoderm stage			Mid- and hindgut differentiation stage				Intestinal growth and differentiation	
H1, H9 hESCs	mTeSR1 Y-27632		Activin A	0.2% dFBS/ Activin A	2% dFBS/ Activin A	dFBS/FGF4/WNT3A				B27/Noggin/RSPO1/EGF	McCracken et al, 2011
miFF1 hiPSCs	mTeSR1 Y-27632		B27/Activin A/CHIR99021			dFBS/FGF4/Noggin/CHIR99021				B27/Noggin/RSPO1/EGF	SRSF v.1
miFF1 hiPSCs	mTeSR1 Y-27632		B27/Activin A/CHIR99021			dFBS/FGF4/Noggin/CHIR99021				B27/Noggin/rRSPO1/EGF	SRSF v.2
miFF1 hiPSCs	mTeSR1 Y-27632		B27/BMP4 /AA/CHIR	B27/Activin A/ CHIR99021		dFBS/FGF4/Noggin/CHIR99021				B27/Noggin/rRSPO1/EGF	SRSF v.3

		D0	D1	D2	D3	D4	D5	D6	D7 →	
		Stem cell stage	Definitive endoderm stage		Mid- and hindgut differentiation stage				Intestinal growth and differentiation	
miFF1 hiPSCs	mTeSR1 Y-27632		B27/CHIR99021	B27	dFBS/FGF4/Noggin/CHIR99021				B27/Noggin/rRSPO1/EGF	SRSF v.4

Figure 3.14 Modified protocols for the generation of iPSC-derived HIOs.
The protocol established by McCracken *et al.* (2011) was used as the basis for the development of an optimized protocol for the generation of iPSC-derived HIOs. SRSF v.1 implemented a new set of conditions for the generation of DE; SRSF v.2 incorporated the use of recombinant R-spondin 1 produced in-house; SRSF v.3 tested the use of BMP4 to improve the differentiation of the DE; finally, SRSF v.4 used small-molecule-driven DE differentiation. Yellow boxes are DE, orange boxes depict Mid- and hindgut and red boxes HIOs. Cell lines are indicated at each row and conditions are described in each step of the process.

We made a comparative assessment of the output from the different versions of our protocol, evaluating the production of spheroids. We monitored this output since testing the organoids generated by each protocol would have been significantly costly and time consuming. A timeline progression of the differentiation protocols is presented below:

SRSF v.1 and v.2 are represented in the same timeline (**Figure 3.15**) since they do not differ until the intestinal growth stage. Furthermore, the conditions for DE differentiation established in these protocols have already been assessed in their capacity to generate HIOs. Therefore, it will serve as a baseline to compare the outcome of protocols 3 (**Figure 3.16**) and 4 (**Figure 3.17**).

In all the conditions iPSCs were seeded on a matrix of laminin-521 [0.5 µg/cm^2] and the main difference relied on the conditions for DE differentiation: **SRSF v.1 and v.2** used AA [100 ng/mL]; **SRSF v.3** used a combination of AA [100 ng/mL] + BMP4 [50 ng/mL] on the first day of DE differentiation, and only AA [100 ng/mL] on the following two days; and **SRSF v.4** used a two-days differentiation with B27 [1x] + CHIR99021 [3 µM] on the first day, and only B27 [1x] on the second day. Mid- and hindgut differentiation conditions remained unchanged: FGF [500 ng/mL] + dFBS [2%] + CHIR99021 [2 µM] + Noggin [100 ng/mL].

In the DE stage there was no apparent difference between the protocols, as the three of them generated cells with the typical cobblestone-and-petal morphology from the DE. However, protocol 4 only required 2 days for this stage.

During the mid- and hindgut stage, protocol **SRSF v.1/SRSF v.2** developed in a similar fashion, as was observed in the first experiments, with randomly distributed overconfluent foci from which the mid- and hindgut spheroids were released at D6 and D7. Under these conditions, the colony produced high (+++) levels of type II and III structures (**Figure 3.15**).

In protocol **SRSF v.3**, the overconfluency was seen in the periphery of the colony: this region started to collapse towards the centre creating a dark cellular mass where low (+) levels of type III structures were released into the supernatant (**Figure 3.16**).

In protocol **SRSF v.4,** we observed a similar contraction of the confluent mass towards the centre of the colony. However, in this case the spheroids were smaller more loosely attached, similar to protocol SRSF v.1 and SRSF v.2. Finally, over the course of days 6 and 7 high (+++) levels of type II and III structures were released into the supernatant (**Figure 3.17**).
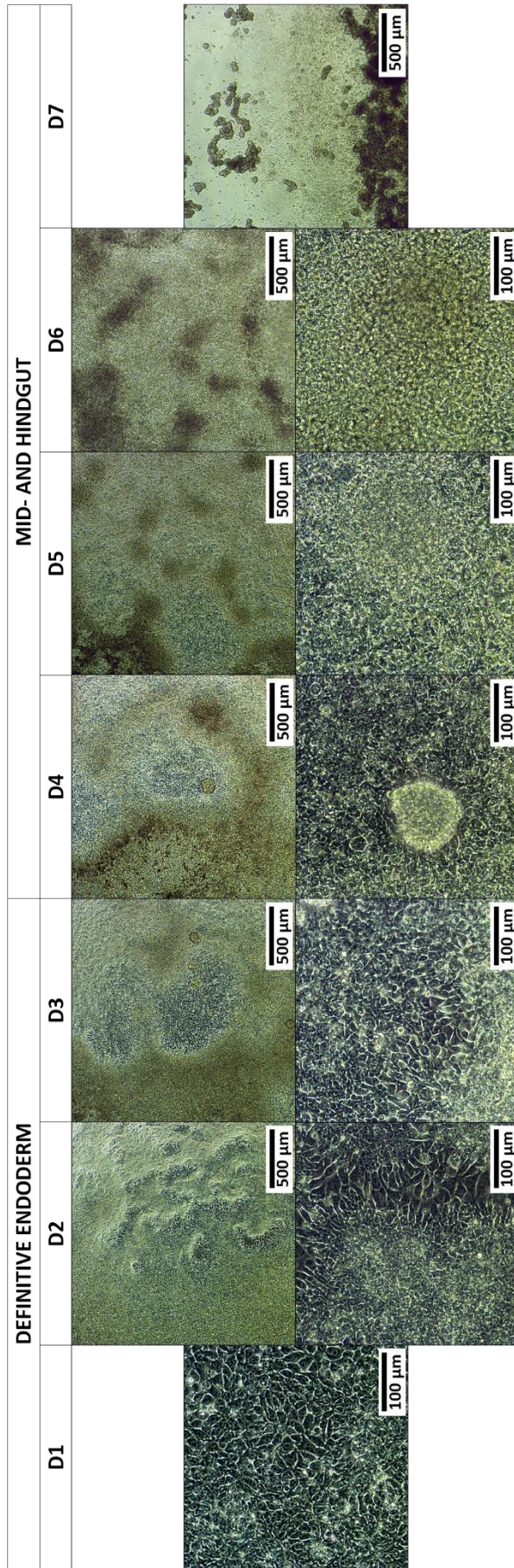
Figure 3.15 Timeline progression of the differentiation of iPSC cells into mid- and hindgut using protocol SRSF v.1/v.2 (AA).

Bright-field images of the differentiation process using protocol SRSF v.1 and 2. AA induction of definitive endoderm generated highly confluent cultures of cells with a cobblestone-and-petal morphology. Mid- and hindgut differentiation conditions lead to the formation of focalized cores of cellular aggregation. These foci facilitated the formation of high levels (>200 OFUs per well) of small, loosely attached aggregates of OFUs and free individual OFUs, distributed over the entire colony. Finally, between days 6 and 7, the OFUs were released into the supernatant in small clusters. Scale bars represent 500 μm (upper panels) and 100 μm (lower panels). OFU: organoid-forming unit.
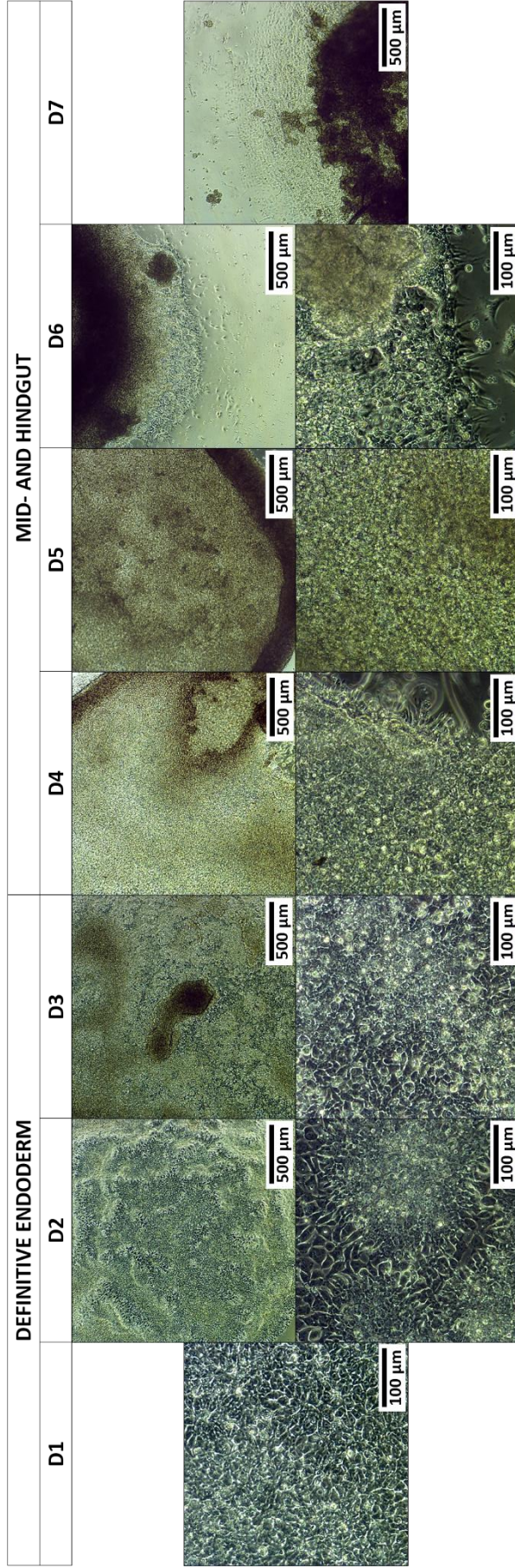
Figure 3.16 Timeline progression of the differentiation of iPSC cells into mid- and hindgut using protocol SRSF v.3 (AA + BMP4).
Bright-field images of the differentiation process using protocol SRSF v.3. Incorporation of BMP4 into the definitive endoderm differentiation medium yielded highly confluent cultures of cells exhibiting a cobblestone-and-petal morphology, with some focalized overgrowth and clumping of cells. During mid- and hindgut differentiation, cells continued proliferating leading to the overlap of cells, particularly in the periphery of the colony. Mid-levels (<200 OFUs per well) of small, loosely attached aggregates of OFUs emerged from the dark mass of clumped cells. However, between days 6 and 7, only a low number (<100 OFUs per well) of these structures were released into the supernatant. Scale bars represent 500 μm (upper panels) and 100 μm (lower panels). OFU: organoid-forming unit.
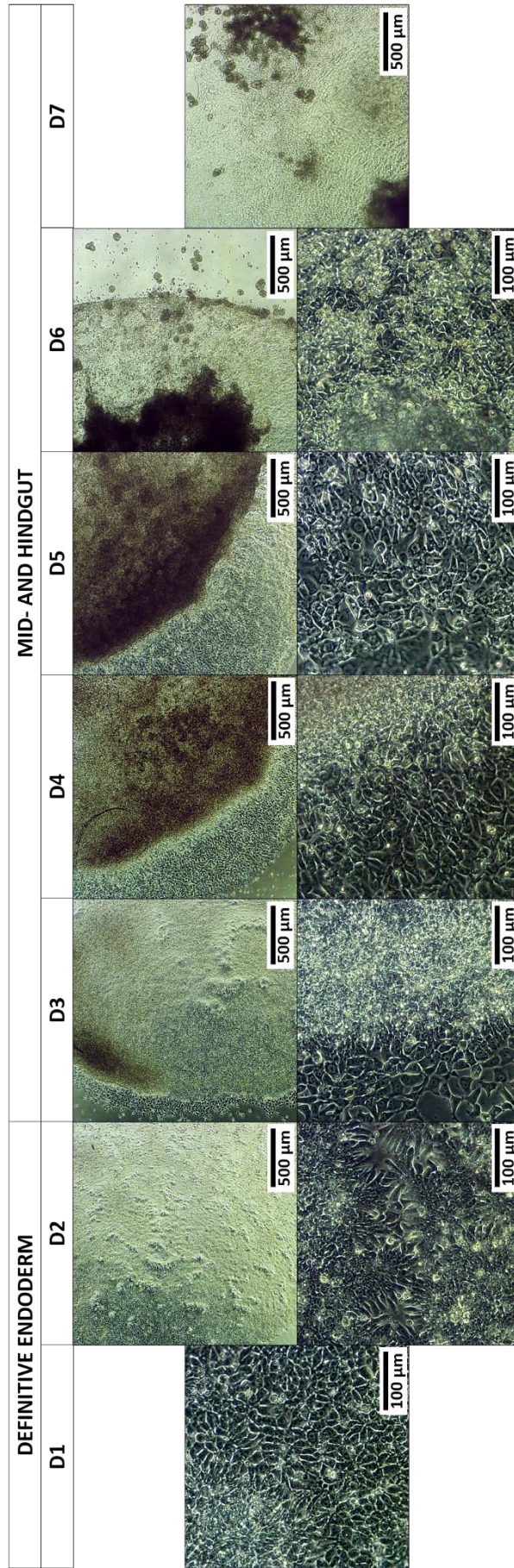
Figure 3.17 Timeline progression of the differentiation of iPSC cells into mid- and hindgut using protocol SRSF v.4 (CHIR).

Bright-field images of the differentiation process using protocol SRSF v.4. The modification to the definitive endoderm differentiation medium yield confluent cultures of cells exhibiting a cobblestone-and-petal morphology. Mid- and hindgut differentiation led to the aggregation of cells in a centralized cellular mass, followed by the release of a high number (>200 OFUs per well) of loose OFUs into the supernatant, on days 6 and 7. Scale bars represent 500 µm (upper panels) and 100 µm (lower panels). OFU: organoid-forming unit.

Protocol SRSF v.3 did not show an improvement in the generation of OFUs, and also required the use of additional growth factors. SRSF v.4 showed a similar OFU output as the previously tested protocol 1, with the advantage of a 2 days DE differentiation stage driven by small molecules rather than recombinant AA. These conditions reduce the time and cost of the protocols. However, it also incorporated the advantage of using recombinant R-spondin 1 produced in-house from protocol 2, reducing the costs even further. The final protocol is summarized in **Figure 3.18** below, followed by a detailed description of the differentiation conditions.
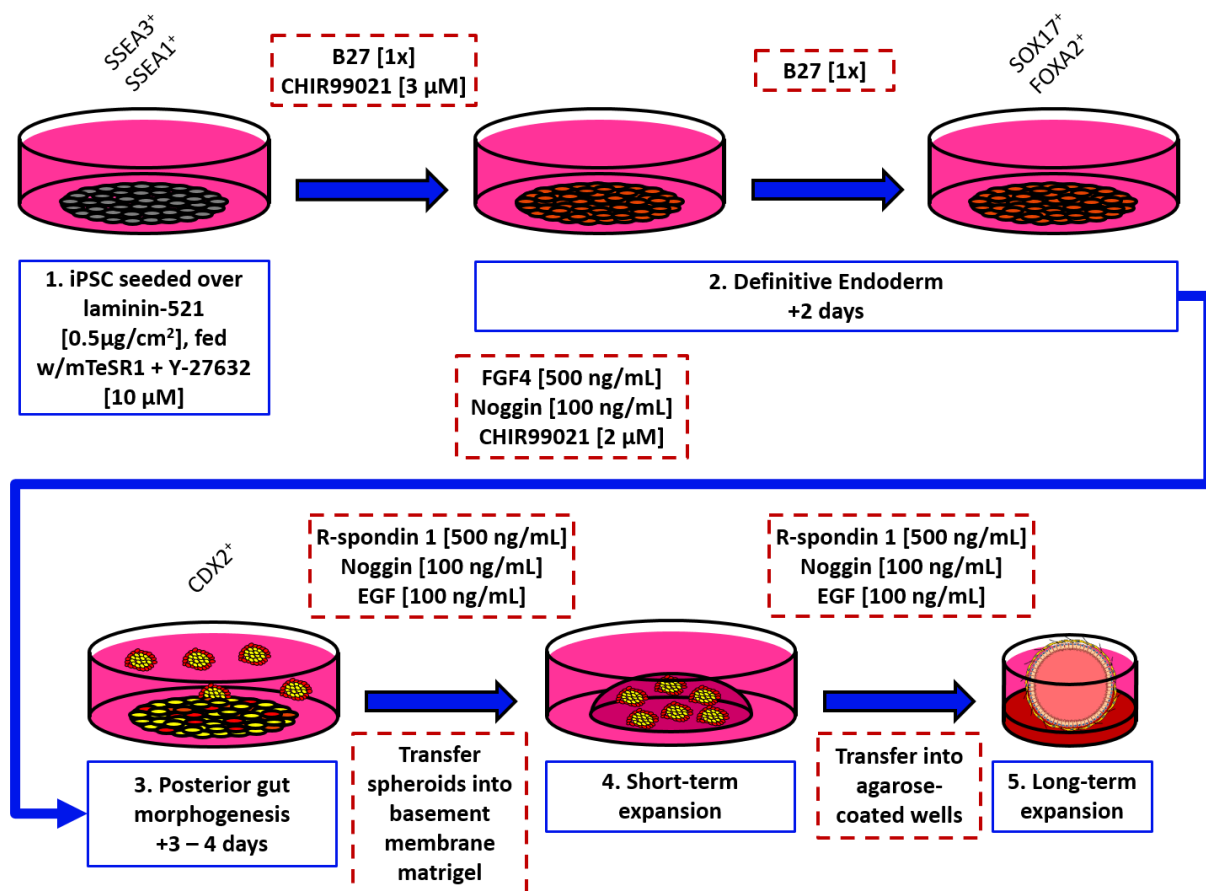
Figure 3.18 Intestinal organoid protocol SRSF v.4 summary.
1) miFF1 cells were seeded in laminin-521, and fed with mTeSR1 medium and Y-27632, these conditions have been shown to maximize the survival of the cells after passaging, while maintaining their pluripotent identity, which was confirmed by the presence of SSEA3 labelling and absence of SSEA1; 2) Definitive endoderm induction was achieved with a combination of B27 supplements and a relatively high concentration of CHIR. This was confirmed by the expression of SOX17 and FOXA2 markers. 3) Posterior gut morphogenesis was induced with Noggin, FGF4 and CHIR, successful differentiation was observed by the expression of CDX2 and the release of gut spheroids. 4) Posterior gut expansion was performed by embedding the gut spheroids in Matrigel and the addition of R-spondin 1, Noggin and EGF. 5) Expansion and amplification of the intestinal organoids was continued in a suspension culture using agarose-coated wells.

3.2.8 Three-dimensional growth of intestinal tissue

After the mid- and hindgut differentiation stage, we recovered a high (+++) number of type II and type III OFUs generated with protocol SRSF v.1. These were embedded in BMM Matrigel and fed with intestinal growth medium, leading to the development of full-size organoids. The main effectors of the intestinal growth medium included: EGF [100 ng/mL] necessary for the proliferation of epithelial cell and the terminal differentiation of absorptive cells in the intestinal epithelium; Noggin [100 ng/mL] to promote cell proliferation and crypt formation; B27 [1x] to promote cell survival and proliferation in long-term cultures; finally, RSPO1 [500 ng/mL], an enhancer of WNT signalling that prevents the recycling of the WNT receptor Frizzled and is critical for the development of the organoid. In this case, we used commercial recombinant RSPO1 to ensure that the output from our initial approach in the generation of HIOs could be compared against the one originally described by McCracken *et al.* (2011).

Figure 3.19 presents a representative timeline of the growth of the intestinal organoids (highlighted in red). Interestingly, prior to day 8, the spheroids appeared to have dissociated and broken apart, which at the time led to the premature, misconstrued conclusion that the differentiation had failed. We speculated this effect could have been caused by the proliferation of mesenchymal cells and opted for continuing with the differentiation protocol. Despite appearances, between days 8 and 10 we observed the development of cyst-like structures arising from the edges of the mesenchymal debri (**Figure 3.19, dashed red line**). Compared to the initial number of OFUs (+++), only a low (+) number of cyst-like structures were detected; we suspect the rest of the OFUs were comprised of mesenchymal cells. Following the progression of their growth, these structures eventually resulted in the formation of organoids as observed in day 42. Between days 16 and 19, the samples were considerably dense. Also, given the amount of growth factors required, the organoids were transferred into agarose-coated wells to reduce the density and volume of medium. We stopped the experiment at day 42, the organoids at this time point reached approximately up to 1.5 – 2.5 mm in diameter.

In summary, following the same semi quantitative guidelines used for the assessment of the production of OFUs (**Table 3.1**), we can state that the final stage of organoid differentiation started with a high (+++) number of putative OFUs, but the resulting organoids yield was low (+). To our current knowledge, we are unable to identify from the beginning which spheroids will develop into a full-size organoid. Furthermore, the high variability in the time and way in which mid- and hindgut spheroids develop into intestinal organoids, restricts the retrieval of quantitative data on the spheroids yield per well, and the overall organoid yield obtained from the differentiation protocol.
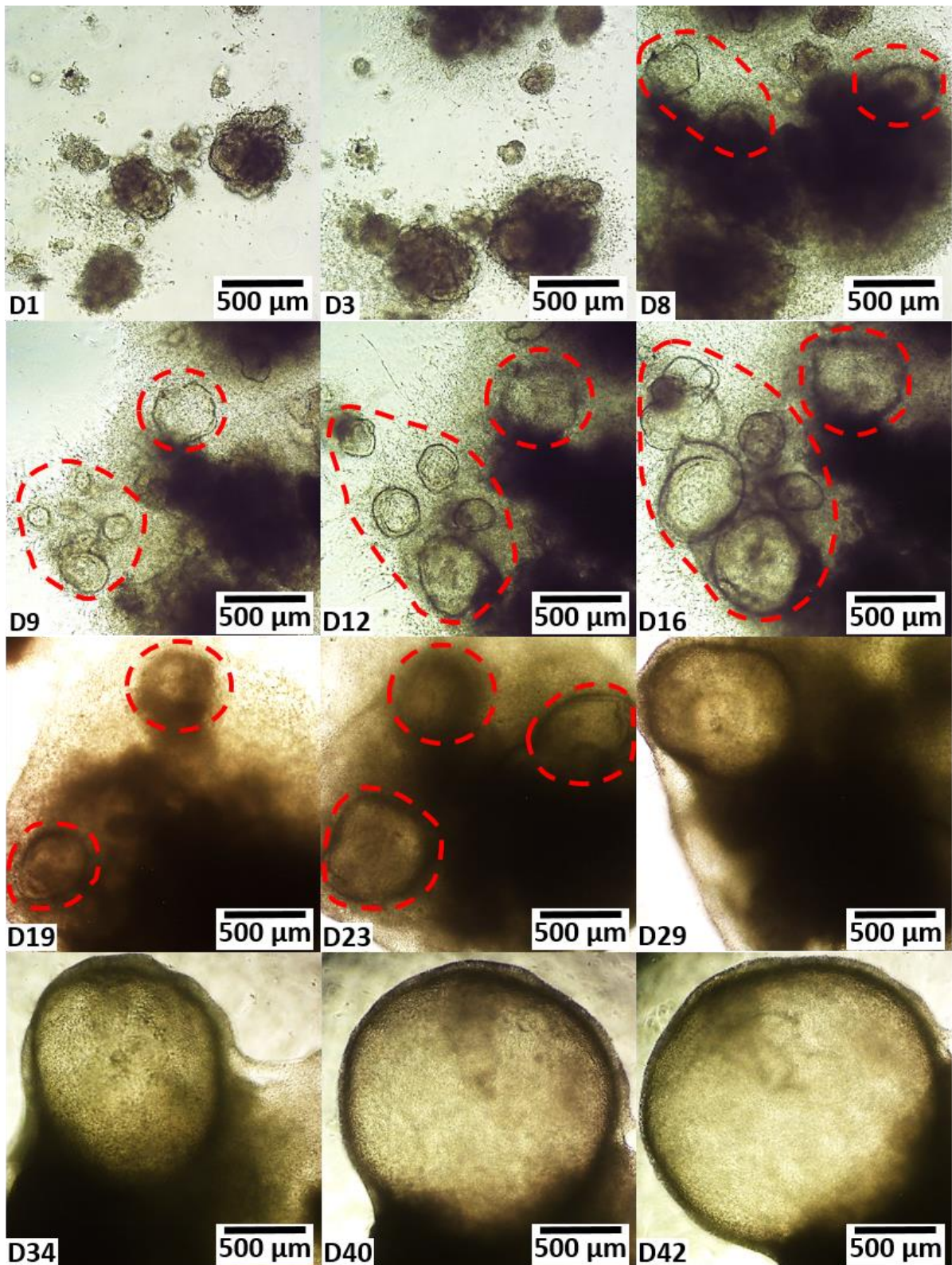
Figure 3.19 Three-dimensional culture of spheroids in intestinal growth conditions.
Bright-field images of the time-course progression of the growth and differentiation of mid- and hindgut spheroids into intestinal organoids. At D2-D8 the masses of cells are dense, but after D8 the organoids begin to clear (red dotted circles/ovals), establishing a luminal quality. The number of organoids obtained is variable, and their size spanned from 1.5 to 2.5 mm in diameter. Scale bars indicate 500 μm.

3.2.9 Characterization of intestinal organoids

HIOs were labelled using a modification from the protocol described O'Rourke *et al.* (2016) and imaged with light sheet microscopy. Immunostaining of D42 HIOs (**Figure 3.20**) showed the colocalization of the nuclei (blue) with the transcription factor CDX2 (yellow), a marker for mid- and hindgut/intestinal lineage, previously shown in 2D wide-field microscopy of earlier cultures (**Figure 3.8**). This suggested the formation of an intestinal epithelium within the lining of the organoid. FITC-phalloidin was used to stain actin microfilaments in the cytoskeleton (green) and revealed that the epithelial monolayer was comprised of columnar cells, consistent with the morphology from the enterocytes/colonocytes. Additionally, COL1A1 (red) was detected labelling an outer layer surrounding the intestinal epithelium which we speculate indicated the formation of a complex ECM, most likely by a mesenchymal compartment in the basement membrane.
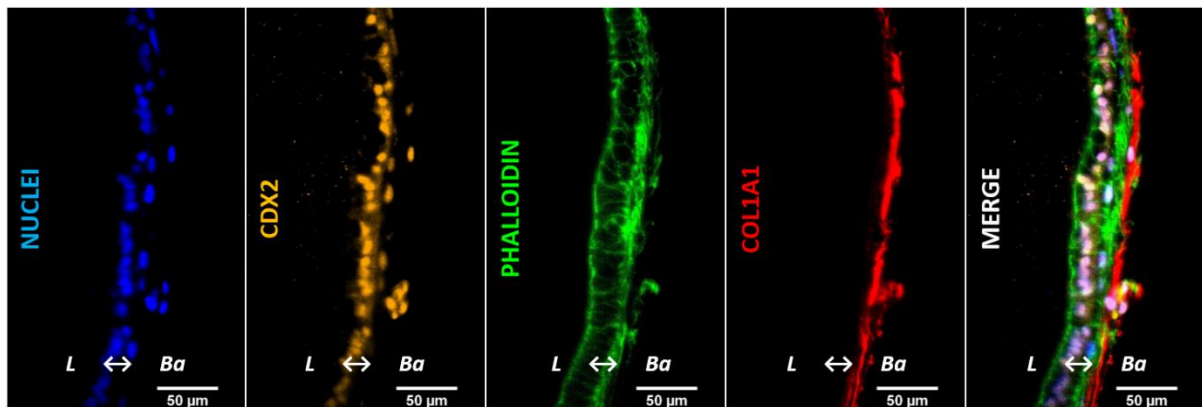
Figure 3.20 Characterization of iPSC-derived human intestinal organoids.
Fluorescent staining of the intestinal organoids generated with protocol SRSF v.1. The organoids are comprised by an inner layer of columnar cells (green) expressing the intestinal lineage transcription factor CDX2 (yellow) colocalized with the cell nuclei (blue). Additionally, the external surface of the organoid was labelled with COL1A1 (red), suggesting the presence of mesenchymal cells generating a structural layer to support the epithelium. Scale bars indicate 50 μm. *L: organoid lumen (to the left)*; *Ba: basolateral compartment (to the right)*.

D7 HIOs were analyzed for the expression of markers to determine the molecular nature of the HIO. D42 samples provided inconsistent RNA extraction of poor quality and were not analyzed. Considering that our model of intestinal organoids was based on the one described by Wells' group (McCracken *et al.*, 2011), the selection of the genes for RT-qPCR analysis was based on those previously used by them in their characterization works (Finkbeiner *et al.*, 2015*a*, 2015*b*). The results from D7 HIOs were normalized with the housekeeping gene *HPRT1* and compared against a control intestinal cell line (CaCo-2), and a cell line of mesenchymal origin (HDFs). The dot plots presented in **Figure 3.21** correspond to the RT-qPCR results of 2 biological and 3 technical replicates (6 data points) of D7 HIOs, and 1 biological with 3 technical replicates of the reference cell lines. Statistical analysis was conducted using non-parametric Mann-Whitney pairwise comparison, with a significance level of 95%.

The expression of the proliferation marker *MKI67* (*p=0.0238*) and the marker for quiescent ISCs *BMI1* (*p=0.0238*) was significantly higher in organoids than in CaCo-2. Notably, *LGR5* was downregulated and not significantly different from CaCo-2 (*p=0.2381*) indicating that the expression of *MKI67* must be linked to a different subpopulation. The low levels of *LGR5* could be associated to the intrinsic low expression of this markers or the depletion of this population due to the cells undergoing differentiation rather than self-renewal. The expression of *BMI1* was significantly higher than CaCo-2 (*p=0.0238*) which could be and indicative that the ISC population within the organoids is mostly comprised of quiescent cells.

The markers for cells from the secretory lineage *ATOH1* (secretory TACs), *MUC2* (goblet cells), *CHGA* (EECs), and *DEFA5* (Paneth cells), were found to be underexpressed by the organoids, below the level of the normalising gene. Still, the expression of *ATOH1* (*p=0.0119*) and *CHGA* (*p=0.0238*) was significantly higher in organoids compared to CaCo-2 cells, which are mostly representative of the absorptive lineage. The results from *ATOH1* and *CHGA* indicated the presence of a small population of secretory TACs and enteroendocrine cells, respectively.

No significant difference was detected in the expression of *MUC2* (*p>0.9999*) and *DEFA5* (*p=0.5000*) compared to CaCo-2, where the expression of these genes was null. The absence of *MUC2* discarded the presence of goblet cells in the organoids. For the particular case of *DEFA5*, we were uncertain about the expression of Paneth cell markers in HIOs, since these are derived from mid- and hindgut spheroids, the latter are not expected to produce these cells. Nevertheless, Finkbeiner *et al.* (2015*b*) searched for the expression of Paneth cell markers *LYZ* and *DEFA5* as a hallmark for intestinal maturation in HIOs derived from mid- and hindgut spheroids using the protocol described by McCracken *et al.* (2011). Therefore, as previously mentioned, we opted for adhering to a similar characterization strategy as the one employed by Wells' group since our protocol was built over the

foundation of their work. However, in spite of *DEFA5* being detected by Wells' group in their model of HIOs, no expression of this gene was detected in our model of intestinal organoids. This indicated the absence of Paneth cells or a population with putative expression of the same markers. Overall, the results from these markers suggested the lack of a representative secretory population within the organoids.

HES1, *VIL1* and *CDH1* are markers for the intestinal epithelium and the first two are specifically associated with the intestinal absorptive lineage. The expression of *HES1* in D7 organoids was considerably upregulated and even significantly higher than in CaCo-2 (*p=0.0238*), this might be related to the upregulation of the proliferation marker *MKI67*. *VIL1* expression was relatively similar to *HES1*, although in this case the expression in CaCo-2 cells was still significantly higher (*p=0.0238*). *CDH1* is a marker for adherent junctions in the intestinal epithelium and its expression in the organoids was statistically similar than in CaCo-2 (*p=0.5476*). These markers could suggest the differentiation of absorptive progenitors and the formation of the intestinal epithelium, though they do not yet indicate the development of a large population of fully differentiated enterocytes/colonocytes. The morphology observations from actin-phalloidin staining confirmed the presence of columnar cells, consistent with the presence of enterocytes/colonocytes. Furthermore, in conjunction with the data from markers of the secretory lineage, these results suggest a generalized bias towards the absorptive lineage within the organoids.

The expression of the mesenchymal marker *VIM* was significantly lower (*p=0.0238*) in the organoids compared to HDFs, though it was upregulated compared to the normalising gene. In addition to the detection of COL1A1, this indicated the presence of a mesenchymal component in the basolateral compartment of the organoid.
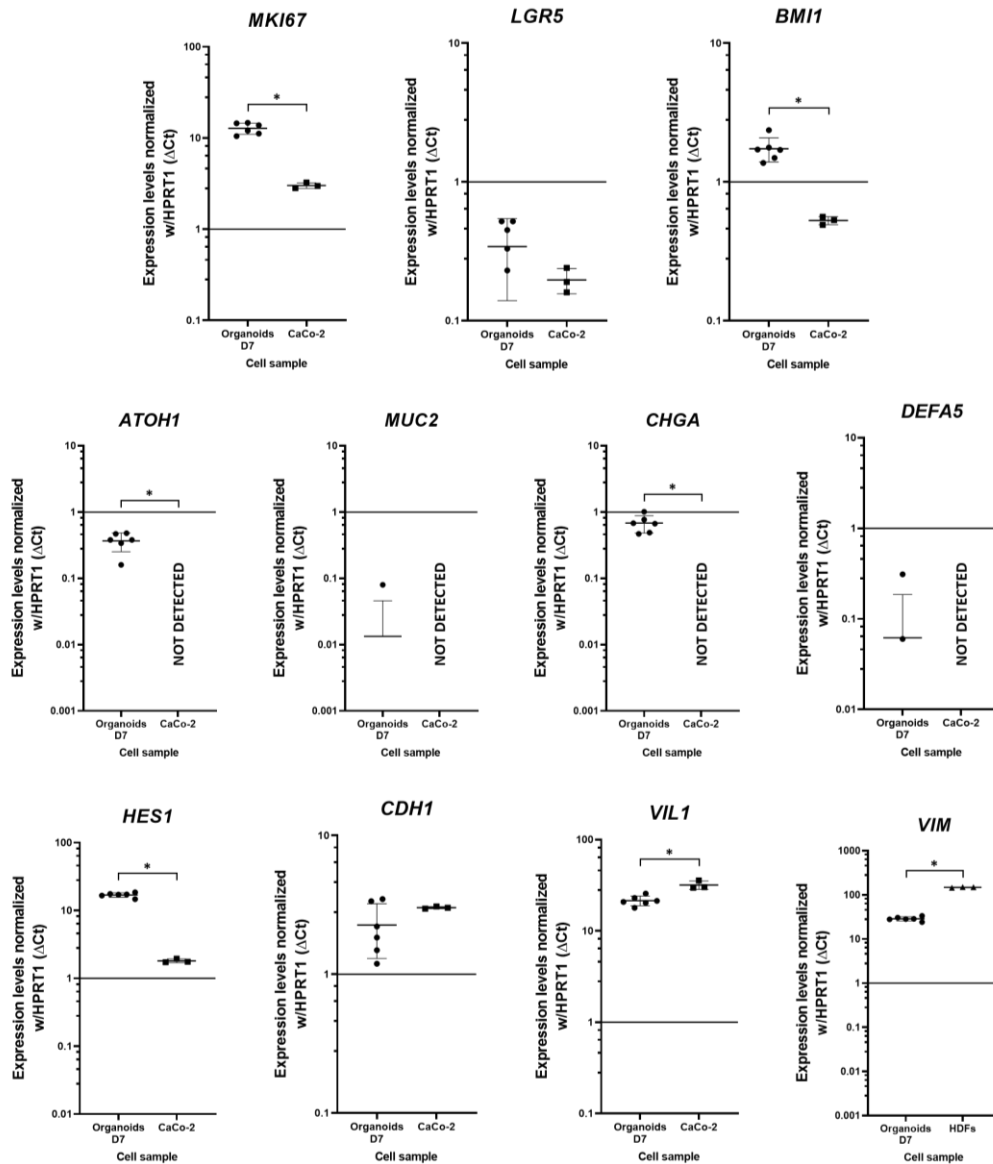
Figure 3.21 Characterization of iPSC-derived human intestinal organoids.
RT-qPCR analysis was used to identify the presence of different subpopulations in D7 organoids and control cells, CaCo-2 and HDFs. Markers were used for ISCs (*MKI67, LGR5, and BMI1*), TACs (*HES, ATOH1*), enterocytes/colonocytes (*CDH1, VIL1*), secretory lineage (*MUC2, CHGA, and DEFA5*) and mesenchyme (*VIM*). The results are presented as the fold change of ΔC$_t$ normalized against the housekeeping gene *HPRT1*. The proliferation marker *MKI67* (*p=0.0238*) and the ISC marker *BMI1* (*p=0.0238*) were found significantly upregulated in organoid samples compared to CaCo-2 cells; the expression of the ISC marker *LGR5* (*p=0.2381*) was also higher, though not significantly and below the expression level of the normalizing gene. The expression of markers for the secretory lineage, *ATOH1* (*p=0.0119*) and *CHGA* (*p=0.0238*), was significantly higher compared to CaCo-2 cells, although it was below the threshold of the *HPRT1*. The expression of *MUC2* (*p>0.9999*) and *DEFA5* (*p=0.5000*) was not consistently detected between replicates, and for all practical purposes it was not significantly different from CaCo-2 where their expression was null. From the two markers of the absorptive lineage, *HES1* (*p=0.0238*) was found significantly upregulated in organoids, whereas the expression of *VIL1* (*p=0.0238*) was significantly lower in these samples. Notably, no significant difference was detected in the expression of *CDH1* (*p=0.5476*), a marker of adherent junctions in the intestinal epithelium. Finally, the expression of the mesenchymal marker *VIM* (*p=0.0238*) was significantly lower in organoid samples compared to HDFs. Dot plots present the mean and standard deviation of 2 biological and 3 technical replicates (6 data points) from the organoid dataset, and 1 biological with 3 technical replicates (3 data points) for CaCo-2 and HDFs datasets. Statistical analysis was conducted using non-parametric Mann-Whitney test under a significance level of 95%, where: *p≤0.0500; **p<0.0100; ***p<0.0010; ****p<0.0001.

127

3.2.10 Generation of organoids-on-a-chip three-dimensional intestinal epithelium

Mimetas is a company dedicated to the development of novel models of organ-on-a-chip using their patented OrganoPlate technology. The basis of their technology was developed by Dr Paul Vulto, co-founder of Mimetas. This system relies on the fabrication of microfluidic chips where the cell culture microchannels are divided by 'phaseguides', which provide control over the fluid dynamics.

The foundation of our mutual collaboration stemmed from our interaction with the Dr Kai Erdmann, principal investigator at the Department of Biomedical Science, in The University of Sheffield. Dr Erdmann's group has focused on the development and optimization of a model of gut-on-a-chip. This led to a partnership with Mimetas, which included a doctoral project for Ms Elena Naumovska, an employee at Mimetas and PhD student at Dr Erdmann's lab. Part of her project included to explore the potential of generating a new model of gut-on-a chip derived from dissociated cells of intestinal organoids. Given our ongoing work in the development and optimization of a model of iPSC-derived HIOs, a proposal was made to collaborate and provide our input in the development of their model.

Their aim was to generate a new model of gut-on-a-chip derived from normal intestinal cells, i.e., organoid cells differentiated from normal iPSCs, as oppose to the existing models derived from adenocarcinoma cells, i.e., CaCo-2 cells. Our aim consisted of testing the robustness and versatility of our newly optimized differentiation protocol SRSF v.4 and capitalize of it by generating a new model of the intestinal epithelium.

Their original approach consisted of generating iPSC-derived HIOs, dissociate the cells, and seed them on an OrganoPlate chip. This raised significant concerns based on our understanding of the protocol: (i) time and cost for the production of the amount of organoids required to prepare an entire OrganoPlate; (ii) difficulties in the dissociation of the organoids due to the presence of the mesenchyme; (iii) cell survival yield following the dissociation of the organoids; and (iv) adhesion efficiency when seeded into the OrganoPlate chips.

Therefore, we recommended using our protocol SRSF v.4 for the direct differentiation of iPSC cells seeded on an OrganoPlate chip. This resulted in a new model of gut-on-a-chip (organoids-on-a-chip), consisting of three-dimensional tubular structures of intestinal epithelium defined by the expression of CDX2.

The OrganoPlate 3-lane chips used in our experiments were prepared as follows: the top channel was coated with vitronectin and seeded with miFF1 cells; the middle channel was coated with collagen I the day prior to the cell seeding; and the bottom channel was filled with growth medium (**Figure 3.22A**). On this configuration, the phaseguides caused the formation of a meniscus with the collagen

128

I ECM, allowing the cells to proliferate through the walls of the channel, thereby generating three-dimensional tubular structures (**Figure 3.22B**).

We monitored the progression of the differentiation protocol for the formation of CDX2$^+$ tubular structures. First, the selection of the coating matrix for the cell channel, and the ECM were based on previous experiments performed in collaboration with Mimetas. In these experiments we evaluated the optimal cell density and the affinity of different ECMs for the culture of iPSCs on OrganoPlates, built on these data and applied our differentiation protocol. The cell density was low following the cell seeding of miFF1 cells on D1, so we delayed DE induction one day. DE differentiation was started on D2 and by the end of D3 the surface of the microchannel was entirely covered with cells and we were unable to visualize the cobblestone-and-petal morphology. By the end of the mid- and hindgut differentiation the cultures appeared overconfluent (**Figure 3.22C**).

Further molecular characterization of the differentiation process confirmed the expression of SOX17 and FOXA2 after the DE stage (D3), and CDX2 at the end of the mid- and hindgut stage (D6). FITC-phalloidin staining of actin microfilaments showed that DE cells tended to overlap on each other while CDX2$^+$ cells appeared more organized and spread across the surface (**Figure 3.23**).

After generating a 3D reconstruction of our model, we confirmed the formation of a tubular structure of intestinal epithelium. Our observations indicate that the cells continued growing and spreading over the ECM until they reconnected on the top of the microchannel, leaving a hollow centre surrounded by CDX2$^+$ cells (highlighted in yellow) (**Figure 3.24**).
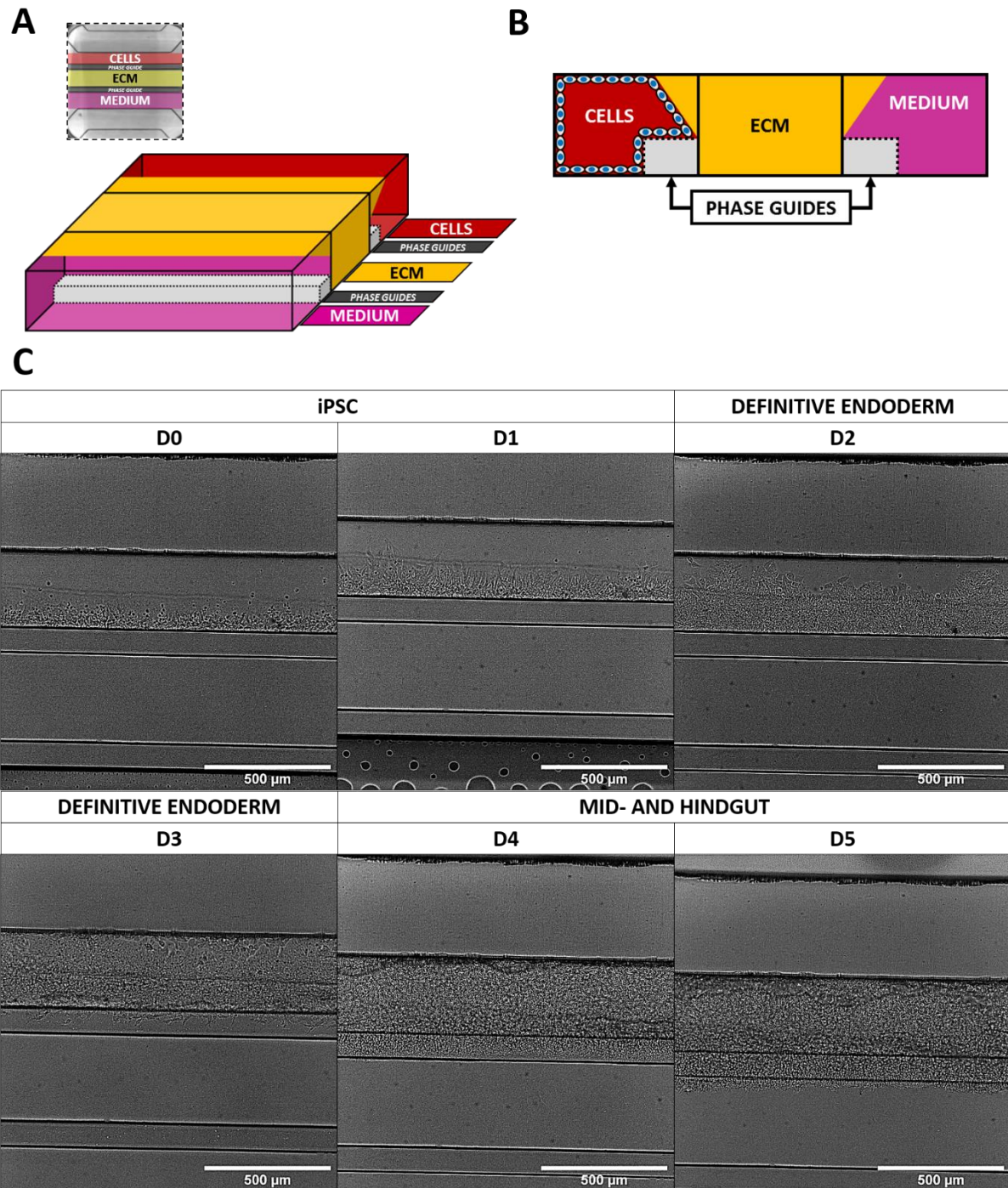
Figure 3.22 Differentiation of iPSC cells into HIOs using OrganoPlate 3-lane chips
(A) Diagram of the Mimetas OrganoPlate 3-lane chip layout. The observation window (central well) of the chips shows the cell channel (top), the extracellular matrix channel (middle), and the medium channel (bottom). The phaseguides between the channels are the key component of the OrganoPlate technology. (B) Schematic cross section of an OrganoPlate chip. The phaseguides between the channels allow for the formation of a meniscus of extracellular matrix supported by the phase guides and the upper portion of the channel. This enables the spreading of the cells around the channel, thereby facilitating the formation of tubular structures. (C) Bright-field images of miFF1 cells differentiated into intestinal epithelium on OrganoPlate chips using protocol SRSF v.4. Cells were seeded over vitronectin and supported with a collagen I ECM. These conditions allowed the attachment, survival, and proliferation of the cells. The time course images show the expansion of the cells over the OrganoPlate surface. By the end of the mid- and hindgut differentiation stage, the cells had fully covered the visible surface of the chip. On D6 the cells were fixed and immunostained for further characterization. Scale bars indicate 500 µm.
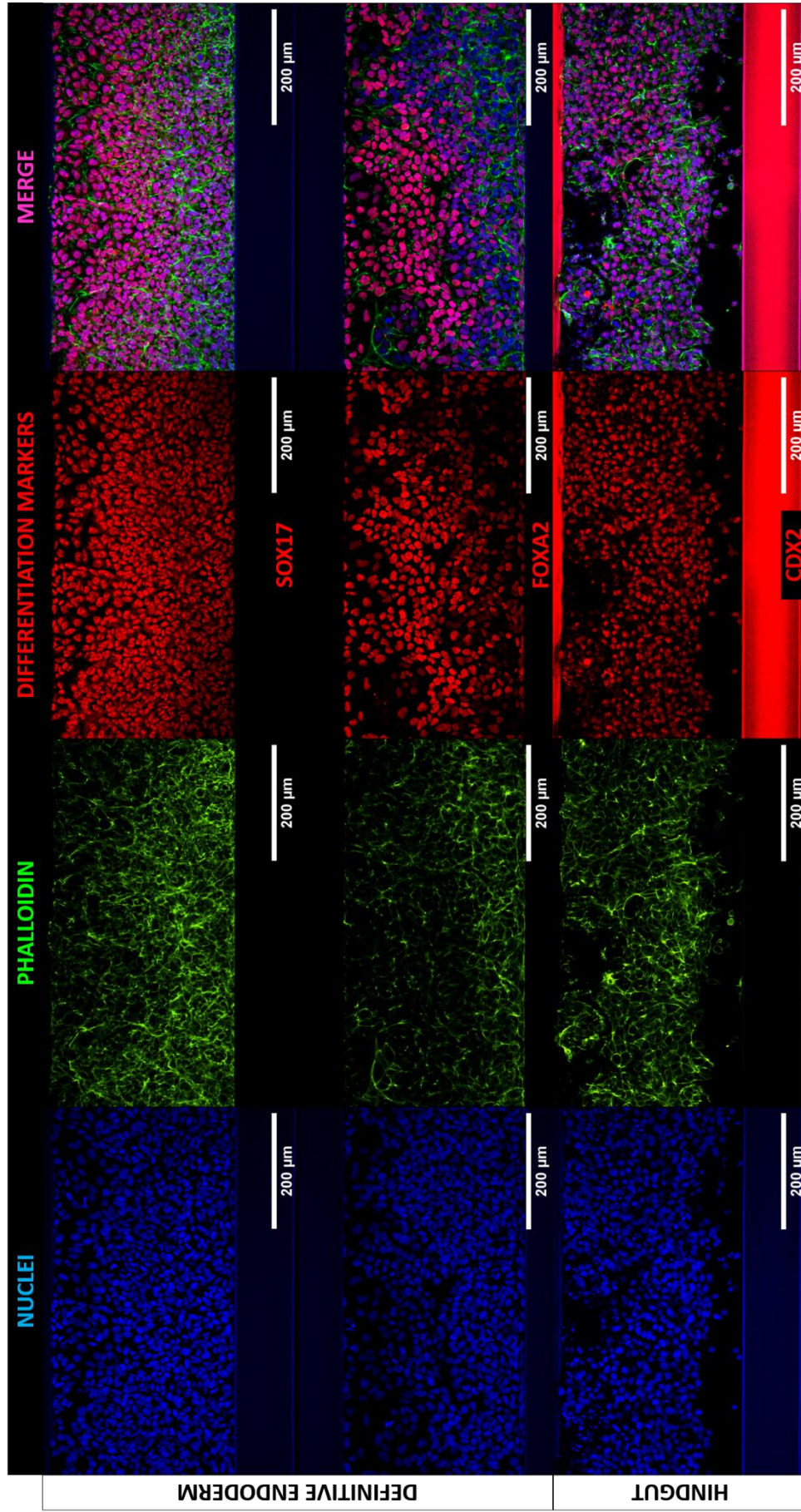
Figure 3.23 Expression of stage-specific differentiation markers on organ-on-a-chip-cultures. miFF1 cells were differentiated into intestinal epithelium following our optimized protocol SRSF v.4. Cell nuclei were stained with Hoechst 33342 (blue); the actin microfilaments from the cytoskeleton were stained with FITC-phalloidin (green); and the outcome of the differentiation process was monitored with stage-specific
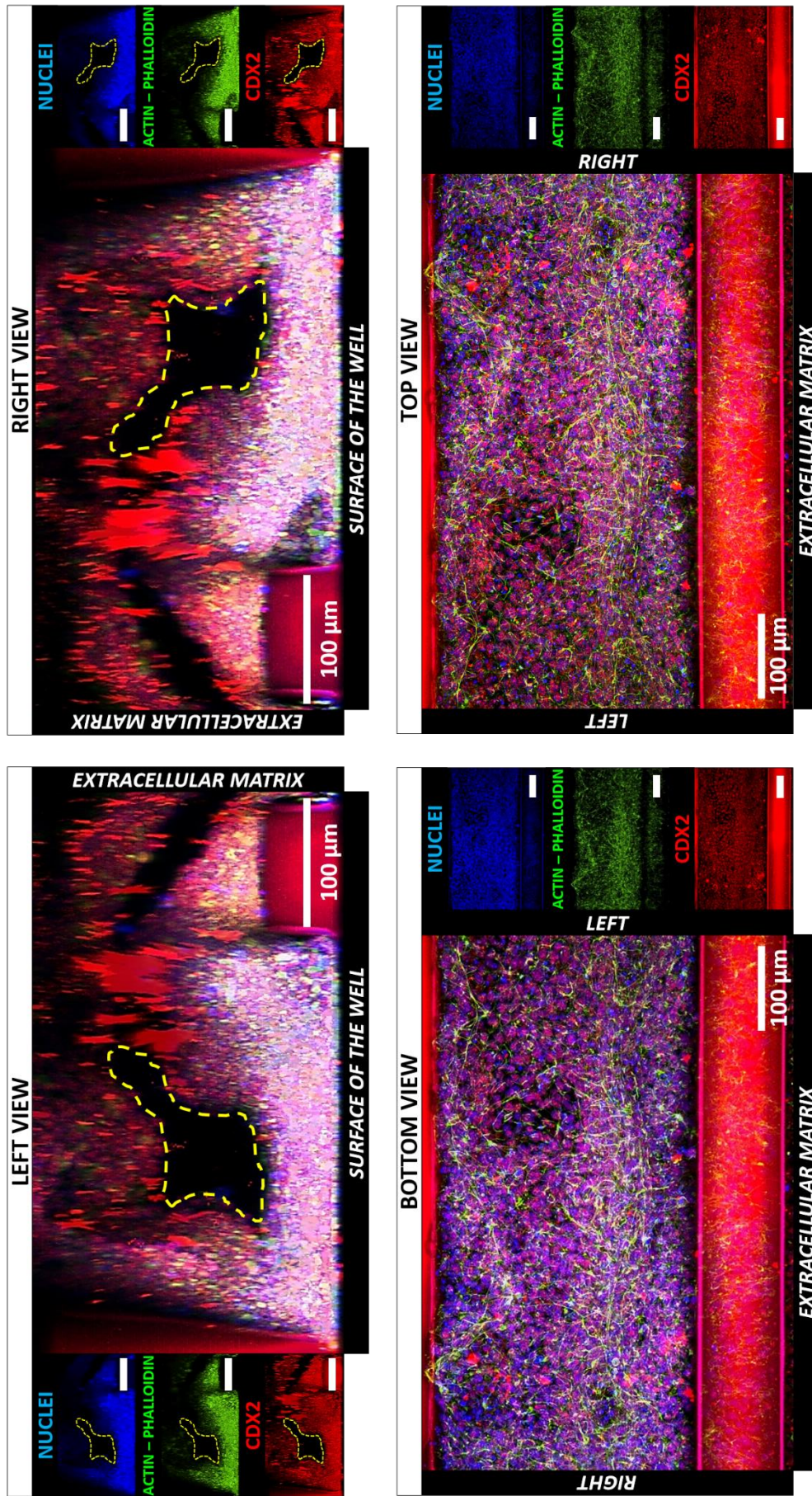
Figure 3.24 Three-dimensional reconstruction of CDX2+ cells cultures on OrganoPlate chips.

3D reconstruction of organ-on-a-chip cultures of iPSC-derived intestinal epithelium. miFF1 cells were differentiated using protocol SRSF v.4. After 6 days of differentiation, CDX2$^+$ intestinal cells (red) assembled in tubular structures (▮) along the channel of the OrganoPlate chip. The formation of a closed 3D tubular structure was confirmed

3.3 Discussion

We started this project looking to incorporate the model of intestinal organoids in a pipeline of HTS. This system will allow us to generate massive amounts of high-quality data with potential applications in drug discovery. However, the existing models are still on development and present significant constraints. Particularly, the cost and time required to generate HIOs make them incompatible with high-throughput experiments. Therefore, we have assessed different modifications to generate a cost-effective protocol with higher yields in organoid production.

The experimental work started with the validation of in-house-produced recombinant proteins and the cell line to be used for the generation of the HIOs. We then continued with the establishment of the differentiation protocol proposed by McCracken *et al.* (2011), followed by the assessment of modifications to optimize the organoid output and finally, the application of the optimized differentiation conditions into the generation of a novel model of the intestinal epithelium. At this point, it is important to highlight that the experimental work had important caveats which could not be addressed during the development of the project; particularly due to lack of technical expertise, limited time and funding, and the necessity to continue with other objectives from the entire project.

The imperative need for R-spondin 1 in the long-term expansion of intestinal organoids (Clevers, 2016), in addition to the high cost of replenishing the medium supplemented with it, constituted a significant constraint for the sustainable application of organoids technology in high-throughput studies (Nam *et al.*, 2018). This issue was identified by other groups leading to the generation of a transgenic cell line for the production of recombinant R-spondin 1 in-house (Ootani *et al.*, 2009). We have acquired this cell line and implemented their production protocols to integrate their technology into our differentiation system (SRSF v.2). We attempted to assess and quantify the WNT enhancing activity of rmRspo1 using Super-DsRed.T4, a modified fluorescence-based version of the SuperTopFlash luciferase reporter. However, we could not obtain a robust expression of the reporter upon transfection into CaCo-2 cells. The lack of functional validation and quantification of our in-house rmRspo-1, using TopFlash luciferase assay, is an important shortcoming of this work which remained unresolved. Future work will validate our in-house rmRSPO1 following the recommendations from the manufacturer, using SuperTopFlash luciferase, as oppose to the modified fluorescent versions, and HEK293 cells instead of CaCo-2.

The first modification to the protocol consisted in the use of miFF1 iPS cells, as the source material for the generation of intestinal organoids. This cell line was developed in-house by the Centre for Stem Cell Biology, from human foreskin fibroblasts of a healthy individual. The cells were originally

reprogrammed through transient expression of mRNA encoding the transcription factors OCT4, SOX2, KLF4, CMYC and LIN28. (Lim *et al.*, 2013; Desmarais *et al.*, 2016).

The multilineage differentiation potential of iPSCs has been characterized using a variety of cell surface markers linked to the pluripotent status and the early stages of transition into a differentiated state. The SSEA and TRA antibody series have been extensively used for the characterization of PSCs (Andrews *et al.*, 1984; Thomson *et al.*, 1998; Wright *et al.*, 2011). In our characterization, we focused on the expression of the stage-specific embryonic antigens-1 and -3 (SSEA1 and SSEA3). SSEA1 monoclonal antibodies were derived through immunization with F9 teratocarcinoma cells. These antibodies recognized an embryonic stage-specific antigen found in preimplantation mouse embryos, leading to the understanding that SSEA1 can identify PSCs (Solter & Knowles, 1978). However, later works found that in humans SSEA1 was expressed in differentiated derivatives of embryonal carcinoma cells and hESC (Bronson *et al.*, 1980; Andrews *et al.*, 1980). SSEA3 monoclonal antibodies were first developed through immunization with 4- to 8-cell-stage mouse embryos. As opposed to SSEA1, SSEA3 antibodies bound to human teratocarcinoma stem cells but did not recognize their murine counterparts (Shevinsky *et al.*, 1982).

In our study, immunostaining of miFF1 cells showed positive expression of SSEA3 and absence of SSEA1, indicating these cells remain pluripotent. This outcome is consistent with previous characterization studies in which hES cell lines identified a similar expression pattern in pluripotent cells (Thomson *et al.*, 1998; Henderson *et al.*, 2002; Enver *et al.*, 2005). Furthermore, the first studies addressing the expression dynamics of SSEA1 and 3, proposed that undifferentiated human embryonic carcinoma cells are SSEA1$^-$/SSEA3$^+$, as differentiation progresses the expression patterns changes into SSEA1$^+$/SSEA3$^+$, and finally differentiated cell are SSEA1$^+$/SSEA3$^-$ (Andrews *et al.*, 1982).

Nevertheless, the following experiments for the generation of definitive endoderm failed to replicate the results described by McCracken *et al.* (2011). A possible explanation for this could the use miFF1-iPSCs, whereas the original protocol used H9 hESCs. The H9 cell line was one of the first hES cell lines to be generated, and has been extensively used in differentiation protocols for a broad spectrum of applications (McCracken *et al.*, 2014; Miller *et al.*, 2019; Boisvert *et al.*, 2020). In contrast, iPSCs such as miFF1, have been reported to potentially carry a differentiation bias towards the identity of the source cell type. Also, previous works have reported an incomplete remodelling of the epigenetic landscape after reprogramming, thereby affecting the differentiation potential of the cells and their response to differentiation factors (Kim *et al.*, 2010; Polo *et al.*, 2010; Papp & Plath, 2011).

In consequence, we modified the culture conditions for the differentiation of the definitive endoderm, discarding the use of dFBS at this stage and incorporating WNT stimulation with CHIR99021. Our modified protocol SRSF v.1 produced definitive endoderm cells expressing SOX17 (RT-qPCR) and FOXA2 (RT-qPCR and Immunofluorescence). These results are consistent with the outcome obtained in the original protocol (McCracken *et al.*, 2011). Further characterization of the DE also found expression of *LGR5*. This is normally found in ISCs, although LGR5 and 4 have also been found in DE (Tsai *et al.*, 2016).

Regarding the RT-qPCR analysis, it is necessary to mention that an important caveat of this work was the selection of a reference cell line to compare the outcome of the differentiation protocol. In our experimental design we intended to focus the analysis of RT-qPCR readouts on a comparison against the terminal stage desired; hence the selection of *bona fide* intestinal (CaCo-2) and mesenchymal (HDFs) cell. After analysing the results, we acknowledge using the parental iPS cell line miFF1 could have provided a better insight into the activation of stage-specific genes in response to the differentiation treatment. In their present state, the results of the RT-qPCR analysis can merely provide an idea of how dissimilar the gene expression profile of differentiated samples is compared to representative cell lines of these lineages. Though, representing the progression of the differentiation program in comparison to the undifferentiated stage would have been more relevant.

Aside from this, another substantial weakness in the development and validation of our protocol was the lack of sufficient biological replicates to perform a solid statistical comparison to confirm our observations from the gene expression analysis. The reason was the high cost required to start, maintain, and differentiate enough cultures for the validation of every stage of the differentiation process using a relatively broad array of genes. Moreover, the characterization of the differentiation stages was still confined to some key specific markers. In this work, we could not cover a larger gene set due to limitations in the amount of template RNA required, the availability of RT-qPCR reagents, the number of replicates needed, and our capacity to process a large number of samples. Overall, to the best of our efforts we have sought to report representative data that properly demonstrates the progression of the differentiation protocol. Nevertheless, a future work is expected to replicate the results with an adequate number of replicates and expand the characterization to include functional markers such as the expression of enzymes, transporters, and other transcription factors.

The results from the statistical analysis were not subjected to a multiple test correction (MTC). We acknowledge that the familywise error rates were not taken into consideration, and therefore were not controlled. This could be considered as a limitation of the study, however there is no consensus across the literature about the usefulness and applicability of MTCs (Cabin & Mitchell, 2000).

Particularly, MTCs have been criticized for disregarding the nature of the hypothesis and rather hyper focusing on the probability that an error in the analysis will occur. Furthermore, if the results from an experiment are analyzed in a setting where multiple statistical tests are required, an MTC will increasingly reduce the α value, i.e., the threshold of significance for rejecting the null hypothesis. This will reduce the likelihood of small, yet significant, changes being detected. Therefore, by focusing on avoiding false positives, MTCs have been reported to incur in a bias which can result in an increase in false negative results (Perneger, 1998; Nakagawa, 2004; White *et al.*, 2019). In addition to this, given the small sample size from the results of our study, an MTC carries the risk of inflating the familywise error rate and discarding small significant changes as false negative. Thus, as mentioned before the results from this study, still require further validation with a larger number of replicates.

Mid- and hindgut cultures showed a persistent expression of the pluripotency marker *OCT4* and the DE marker *SOX17*; this could be indicative of the presence of subpopulations which resisted the differentiation treatment and may compromise the efficiency of the production of OFUs. Still, immunofluorescence results confirmed the expression of CDX2 in high confluency foci within the culture, and RT-qPCR analysis detected the expression of *HES1, VIL1* and *CDH1.* The expression of CDX2 is a hallmark of the intestinal lineage (Gao *et al.*, 2009). CDH1, is a major component of adherent junctions and it is essential for intestinal homeostasis and maturation of epithelial cells (Schneider *et al.*, 2010; Bondow *et al.*, 2012). Finally, the presence of *HES1* and *VIL1* suggested the cells were committing toward the absorptive lineage (VanDussen *et al.*, 2012). Additionally, the expression of *VIM*, has been used to establish the presence of mesenchymal cells in iPSC-derived HIOs (Finkbeiner *et al.*, 2015*b*). We obtained a relatively high number of putative OFUS (>200 per well), however considering that not all of these structures could develop into an organoid, in a high-throughput setting this yield was insufficient.

Consequently, we assessed modifications into the ECM and the composition of the DE differentiation medium to improve the differentiation efficiency and the production of OFUs. Several studies have highlighted the importance of the ECM composition not only in maintaining the pluripotent state of stem cells, but also in the efficiency of the differentiation protocols (Gattazzo *et al.*, 2014; Ahmed & Ffrench-Constant, 2016). In spite of this, the composition of the ECM has often been neglected. Therefore, to optimize the output of our differentiation protocol, we evaluated different ECM proteins in order to find a stage-specific ECM with a coverage broad enough to support the attachment, survival and differentiation of PSC, DE, and mid- and hindgut alike (SRSF v.3).

The protocol from McCracken *et al*. (2011) used hESC-qualified Matrigel since it has shown to be a good matrix for the culture of PSCs without affecting their pluripotency. Matrigel is mostly comprised

by laminin-111, and PSCs express integrins α6β1 and α7X2β1, which mediate the binding to laminin-111, making it an ideal candidate to support their growth and proliferation. However, the receptor turnover after induction of DE differentiation provokes the downregulation of *ITGA6* and *ITGA7X2*, resulting in poor attachment of hPSC-derived DE cells to laminin-111 and Matrigel (Brafman *et al.*, 2013; Cameron *et al.*, 2015; Kanninen *et al.*, 2016). Furthermore, since Matrigel is a relatively expensive, undefined matrix derived from dissociated animal tissue with high batch-to batch variability, its use in the production of organoids may hinder their application in high-throughput studies (Takahashi *et al.*, 2018).

In contrast, previous studies have reported laminin-521 can efficiently support the growth of PSCs without compromising their pluripotency (Rodin *et al.*, 2014; Albalushi *et al.*, 2018). hPSC-derived DE cells mostly express integrins α3β1, α6β4, and α7X1β1 which have shown a clear binding specificity to laminin-511 and laminin-521(Cameron *et al.*, 2015; Kanninen *et al.*, 2016). Furthermore, it has been extensively reported that LAM α5 (511 and 521) are the most influential in the architecture of the intestinal mucosa (Mahoney *et al.*, 2008). Therefore, we initially substituted the use of Matrigel for laminin-521 in the culture of iPSCs for the production of HIOs.

Additionally, previous studies have also found that hESCs and hESC-derived DE express integrin αVβ5 which mediates the binding to vitronectin (Braam *et al.*, 2008; Wong *et al.*, 2010; Laperle *et al.*, 2015). Thus, we also assessed the capacity of vitronectin to support the differentiation of iPSCs into a mid- and hindgut identity.

Our results suggest that LAM, VTN and the combination of L/V support the survival and proliferation of iPSCs, though not all of them allowed the generation of mid- and hindgut spheroids. L/V had a low production of OFUs (<100 per well), and even though VTN produced a high number of OFUs (>200), these structures were unable to develop into organoids. Based on the output of putative OFUs, it appeared the best differentiation conditions was LAM. Also, these results suggest that confluency might be a driving force for the transition from definitive endoderm into mid- and hindgut. The effect of high cell confluency has been associated with the inactivation of Hippo-YAP/TAZ and integrin-mediated signalling, which in consequence might increase cell differentiation but also apoptosis (Totaro *et al.*, 2017).

Parallel to these studies, we also tested the effect of BMP4 in the differentiation protocol (SRSF v.3). Previous studies have shown that the combination of BMP4 with AA increased the yield of DE induction by up to 20% (Teo *et al.*, 2012, 2014). However, in our study we did not detect a significant difference in the production of OFUs between samples treated with and without BMP4. Furthermore,

in samples grown over VTN, the addition of BMP4 led to the detachment of the entire colony. A possible explanation of why BMP4 did not provide an improvement in the overall differentiation protocol might be because the experiments where BMP4 has been used, aimed to increase the percentage of DE cells, in order to achieve a homogeneous culture of DE. However, our protocol relies on this inefficiency to generate completely homogeneous culture of DE; instead, a heterogeneous mix of DE and mesodermal cells might play a role in the formation of heterogeneous spheroids and organoids with an epithelial and mesenchymal compartment.

The combination of L/V, as well as the addition of BMP4 did not improve the outcome of the differentiation protocol and resulted in low production of OFUs (<100 per well). Only the combination of LAM+BMP4 produced mid-levels of OFUs (<200 per well), with similar morphological features as observed with LAM alone. This might be explained because the aforementioned studies merely evaluated the expression of differentiation markers, but none were interested in the formation of mid- and hindgut spheroids. These matrixes were capable of supporting the differentiation of iPSCs into mid- and hindgut, confirmed by the expression of FOXA2 and CDX2; however, this does not necessarily mean it could be implemented in the production of mid- and hindgut spheroids, and the generation of HIOs.

Finally, we implemented a small-molecule-driven differentiation of the DE, based on an initial boost on WNT activation using high concentrations of CHIR99021 (SRSF v.4). Originally, these conditions were intended for the production of hepatocytes, therefore there is no precedent of their capacity to support differentiation of the intestinal lineage. The resulting cultures exhibit a typical cobblestone-and-petal morphology which was reported as an indicator of DE induction under these conditions (Siller *et al.*, 2015). Following mid- and hindgut differentiation, the semi quantitative assessment of the production of putative OFUs was comparatively similar to the one reported by SRSF v.1 (laminin-521 ECM, and DE induction with AA), and higher than with SRSF v.3 (laminin-521 ECM, and DE induction with AA+BMP4). As an additional advantage, SRSF v.4 rescinded the use of AA and shortened the time for DE induction to two days.

A significant shortcoming of all these protocols was the selection and quantification of OFUs from the supernatant of differentiated mid- and hindgut cultures. Due to the high variability in the behaviour and development of the putative OFUs we encountered considerable technical limitations to identify which structures could actually develop into functional full-size organoids. Also, because of this variability, the quantification of OFU could not be standardized and still requires of technical expertise to distinguish putative OFUs from cellular debris. Therefore, we were unable to obtain an accurate readout of the efficiency of organoid production and could only provide a semiquantitative

assessment and comparison between the initial amount of putative OFUs harvested and embedded into Matrigel, and the estimated number of OFUs that actually survived and developed into full sized organoids. We speculate this could be related to an incomplete or inefficient differentiation in the DE or mid- and hindgut stages, which in turn supports the need for additional optimization of the differentiation conditions.

OFUs harvested from cultures differentiated with protocol SRSF v.1. were embedded into Matrigel to enter the final stage of organoid differentiation. Interestingly, we found that between days 16 and 19 of culture and once the cyst-like organoids had reached an approximate size of 350 µm, these could be transferred into agarose-coated wells to continue with the culture of the organoids in suspension. This greatly reduced the volume of medium and in consequence the cost required to maintain the cultures. Additionally, removing the organoids from the Matrigel beads facilitated their manipulation as individual structures, and allowed direct access to them for applications that required the physical interaction of the organoids with other cellular systems (e.g., immune, vascular, or nervous system). This is a significant contribution since, to the extent of our knowledge, the culture of organoids in suspension had not been done in any previous publication using human intestinal organoids or enteroids. However, just recently parallel to the development of this project, a new study reported the use of Happy Cell Advanced Suspension Medium to grow iPSC-derived organoids without a Matrigel matrix (Takahashi *et al.*, 2018).

Immunofluorescence results of D42 HIOS showed nuclear expression of the intestinal marker CDX2, indicating the formation of an intestinal epithelium. Also, it was found that COL1A1 partially colocalized with some of the CDX2$^+$ nuclei, this is consistent with a previous report describing the colocalization of ECM components with non-polarized CDX2$^+$ mesenchymal cells (Spence *et al.*, 2011). Overall, this evidence indicated the formation of a hollow spherical structure comprised of an inner layer of putative intestinal epithelium expressing CDX2, and an outer layer of mesenchymal components such as COL1A1, suggesting the presence of a mesenchymal population.

Gene expression analysis of D7 organoids generated with our protocol SRSF v.1, was consistent with the organoids developed by Wells' group. The gene expression profile identified an upregulation of the proliferation marker *MKI67*, though it appeared unlikely this was linked to the ISC population due to the low expression of the ISC markers *LGR5* and *BMI*. *HES1*, *VIL1*, *CDH1,* and *VIM* were also found upregulated in the organoids, though not at the same level as the reference cell lines. From the secretory lineage only *ATOH1* and *CHGA* were found expressed at low levels, whereas *MUC2* and *DEFA5* were not detected.

Overall, the evidence suggests the presence of a mesenchymal component (*VIM*) and the formation of an intestinal epithelium (*HES1*, *VIL1* and *CDH1*) within the organoids. It also indicated the presence of a proliferative population (*MKI67*), not necessarily of stem cells (*LGR5* and *BMI*) but perhaps progenitor cells. More importantly there appeared to be a differentiation bias towards the absorptive lineage (*HES1* and *VIL1*) and lack of a representative population of the secretory lineage (*ATOH1 CHGA MUC2*, and *DEFA5*). These observations are consistent with the result from the model developed by Wells' group, specifically, regarding the absent expression of genes from the secretory lineage. Also, their study found that the transcriptomic profile of iPSC-derived HIOs resemble a foetal phenotype, and require further manipulation to induce the maturation into adult intestinal organoids (Finkbeiner *et al.*, 2015*b*). This is a significant limitation of our model of HIOs and more research is needed to identify drugs, compounds, or growth factors which could regulate the differentiation bias in the cell populations within the organoids. Studies have explored the use of valproic acid and DAPT to promote the expansion of the ISC population and the secretory lineage, respectively (VanDussen *et al.*, 2012; Yin *et al.*, 2014; Chen *et al.*, 2017); alternatively, other works have used exogenous expression of *NEUROG3* to induce the differentiation of enteroendocrine cells (Sinagoga *et al.*, 2018).

Moreover, as mentioned before, we used a similar characterization strategy as the one used by the authors of the original protocol (Finkbeiner *et al.*, 2015*a*, 2015*b*). Particularly for the analysis of the gene expression profile of the intestinal organoids, we searched for the expression of *DEFA5*, a marker to detect the presence of Paneth cells. This may appear counterintuitive since the OFUs/spheroids emerged from the patterning of the posterior gut which in several works, including the original protocol, is referred as the "hindgut differentiation stage" (Spence *et al.*, 2011; McCracken *et al.*, 2011; Finkbeiner *et al.*, 2015*b*; Múnera & Wells, 2017; Jose *et al.*, 2020; Holloway *et al.*, 2020). These studies have searched for the expression of *DEFA5* and the presence of Paneth cells even though the hindgut i.e., the large intestine, does not give rise to this cell type. Furthermore, a study referred to the "patterning of duodenal identity" in hindgut spheroids, which by itself does not make sense (Holloway *et al.*, 2020). Therefore, we speculate there has been a continuous mistake in the nomenclature of the differentiation stages. Even though the term "hindgut differentiation" was indeed used in the original protocol, it was also referred to as "mid- and hindgut differentiation". In this instance, it would be justified to the search for Paneth cells in HIOs derived from midgut spheroids. This issue has been ignored so far and could lead to a misinterpretation of the lineage identity of the resulting organoids.

Another issue with organoid models is the lack of complex multisystemic interactions. Even though this model incorporates the crosstalk between the intestinal epithelium and the surrounding mesenchymal population, it still lacks the interaction with the microbiome, the immune and nervous

system, and the vascularization. Recent studies have reported some success in the integration of these systems into the model of iPSC-derived HIOs, though this have been mostly proof-of-principle studies and their functional application is still a work in progress (Workman *et al.*, 2017; Min *et al.*, 2020; Jose *et al.*, 2020; Holloway *et al.*, 2020).

In spite of the modifications introduced into the protocol, it is still considerably expensive to generate a sufficient number of organoids for high-throughput applications. These restrictions have been noticed in the literature, hence the use of organoids has only been indicated for low and medium throughput studies (Zanoni *et al.*, 2020; Fong *et al.*, 2020). Until now, even with our optimized protocol, the use of iPSC-derived HIOs for high-throughput assays is considerably expensive. This model could better be fitted into the validation of smaller datasets obtained from high-throughput experiments conducted in more economic models such as intestinal cell lines. Alternatively, Clevers' model is more time and cost effective since it starts directly with the intestinal growth stage, thereby requiring of less growth factors for the generation of organoids (Sato *et al.*, 2009, 2011*b*). Their protocol has been applied to the generation of patient-derived organoids in a relatively large scale, for the generation of biobanks of colorectal cancer patients (Van De Wetering *et al.*, 2015). Therefore, this model could provide a solution to a certain extent. However, the need for biopsy samples to isolate the intestinal crypts is an important limitation. Additionally, Clevers' model does not develop mesenchymal cells, and so it cannot be used to assess their interaction with the ISC niche and the intestinal epithelium.

Another limitation that hinders the application of this model in high-throughput studies is the lack of automation. The steps required for the selection of OFUs and the handling of organoid cultures cannot be automated since it still relies on technical expertise to assess the quality of the OFUs and the developmental features of the organoids. Automation in the handling and experimental analysis of the organoids is a complex issue and a significant limitation of this model. During the development of this project a publication by Wells' group reported the development of an automated sorting system for the selection of 'pre organoids' based on the size and spheroidicity of the organoids. This system provided a significant yet modest improvement; alternatively, the use of molecular markers could benefit the selection process. Nevertheless, this technology is still in development and not yet widely accessible (Arora *et al.*, 2017). Emerging studies have proposed the use of artificial intelligence and machine learning algorithms to facilitate the identification, segmentation, and analysis of representative features in three-dimensional objects, such as the organoid. This could significantly enhance the processing speed of the samples, improve the accuracy in the identification of successful

OFUs, and facilitate the quantification of multiple morphological features and/or functional markers in the organoids (Fong *et al.*, 2020; Kim *et al.*, 2020).

Regardless of the aforementioned limitations, our model of HIOs derived from iPSCs is a robust system for modelling normal human intestinal epithelium and the effects from the interaction with the mesenchymal compartment. Considering our model of HIOs was derived from the one developed by Wells' group, some of the potential applications for our model, which have already been described for theirs, are: (i) to study the infection of viral (Finkbeiner *et al.*, 2012) and bacterial pathogens (Forbester *et al.*, 2015; Leslie *et al.*, 2015; Liu *et al.*, 2019*b*; Pradhan *et al.*, 2020); (ii) to emulate the intestinal fibrogenic response caused by inflammatory diseases (Rodansky *et al.*, 2015); (iii) to investigate and identify the molecular cues (physical and/or biochemical) that regulate intestinal organogenesis and the maturation of the foetal intestine (Poling *et al.*, 2018); and (iv) to assess the radio- and chemosensitivity of normal intestinal epithelium (Nowrouzi *et al.*, 2020).

However, we are particularly interested in the application of HIOs to: (i) identify the elements that control the homeostasis and regeneration of the ISC niche, particularly in response to radio- or chemotherapy; (ii) study the crosstalk with the mesenchymal compartment; (iii) investigate the regulation of differentiation events and commitment acquisition towards the different lineages in the intestinal epithelium; and (iv) explore the suitability of this model in the study of intestinal cancer, particularly the events associated with the malignant conversion of ISC into CSCs.

The potential of implementing the model of iPSC-derived HIOs in the study of intestinal cancer has been proposed in previous reports (Sinagoga & Wells, 2015). However, considering that these organoids might actually be derived from the midgut (small intestine), rather than the hindgut (large intestine and colon), it is unlikely this system can accurately recapitulate the progression of the malignancy. Nevertheless, we speculate this model can still be applied into the study of ISC biology, and malignant transformation of ISCs into CSCs in response to external stimuli and genetic mutations (Snippert *et al.*, 2014; Drost *et al.*, 2015).

Alternatively, during the development of this project, new protocols have been published which address specifically the generation of iPSC-derived colonic organoids simply through the addition of BMP2 in the final stage of HIOs differentiation (Múnera *et al.*, 2017). However, due to the advanced stage of our project, this model could not be explored. Future work can test whether incorporating BMP2 into out protocol SRSFv.4 would be sufficient for the differentiation into colonic organoids, thereby providing a better model for the study of CRC.

Apart from the organoid models, the development of new 3D culture modelling systems has gained interest and it has focused on the generation of heterotypic cultures to assess the interaction of cell lines from the same or different tissues. Also, 3D culture techniques have been employed to evaluate the role of extracellular matrix components and the compatibility with scaffolds of different biomaterials. As opposed to monolayer *in vitro* cultures, this approach allows the study of features regarding the cellular microenvironment such as organization, distribution, and cell-to-cell interaction in a 3D space (Chen *et al.*, 2015). Several studies have focused on generating models of gut-on-a-chip, of which two models stand out: Ingber's group, gut-on-a-chip microfluidics device, and the Mimetas OrganoPlate. In this study we have collaborated with Mimetas to generate a new model of gut-on-a-chip using OrganoPlate technology in combination with our newly optimized protocol SRSF v.4. This system applied *in situ* differentiation of miFF1 iPSCs seeded over OrganoPlates, into three dimensional tubular structures of CDX2$^+$ intestinal epithelium.

Previous studies have successfully generated 3D tubular structures of intestinal epithelium using CaCo-2 cells (Trietsch *et al.*, 2017). However, this is still a colorectal adenocarcinoma cell line and therefore some artefacts or limitations in behaviour may still be expected (Jesch *et al.*, 2009; Attene-Ramos *et al.*, 2010). In contrast, our approach employed iPS cells from a healthy donor, resulting in the generation of 3D tubular structures of normal intestinal epithelium, as evidenced by the characterization and 3D reconstruction of our model.

Furthermore, a recent study proposed the generation of Intestine-Chips by preparing, dissociating, sorting and replating cells derived from differentiated HIOs into micro engineered chips (Workman *et al.*, 2018). Our protocol proposed the implementation of *in situ* differentiation of iPS cells cultures in OrganoPlate chips; this constitutes a more efficient, cost-effective, and time-saving alternative. In addition to this, our differentiation protocol recapitulates the stages of gastrointestinal organogenesis. The formation of DE is characterized by the expression of SOX17 and FOXA2, and the patterning of the mid- and hindgut is indicated by the appearance of CDX2. In consequence, the resulting intestinal epithelium might be comprised by an heterotypic array of cell types (Wells & Spence, 2014; Finkbeiner *et al.*, 2015*b*). Though, this still requires further characterization of the system with a broader panel of molecular markers.

As opposed to the model established by Ingber (Kim *et al.*, 2012, 2016; Kim & Ingber, 2013), the OrganoPlates do not require the use of vacuum pumps and/or more elaborated microfluidics equipment: a simple plate rocker creates the necessary perfusion (van Duinen *et al.*, 2015). Also, the evidence presented in this study demonstrated that miFF1 cells are capable of attaching, surviving, proliferating, and differentiating over vitronectin-coated OrganoPlates without any major

inconveniences. Conversely, PDMS scaffolds such as the one from Ingber's model, have reported important constraints due to its affinity for absorbing hydrophobic compounds, which can intervene in cell adhesion, proliferation, and even cell signalling (Domansky *et al.*, 2013; Halldorsson *et al.*, 2015)

Finally, due to its simplicity the OrganoPlate system is commercially available in a plate format, allowing its implementation in HTS studies (Trietsch *et al.*, 2013; van Duinen *et al.*, 2015). Consequently, the combination of the OrganoPlate system with the use of iPSC cells, narrows the distance into achieving one of the goal of organ-on-a-chip technology: its implementation for high-throughput personalized medicine (van Duinen *et al.*, 2015; Marx *et al.*, 2016).

In summary, after attempting to reproduce the protocol described by McCracken *et al.* (2011) for the generation of HIOs, we conducted a series of modifications to the differentiation conditions to improve the output of the protocol. The original protocol preferred the use of Matrigel for the initial seeding of PSCs, since this is a richer matrix with a variety of ECM components which may favour the differentiation of the cells. Nevertheless, in this work we have shown that laminin-521, a defined xeno-free ECM, was sufficient to support the growth of miFF1-iPSCs without affecting their stemness or differentiation potential, and generate HIOs. Next, we modified the culture conditions for DE differentiation, discarding the use of Activin A and using a small-molecule driven protocol that reduced the differentiation time to two days. The use of WNT3A for the patterning of the posterior gut was substituted for an economic alternative, the small molecule CHIR99021. Also, the use of commercial RSPO1 was replaced by in-house-produced rmRspo1. Finally, during the intestinal differentiation stage, after an initial growth phase of approximately 16 days, the Matrigel support was removed and we successfully continued the growth of the organoids in suspension. This reduced the volume of medium needed for the maintenance of the organoids, resulting in a significant cost reduction. Consistent with previous reports, our model of HIOs was comprised by an inner layer of intestinal epithelium (CDX2$^+$) and an outer support layer of mesenchyme (COL1A1$^+$). The organoids contained mostly cells from the absorptive lineage and lacked a representative population of secretory cells. Overall, our modified protocol has accomplished a considerable reduction in the time and cost needed for the differentiation process, and provides a new alternative for the generation of iPSC-derived HIOs. Finally, after developing and testing our newly optimized protocol SRSF v.4, we applied it into the direct differentiation of iPSCs seeded over an OrganoPlate microfluidics chip. This resulted in the formation of three-dimensional tubular structures of intestinal epithelium characterized by the expression of CDX2. In conclusion, this chapter has described the successful development of a new optimized protocol for the generation of iPSC-derived HIOs and a novel model of gut-on-a-chip (organoid-on-a-chip).

4.1 Introduction

4.1.1 Discovery and development of LGR5 as a biomarker for normal and cancerous stem cells in the intestinal epithelium

LGR5, also known as G-protein-coupled receptor 49 (GPR49), is an orphan receptor member of the G-protein-coupled receptor (GPCR) family. LGR5 is a transmembrane protein, originally discovered in 1998 from samples of human placenta and later found in muscle, spinal cord and brain (Hsu *et al.*, 1998). The function of LGR5 has been postulated as an enhancer of WNT signal. Studies have found LGR5, R-spondin and RNF43/ZNRF3 are all involved in a negative feedback loop in charge of regulating the strength of WNT signals. In the absence of R-spondins, RNF43/ZNRF3 binds to the Frizzled receptor, triggering the recycling of the receptor and diminishing the intensity of the WNT signal received by the cell. However, independent studies have found that R-spondins associate with RNF43/ZNRF3 and LGR5, forming a heterotrimer LGR5/R-spondin/RNF43, which induces the membrane clearance of RNF43, therefore preventing it from recycling WNT ligand receptors (de Lau *et al.*, 2011, 2014; Hao *et al.*, 2012; Zebisch *et al.*, 2013).

In 2007, Clevers' group identified Lgr5 as a marker of the stem cell population in the small intestine and colon of mouse. The authors developed a transgenic mouse model expressing fluorescently labelled Lgr5. In this model, the expression of Lgr5 was confined to a small subpopulation of mitotically active columnar cells residing at the bottom of the intestinal crypts. Lineage-tracing experiments later confirmed this subpopulation differentiated into all the lineages from the intestinal epithelium (Barker et al., 2007). The model developed by Clevers' group cemented the importance of Lgr5 as the marker for the ISC population. Moreover, its role in the regulation of WNT signalling opened the possibility for further studies looking into its association with colorectal cancer, although it was necessary to first develop reliable detection tools to track the LGR5^{+} putative ISCs in human samples. This highlighted the need for the generation of antibodies against human LGR5; however, currently available commercial antibodies have not been able to provide a robust fluorescent readout in samples of normal intestinal epithelium (Rizk & Barker, 2012; Barker, 2014; Baker *et al.*, 2015).

Becker *et al.* described the detection of LGR5 expressed by putative intestinal stem cells located at the bottom of the crypts in samples of normal and adenomatous human small intestine and colon tissue. This study used a rabbit polyclonal anti human LGR5 antibody (MBL International Co., Cat. No. LS-A1235 and LS-A1232). Immunohistochemical (IHC) analysis of normal samples showed a rather faint signal of LGR5-labelled cells at the bottom of the crypts in the small intestine and colon. Conversely, premalignant samples showed a robust LGR5 staining on a significantly higher population

145

of cells, which were not confined to the crypts, but rather spread through the luminal epithelium. Interestingly, immunofluorescent images of LGR5 staining were only presented for samples of adenoma tissue, detection with fluorescent microscopy in normal samples was not presented (Becker et al., 2008).

Another study measured the expression of LGR5 in 11 colon cancer cell lines, using RT-qPCR. The results showed almost a 9-fold upregulation of LGR5 in CaCo-2 cells, compared to the average expression. In patient samples, LGR5 was found to be significantly upregulated in primary adenoma samples and at even higher levels on metastatic samples. A similar effect was observed in cell lines derived from primary tumours compared to those derived from metastatic sites. This highlights the relevance of LGR5 not only for the study of intestinal stem cell biology, but also as a prognostic marker for CRC (Uchida et al., 2010).

Further studies deepened into the potential correlation between the expression levels of LGR5, and the onset and progression of CRC. Fan *et al*. used IHC analysis to study the expression of LGR5 in colonic normal mucosa, adenomas, and carcinomas. Based on the clinicopathological assessment, the scarcity of immunopositive cells in the normal mucosa was deemed negative for LGR5 immunoreactivity. In contrast, adenoma and carcinoma samples showed a significant increase of LGR5-immunoreactive cells, mostly located in the cytoplasm. LGR5$^+$ cells, in adenoma and carcinoma samples, were not restricted to the crypt, but rather spread in patchy and diffuse patterns across the tissue sections. Finally, the overexpression of LGR5 was found to be correlated with that of β-catenin, supporting the link between LGR5, WNT signalling, and the onset of CRC (Fan *et al.*, 2010).

A study conducted by Ziskin et al, seek to identify a novel molecular signature defining the CSC population in CRC samples. Using IHC analysis and *in situ* hybridization (ISH), the authors analyzed 19 putative intestinal stem cell markers, such as LGR5, ASCL2, OLFM4, and BMI1. Interestingly, LGR5 was found in ~74% of the samples analyzed, while it has hypothesized the LGR5- samples may have originated from deficient mismatch repair or B-raf mutations. However, its lack of predictive capacity towards the aggressiveness of the tumours limited its candidacy as a novel marker for CSCs in large intestine (Ziskin *et al.*, 2013).

Later, Baker *et al*. performed a thorough analysis of the expression of LGR5 on CRC samples at different stages, with different histopathological characteristics and genetic mutations. Adenoma samples were divided in two classifications: (i) conventional adenomas, which represent 80-90% of cases, and arise from the sequential mutation of *APC*, *KRAS*, and *TP53*; and (ii) serrated lesions, representing 10-20% of cases, and characterized by mutations in BRAF and KRAS. Both showed a significant increase in LGR5

expression, but the cryptal architecture was disrupted in conventional adenomas, revealing a widespread expression of LGR5. Conversely, serrated lesion did not loss the organization of the crypts, and the expression of LGR was confined to this compartment (Baker et al., 2015).

A study by Ihemelandu *et al.* performed IHC analysis on patient CRC samples using monoclonal anti LGR5. Similar to other studies, LGR5 was found overexpressed in CRC samples, compared to non-cancerous tissue. Also, a comparison on the signal emitted by LGR5 in samples at different stages of CRC, exhibited a pattern of gradual increase, with a slight drop in samples of CRC stage IV. Their proposed explanation suggested that the expression of LGR5 increases during the clonal expansion phase, and in the late stages of tumour progression and metastasis, the LGR5 population may be exhausted. Finally, given the observed correlation between LGR5 and CRC progression, the regulation of LGR5 has been proposed as a potential target for immuno- and chemotherapy (Ihemelandu *et al.*, 2019).

To this date there have been two phase I clinical trials targeting LGR5 as a treatment against CRC. Both trials consisted of dose escalation studies to determine the maximum dose, safety, and pharmacokinetics. The first compound, BCN101 (Identifier number: NCT02726334), consisted of an anti LGR5 humanized monoclonal antibody aimed at patients with metastatic CRC who have not responded to 1-2 lines of chemotherapy; the study was terminated and no results were published (ClinicalTrials.gov, 2016). The second compound, MCLA-158 (Identifier number: NCT03526835), consists of an anti EGFRxLGR5 bispecific antibody aimed to patients with metastatic CRC and other non-colorectal solid tumours; this study is still ongoing and no results have been made public yet (ClinicalTrials.gov, 2018).

In summary, after identifying LGR5 as the marker for the ISC population, a branch of research has focused on its implications in the study of CSCs in CRC. Additionally, studies have found a significant increase in LGR5 expression during colorectal carcinogenesis, leading to the notion that it could be exploited in the detection of CSCs and as a prognostic marker against CRC. Finally, given its role in the regulation of WNT signalling and therefore in the survival and proliferation of cancerous cells, LGR5 has also been proposed as a potential therapeutic target.

The detection of human LGR5 protein in normal intestinal epithelium has been hindered by the low levels of expression displayed by this marker (van der Flier *et al.*, 2009*b*; Yamazaki *et al.*, 2015). Currently, the use of LGR5 as a biomarker for the human ISCs has been limited to IHC, ISH, and RT-qPCR (Becker *et al.*, 2008; Fan *et al.*, 2010; Uchida *et al.*, 2010; Takeda *et al.*, 2011; Ziskin *et al.*, 2013; Baker *et al.*, 2015; Ihemelandu *et al.*, 2019). These methods have provided valuable information on

the location and expression levels of LGR5^{+} ISCs and CSCs within tissue samples. However, the use of immunofluorescence may provide a greater detail on the subcellular localization of the protein, quantification of the expression levels based on fluorescence intensity, and automated image analysis without having to rely on the assessment of expert pathologists (Goding, 1996; Hofman, 2002; O'Hurley *et al.*, 2014; Kessler *et al.*, 2015; Xie *et al.*, 2017). The broadly used commercial rabbit polyclonal anti LGR5 antibody has been unable to present reliable immunofluorescent images of intestinal LGR5 in non-cancerous samples (Becker *et al.*, 2008; Fan *et al.*, 2010; Takeda *et al.*, 2011). Notably, newly developed monoclonal anti LGR5 antibodies have shown some success when tested against CRC tissue samples, and modified cell lines that overexpress the LGR5 receptor (Kemper *et al.*, 2012; Ihemelandu *et al.*, 2019). These have been promising outcomes, but its effectiveness in fluorescence microscopy applications remains to be tested.

4.1.2 Current models for the expression of endogenous LGR5 reporters

ISC biology research has continued using the mouse model reporter developed by Clevers' group. Furthermore, this system allowed the isolation of single Lgr5^{+} ISC, which was paramount in the development of the first model of intestinal organoids. With the emerge of organoid technology, the use of Lgr5 has broadened for its applications in monitoring the self-renewal, development, differentiation and death of ISCs within the organoids (Sato *et al.*, 2009, 2011*a*, 2011*b*; Snippert *et al.*, 2010). Following studies accepted Lgr5 as the *de facto* marker for the intestinal stem cell population and have continued working with organoids derived from the transgenic LGR5-GFP mouse model developed by Clevers' group. After this, there have been 3 studies that have claimed to successfully generate human LGR5-GFP reporter cell lines using different transgenesis approaches, such as: bacterial artificial chromosomes (Watson *et al.*, 2014), zinc-finger nucleases (ZFN) (Forster *et al.*, 2014), and CRISPR/Cas9 (Shimokawa *et al.*, 2017).

The first reporter cell line was developed by Wells' group using bacterial artificial chromosomes (BACs) to introduce an LGR5-GFP reporter into H9 PSCs, to track the ISC population within the organoids. Notably, even though this model is an outstanding tool for the study of ISCs, little information is provided regarding the validation of the reporter, and its co expression with endogenous LGR5 (Watson *et al.*, 2014). This model has been used to evaluate the expression of LGR5-GFP in intestinal and colonic organoids. Interestingly, fluorescence microscopy images of the organoids suggest the presence of a very high population of putative ISC expressing the reporter (Tsai *et al.*, 2016; Múnera *et al.*, 2017); however, previous reports have highlighted the low number of LGR5^{+} crypt cells in normal tissue samples (Becker *et al.*, 2008; Fan *et al.*, 2010). Albeit, other studies from Wells' group have

suggested the high number of LGR5$^+$ cells in the organoids might be an exclusive feature from the expression of a foetal phenotype (Finkbeiner *et al.*, 2015*b*).

The second model, developed by Clevers' group, used ZFN-mediated genome edition to introduce a GFP reporter at both ends (N- and C-terminus) of the endogenous LGR5 protein, in WIBR3 hESCs. Next, hESCs were differentiated using a teratoma assay, producing patches of partially developed tissue from all germinal layers. The presence of putative intestinal stem cells expressing the LGR-GFP$^+$ reporter was confirmed with IHC. It is important to highlight that the authors acknowledged the low fluorescent output obtained from this reporter, and therefore it does not seem suitable for fluorescent microscopy applications. LGR-GFP$^+$ cells were isolated using FACS, and then were used for the generation of HIOs. The model of teratoma-derived organoids obtained from isolating LGR-GFP$^+$ cells was developed as an attempt to circumvent the time and cost required to undergo the stepwise differentiation process necessary to produce organoids from PSCs. (Forster *et al.*, 2014).

The third cell line was developed by Sato's group using CRISPR/Cas9-mediated genome edition in colorectal cancer organoids (CCOs). The authors identified samples of patient colon tumours that exhibit an upregulation in the expression of LGR5. Next, they assembled a reporter cassette containing left and right homology arms, an IRES sequence followed by the GFP reporter, and an antibiotic resistance gene. The construct was inserted using CRISPR/Cas9, targeting the final exon of the LGR5 gene, between the stop codon and the 3'-UTR. Interestingly, the results presented in this study do not show the actual fluorescence of the reporter LGR5-GFP, but rather from immunostaining using anti GFP antibodies to enhance the signal. Moreover, this study also reported the generation of a rainbow reporter cell line using a similar transgenesis strategy. In this instance, Cre recombinase was inserted in the final exon of LGR5, similar to the GFP reporter, and a multi colour reporter was co transfected into the CCOs. Tamoxifen activation of Cre prompted the stochastic expression of different fluorescent reporters. This resulted in an indirect approach to enhance the 'signal' emitted by the reporters co expressed with endogenous LGR5, while still obtaining a fluorescent output (Shimokawa *et al.*, 2017).

Given the importance that the reporter mouse model has had over the years, it would have been expected that a successful reporter human model encountered a broader embrace from the field. However, as mentioned before, few works have referred to the actual use of either of these human reporter cell lines, which puts in doubt their efficacy. The need for a robust reporter system of the human ISC population stands, and so far, LGR5 still remains as the single most suitable candidate biomarker. Therefore, the aim of this work is to generate a cell line of iPSCs modified for the expression of an LGR5-GFP reporter. The prospective outcome is to generate HIOs where it is possible to track in real time the population of ISC (LGR5$^+$), allowing us to assess their response towards different stimuli.

4.2 Results

4.2.1 Evaluation of commercial monoclonal anti LGR5 antibodies on intestinal epithelial cells lines

Initially, the expression of LGR5 on miFF1 and CaCo-2 cells was assessed at the transcriptional level using RT-PCR. Total RNA of both cell lines was isolated and processed for cDNA synthesis using RT-PCR, followed by standard end point PCR amplification targeting LGR5 transcripts. No positive control was available at the time, however, in both cell lines an amplification band was detected within the expected size range (~76 bp) (**Figure 4.1**), according to *in silico* analysis (See Appendix section 2 and 3). This evidence confirms the expression of LGR5 by miFF1 and CaCo-2 cells, at least on the transcriptional level, through the detection of mRNA. Interestingly, the relative intensity of the band was dimmer on miFF1 samples and brighter in CaCo-2 cells, suggesting a higher expression level of LGR5 on CaCo-2 cells, or a higher number of LGR5$^+$ CaCo-2 cells compared to miFF1.
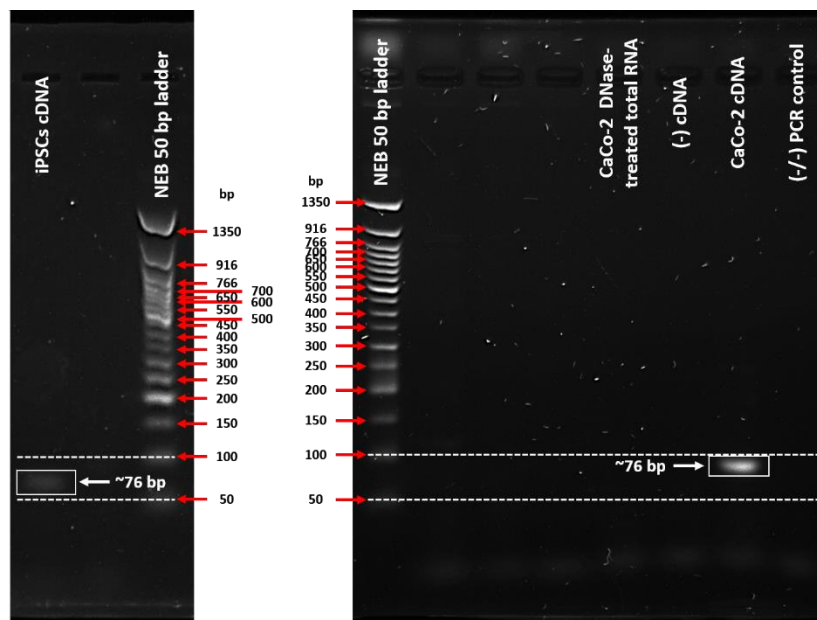
Figure 4.1 RT-PCR analysis to detect the expression of LGR5 on miFF1 and CaCo-2 cells.
The expression of the intestinal stem cell marker LGR5 in miFF1 and CaCo-2 cells was tested at the transcriptional level using RT-PCR to detect the presence of mRNA from LGR5. Intron-spanning primers were used on samples of miFF1 and CaCo-2 cells cDNA. RT-PCR produced amplification bands within the range of the expected size (~76 bp), in both cell lines. No positive control was included, however, *in silico* analysis confirmed the correct size of the amplicon. This evidence confirmed the expression of LGR5 on both cell lines, at least on the transcriptional level.

The functionality of a commercially available mouse monoclonal anti human LGR5 antibody (clone OTI2A2; Invitrogen Cat. No. MA5-25644) was tested using CaCo-2 and HT-29 cells. RT-qPCR analysis had already confirmed the expression of *LGR5* in CaCo-2 cells, and HT-29 cells are the positive control recommended by the supplier.

We tested different processing conditions to assess any potential improvement to the immunolabelling of LGR5: Standard and mild fixation with 3.7 and 1.85% formaldehyde (FA), respectively; and with and without permeabilization using 0.1% triton X-100. Also, we tested two different batches of LGR5 monoclonal antibody. LGR5 signal was compared against the pan-human cell surface marker Tra-1-85 (positive control), and the isotype/negative control.

Side-by-side comparison of CaCo-2 cells processed with and without permeabilization (**Figure 4.2**), and HT-29 cells with and without permeabilization (**Figure 4.3**), showed an evident difference in the RFI between the positive control and the samples; however, when compared against the isotype controls, the samples did not show a clear distinction in the RFI. The expression of Tra-1-85 was clearly defined in the borders of the cell; however, no clear structures or organelles appeared differentially stained by LGR5 between the samples and the negative control. Furthermore, there was no clear visual distinction between these sets of images.

The highlights from the RFI quantification of CaCo-2 samples (**Figure 4.4A**) are as follow: the samples processed using 1.85% FA and permeabilization showed a significant difference with the isotype control (Batch 1 vs isotype, *p=0.0024*; Batch 2 vs isotype, *p<0.0001*), but also between the two batches of antibodies (Batch 1 vs Batch 2, *p<0.0001*); 1.85% FA without permeabilization led to a significant difference between the two batches of LGR5 antibodies (Batch 1 vs Batch 2, *p<0.0001*); 3.7% FA and permeabilization showed a significant difference against the isotype control (*p<0.0001*, with both antibody batches), but no difference with the positive control (Batch 1 vs TRA-1-85, *p=0.7663*; Batch 2 vs TRA-1-85, *p>0.9999*); 3.7% FA and no permeabilization did not show a significant fluorescence signal (Batch 1 vs isotype, *p=0.7142*; Batch 2 vs isotype, *p=0.1172*).

The fluorescence quantification from HT-29 samples (**Figure 4.4B**) showed, in all the conditions, a significant difference between the positive controls and the samples (*p<0.0001*, with all processing conditions and both antibody batches), but no difference with the isotype control (1.85% FA and permeabilization: Batch 1 vs isotype, *p=0.4296* and Batch 2 vs isotype, *p=0.9961*; 1.85% FA and without permeabilization: Batch 1 vs isotype, *p=0.2187* and Batch 2 vs isotype, *p=0.4912*; 3.7% FA and permeabilization: Batch 1 vs isotype, *p=0.1008* and Batch 2 vs isotype, *p=0.0899*). Only samples processed using 3.7% FA without permeabilization showed this pattern and also a significant difference against the isotype control (*p<0.0001*, with both antibody batches).
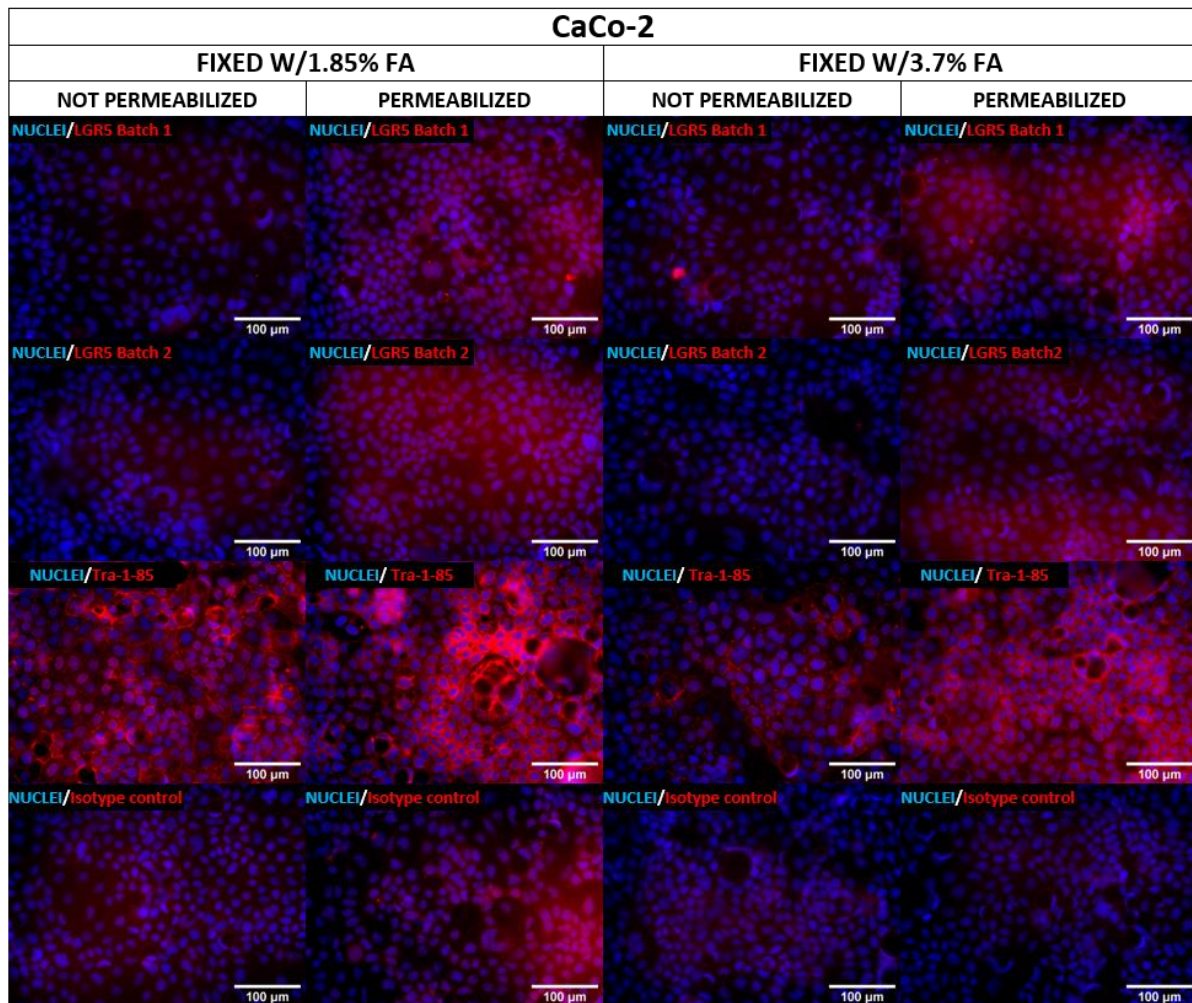
Figure 4.2 Evaluation of the binding capacity of commercial LGR5 monoclonal antibodies on CaCo-2 cells.
On samples of CaCo-2 cells labelled with either batch of LGR5 antibodies, without permeabilization treatment and fixed with either 1.85 or 3.7% formaldehyde, the relative fluorescence intensity (RFI) did not seem to exhibit an evident increase compared to the isotype control. The RFI emitted by permeabilized LGR5-labelled CaCo-2 samples, fixed with either method, did appear to rise above the background threshold defined by the isotype control. Furthermore, regardless of the fixation method or permeabilization treatment, the RFI of both batches of LGR5-labelled samples appeared lower in comparison to the Tra-1-85 control. Additionally, the fluorescence emitted by the Tra-1-85 antibody appeared defined and, as expected, localized to the contours of the cells, whereas the overall fluorescence shown by CaCo-2 cells labelled with LGR5 antibodies, appeared diffuse and scattered across the sample. CaCo-2 cells were fixed using mild (1.85%) and standard (3.7%) fixation with formaldehyde, with and without permeabilization with 0.1% triton X-100. Immunostaining was performed using two different batches of LGR5 monoclonal antibody. The pan-human cell surface marker Tra-1-85 was used as a positive control (red). Nuclei were stained with Hoechst 33342 (blue). White scale bars indicate 100 μm. Experiments were performed by duplicate, and nine different fields per replicate were imaged.
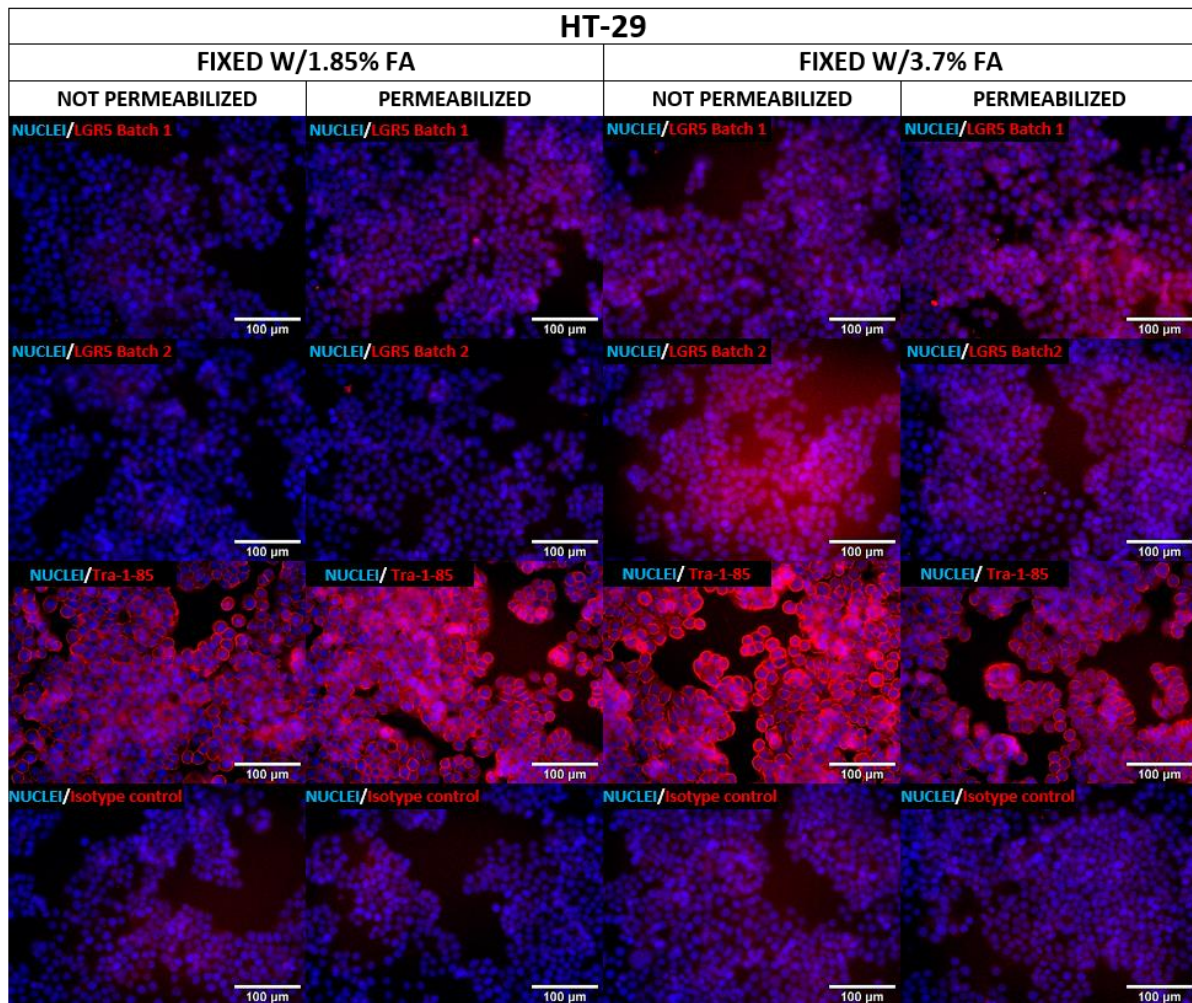
Figure 4.3 Evaluation of the binding capacity of commercial LGR5 monoclonal antibodies on HT-29 cells.
Overall immunostaining results from HT-29 cells appeared consistent between the different pre staining treatments. The relative fluorescence intensity (RFI) of LGR5-labelled HT-29 cells fixed with 1.85% of formaldehyde, did not seem higher than the isotype control, also the permeabilization treatment did not appear to exert any effect on the RFI. Similar results were seen on cells fixed with 3.7% formaldehyde and permeabilized. Notably, HT-29 cells treated with either batch of LGR5 antibody, fixed with 3.7% formaldehyde and without permeabilization, showed a higher RFI compared to the isotype control. Nevertheless, regardless of the pre staining treatments, the RFI shown with either batch of LGR5 antibody was evidently lower than that of samples labelled with the Tra-1-85 positive control. HT-29 cells were fixed using mild (1.85%) and standard (3.7%) fixation with formaldehyde, with and without permeabilization, with 0.1% triton X-100. Immunostaining was performed using two different batches of LGR5 monoclonal antibody. The pan-human cell surface marker Tra-1-85 was used as a positive control (red). Nuclei were stained with Hoechst 33342 (blue). White scale bars indicate 100 µm. Experiments were performed by duplicate, and nine different fields per replicate were imaged.
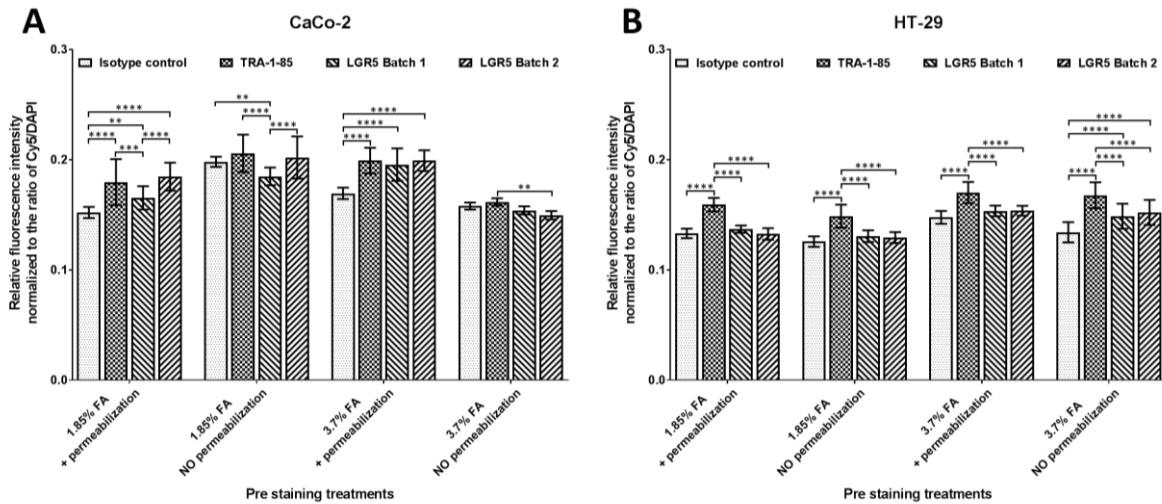
Figure 4.4 Quantification of LGR5 immunostaining on CaCo-2 and HT-29 cells.
(A) Quantification of the RFI in samples of CaCo-2 cells. Interestingly, samples treated with 3.7% FA and triton permeabilization showed a significant difference between the isotype control and the LGR5 antibody ($p<0.0001$, with both antibody batches), but not between the LGR5 and Tra-1-85 (Batch 1 vs TRA-1-85, $p=0.7663$; Batch 2 vs TRA-1-85, $p>0.9999$). The rest of the samples showed varying results, and even found significant differences between the RFI of both batches of LGR5 ($p<0.0001$, using 1.85% FA with and without permeabilization). (B) Quantification of the RFI in samples of HT-29 cells. In the four processing conditions there was a significant difference between the RFI of Tra-1-85 and the LGR5 samples ($p<0.0001$, with all processing conditions and both antibody batches). Only in samples treated with 3.7% FA and without permeabilization, a significant difference between the isotype control and the LGR5 antibody was found ($p<0.0001$, with both antibody batches). Experiments were performed by duplicate, and the fluorescence output was measured in nine different fields per replicate. Statistical analysis was performed using a 2-way ANOVA, with *post hoc* multiple comparison using Tukey's test. Both were assessed under a significance level of 95%, where: *$p≤0.0500$; **$p<0.0100$; ***$p<0.0010$; ****$p<0.0001$.

In summary, the conditions that delivered a better outcome were: 3.7% FA fixation with permeabilization for CaCo-2 cells, and without permeabilization for HT-29 cells. Beyond which condition performed better, the results from this experiment indicate that the current commercially available antibodies for the detection of LGR5 are unable to provide an accurate, reliable, and consistent result across different cell lines.

In spite of the results from the quantifications, there was no visible difference in the fluorescence output between the samples stained with LGR5 antibodies and the isotype control. Also, the staining was diffuse and did not colocalize with the membrane. Furthermore, aside from HT-29, the positive controls recommended by the suppliers do not represent the endogenous expression of LGR5 by the intestinal lineage, but rather rely on transgenic cell lines overexpressing the protein.

This highlighted the need for a reporter model that allows the visualization of the intestinal stem cells in cell cultures and more importantly in HIOs. Therefore, we opted for the generation of a transgenic cell line of iPSCs capable of expressing a reporter for the ISC population in a model of iPSC-derived HIOs.

4.2.2 Design and assembly of the LGR5-GFP reporter

We have targeted the final exon (exon 18) of the *LGR5* gene, transcript variant 1 (NM_003667.3). The sequence information was taken from the UCSC genome browser and the NCBI. The identification of candidate gRNAs within this genomic region was performed using the predictive algorithm 'CRISPR Design Tool' developed by Zhang's Lab (Hsu *et al.*, 2013). **Figure 4.5** summarizes the results of these analysis, here the region shown in green was selected as a likely candidate being the closest to the stop codon.
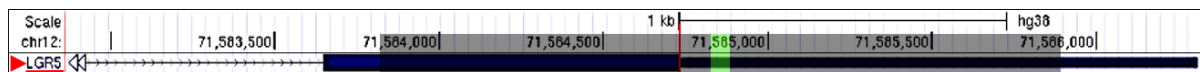
Figure 4.5 Candidate regions for homologous recombination targeting the last exon of LGR5.
Red line indicates the position of the stop codon, the region in bold blue to the left corresponds to the exon 18, and to the right the 3'UTR; green shading highlights the candidate position to insert the fluorescent reporter cassette; and the black shading marks the left and right homology arms.

The candidate gRNAs were cloned into the All-In-One (AIO-Puro) plasmid (Addgene #74630) developed at Zhang's lab (Chiang *et al.*, 2016) (**Figure 4.6A**). AIO-Puro expresses nCas9D10A, a mutated version of endonuclease Cas9, which has nickase activity targeted into specific sites of the DNA through gRNAs. AIO-Puro allows the parallel expression of nCas9D10A driven by the strong promoter CBh and two independent gRNA. This facilitates the transfection into the cell of all the necessary elements for genomic edition. During the cloning of the gRNAs, the use of two rare restriction enzymes, *BpiI* and *BsaI*, guarantees the directional insertion of the probes and prevents the recircularization of the plasmids, thus ensuring that the colonies generated from the transformation will contain the plasmid with the gRNAs.

AIO-Puro was designed with two distinctive restriction sites, *BamHI* and *ClaI*, located within the cloning sites of gRNAs-A and -B, respectively. Therefore, the insertion of the gRNAs led to the loss of the restrictions site. The outcome of this process was assessed by double digestion using *EcoRV* and either *BamHI* or *ClaI*. The candidates that did not incorporate the gRNA generated two bands in the gel, while candidates containing the gRNAs only showed one band produced by the linearization of the plasmid with *EcoRV* (**Figure 4.6B**).
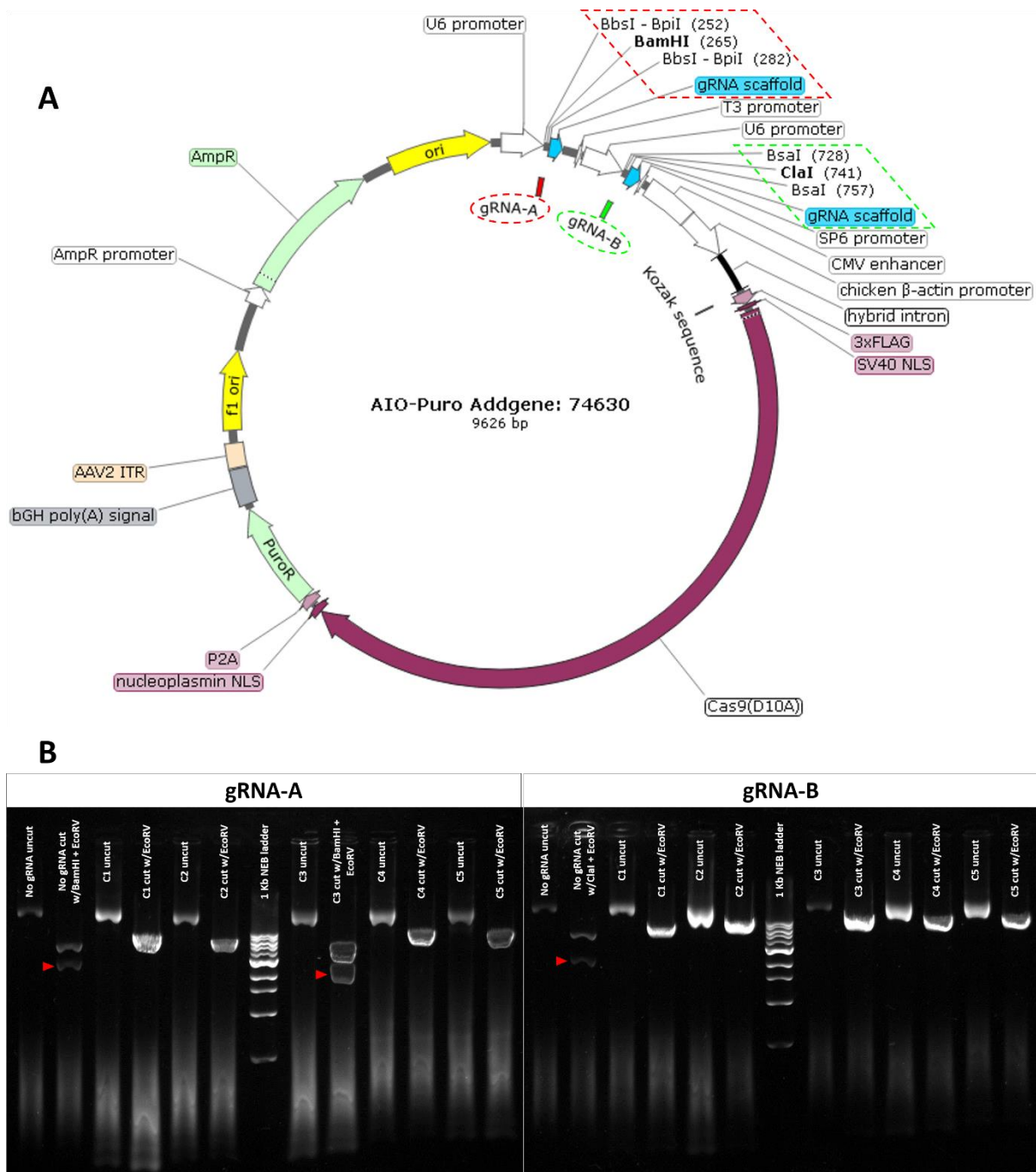
Figure 4.6 Plasmid AIO-Puro (Addgene #74630) and restriction of AIO-PuroAB
(A) The AIO-Puro plasmid allows for the transfection of all the elements necessary for Cas9-mediated genome edition: Two cloning sites for the insertion of gRNAs and the expression cassette of nCas9D10A. (B) Successful insertion of the gRNAs was confirmed by digestion with restriction enzymes. The insertion of gRNAs A and B led to the loss of the restriction sites for *BamHI* and *ClaI*, respectively. Samples were double digested with these enzymes plus *EcoRV* as an internal control. Samples which incorporated the gRNA just showed a single band product of the linearization of the plasmid with *EcoRV*. If the insertion had failed, two bands were seen in the gel (arrowheads).

Parallel to this the reporter construct was assembled using an already existing construct from the plasmid pCAGMKOSiE. Briefly, this plasmid was intended for reprogramming somatic cells into induced pluripotent stem cells and contains the sequence for the Yamanaka factors (Kaji *et al.*, 2009). For the purposes of this study, the region of interest is highlighted in **Figure 4.7,** and the expression cassette is shown at the bottom of the image.
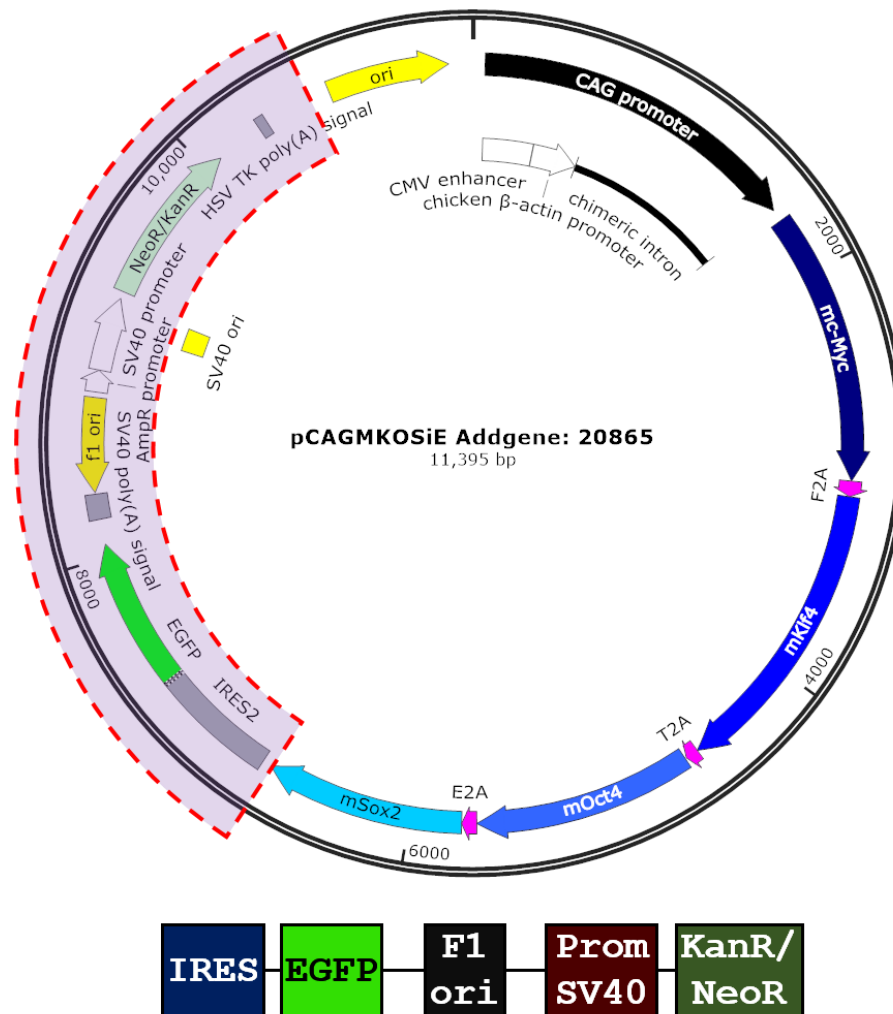
Figure 4.7 EGFP reporter cassette from plasmid pCAGMKOSiE (Addgene #20865).
The plasmid pCAGMKOSiE contains a cassette with an IRES-EGFP reporter that allowed the bicistronic transcription of a gene upstream, and the fluorescent reporter. The region of interest is marked in red and the main features are shown at the bottom of the image.

We have selected this plasmid as the template for our reporter because it contained the internal ribosome entry site (IRES) coupled with an EGFP reporter. The construct was designed for the tandem transcription of a gene upstream from the EGFP reporter, in our case the endogenous *LGR5*. The stop codon and the IRES allowed the independent translation of both proteins, to prevent the reporter from interfering with the folding of LGR5.

Aside from cloning the reporter cassette from pCAGMKOSiE, the process of homologous recombination required the addition of homology arms complementary to the genomic region of interest (**Figure 4.80A**). The PAM sequences found in the homology arms had to be modified using site directed mutagenesis, in order to prevent the construct from being cleaved by nCas9D10A. The LGR5-GFP reporter (**Figure 4.8B**) was cloned into a pCR-XL-2-TOPO.

AIO-Puro and LGR5-GFP plasmids were simultaneously introduced into miFF1. Upon transfection, nCas9D10A was expected to cleave the genomic region flanked by the gRNAs, followed by the incorporation of the LGR5-GFP reporter into the genome through the process of homologous recombination (**Figure 4.8C-D**). The neomycin resistance gene allowed for the selection of cells which had incorporated the transgene into the genome. The incorporation of LGR5-GFP into the genome was assessed by PCR and through the functional expression of the GFP reporter.
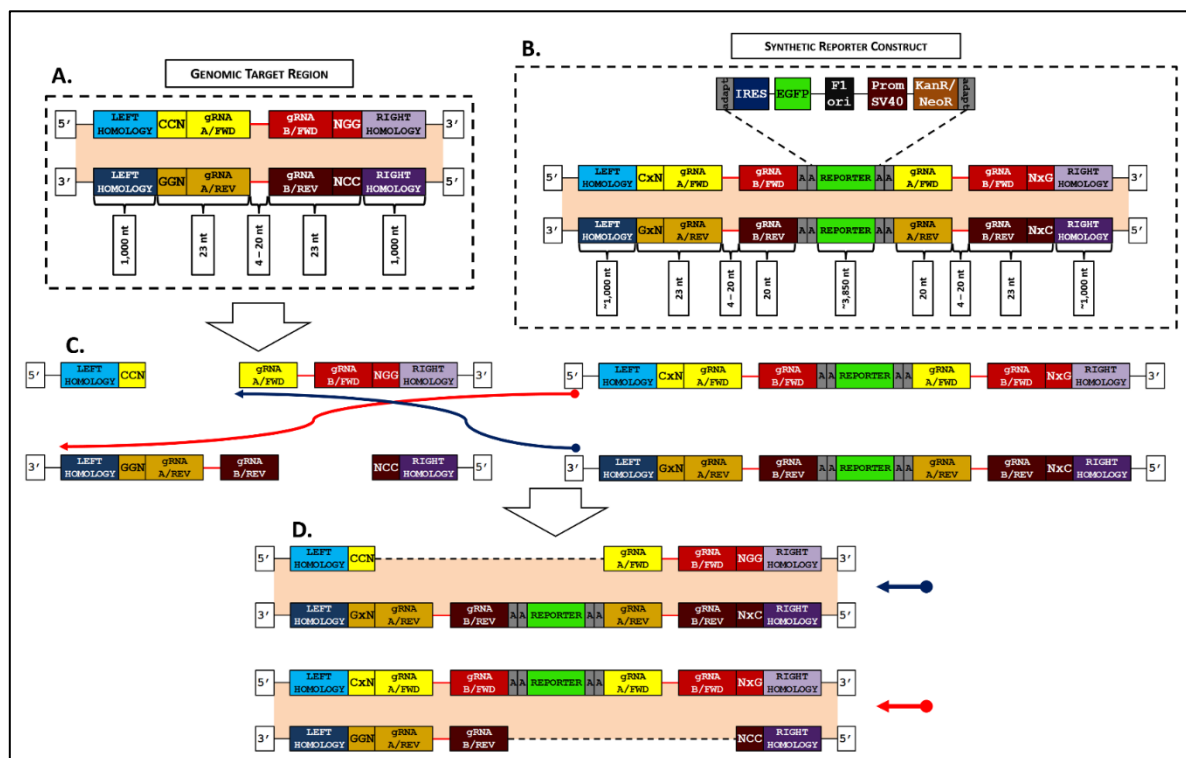
Figure 4.8 Homologous recombination of the LGR5-GFP reporter into the target genomic region.
The process of homologous recombination requires the selection of target site flanked by PAM sequences. (A) Upon identifying the target site, genomic regions of ~1,000 bp up- and downstream are cloned to generate the homology arms. (B) These homology arms are added at the ends of the reporter construct, and the PAM sequences in the arms are modified with site-directed mutagenesis. In the recombination process, nCas9D10A will cleave a single strand of genomic DNA at 2 different positions using 2 different gRNAs. (C) Then the reporter construct is incorporated into the genome by the process of homologous recombination. (D) The resulting product will have incorporated the reporter in the middle of the sequences of the two gRNAs, and the endogenous machinery for DNA damage repair will generate the sequence complementary to the reporter.

The homology arms spanned ~1 Kb upstream (left homology arm, LHA) and downstream (right homology arm, RHA) from the target region flanked by the PAM sequences. These and the IGK (IRES1, EGFP, and Kanamycin/Neomycin resistance gene) reporter construct from pCAGMKOSiE (~3.8 Kb) were amplified using high fidelity polymerase (**Figure 4.9**).
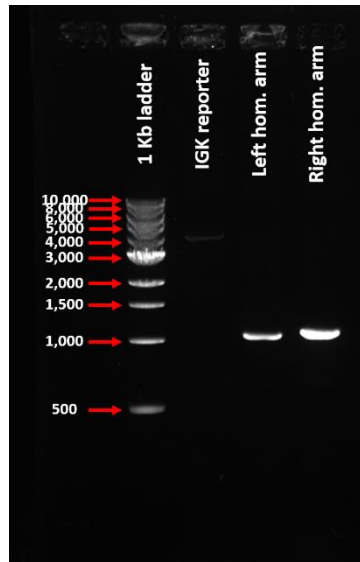
Figure 4.9 Amplification of the components of the LGR5-GFP reporter.
The components required to assemble the LGR5-GFP reporter were amplified by PCR. The results from the amplification were confirmed by agarose-gel electrophoresis. Lane 1: NEB 1 Kb molecular weight marker; Lane 2: GFP expression cassette (3.8 Kb); LHA (1 Kb); RHA (1.1 Kb).

Next, the three elements were sequentially ligated, using a combination of different restriction enzymes to ensure the proper assembly of the construct. The final product contained: left and right homology arms to facilitate and target the insertion of the reporter into a specific locus of the genome; IRES-EGFP, for the tandem expression along with the endogenous LGR5 gene; and neomycin resistance gene (NeoR) for clonal selection. These elements were cloned into the backbone of pCR-XL-2-TOPO (**Figure 4.10A-B**). Preliminary characterization of the LGR5-GFP plasmid, detected the presence of LHA (1 Kb), RHA (1.1 Kb) and EGFP (0.7 Kb), the three main blocks of the reporter (**Figure 4.10C**); although, the entire LGR5-GFP construct (~6 Kb) could not be amplified likely due to limited amplification capacity from standard *Taq* polymerase to amplify large fragments.
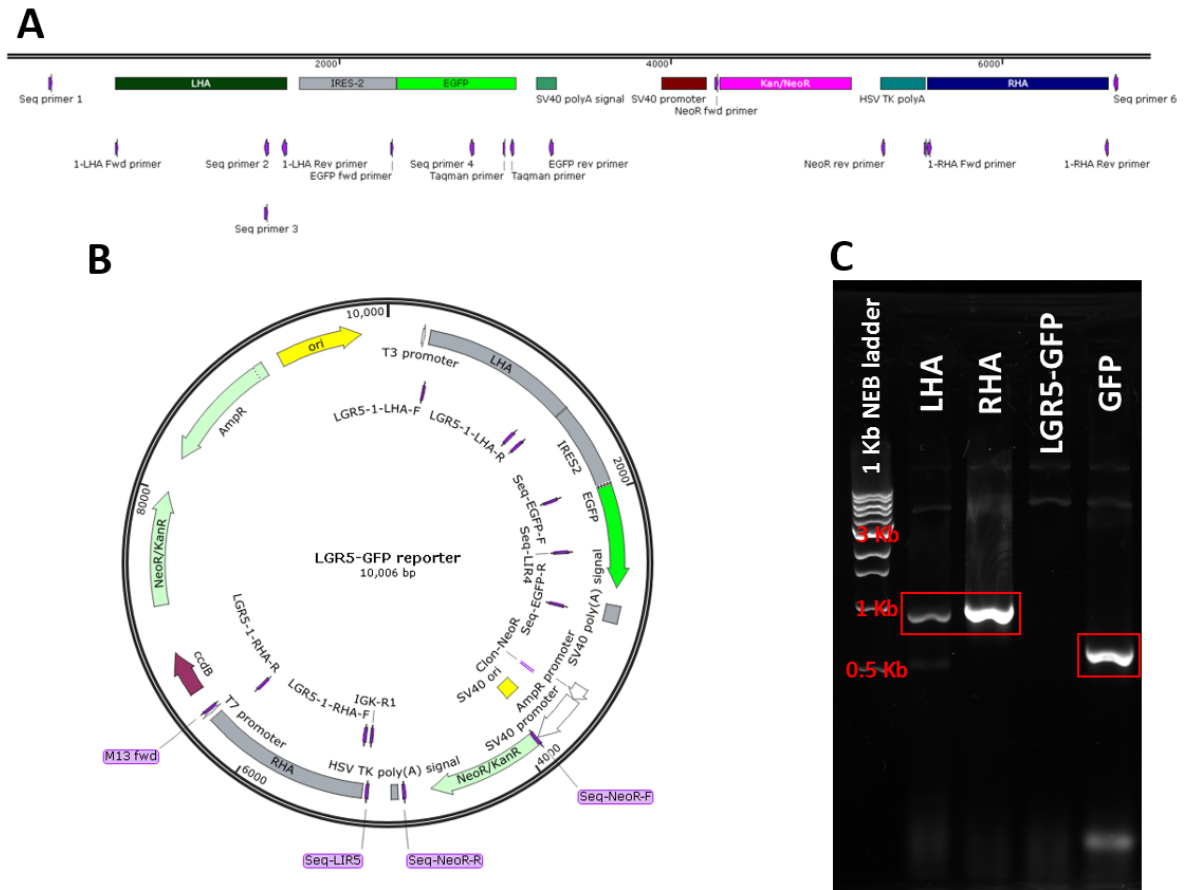
Figure 4.10 Assembled LGR5-GFP plasmid.
(A) Representation of the reporter construct if integrated into the genome. The annotations highlight the key elements of the construct: homology arms, IRES-GFP cassette, selection gene for kanamycin/neomycin resistance (Kan/NeoR), the primers used during the assembly of the construct, and primers used for further characterization. (B) LGR5-GFP plasmid containing the reporter cassette within the backbone of pCR-XL-2-TOPO. (C) Preliminary characterization of LGR5-GFP plasmid after cloning the reporter cassette. The three main blocks used for the assembly of the reporter were amplified by PCR: GFP (0.7 Kb); LHA (1 Kb); RHA (1.1 Kb). The amplification of the entire construct was not achieved.

To overcome this limitation, and confirm the correct assembly and cloning of the LGR5-GFP plasmid, we desgined an array of characterization primers targeting key elements of the plasmid (See Methods and Methods section, Table 2.1). The primers were paired in such way as to generate redundant amplicons; therefore, if a set of primers was unable to amplify its target, a different set of primers or combination of these should be able to provide evidence of the presence of a specific feature (**Figure 4.11A**). From the 20 amplifications performed, gel electrophoresis confirmed 11 produced a band of the correct size. Interestingly, most bands with high molecular weight (>1.2 Kb) appear dimmer, reflecting the limited capacity of *Taq* to amplify large fragments. Negative results were likely due to suboptimal melting temperature and/or amplification conditions (**Figure 4.11B**).

A detailed summary of the results is presented in **Table 4.1**. Briefly, amplicons ***M13-Rev/LGR5-LHA-Rev*** and ***M13-Rev/Seq-LIR2*** confirmed the connection between the left end of the backbone of pCR-XL-2-TOPO and the left homology arm of the reporter cassette. ***LGR5-LHA-Fwd/LGR5-LHA-Rev*** and ***LGR5-LHA-Fwd/Seq-LIR2*** amplified the entire left homology arm. ***Seq-EGFP-Fwd/Seq-EGFP-Rev*** and ***Seq-EGFP-Fwd/Seq-LIR4*** covered a fragment of the IRES2 sequence and EGFP. ***Clon-NeoR-Fwd/Seq-NeoR-Rev*** and ***Seq-NeoR-Fwd/Seq-NeoR-Rev*** amplified the entire NeoR gene. ***Clon-NeoR-Fwd/IGK-R1*** and ***Seq-NeoR-Fwd/IGK-R1*** covered the NeoR gene; also, the sequence of primer IGK1 overlaps with the sequence of Seq-LIR5, therefore providing a connection between ***Clon-NeoR-Fwd/IGK-R1*** and ***Clon-NeoR-Fwd/IGK-R1***. Finally, ***Seq-LIR5/M13-Fwd*** amplified a small fragment of the IGK cassette, the entire right homology arm, and established a connection between this and the right end of the pCR-XL-2-TOPO backbone. Altogether, the evidence provided by these positive amplifications appears sufficient to demonstrate the presence of the main features of the plasmid assembled in the correct order, and therefore the successful assembly of the LGR5-GFP plasmid.
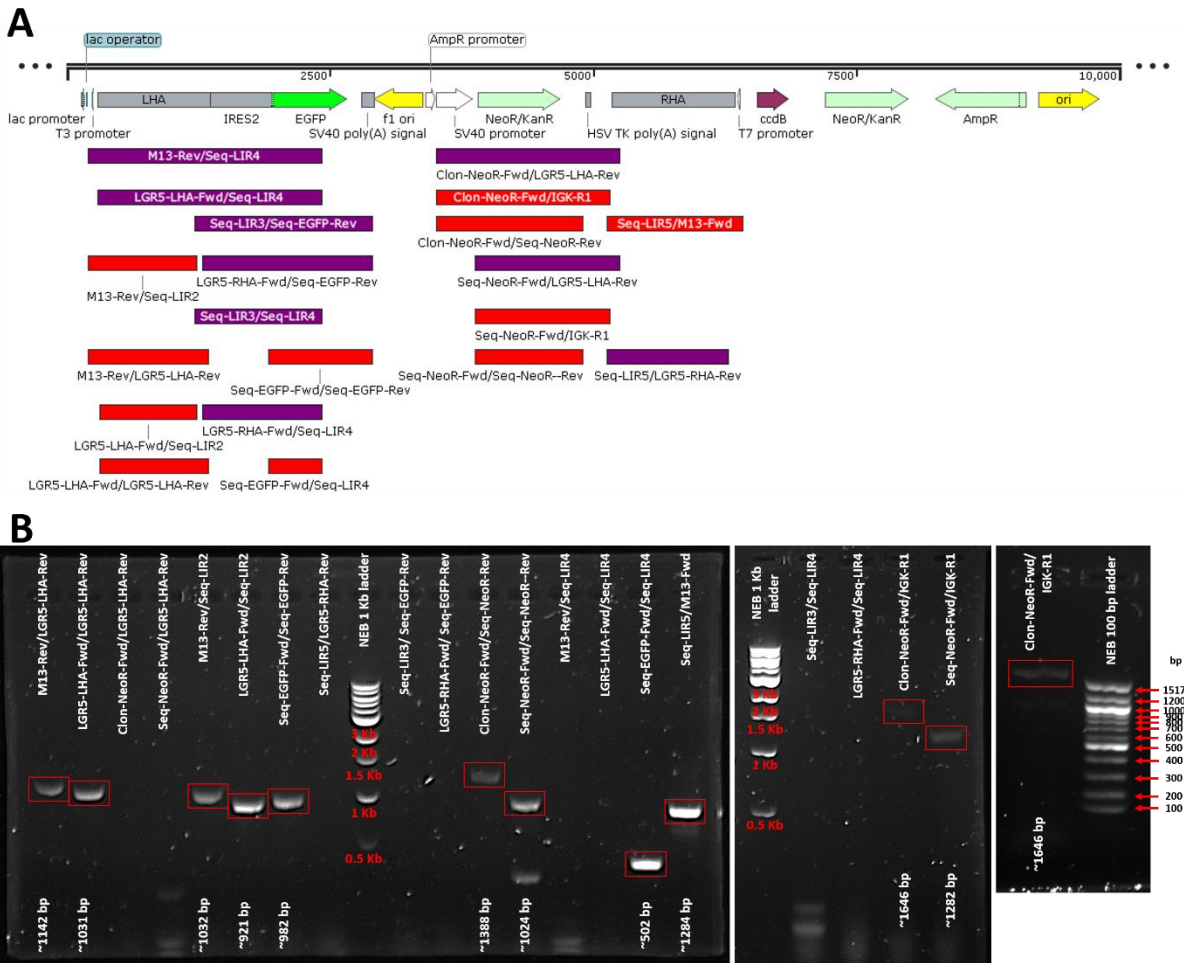
Figure 4.11 Characterization of LGR5-GFP reporter.
(A) Linear map of the LGR5-GFP reporter construct cloned into a backbone of pCR-XL-2-TOPO vector. The characterization of the plasmid focused on the detection of specific key features: plasmid backbone, left and right homology arms, IRES2, EGFP, and NeoR. The host vector contains binding sequences for primers M13-Rev and M13-Fwd flanking the construct; additionally, several primers were designed targeting different elements within the reporter construct. Red and purple bars represent the PCR amplicons targeted to corroborate the presence of these key features. Red represents targets with positive amplifications evidenced by gel electrophoresis; purple indicate unsuccessful amplification. (B) Electrophoresis results from PCR amplification, the positive bands are framed in red, and the amplicon size is consistent with *in silico* analysis. The following amplifications provide sufficient evidence of the successful assembly of the reporter vector: M13-Rev/Seq-LIR2, indicate the ligation of one end of the plasmid backbone with the left homology arm; Seq-EGFP-Fwd/Seq-EGFP-Rev, spans a small fragment of IRES2 and the coding sequence of EGFP; Clon-NeoR-Fwd/IGK-R1, amplifies NeoR. Also, the sequence of primer IGK-R1 overlaps with the one of Seq-LIR5, providing the link between the IGK cassette and the right homology arm. Finally, Seq-LIR5/M13-Fwd indicate the ligation of the right homology arm with the other end of the plasmid backbone.

162

Fwd primer	Overlapping construct	Rev primer	Overlapping construct	Amplified fragments	Amplicon size (bp)	Gel result
M13-Rev	pCR-XL-2-TOPO	LGR5-LHA-Rev	LHA	pCR-XL-2-TOPO // LHA	1142	+
LGR5-LHA-Fwd	LHA	LGR5-LHA-Rev	LHA	LHA	1031	+
Clon-NeoR-Fwd	SV40 promoter	LGR5-LHA-Rev	RHA	NeoR/KanR // RHA	1741	-
Seq-NeoR-Fwd	NeoR/KanR	LGR5-LHA-Rev	RHA	NeoR/KanR // RHA	1377	-
M13-Rev	pCR-XL-2-TOPO	Seq-LIR2	LHA	pCR-XL-2-TOPO // LHA	1032	+
LGR5-LHA-Fwd	LHA	Seq-LIR2	LHA	LHA	921	+
Seq-EGFP-Fwd	IRES2	Seq-EGFP-Rev	SV40 poly (A) signal	IRES2 // EGFP	982	+
Seq-LIR5	IGK (no feature)	LGR5-RHA-Rev	RHA	IGK (no feature) // RHA	1148	-
Seq-LIR3	LHA	Seq-EGFP-Rev	SV40 poly (A) signal	LHA // IRES2 // EGFP	1683	-
LGR5-RHA-Fwd	LHA	Seq-EGFP-Rev	SV40 poly (A) signal	LHA // IRES2 // EGFP	1611	-
Clon-NeoR-Fwd	SV40 promoter	Seq-NeoR-Rev	IGK (no feature)	NeoR/KanR	1388	+
Seq-NeoR-Fwd	NeoR/KanR	Seq-NeoR-Rev	IGK (no feature)	NeoR/KanR	1024	+
M13-Rev	pCR-XL-2-TOPO	Seq-LIR4	EGFP	pCR-XL-2-TOPO // LHA // IRES2 // EGFP	2215	-
LGR5-LHA-Fwd	LHA	Seq-LIR4	EGFP	LHA // IRES2 // EGFP	2125	-
Seq-EGFP-Fwd	IRES2	Seq-LIR4	EGFP	IRES2 // EGFP	502	+
Seq-LIR5	IGK (no feature)	M13-Fwd	pCR-XL-2-TOPO	IGK (no feature) // RHA // pCR-XL-2-TOPO	1284	+
Seq-LIR3	LHA	Seq-LIR4	EGFP	LHA // IRES2 // EGFP	1203	-
LGR5-RHA-Fwd	LHA	Seq-LIR4	EGFP	LHA // IRES2 // EGFP	1131	-
Clon-NeoR-Fwd	SV40 promoter	IGK-R1	IGK (no feature)	NeoR/KanR	1646	+
Seq-NeoR-Fwd	NeoR/KanR	IGK-R1	IGK (no feature)	NeoR/KanR	1282	+

Table 4.1 Summary of the PCR results for the characterization of the LGR5-GFP vector.

4.2.2 CRISPR-nCas9 genomic edition for the integration of the LGR5-GFP reporter

After assembling the reporter and confirming the presence of the necessary elements for the generation of an intestinal stem cell reporter cell lines, we proceed to the transfection of the construct into miFF1 iPSCs.

LGR5-GFP was introduced into miFF1 by nucleofection, followed by selection with neomycin for 2-3 weeks to generate a stable cell line. Previously, we had confirmed a low expression of LGR5 in iPSCs (**Figure 4.1**), and the differentiation process into ISCs would result costly and time consuming. Therefore, we isolated the genomic DNA of transfected cells to investigate whether they had incorporated the reporter into the genome. Next, we used standard PCR to amplify representative elements of the reporter (**Figure 4.12**). A set of primers were designed to anneal into a segment of the genome outside of the sequence of the reporter. The external primers were expected to amplify a fragment of ~6.4 Kb when the reporter cassette is inserted in the target position and ~2.5 Kb without the reporter. Each one of the characterization primers for EGFP and NeoR amplify a fragment of ~1 Kb.

We used the LGR5-GFP plasmid as a positive control for the elements of the reporter, and genomic DNA from wild-type miFF1 as a negative control, and as a control for the external primers. Additionally, we evaluated whether the transfection with linear or circular plasmid could provide better integration results.

Amplification using the transfection plasmid as template identified the homology arm (1 Kb), GFP (1 Kb) and NeoR (1 Kb); as expected the external primers did not produce any amplicon, since these are designed to target the genomic region flanking the homology arms. Amplification using genome of WT-miFF1 identified the homology arm (1 Kb) and a 2.5 Kb product from the external primers. It did not amplify GFP nor NeoR. Both of the samples from transfected cells showed the same results as WT-miFF1, indicating a failure in the integration of the reporter into the genome. The configuration of the plasmid (linear or circular) did not show any effect in the outcome of the transfection.
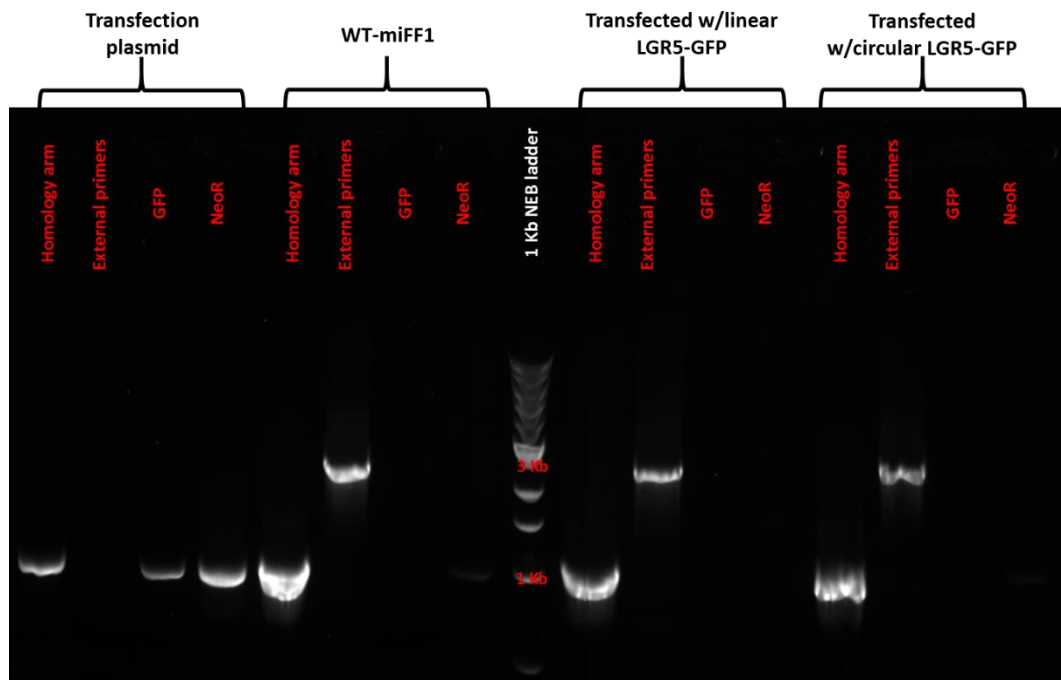
Figure 4.12 Molecular characterization of iPSCs transfected with LGR5-GFP.
PCR amplification of representative elements of LGR5-GFP did not detect the presence of GFP or
NeoR, and the external primers returned a product of ~2.5 Kb corresponding to the genomic size of
the native region without the insertion of the reporter construct. The left homology arm was used
as an internal positive control; also, no difference was seen between linearized and circular plasmid.

To assess whether this process was due to an unforeseen effect from working with stem cells, we used
CaCo-2 cells as a control cell line, and the FUCCI plasmid as a control plasmid. These were selected as
we already had evidence that FUCCI can spontaneously integrate into the genome of CaCo-2 cells.
Additionally, we co-transfected H2B-mCherry along with the LGR5-GFP reporter to confirm the cells
were up taking the plasmids.

Cells co transfected with H2B-mCherry and LGR5-GFP, displayed the fluorescence from the first but
not the latter. As expected CaCo-2 cells integrated and expressed the reporter encoded in FUCCI.
Similar to miFF1, the configuration of the plasmid (linear or circular) did not influence the final
outcome (**Figure 4.13**).
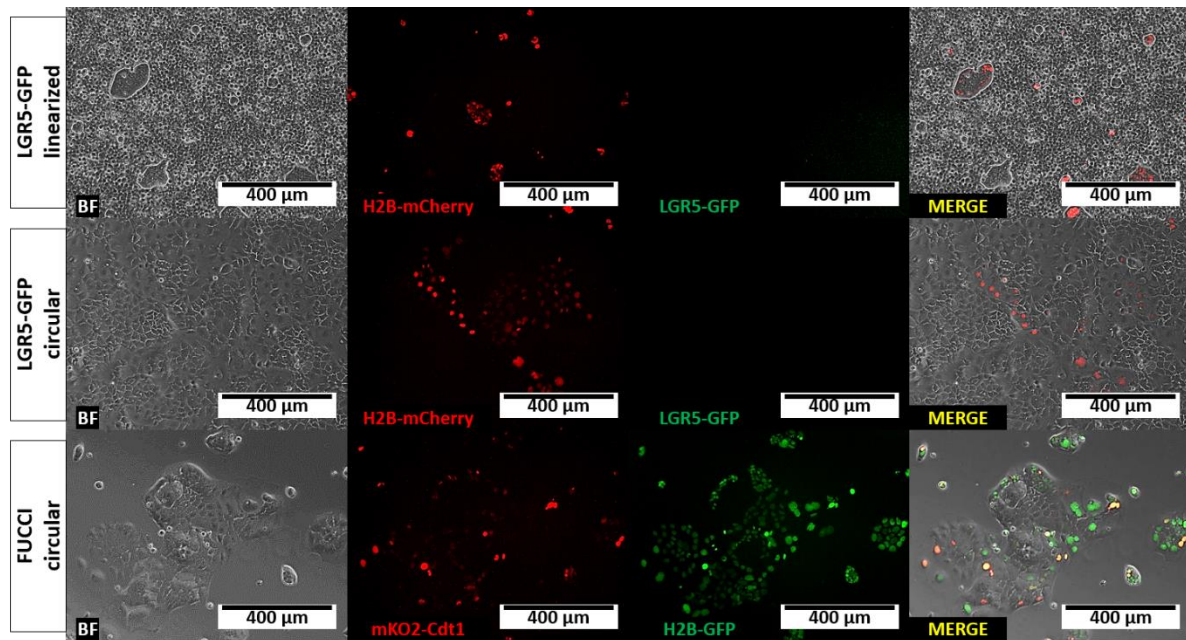
Figure 4.13 Transfection of CaCo-2 cells with the LGR5-GFP reporter.
CaCo-2 cells were transfected with the LGR5-GFP linearized (top row) and circular (middle row) to assess any potential improvement in the integration efficiency of the reporter. H2B-mCherry was co-transfected as a positive control for the transfection. A control experiment was performed using the FUCCI plasmid to confirm the quality of the transfection reagents and permissiveness of the cells to accepting exogenous material (bottom row). White scale bars indicate 400 μm.

Finally, to discard the possibility of epigenetic silencing of the transgene or even the absent expression of it, we performed PCR characterization of the transfected cells. The amplification did not show evidence of the integration of the reporter, GFP and NeoR were not amplified and the external primers returned a 2.5 Kb amplicon (**Figure 4.14**).
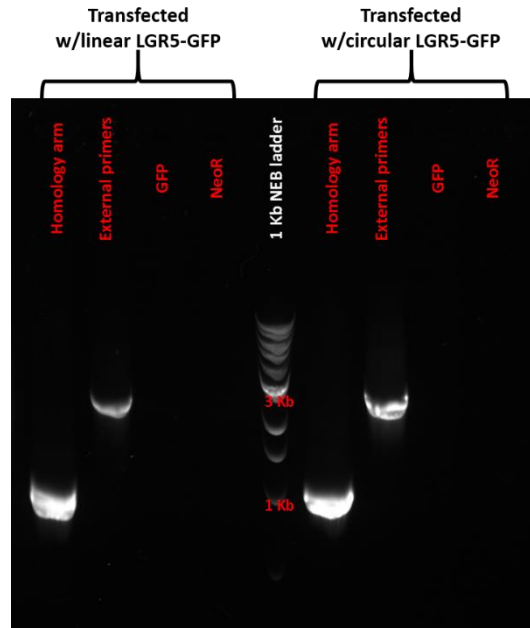
Figure 4.14 Molecular characterization of CaCo-2 cells transfected with LGR5-GFP. PCR amplification of representative elements of LGR5-GFP did not detect the presence of GFP or NeoR, and the external primers returned a product of ~2.5 Kb corresponding to the genomic size of the native region without the insertion of the reporter construct. The left homology arm was used as an internal positive control; also, no difference was seen between linearized and circular plasmid.

4.3 Discussion

Perhaps one of the most important caveats in the study of intestinal stem cell biology, is that most of the research coupling organoids with a Lgr5 fluorescent reporter is conducted using mouse models (Barker et al., 2007; Morgan et al., 2018). Not enough has been discussed regarding the limitations of LGR5 as an ISC marker in non-cancerous human models. Regardless, some work has claimed success generating a human LGR5-GFP reporter cell line; although, its use has been considerably limited and in some cases the reporters have been unable to actually provide a strong fluorescence and require additional steps to enhance this signal (Forster et al., 2014; Watson et al., 2014; Shimokawa et al., 2017). It is essential to know whether the mouse model recapitulates, in human cell lines, and if we can improve on the current human model with uncertainty about LGR5 expression. In this section we test the currently available LGR5 antibodies, describe the design and assembly of an LGR5-GFP fluorescent reporter and our attempts to incorporate it, using CRISPR/nCas9, into iPSCs and an intestinal epithelium cell line.

First, we evaluated the expression of LGR5 transcripts in two human cell lines: miFF1 and CaCo-2 cells. RT-PCR detected LGR5 mRNA in both cell lines. The size of the electrophoretic bands (~76 bp) was correct according to *in silico* analysis of the amplification site; however, a limitation of this experiment is the lack of a positive control, which was not available at the time, and a possible solution to this would be to obtain a purified sample of LGR5 cDNA. In addition to this, based on the intensity of the electrophoretic bands, the expression was lower in miFF1 cells compared to CaCo-2. No reports address the expression of LGR5 in iPSCs, though, it is plausible for it to be expressed given the importance of WNT signalling in the maintenance of the pluripotency and self-renewal (Nusse et al., 2008; de Lau et al., 2011; Clevers & Nusse, 2012). In contrast, studies have found CaCo-2 cells exhibit a 9-fold increase in LGR5 expression compared to average expression of a colorectal cancer cell line (Uchida et al., 2010); also, several reports have mentioned a significant increase in the expression of LGR5 in samples of colorectal cancer (Becker et al., 2008; Ziskin et al., 2013; Baker et al., 2015; Ihemelandu et al., 2019).

Next, we tested the activity of a commercially available human anti LGR5 monoclonal antibody (clone OTI2A2) in CaCo-2 and HT-29 cells. This antibody had already shown success in detecting the presence of LGR5+ in putative colon CSCs, using IHC analysis on CRC patient samples (Ihemelandu et al., 2019). In this study, we assessed an array of different prestaining conditions (with or without permeabilization, mild or standard fixation), two different antibody batches, and two control cell lines of the intestinal epithelium (HT-29 and CaCo-2). The staining was not consistent between antibody

batches or cell lines, and the signal did not colocalize with the plasma membrane as is expected from LGR5. Our results did not show an efficient and robust detection of LGR5.

Reports from the literature have found the generation of LGR5 antibodies considerably troublesome, and the existing commercial LGR5 antibodies may present considerable detection constraints and/or questionable specificity (Rizk & Barker, 2012; Barker, 2014). Studies referring to the detection of LGR5 in human intestinal samples, have used an anti LGR5 polyclonal antibody which is targeted to adenoma samples, and/or used for immunohistochemistry rather than immunofluorescence (Becker et al., 2008; Fan et al., 2010; Takeda et al., 2011). This poses two issues: first, polyclonal antibodies have an inherent risk of lower specificity and higher background signal, compared to its monoclonal counterpart; second, IHC uses chromogenic reactions which greatly amplify the signal output, overrepresenting the expression of the biomarker in the sample, and compromising its use for quantitative purposes (Hofman, 2002; Bourgeois & Oaks, 2013; O'Hurley et al., 2014). In addition to this, different monoclonal antibodies have been developed to identify the LGR5^{+} ISC population, however, they have mostly worked with cancerous cell lines, CRC tissue samples or cells modified for the overexpression of this specific protein (Kemper et al., 2012). Overall, even with the currently available commercial antibodies, the detection of LGR5 has been described as an issue due to the low amounts of mRNA and/or proteins (van der Flier et al., 2009b).

The main objective of this section was to design and assemble an LGR5-GFP reporter cell line. Our reporter construct followed a similar structure to the one reported by Shimokawa et al (2017). The construct consisted of an IRES sequence, an EGFP reporter and a neomycin resistance gen, flanked by homology arms targeting the final exon of the human LGR5 gene. Preliminary characterization of the LGR5-GFP plasmid confirmed the presence of three main blocks: LHA, RHA, and GFP; however, the amplification of the entire construct (~6 Kb) was not achieved. The likely cause for this lies on the inability of standard *Taq* polymerase to amplify fragments longer than 5 Kb, as specified by the manufacturer (Meridian Bioscience, 2020a). Alternative polymerases, such as MyFi or RANGER DNA polymerases, could have been used to amplify the full extent of the reporter (Meridian Bioscience, 2020b). Nevertheless, in this work, the correct assembly of the LGR5-GFP plasmid was confirmed by PCR amplification directed to an array of several key fragments of the construct. The results of the amplification provided sufficient evidence of the correct assembly of the reporter.

The next step consisted in using CRISPR/nCas9 edition to integrate the reporter construct into the genome of miFF1 and CaCo-2 cells, via homologous recombination. Cells were nucleofected with a combination of the LGR5-GFP plasmid and the AIO-Puro plasmid, the latter contained the sequences for the expression of the sgRNAs and nCas9. Stable clones were selected for 2-3 weeks with the

appropriate antibiotic, and then expanded for molecular characterization. The integration of the reporter was assessed by PCR, but no bands were detected with any of the amplification targets, in either cell line.

Considering the possibility of unforeseen limitations, which could have hindered the molecular detection of the reporter by PCR, we sought to confirm the expression of the fluorescent LGR5-GFP reporter in CaCo-2 cells. We have previously confirmed, by RT-PCR, the expression of LGR5 in CaCo-2 cells; miFF1 was not considered due to its low expression of LGR5. No fluorescence was detected on CaCo-2 cells transfected with the LGR5-GFP reporter. The generation of an LGR5-GFP reporter cell line was unsuccessful.

In light of these results, we have reassessed our approach and identified three aspects in which potential modifications might change the outcome of the project: (i) the use of CRISPR/Cas9-mediated genome edition, (ii) the use of an EGFP reporter system, and (iii) the use of LGR5 as a biomarker for the ISC and CSC population.

Regarding the use of CRISPR/Cas9, we opted for this approach as it has been reported to be sufficiently effective to perform the insertion of a transgenic fluorescent reporter in a cost-effective manner. Over the years different methods have been developed for the insertion of transgenic reporters into host organisms, the most notable are: ZFN, TALENs and CRISPR/Cas9. These systems induce DNA strand breaks to trigger the repair machinery of the host, allowing for the insertion of transgenes by recombination with its genome (He et al., 2016; Lino et al., 2018). The insertion of transgenes may occur either by homology-direct repair (HDR) or nonhomologous end joining (NHEJ); while HDR reduces the risk of off-target effect (OTE), it also results in lower edition efficiency. Conversely, NHEJ increases the possibility of retrieving modified clones, but the editions have a higher risk of occur off-target (Lino et al., 2018; Ryu et al., 2019).

CRISPR/Cas9 has been preferred as the method of choice for a broad spectrum of genomic edition application, mainly due to its robustness, low cost, lower OTE, easy preparation, and high edition efficiency. However, even this system is not without constraints and the main limitations of this system are cytotoxicity, chromosomal destabilization, and the occurrence of OTEs. (He et al., 2016; Manghwar et al., 2019; Uddin et al., 2020).

A previous work conducted on CRC cell lines, confirmed that in addition to OTE involving small indels, Cas9 is prone to elicit large-scale chromosomal rearrangements. The study also highlighted the inherent instability of cancer cell lines may be a factor that predisposes the cells to OTE and chromosomal destabilization (Rayner et al., 2019). In relationship to our study, it is possible that the

activity nCas9 had been affected by the inherent chromosomal instability of CaCo-2 cells, thereby diminishing its activity or even affecting the expression of the reporter and/or the endogenous LGR5.

OTE from Cas9 activity have been observed in >50% of the cases. Significant effort has been invested in the development of predictive algorithms for the detection of off-target sites; however, simply analysing the DNA sequence has been insufficient due to the influence of epigenetic factors/modifications in the activity of Cas9 (Zhang et al., 2015). Additionally, different versions of Cas9 have been developed, such as nickase Cas9 (nCas9). Conventional wild type Cas9 performs double strand breaks (DSBs) in the DNA, while nCas9 creates single-strand breaks (SSBs). This contributes to a substantial reduction in the occurrence OTEs, without compromising the efficiency of edition (Ran et al., 2013; Chiang et al., 2016). Moreover, studies have succesfully used nCas9 to generate a reporter cell line of iPSCs with a neuronal lineage fluorescent reporter (Li et al., 2015), and U2OS cells expressing a GFP-luciferase reporter (Rojas-Fernandez et al., 2015).

Additionally, some cell lines have been found more relucatant to transfection. The need of introducing sgRNAs and a plasmid containing the sequence for Cas9, has considerably diminished the effectiveness of Cas9-mediated edition. This led to the development of all-in-one plasmids that contain the sequence for the expression of sgRNAs and Cas9, driven by a strong U6 or H1 promoter. According to reports from the literature, this is a simple and cost effective alternative to work with CRISPR/Cas9 (Chiang et al., 2016; Jin et al., 2019)

These works supported our decision to use nCas9 and an AIO plasmid for the generation of our reporter cell line. However, DNA-based Cas9 delivery systems, like AIO plasmids, have shown important disadvantages, such as: (i) increased damage to the cell during transfection; (ii) higher risk of OTE; and (iii) potential integration of the plasmid into the genome. To overcome these issues, previous studies have proposed the use Cas9/sgRNA ribonucleoprotein complexes (RNPs). RNPs rescind from the use of DNA, therefore eliminating the risk of plasmid integration into the genome; upon transfection into the cell are readily available, providing faster results; the rapid turnover of RNPs reduces its exposure time within the cell, thus decreasing the risk of generating off-target mutations; the transfection has shown to be less stressful to the cells, and even in recalcitrant iPSCs provides relatively high efficiency of nuclease activity (Kim et al., 2014). Furthermore, a comparative study of different delivery methods of Cas9, found that direct electroporation of RNPs greatly outperformed AIO plasmids and mRNA transfection. The results indicated that even in IPSCs, there was up to an 87% efficiency of nuclease-mediated indels. The possible explanations provided by the authors suggested: (i) in vitro assembly of RNPs produced better complexing yields; (ii) RNPs protect sgRNA from degradation; and (iii) lack of DNA-derived cytotoxicity (Liang et al., 2015).

The use of RNPs was not initially considered due to being considerably more expensive, and required large amounts of purified Cas9 protein and sgRNAs; however, in the aftermath of our results, we have re-evaluated the cost-benefit of this alternative and consider it a viable worth exploring solution in combination with nCas9.

In reference to the incorporation of EGFP into our reporter system, we opted for this approach for its simplicity and robust fluorescence. As oppose to end point chromogenic and luminometric assays, fluorescent proteins do not require cell lysis, fixation, or substrate additions. This has made it a highly attractive system for studies that require continuous time-lapse observations of the biomarker or the tagged cell (Gasparri & Galvani, 2010). Studies have confirmed the fluorescence of GFP is directly proportional to mRNA and protein levels, making it an ideal quantitative reporter (Soboleski et al., 2005). Furthermore, fluorescent reporters, generated from the fusion of a fluorescent protein and a physiologically relevant biomarker, offer significant advantages over other immunodetection procedures, such as: (i) detection of the intracellular localization of the protein; (ii) real-time visualization of tagged cells, particularly when using three-dimensional culture systems; (iii) enables live imaging to follow the lifespan of chimeric proteins and/or cells; (iv) quantification of the expression levels of the biomarker, based on RFI; (v) quantification of the number of cells expressing the chimeric protein; (vi) compatibility with high-throughput experiments; (vii) the interpretation and analysis of the results is relatively simple, less subjective, and does not require an expert histopathologist; and (viii) cost and time saving (Liu *et al.*, 1999*a*; Steff *et al.*, 2001; Soboleski *et al.*, 2005; Gasparri & Galvani, 2010).

However, this system is not without limitations, and it remains possible some of these constraints might have had an impact on the success of our reporter system. Based on previous reports from the literature, GFP-associated cell dead has been proposed as significant limitation in the generation of stable GFP reporter cell lines (Liu *et al.*, 1999*a*; Baens *et al.*, 2006). GFP-associated cytotoxicity could have eliminated GFP+ clones prior to their detection, leading to the results observed in this study.

Early reports have found cytotoxic effects and apoptotic induction directly derived from GFP expression (Liu *et al.*, 1999*a*). The exact molecular mechanism for GFP-associated cytotoxicity has not been fully defined. However, studies have found an association between GFP expression and defective polyubiquitination in the cells. On this scenario, deficient polyubiquitination would affect kinase activation and proteasomal degradation, therefore disrupting a broad spectrum of signalling pathways (Baens et al., 2006). Other reports have suggested the occurrence of general phototoxicity due to the production of reactive oxygen species (Goto et al., 2003; Ansari et al., 2016). Additionally, studies using the acetylcholine receptor fused to GFP, found that GFP altered the functionality of the receptor

(Fucile et al., 2002). Also, GFP has been reported to interfere with the folding of the native proteins, resulting in improper subcellular localization of the protein, formation of aggregates, or lack of GFP fluorescence (Hanson & Köhler, 2001). These caveats are important considerations which may justify the lack of detectable fluorescence from our LGR-GFP reporter.

Alternatively, studies have found that other fluorescent proteins may exhibit less cytotoxicity (Ansari et al., 2016). Also, unnatural fluorescent amino acid like 3-(6-acetylnaphthalen-2-ylamino)-2-aminopropanoic acid (Anap), has shown relative success when incorporated into the sequence of endogenous proteins to track its subcellular localization in living cells (Chatterjee et al., 2013). More alternative labels have been developed to replace the use of fluorescent proteins, and further analysis may indicate the most suitable option (Buckley et al., 2015; Lotze et al., 2016).

Finally, the core issue in this study appeared to rely on the expression of LGR5 and the overall difficulties to detect it with fluorescence-based techniques in normal intestinal epithelium. Since its publication in 2007, numerous papers have cited the use of LGR5 as a reliable marker for the ISC population; although no emphasis is made on the fact that, as a fluorescent reporter, this marker has only been able to produce reliable results on mouse models (Barker *et al.*, 2007; Snippert *et al.*, 2010; Koo *et al.*, 2011; Muñoz *et al.*, 2012; Scheper *et al.*, 2012; Yui *et al.*, 2012; Basak *et al.*, 2014; Yin *et al.*, 2014; Sachs *et al.*, 2017; Liu *et al.*, 2019*a*). Studies have highlighted the low expression levels of LGR5 mRNA and protein, and/or the limited stem cell population may hinder the detection of the marker (van der Flier et al., 2009b).

LGR5 has been detected at the transcriptional level using RT-qPCR and in situ hybridization (Uchida et al., 2010; Baker et al., 2015), however, this is not necessarily a direct reflection of the expression of the final functional transmembrane protein. Other studies have employed LGR5 antibodies for the detection of the protein within the cytoplasm (Fan et al., 2010). Although LGR5 is a transmembrane protein, its cytoplasmic localization may refer to the formation of misfolded protein aggregates, which is not a sign of normal expression of LGR5 by ISC (Aigelsreiter et al., 2007; Brüning & Jückstock, 2015). Some studies have found that LGR5^{+} cells are not necessarily "functioning stem cells". It has been reported that not all LGR5+ cryptal cells actively participate in the tissue renewal, although they maintain their stem cell potential (Baker et al., 2015). Therefore, some authors have opted for metabolic assays, such as measuring cytochrome oxidase activity to detect the presence of functionally active cryptal stem cells, rather than resourcing to LGR5 labelling (Baker et al., 2014).

To the extent of the literature reviewed, there are no reports of immunofluorescent images of LGR5 in non-cancerous human ISC. (Immuno-) fluorescent detection of LGR5 has only been reported with

CRC tissue samples, where the biomarker has been found to be aberrantly overexpressed (Becker et al., 2008; Takeda et al., 2011; Ziskin et al., 2013; Baker et al., 2015; Ihemelandu et al., 2019).

Previous studies have claimed the generation of LGR-GFP organoids; however, no direct evidence on the expression and activity of the fluorescent reporter was presented. These works relied on indirect detection of LGR5 accompanied with signal-enhancing steps. Also, the reporter was detected in glandular cells of iPSC-derived teratomas, patient biopsies or patient-derived organoids. These systems have also reported overexpression of LGR5 which may facilitate its detection, but it does not allow for a comparison with non-cancerous intestinal cultures (Forster et al., 2014; Shimokawa et al., 2017).

During the design of the reporter, we found that there are considerably few publications that address the problems and limitations of LGR5, compared with the number of works that praise it as the de facto marker of the ISCs. Nevertheless, extensive anecdotal reports from other research groups have referred to LGR5 as a particularly troublesome marker and hard to visualize using standard immunofluorescence. Furthermore, these groups have also tried, with no success, to develop their own reporter or replicate the models described by Wells, Clevers, and Sato.

Combined, these reports and the results from our work, highlight the need for an alternative marker of the ISC population. A suitable new candidate should exhibit a robust expression that permits the development of antibodies and reporter systems for its visualization using fluorescence microscopy. Transcriptomic analysis of LGR5 cells has proposed two potential candidates that are co expressed alongside with LGR5: OLFM4 and ASCL2 (van der Flier et al., 2009a, 2009b). In situ validation of different putative intestinal stem cell markers confirmed a correlation between the expression of LGR5 and ASCL2, but not OLFM4 (Ziskin et al., 2013). ASCL2 is a WNT-target gene with a self-regulatory feedback loop activated by WNT/R-spondin; it works as a transcription factor involved in the control of self-renewal, proliferation and stemness of ISC (van der Flier et al., 2009a; Schuijers et al., 2015). Furthermore, after ablating the ISC population, the expression of *ASCL2* proved to be essential for the regeneration of the crypt cells evene before *LGR5* (Murata *et al.*, 2020). A recent study reported the generation of a new ASCL2-responsive minigene named STAR (stem cell ASCL2 reporter), to mark the ISC population in intestinal and colonic organoids. The evidence presented showed a clear expression of the reporter in the ISC population within the organoids, colocalizing with LGR5. However, it is important to highlight that the transfection of the reporter was performed in the organoids (Oost *et al.*, 2018; Heinz *et al.*, 2020). It remains to be studied if this reporter can be incorporated into a human pluripotent stem cell line, although the evidence suggests that ASCL2 could be a suitable candidate to replace LGR5.

In addition to this, a study described a signal-enhancing system that might allow to circumvent the issue of the low expression of LGR5, by increasing the signal output produced by the reporter. First, a CRE recombinase is introduced into the final exon of LGR5, instead of a fluorescent protein. Next, a plasmid carrying a fluorescent reporter is introduced into the cells and, following tamoxifen activation, CRE recombinase rearranges the sequence of the reporter to allow for its expression. Assuming a single CRE recombinase can activate several reporter plasmids, this may result in an overall increase in the signal emitted by the cells (Shimokawa et al., 2017).

In conclusion, this chapter has described our attempt to generate an LGR5-GFP reporter cell line, using CRISPR/Cas9-mediated genome edition, to produce a model that allowed the visualization of the LGR5+ ISC and CSC population. Our work confirmed the expression of LGR5, on a transcriptional level, in miFF1 and CaCo-2 cells; however, we could not detect the presence of the receptor using commercial anti LGR5 human monoclonal antibodies in control cancer cell lines of the intestinal epithelium. We succeeded in assembling an LGR5-GFP expression cassette flanked by homology arms directed to the final exon of the LGR5 gene, but our efforts to introduce and express it in miFF1 and CaCo-2 cells were unsuccessful. It is still unclear why this particular receptor poses such constraints. However, in the aftermath of these results, we have identified alternative approaches that may overcome these limitations in future experiments. In the future, the constructs presented here will be used in the laboartory to generate cell lines which could be applied in validating the role of small molecules in an organoid model and this could be exploited in further publications.

CHAPTER 5. PRELIMINARY SMALL-MOLECULES HIGH-THROUGHPUT SCREENING FOR THE IDENTIFICATION OF COMPOUNDS WITH AN EFFECT ON THE CELL CYCLE USING CaCo-2 CELLS AS A MODEL FOR THE INTESTINAL EPITHELIUM

5.1 Introduction

5.1.1 Current obstacles on colorectal cancer drug discovery

CRC is the third most common cancer and the second leading cause of cancer-related mortality (Karim & Huso, 2013); however, the development of new therapies is remarkably difficult and expensive. It has been estimated that new drugs take between 10 to 15 years to get approved, with an average cost of 2.6 billion USD (DiMasi *et al.*, 2016). On top of this, recent reports have indicated that less than 10% of new antineoplastic drug candidates commencing Phase I of clinical trials, would eventually be approved by regulatory authorities such as the Food and Drug Administrations (FDA) (Nass *et al.*, 2018). To overcome this issue, current approaches have explored the repurposing of drugs which have already been granted FDA approval, and incorporate them into new chemotherapy regimens (Lo *et al.*, 2017*a*; Nowak-Sliwinska *et al.*, 2019).

The operative premise of current antineoplastic agents is to target rapidly dividing cells, assuming this will have a greater effect on cancer cells than on somatic cells. However, this assumption does not account for the fact that adult stem cells, such as the ones in the GI tract, also constitute a rapidly dividing population. Therefore, even if chemotherapeutic compounds do not directly exert an effect on differentiated somatic cells, the ablation of the adult stem cell population could be just as detrimental (Thirumaran *et al.*, 2007; Yu, 2013). Chemotherapy-induced enterotoxicity (CIE) describes an array of adverse effect caused by antineoplastic drugs such as 5-fluorouracil, irinotecan, and EGFR inhibitors (Leibowitz *et al.*, 2018). Common manifestations of CIE include depletion of the active ISC population, intestinal mucositis, inflammation, nausea, vomiting, abdominal cramps, GI bleeding, diarrhoea, and constipation (Davila & Bresalier, 2008). Furthermore, the severity of these adverse effects might limit the dose of chemotherapy regimens, resulting in extended periods of treatment, propension to secondary infections, development of resistance mechanisms by the CSC population, and an overall reduction in the quality of life of the patients (Lee *et al.*, 2014; Miranda Pessoa *et al.*, 2018). These highlights the need for the development, not only of new alternatives to combat CRC, but complementary therapies to combat the side effects caused by the same chemotherapy (van der Vorst *et al.*, 2015).

5.1.2 HIOs in the study of CRC and drug discovery

Current understanding of the onset, development and treatment of CRC, is still hampered by the limitations of the existing models of the intestinal epithelium; hence, the development and implementation of new better models for drug discovery can significantly reduce the time and cost spent on the generation of new therapies. (Szabó & Merks, 2013; Sottoriva *et al.*, 2015).

Organoids technology has emerged as a novel alternative providing significant advantages over other modelling systems, such as: (i) three-dimensional organization and development of major microarchitectural features; (ii) heterogeneous representation of the main cell types from the tissue; (iii) can be derived from adult or pluripotent human stem cell, thereby overcoming interspecies translational constraints; (iv) allow for a personalized medicine approach, since it is possible to isolate healthy and cancerous tissue from the same patient (Ranga *et al.*, 2014; Yin *et al.*, 2016; Gilazieva *et al.*, 2020).

Previous works have reported the use of healthy colonic organoids to study the phenotypical impact of single mutation in key genes (*APC*, *KRAS*, *SMAD4*, and *TP53*) linked to colorectal carcinogenesis (Matano *et al.*, 2015). Nevertheless, this model merely describes a small subset of mutations and does not compare with the large heterogeneity of mutations found in an actual tumour. In response to this, previous works have described the generation of patient-derived tumour organoids (PDTOs) obtained from CRC biopsy samples. This model is capable of recapitulating the complex genetic background of a tumour, in a setting compatible with HTS application (Sachs & Clevers, 2014; Zanoni *et al.*, 2020; Kim *et al.*, 2020). Furthermore, the generation of large biobanks of PDTOs has provided a vast source of epidemiological information. This has allowed the establishment of gene-drug associations, revealing new links between complex multigenic interactions and the sensitivity to specific chemotherapeutic agents. Moreover, it is expected that this could contribute in the development of more efficient therapies targeted to specific subpopulations with common genetic characteristics (Van De Wetering *et al.*, 2015).

Organoid models are not without limitations, some of the most significant being: (i) long time and high cost of production; (ii) limited availability of source material, in the case of enteroids and PDTOs; (iii) lack of immune system, vascularization, and microbiota; (iv) some cell types may be absent or underrepresented, requiring of additional maturation steps; (v) limited access to the luminal compartment of the organoid; (vi) *ex vivo* cultures of PDTOs do not undergo the same stream of genetic alterations that occurs to the parental tumour *in vivo*; (vii) batch-to-batch variability could have an impact in the reproducibility of the results; and (viii) difficulties in the data collection stage,

as their three-dimensional configuration hinders the obtention of an accurate readout, particularly when using fluorescence outputs (Sachs & Clevers, 2014; Fang & Eglen, 2017; Kim *et al.*, 2020).

Our optimized model of HIOs represents a new option for screening applications in the intestinal epithelium. This model could be applied in the study of the normal physiology of the ISC population, the crosstalk between the ISC niche and the mesenchymal compartment, and their involvement in colorectal carcinogenesis. Nevertheless, in spite of our modifications, at the moment its use in HTS still poses considerable limitations. Furthermore, the generation of large quantities of HIOs to the scale required for HTS, is still significantly expensive. Alternatively, in the early phases of drug discovery, the model of CaCo-2 culture remains as the gold standard for drug screening assays (Tan *et al.*, 2018; Keemink & Bergström, 2018). Therefore, regardless of the limitations previously addressed in this work, we have opted for the use of CaCo-2 cells to perform a pilot HTS assay, in order to obtain preliminary data which can be further validated in our model of HIOs.

5.1.3 Study of cell cycle hallmarks on intestinal and cancer stem cells

The cell cycle has been extensively studied for its potential in the discovery of new therapeutic targets and the development of anticancer drugs. Particularly the length and proportion of cells going through the G1 phase, has been recognized as a hallmark of carcinogenesis in CSCs (Hanahan & Weinberg, 2000); but has also been linked to proliferation and fate determination in non-malignant stem cells (Calder *et al.*, 2013; Soufi & Dalton, 2016).

Cancer cells exhibit a truncated G1 phase compared to normal cells, the explanation for this suggests that a shorter G1 allows the cell to circumvent quality control checkpoints, and ignore antiproliferative and/or pro apoptotic signals (Hanahan & Weinberg, 2000). CSCs are a particularly elusive population which exhibit both stem-like properties and tumorigenic potential; hence, it is solely capable of regenerating a tumour. CSCs exist in a quiescent state, which protects them from antiproliferative drugs, and does not re-enter the cell cycle unless indicated by external stimuli. This has raised the need for new chemotherapeutics to either target the quiescent populations, or force the cells to re-enter the cell cycle and arrest them in a vulnerable state, such as G1 (Chen *et al.*, 2016).

LGR5 has been found expressed in CSCs from breast, colon, glioblastoma, and neuroblastoma, where it has been found to amplify WNT signalling. Studies in neuroblastoma have found that downregulation of LGR5 led to reduced MEK/ERK signalling, resulting in G1 cell cycle arrest. This work identified a link between LGR5 expression and the cell cycle. In this scenario, LGR5 is expressed at low levels during early G1, reaches its maximum expression at the transition point G1/S, and decreases its expression through the S phase. Overall, this evidence reveals a potential mechanism for controlling

the proliferation of CSCs driven by LGR5 through pharmacological regulation of the G1 phase (Vieira *et al.*, 2015).

On the other hand, the cell cycle of hESCs is characterized by shortened G1 phase and 65-70% of the cell population in S phase. The main explanation for the truncated G1 phase, is to reduce the exposure to differentiation signals from the microenvironment, and rapidly initiate DNA replication thereby accelerating the rate of cell proliferation (Becker *et al.*, 2006; Soufi & Dalton, 2016). It has been proposed that during the G1 phase, cells are uniquely receptive to extracellular signals, which could potentially push them toward differentiation. This has been explained through several molecular mechanisms, such as: (i) a permissive configuration of the chromatin; (ii) primed epigenetic landscape; and (iii) recruitment of transcription factors (Dalton, 2015).

Further studies in hESCs have identified the complex cyclin D – CDK4/6 as a potential responsible for facilitating differentiation during G1. This complex promotes the recruitment and nuclear translocation of transcriptional co repressor and/or co activator proteins in charge of the expression of developmental genes. This work has found that a gradient of cyclin D across the G1 phase is responsible for the formation of different germinal lineages. In this scenario, low expression of cyclin D, during early G1 phase, resulted in the formation of endoderm. Meanwhile, high levels of cyclin D, in late G1, led to the formation of neuroectoderm. Moreover, lengthened G1 phase resulted in a higher percentage of cells in early G1, thus, resulting in a higher probability of endodermal differentiation. This highlights the role of cell cycle modulators in inducing and controlling the differentiation process and terminal fate determination; also the potential applications of G1 length as a predictive marker for differentiation (Pauklin & Vallier, 2013; Pauklin *et al.*, 2016).

Additional studies in a model of mouse ESCs found that G1 lengthening, on itself, was insufficient to trigger a differentiation program; however, it plays a role in facilitating this process (Li *et al.*, 2012). Further studies showed that in adult/neural stem cells, inhibition of CDK4 (G1 lengthening) led to an increased differentiation output. Interestingly, this was phrased as "an increase in the likelihood of commitment", rather than as a direct consequence from G1 modulation (Roccio *et al.*, 2013).

Furthermore, a recent study found that LGR5^{+} ISCs exist in an unlicensed state of G1. In this model, licensing proteins MCM2-7 are present in cells, but not bound to the DNA. This unlicensed 'stand-by' period results in an uncharacteristic lengthening of G1 in which the cells could: (i) return to the normal cell cycle and replicate; (ii) undergo differentiation in response to signalling cues from the ISC niche, such as EGF, WNT, and NOTCH; or (iii) enter a deep state of quiescence (G0) due to the degradation of MCM proteins after a long period of G1 arrest, which also explains the origin of the '+4' quiescent

ISCs. Moreover, it has also been speculated that the lengthening of G1 might be necessary to allow for the accumulation of cell fate determinants. This might have been developed as a mechanism to better assess the needs of the environment, and whether if the external conditions are sufficient to demand the transition into differentiation, or if self-renewal is still a better path (Carroll *et al.*, 2018).

The duality on the significance of the G1 phase makes it an ideal target to measure the output of our HTS assay, using a cell cycle reporter. Consequentially, compounds capable of modifying the length of G1 could potentially be repurposed and used as cell cycle modulators in both ISCs and CSCs.

5.1.4 Development of cell cycle reporters

The Fluorescent Ubiquitination-based Cell Cycle Indicator (FUCCI) is a dual-colour oscillatory cell cycle reporter that allows live imaging and spatiotemporal observations of cell cycle patterns. The original design of FUCCI consisted of a green and red fluorescent reporter alternating their expression at different phases of the cell cycle. The green fluorescent reporter consisted of a monomeric Azami Green (mAG) fused to the 110 amino acids N-terminus of human Geminin (hGem). The hGem fragment tagged the reporter for degradation at the end of the M phase and prior to the beginning of G1; therefore, the green fluorescence was only detectable during the S/G2/M phases of the cell cycle. A second construct expressed the red fluorescent reporter monomeric Kusabira Orange 2 (mKO2) during the G1 phase. The mKO2 was tagged with amino acids 30-120 of human CDT1, leading to its degradation at the end of G1. Furthermore, a yellow fluorescence was detected at the transition point between G1 and S phase. This occurred due to an overlap between to the complete degradation of mKO2-hCDT1$_{30-120}$ and the beginning of the expression of mAG-hGem$_{1-110}$ (Sakaue-Sawano *et al.*, 2008).

A new version of FUCCI was designed to monitor variations in the cell cycle of hESCs, particularly in the length of the G1 phase. Since hESCs tend to display mosaic expression of transgenic reporters, it was difficult to obtain an accurate readout of the expression of mKO2-CDT1 during G1 (Calder *et al.*, 2013). Therefore, the chromatin marker H2B-GFP was used to confirm the ubiquitous expression of the reporters and track the cells along the entire cell cycle (**Figure 5.1A**). In this instance, mKO2-CDT1 was inserted downstream from the sequence of H2B-GFP. The two reporters were separated by a F2A self-cleavage peptide sequence to allow a bicistronic transcription with a simultaneous, but separate translation. Additionally, a puromycin selection cassette was linked downstream from the reporters, and an IRES site was used to regulate its translation independent from the reporters. The whole construct was incorporated into a pCAG expression vector, leaving the dual reporter cassette under the control of the CAG ubiquitous promoter (**Figure 5.1B**) (Calder, 2011; Calder *et al.*, 2013).
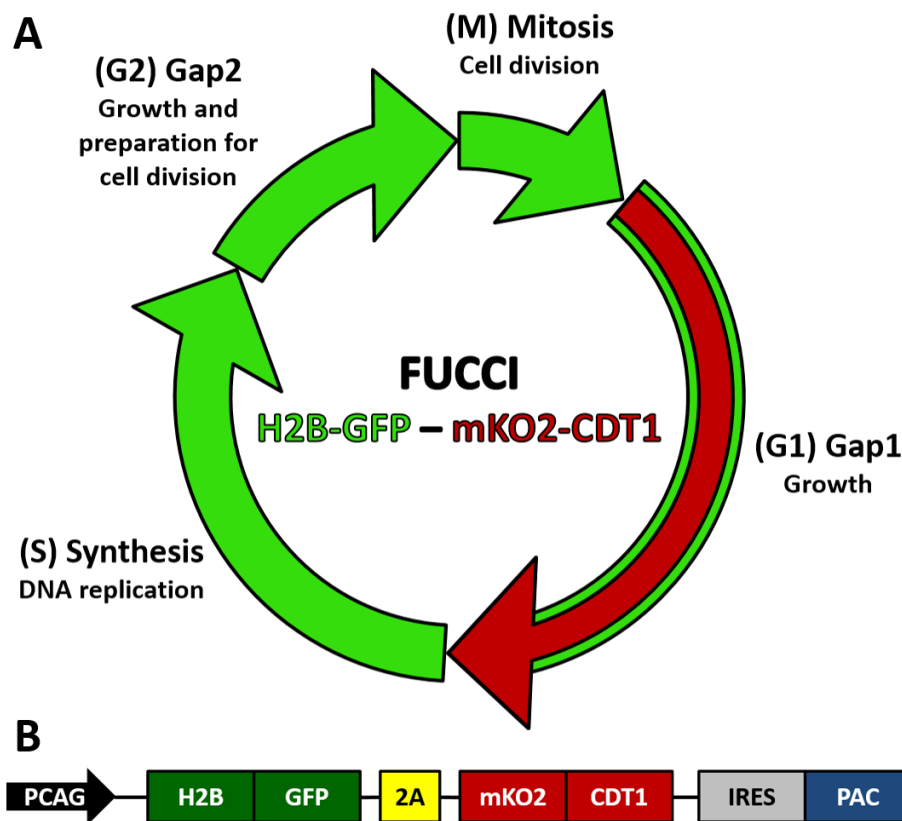
Figure 5.1 FUCCI expression cassette developed by Calder *et al.* (2013)
(A) In this system, the two reporters are simultaneously expressed: H2B-GFP (green) is active through the entire cell cycle, while mKO2-CDT1 (red) is only detected during G1 phase. (B) This version of FUCCI was designed for the bicistronic transcription of H2B-GFP and mKO2-CDT1 on the backbone of a pCAG vector. Also, a puromycin N-acetyltransferase (PAC) gene was inserted downstream from the reporters to allow the generation of stable cell lines.

5.1.5 Study and applications of FUCCI reporters

The visualization of cell cycle events within solid tumours may provide outstanding information regarding their physiology and response to anticancer agents. However, since fluorescent proteins require the oxidation of the chromophore as part of their maturation process, the hypoxic microenvironment of the tumours poses a significant obstacle for their implementation. Furthermore, the fluorescence from FUCCI has been reported to disappear under hypoxic conditions. This was explained due to the normal degradation of existing fluorescent proteins and the synthesis of new non-oxidized proteins unable to contribute to the fluorescence (Kaida & Miura, 2012*a*). Subsequent studies found that mKO2-CDT1 was particularly more dependent on oxygen than mAG-hGem (Kaida & Miura, 2012*b*). Additionally, other reports revealed that hypoxia led to inconsistencies between the DNA content and the cell-cycle progression based on FUCCI expression patterns (Goto *et al.*, 2015).

Early studies sought to assess the correlation between the fluorescence kinetics of FUCCI and the cell cycle dynamics, both in normal conditions and upon exposure to different stimuli. The initial

experiments tested different anticancer agents due to the potential applications of FUCCI in the study of cancer biology. Exposure to X-rays and hydroxyurea showed the expected expression pattern, i.e. the accumulation of Geminin/green fluorescence, and absence of CDT1/red fluorescence (Kaida *et al.*, 2011). Another study found that the effect of different chemotherapeutic agents over the cell cycle varied depending on the concentration of the drugs, the cell lines it was used on, and also the phase of the cell cycle on which the drugs were added (Sakaue-Sawano *et al.*, 2011).

Interestingly, further studies found that anti-microtubule agents such as nocodazole (Kaida *et al.*, 2011), plinabulin (Honda-Uezono *et al.*, 2012), and KPU-300 (Okuyama *et al.*, 2015), provoked aberrant expression of mKO2-CDT1 on cells arrested in M phase. The proposed explanation suggested that the cell cycle disruption affected the activity of E3 ligases responsible for the degradation of the FUCCI reporters. These studies provided essential information regarding potential flaws with this system, and that the effect of some compounds may result in a misleading output from the G1 reporter

The FUCCI reporter is a simple and robust system that allows monitoring variations in the cell cycle. Therefore, we have generated a cell line of CaCo-2 cells expressing the FUCCI reporter comprised by 2 components: a constitutively expressed H2B-GFP present through the entire cell cycle, which allows us to track the cell and the chromatin status; and the mKO2-CDT1 reporter, which is only present during G1 phase, after which the CDT1 portion tags it for degradation in the S phase (Sakaue-Sawano *et al.*, 2008; Calder *et al.*, 2013).

We have applied this model of FUCCI-CaCo-2 cells to perform HTS of small-molecules that display an effect over the cell cycle, particularly G1 phase, as it has shown to be critical in stem cell differentiation, and is also a potential target for cancer therapy. We envision that the hits found in this screening, can be further validated, and used for: (i) Drug repurposing as potential antineoplastic agents, and/or as a parallel treatment to ameliorate the effects of chemotherapy over the intestinal epithelium, in order to assist the regeneration of the epithelium upon damage from the chemotherapy; and (ii) incorporate these compounds in the differentiation protocol for the generation of HIOs, in order to obtain a more biologically accurate screening model.

5.2 Results

The aim of this chapter was to perform a preliminary HTS on FUCCI-CaCo-2 cells, using a commercially available library of compounds and evaluate their effect over the cell cycle, specifically the G1 phase. This part of the cell cycle has been specifically targeted due to its association with cancer, but also as an indirect marker related to the differentiation of intestinal stem cells.

Prior to performing the screening, it was necessary to generate an efficient, reliable, and economic system to obtain a read out of the results. The use of antibodies for a screening of this magnitude was not feasible, therefore, to evaluate the effect of the library of compounds on the cell cycle of the intestinal epithelium we generated a stable cell line of CaCo-2 cells for the expression of a cell cycle reporter. CaCo-2 cells were transfected with the FUCCI reporter developed by Calder *et al.* (2013). As mentioned before this is contains G1 phase-specific reporter (**Figure 5.2**).

CaCo-2 cells were nucleofected with the FUCCI reporter and a stable cell lines was generated after two weeks on selection medium with puromycin. FUCCI-CaCo-2 cells were treated the TocrisTotal library of bioactive compounds, and a subset of handpicked compounds, which we have selected due to their potential applications in HIOs (*See Chapter 2. Materials and methods*). The full library was plated out into 4 384 well plates and processed in triplicate. The preparation of the screening was performed following the pipeline described in **Figure 5.3**. Next the data collected from the high-content imaging, was analyzed using MetaXpress software for high content analysis. The details regarding the algorithm and the design of the masks for cell sorting are outlined in **Figure 5.4.**
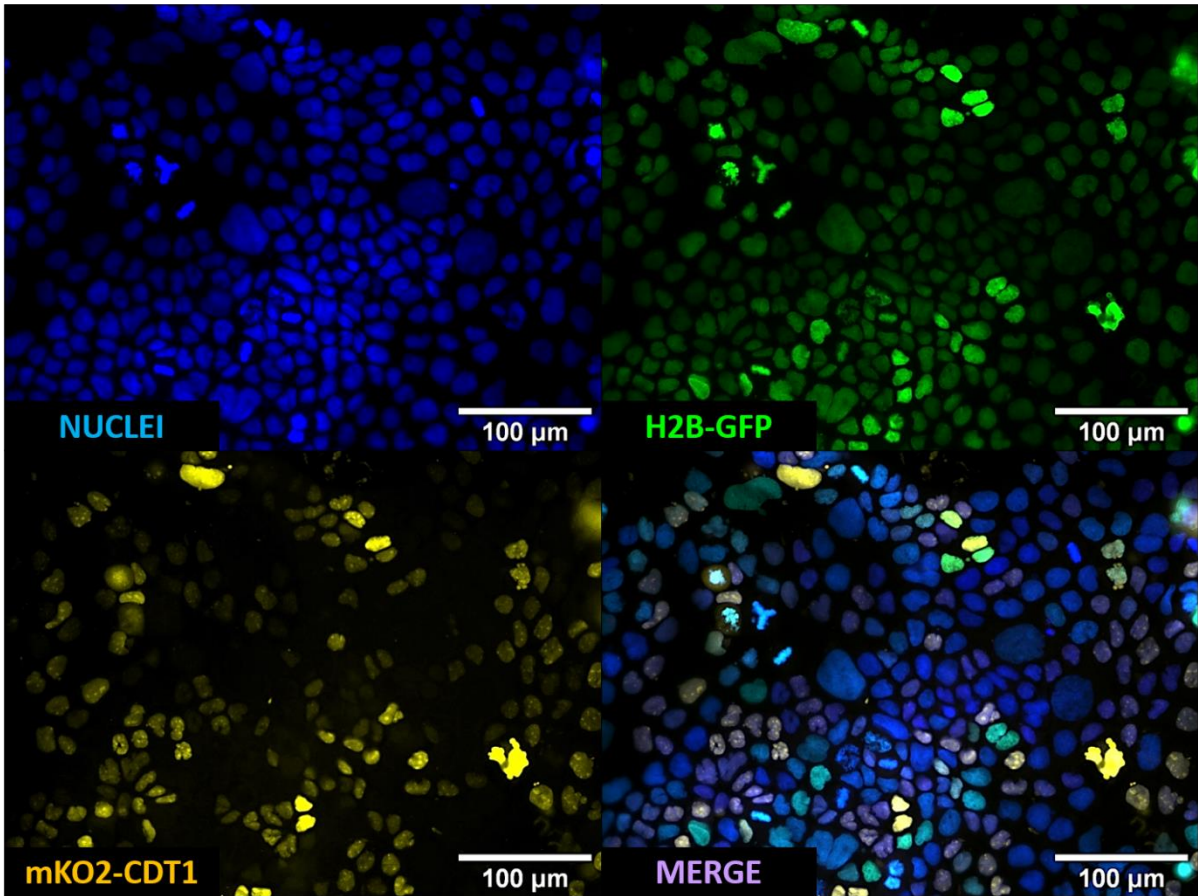
Figure 5.2 FUCCI-CaCo-2 cell reporter expression.
CaCo-2 cells were transfected with a FUCCI expression plasmid. The nuclei of the cells (blue) colocalized with H2B-GFP (green) constitutively labelling the chromatin, and mKO2-CDT1 (yellow) the G1 phase-specific reporter.
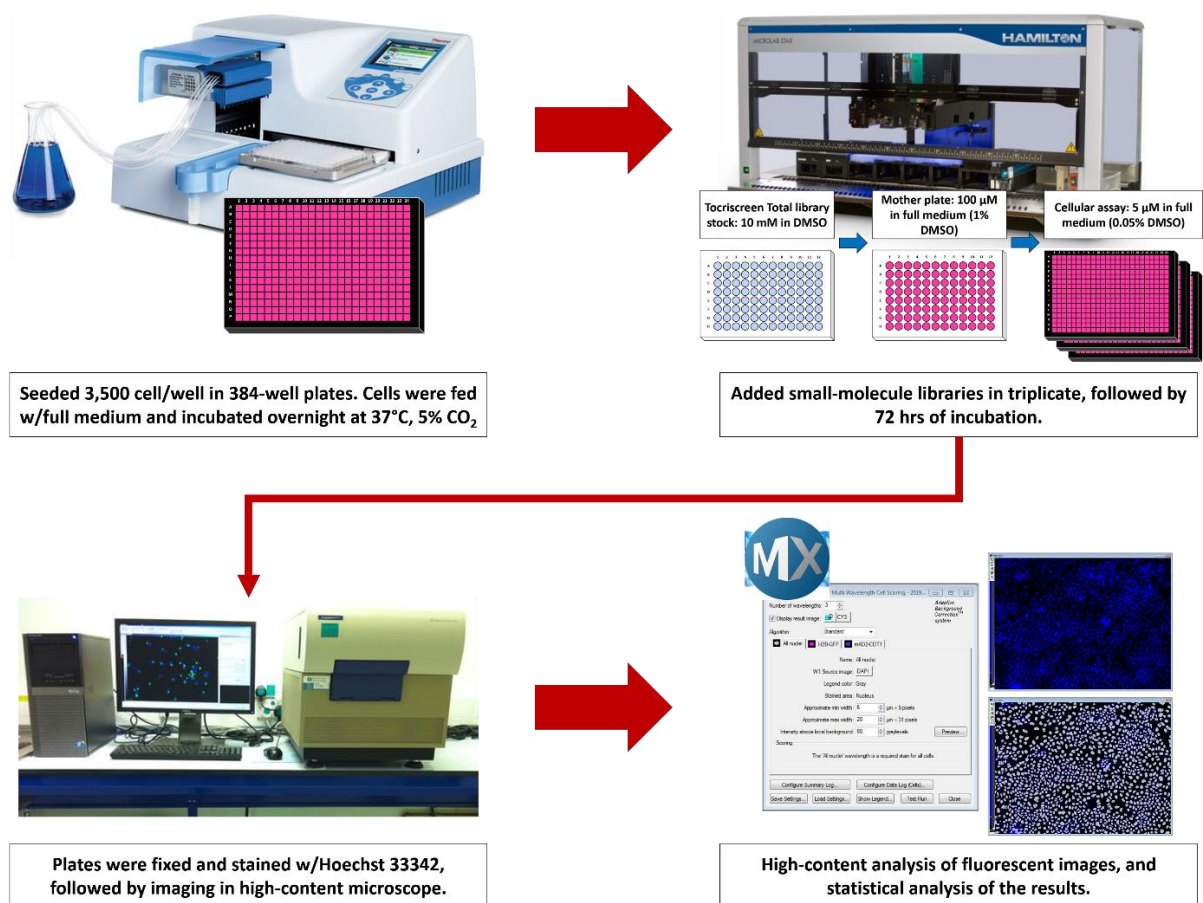
Figure 5.3 Work pipeline for the high-throughput small-molecule screening.
First, CaCo-2 cells were seeded on 384-well plates using a MultiDrop™ automated dispensing system; enough plates were prepared to cover the entire Tocriscreen Total compound library collection by triplicate. Next, a Microlab STAR Liquid Handling System was used to prepare diluted mother plates from the stock library of compounds. The mother plates were used to dispense the compounds into the cells at a final concentration of 5 µM, and an equivalent of 0.005% of DMSO carried over from the stock solutions. After 72 hrs of incubation, the cell cultures were fixed and using automated plate washers and the nuclei were stained with Hoechst 33342. The imaging was performed with an ImageXpress Micro high-content imaging system, and the images were analyzed with the MetaXpress high-content analysis software.

The controls of the screening were selected using the vehicle in which the compounds were reconstituted: DMSO, water and ethanol. These were included in random positions within the plates. The threshold of significance was established using a normalizing control placed at position A2 in all the plates. The z-scores were calculated following the formula below, the mean value of the plate is subtracted to each individual value of the samples and then divided by the standard deviation of the plate.

$$z = \frac{x - \mu}{\sigma}$$

The threshold of significance was set at +/- 2.5 standard deviations from the mean z-score of the plates, any outliers which fell outside this range were selected as hits.

The data was evaluated in 5 analysis streams:

Experiment 0: Consists of the total cell count, the output of this data is also used for the normalization of the other 4 experiments. In terms of the biological interpretations, an increase above the threshold of significance might indicate the treatment induced cell proliferation, whereas a lower z-score could indicate cytotoxicity or induction of apoptosis.

Experiment 1: Indicated the percentage of cells expressing the reporter mKO2-CDT1. Biologically speaking, mKO2-CDT1 represents the subpopulation going through G1 phase of the cell cycle; increase above the normal indicate cell cycle arrest in G1 phase; in contrast a decrease below the normal might suggest cell cycle arrest in a different phase or an early transition into S phase, which could be interpreted as the cells ignoring some checkpoints due to the stimulation of proliferation signalling pathways or the insensitivity toward antiproliferative signals.

Experiment 2: Measured the fluorescence intensity of the reporter mKO2-CDT1. The biological interpretation of this parameter indicates the turnover cycle of representative proteins (CDT1) from G1 phase. Increase above the normal suggest the accumulation of the protein which might be caused by an affection towards the degradation complex; however, a decrease below the normal could indicate a rapid protein turnover and possibly an early transition into S phase and/or the induction of cell proliferation.

Experiment 3: Indicated the percentage of cells expressing the reporter H2B-GFP. Normally it allows us to confirm the successful integration of the reporter into the genome. An increase in the percentage could be due a higher number of cells undergoing division which could lead to an increase in the numbers of particles detected. Decrease below the normal might be caused due to loss/silencing of the reporter or an increase in cell death.

Experiment 4: Measured the fluorescence intensity of the reporter H2B-GFP. Biologically speaking, H2B-GFP labels the chromatin and its expression is persistent through the entire cell cycle. Increase above the normal indicate the condensation of the chromatin during mitosis or the duplication of the genetic material during S- and G2-phase; in contrast a decrease could be due to an overall decrease in the H2B-GFP population caused by an increase in cell death.
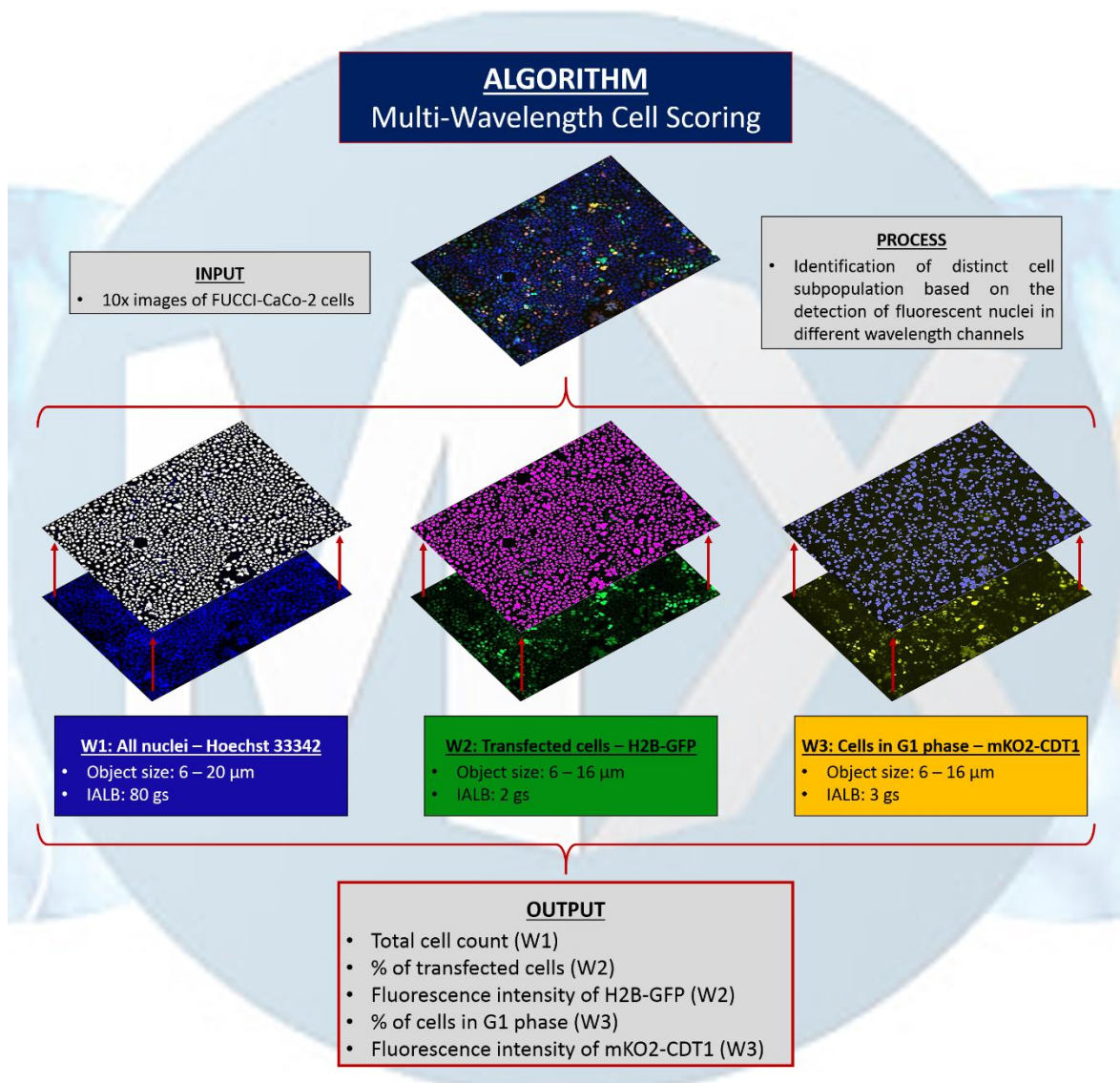
Figure 5.4 Multi-Wavelength Cell Scoring (MWCS) algorithm for the identification of distinct subpopulations of FUCCI-CaCo-2 cells.
The data collected from the screening consisted of 10x images in three different wavelength channels of CaCo-2 cells expressing the FUCCI reporter. All the nuclei were stained with Hoechst 33342 and imaged using the DAPI/blue channel; transfected cells ubiquitously expressed H2B-GFP, shown in the GFP/green channel; cells in G1 phase expressed the mKO2-CDT1 reporter and were imaged through the Cy3/yellow channel. Images were analyzed using the MWCS algorithm and the sorting masks were set to detect the fluorescent nuclei in the different channels. This led to the identification of different subpopulations based on their cell cycle status. The output showed variations in the proportion and fluorescence intensity from the cells in G1 phase. *W: wavelength; IALB: intensity above local background; gs: graylevels.*

To understand the data and quality control it for abnormalities, a number of graphical representations were done to assess the results. The results from Experiments 1 (**Figure 5.5**), 2 (**Figure 5.6**), 3 (**Figure 5.7**), and 4 (**Figure 5.8**) are displayed in three forms: (A) Heat map, a bidimensional representation showing whether the variations in the Z-score were above or below the mean, and the distribution of the hits across the plate to identify potential positional bias in the occurrence of the hits. (B) Intensity plot to confirm the normal distribution of the data and visualize the presence of outliers, which constitute the hits from the screening. (C) Q-Q plot contrasts the theoretical predictions vs experimental results from the screening.

The pattern displayed by Plate 4 was due to an incorrect placement of the plate in the automated dispensers. These samples were not treated with the small molecules library and were not considered during the selection of hits.
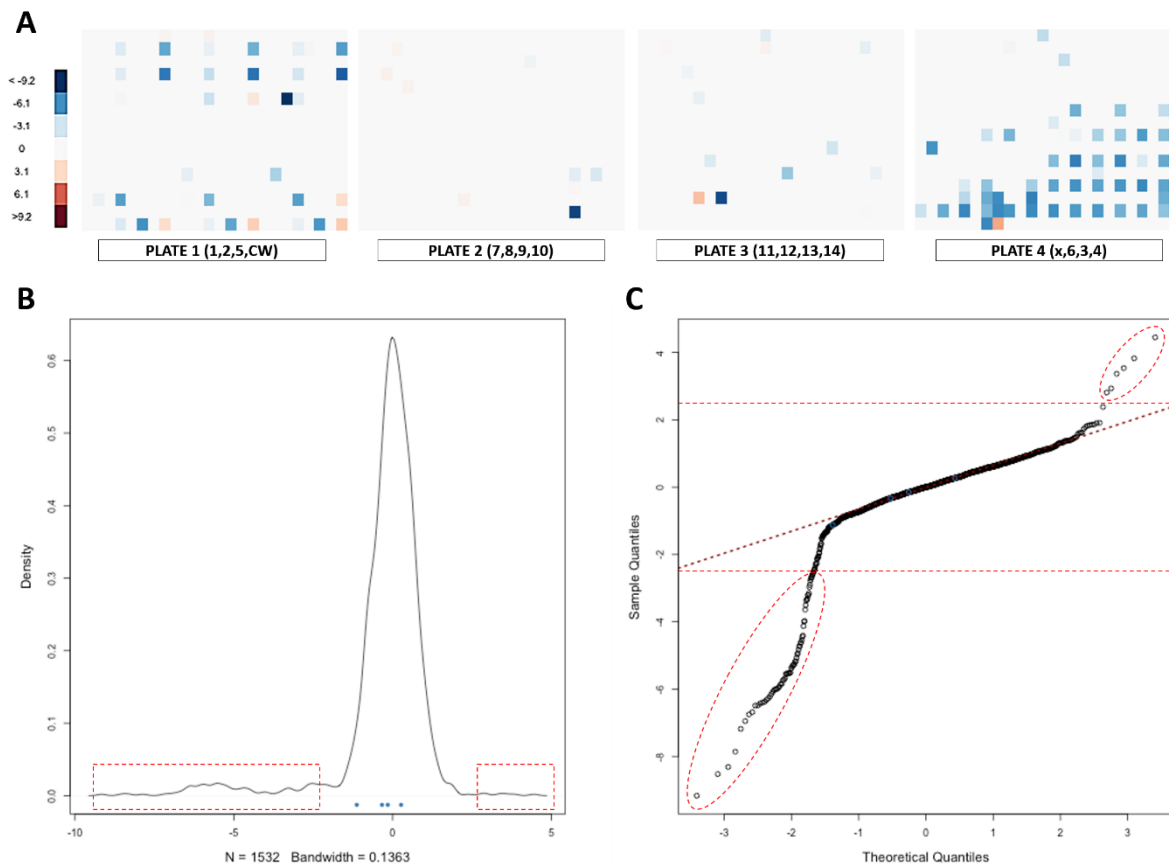
Figure 5.5 Potential hits with an effect in the percentage of cells in G1 phase.

HTS experiment 1 measured the percentage of FUCCI-CaCo-2 cells in G1 phase, based on the expression of the reporter mKO2-CDT1. Hit sorting was performed selecting the outliers where z-scores fall outside of the cut off threshold of +/- 2.5 standard deviations from the mean. (A) Heat map showing the distribution of the hits and their scoring intensity across the plate. Shading annotations based on standard deviation values: blue < 0 < red; (B) Density plot showing a normal distribution of the z-score values from all the compound included in the screening. X-axis represents standard deviations from the mean (C) Q-Q plot showing the correlation between the theoretical predictions and the experimental z-scores obtained from all the compounds assessed in the screening. The potential hits are highlighted (----) in both plots.
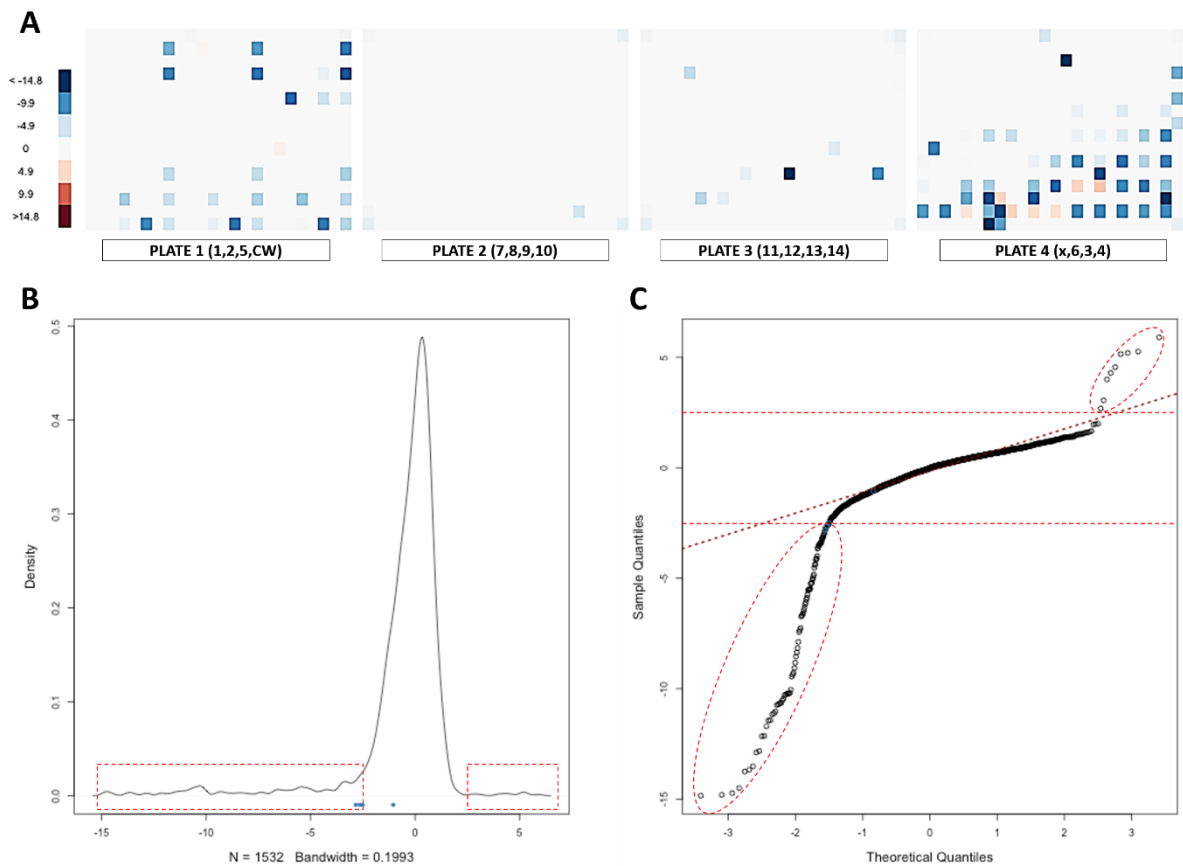
Figure 5.6 Potential hits with an effect in the RFI of the reporter mKO2-CDT1.
HTS experiment 2 measured the RFI of the reporter mKO2-CDT1 in FUCCI-CaCo-2 cells. Hit sorting was performed selecting the outliers which z-scores fall outside from the cut off threshold of +/- 2.5 standard deviations from the mean. (A) Heat map showing the distribution of the hits and their scoring intensity across the plate. Shading annotations based on standard deviation values: blue < 0 < red. (B) Density plot showing a normal distribution of the z-score values from all the compounds included in the screening. X-axis represents standard deviations from the mean. (C) Q-Q plot showing the correlation between the theoretical predictions and the experimental z-scores obtained from all the compounds assessed in the screening. The potential hits are highlighted (----) in both plots.

Figure 5.7 Potential hits with an effect in the percentage of cells expressing H2B-GFP.
HTS experiment 2 measured the percentage of FUCCI-CaCo-2 cells expressing H2B-GFP. Hit sorting was performed selecting the outliers which z-scores fall outside from the cut off threshold of +/- 2.5 standard deviations from the mean. (A) Heat map showing the distribution of the hits and their scoring intensity across the plate. Shading annotations based on standard deviation values: blue < 0 < red. (B) Density plot showing a normal distribution of the z-score values from all compounds included in the screening. X-axis represents standard deviations from the mean. (C) Q-Q plot showing the correlation between the theoretical predictions and the experimental z-scores obtained from all the compounds assessed in the screening. The potential hits are highlighted (----) in both plots.

Figure 5.8 Potential hits with an effect in the RFI of the reporter H2B-GFP

HTS experiment 4 measured the RFI of the reporter H2B-GFP in FUCCI-CaCo-2 cells. Hit sorting was performed selecting the outliers which z-scores fall outside from the cut off threshold of +/- 2.5 standard deviations from the mean. (A) Heat map showing the distribution of the hits and their scoring intensity across the plate. Shading annotations based on standard deviation values: blue < 0 < red. (B) Density plot showing a normal distribution of the z-score values from all compounds included in the screening. X-axis represents standard deviations from the mean. (C) Q-Q plot showing the correlation between the theoretical predictions and the experimental z-scores obtained from all the compounds assessed in the screening. The potential hits are highlighted (----) in both plots.

From an original total of 1536 compounds (controls included) analyzed in the screening, a subset of 27 hits were selected for showing a statistically significant effect in at least one of the parameters measured, based on the z-score values. These compounds were divided in 8 different subgroups based on their general molecular mechanism of action (MMOA) (**Table 5.1**): (i) DNA topoisomerase inhibitors; (ii) Protein inhibitors; (iii) Antimicrotubule agents; (iv) Nucleoside analogues; (v) Antioxidants; (vi) Neuroactive drugs and ion channel blockers; (vii) Other signalling pathway effectors; (viii) Others (MMOA not defined).

From the selected 27 compounds: 16 have known antineoplastic effects (Groups I, II, II, IV, V); at least 10 drugs (CPT, SN38, DBN, HHT, VBL, VCR, DTB, CFB, DAS, and MTX) have directly or indirectly (through a modified derivative compound) been approved for the treatment of different types of cancer; and the remaining 6 compounds (BFA, CCN, DAPT, VA, CR8, BIBU) have mechanisms of action involved in the regulation of cell proliferation and/or apoptosis.

Group VI consisted mostly of neuroactive compounds indicated for the treatment of psychiatric and neurodegenerative conditions, and ion channel inhibitors used for the modulation of cardiac and skeletal muscle contractions. These compounds had no reported relationship with either the intestinal epithelium or the cell cycle.

Groups V and VIII are not directly associated with the intestinal epithelium, but through some indirect mechanism might exert some influence over the cell cycle. The information about these compounds was scarce, but they appeared to have no direct association with DNA replication, protein synthesis, cell division nor with any of the main signalling pathways involved in the control of cell proliferation, differentiation, and apoptosis (WNT, NOTCH, MAPK, among others.)

Table 5.1. presents a breakdown of the hits and the z-scores obtained for each parameter; N.E. (no effect) was used when the value fell within the pre-established threshold of significance (+/- 2.5 standard deviations of the mean). This is followed by a brief description of the compounds, their MMOA, and an interpretation of the values from the table. The information of the compounds was obtained from public access databases: https://www.drugbank.com/ and https://pubchem.ncbi.nlm.nih.gov/. Further analysis of the results is provided in the discussion section.

Compounds	Total cell count	% of H2B-GFP$^+$ cells	Intensity of H2B-GFP$^+$ fluorescence	% of mKO2-CDT1$^+$ cells	Intensity of mKO2-CDT1 fluorescence
I. *DNA topoisomerase inhibitors*					
Camptothecin (CPT)	-8.27	-5.33	-8.75	-2.95	-4.14
SN38	-5.71	-3.41	-7.03	N.E.	N.E.
Daunorubicin HCl (DBN)	-2.52	N.E.	N.E.	-8.30	-3.51
II. *Protein inhibitors*					
Homoharringtonine (HHT)	-4.41	3.17	-3.91	4.31	-5.31
Brefeldin A (BFA)	-3.94	N.E.	N.E.	-3.43	-4.42
III. *Antimicrotubule agents*					
Vinblastine sulfate (VBL)	-13.58	N.E.	-12.22	-3.12	-15.14
Vincristine sulfate (VCR)	-14.11	N.E.	-12.27	-4.41	-14.39
Colchicine (CCN)	-8.97	N.E.	-8.17	N.E.	-10.15
IV. *Nucleoside analogues*					
Decitabine (DTB)	-2.56	N.E.	N.E.	-2.85	N.E.
Clofarabine (CFB)	N.E.	-2.98	N.E.	N.E.	N.E.
V. *Antioxidants*					
N-acetyl-L-cysteine [500 µM] (NAC)	-7.41	N.E.	-6.49	N.E.	-5.16
Diphenyleneiodonium Cl (DPI)	-2.76	N.E.	-2.54	N.E.	N.E.
VI. *Neuroactive drugs and ion channel blockers*					
ZK 93423 (ZK)	-3.72	N.E.	-3.96	-7.92	-4.63
Ouabain (OUA)	-16.28	N.E.	-10.74	-8.23	-13.45
DNQX	N.E.	N.E.	N.E.	N.E.	-2.51
Dantrolene, sodium salt (DTL)	N.E.	3.26	N.E.	N.E.	N.E.
Linopirdine 2HCl (LPD)	N.E.	2.59	N.E.	N.E.	N.E.
BMY 14802 HCl (BMY)	N.E.	2.82	N.E.	N.E.	N.E.
LY 344864 HCl (LY)	-2.90	N.E.	N.E.	N.E.	N.E.
VII. *Other signalling pathway effectors*					
Dasatinib [20 µM] (DAS)	-14.71	6.19	-9.37	-8.22	-13.80
Methotrexate [100 nM] (MTX)	-6.99	N.E.	-5.64	3.53	-4.52
DAPT [20 µM]	-5.57	3.97	-2.76	N.E.	-4.87
(R)-CR8	-5.02	N.E.	-5.60	N.E.	-5.39
Valproic acid [1 mM] (VA)	N.E.	-2.76	N.E.	-3.50	N.E.
BIBU 1361 2HCl (BIBU)	N.E.	N.E.	N.E.	-2.91	N.E.
VIII. *Others (MMOA not defined)*					
Nicotinamide [20 mM] (NAM)	-6.23	N.E.	-4.54	-5.02	-6.70
Taurodeoxycholic acid [100 nM] (TDCA)	N.E.	N.E.	N.E.	N.E.	-2.56

Table 5.1 Z-score values obtained from the statistical analysis of the data collected from High Content Analysis. Compounds have been classified in groups based on their MMOA.

N.E.: No effect, the z-score for this parameter fell within the threshold of significance, +/- 2.5 standard deviation from the mean

I. DNA topoisomerase inhibitors

Camptothecin (CPT) and its derivative **SN38**, are antineoplastic alkaloids that selectively inhibit DNA topoisomerase type I. CPT is a plant alkaloid isolated from *Camptotheca acuminata*, while SN38 is a liposomal formulation of the bioactive metabolite produced by irinotecan, which is semisynthetic derivative of CPT. Their MMOA consist of stabilizing covalent complexes of DNA and topoisomerase I during the S phase of the cell cycle by; this hinders the religation of single strand breaks, potentially causing double strand breaks which, when encountered by the DNA replication machinery, trigger apoptosis. In our study both, CPT and SN38, showed a decrease in the total cell count, and the percentage and RFI of cells expressing H2B-GFP; however, CPT treatment also led to a decrease in the percentage of cells in G1 phase, and the RFI of mKO2-CDT1, whereas SN38 did not show any effect on these parameters.

Daunorubicin (DBN) is an antineoplastic bacterial anthracycline and aminoglycoside antibiotic isolated from *Streptomyces peucetius*. It has shown to inhibit DNA topoisomerase type II through a similar mechanism as the one described by CPT and SN38, but with no selectivity to any phase of the cell cycle. Additionally, DBN has shown to act as an intercalating agent between base pairs, affects gene expression by inhibiting polymerase activity, and damages the DNA through the production of free radicals. Our results showed DBN decreased: total cell count, percentage of cells in G1 phase, and RFI of mKO2-CDT1; it had no effect in the percentage or RFI of cells expressing H2B-GFP.

I. Protein inhibitors

Homoharringtonine (HHT) is an antineoplastic plant alkaloid isolated from *Cephalotaxus fortunei*, also known for its semisynthetic derivative **omacetaxine mepesuccinate**. It acts as competitive inhibitor of protein synthesis by binding to the A site of 80S ribosomes, thereby preventing the entry of aminoacyl-tRNA and disabling the elongation of the peptide chain. This leads to an overall reduction of oncogenic proteins such as BCR-ABL. In this study, we found that FUCCI-CaCo-2 cells treated with HHT exhibited a decrease in the total cell count, the RFI of H2B-GFP, and the RFI of mKO2-CDT1; notably, the percentage of cells in G1 phase was increased.

Brefeldin A (BFA) is an antibiotic and antiviral fungal macrocyclic lactone isolated from *Penicillium brefeldianum*. It acts by inhibiting the vesicular transport of proteins from the endoplasmic reticulum into the Golgi apparatus. Additionally, by blocking the vesicle formation, BFA treatment eventually leads to the collapse of the Golgi apparatus, triggering the unfolded protein response which results in apoptosis. HTS results showed BFA treatment led to a decrease in the total cell count, the percentage

of cells in G1 phase, and the RFI of mKO2-CDT1; it had no effect in the percentage or RFI of cells expressing H2B-GFP.

II.   Antimicrotubule agents

Vinblastine (VBL), **Vincristine (VCR)**, and **Colchicine (CCN)** are plant alkaloids and antimicrotubule agents with antimitotic activity. VBL and VCR belong to a group of chemotherapeutic compounds known as vinca alkaloids, isolated from *Vinca rosea* currently known as *Madagascar periwinkle*; whereas, CCN is isolated from *Colchicum autumnale*, and is mostly known for its use in the treatment of gout and certain inflammatory diseases. Antimicrotubule agents bind to tubulin during the S phase, inhibiting the polymerization of the microtubules and disrupting the formation of the mitotic spindle. In consequence, this interferes with the appropriate segregation of the chromosomes, leading to cell cycle arrest at the metaphase stage, and eventually resulting in cell death. Alternatively, VBL and VCR can also block cellular utilization of glutamic acid, thereby disturbing the synthesis of proteins and nucleic acids. In our screening assay, VBL and VCR performed strikingly similar, both showing an overall decrease in the total cell count, RFI of H2B-GFP, percentage of cells in G1 phase, and RFI of mKO2-CDT1. The results from CCN treatment were almost the same, except for the percentage of cells in G1 phase, where no significant effect was registered.

III.   Nucleoside analogues

Decitabine (DTB) is an antineoplastic cytidine antimetabolite analogue which upon intracellular phosphorylation is incorporated by polymerases into DNA or RNA strands during the replication or transcription, respectively. The presence of DTB in the nucleotide chains inhibits the activity of DNA and RNA methyltransferases by forming a covalent bond with the enzyme. The hypomethylation disrupts the recruitment of regulatory components involved in the processing of DNA and/or RNA. When the disruption occurs in DNA replication, it leads to S-phase arrest and reports suggest it does not stop the transition from G1 into S phase. Also, DNA hypomethylation could potentially induce differentiation, trigger apoptosis, and restore the normal expression of critical genes such as tumour suppressor genes. The result from our screening showed a decrease in the total cell count and the percentage of cells in G1 phase.

Clofarabine (CFB) is an antineoplastic purine antimetabolite analogue that requires intracellular conversion into a bioactive 5'-triphosphate metabolite. During the S phase, CFB inhibits DNA synthesis through three mechanisms: inhibition of ribonucleotide reductase, terminating the elongation of the DNA chain, and depletion of intracellular dNTPs. Additionally, CFB could potentially damage the mitochondrial membrane, hence releasing pro apoptotic mitochondrial proteins. In spite of the

molecular similarities with DTB, the mechanism of action of CFB is entirely different. Consequentially, HTS results showed CFB had no effect in the total cell count or the percentage of cells in G1 phase, but rather decreased the percentage of cells expressing H2B-GFP.

IV. Antioxidants

N-acetyl-L-cysteine (NAC) is a prodrug absorbed by the intestine where it is processed and converted into L-cysteine. In turn, L-cysteine is a precursor for the synthesis of glutathione, a hepatoprotective antioxidant enzyme. Therefore, NAC has been used to ameliorate the damage caused by ROS, and to counteract the effects of acetaminophen overdose. Additionally, it has been used as a mucolytic agent, and to treat certain psychiatric and neurodegenerative conditions. NAC has shown anti-apoptotic capabilities, and anti-inflammatory properties via inhibition of NF-κB. The results from our study found that cells treated with NAC showed a decrease in the total cell count, the RFI of H2B-GFP, and the RFI of mKO2-CDT1.

Diphenyleneiodonium (DPI) is an inhibitor of NAD(P)H oxidases (NOXs) which has shown to induce cell cycle arrest and apoptosis. A proposed mechanism of action suggested that a consequence of NOXs inhibition is the reduction of ROS and the accumulation of lactic acid; this might lead to lactic acidosis, and cause G2-M cell cycle arrest, which would eventually trigger apoptosis. An alternative mechanism proposed that DPI might induce apoptosis through the upregulation of p53. In our study, DPI decreased the total cell count and the RFI of cells expressing H2B-GFP, but it did not affect the percentage of cells in G1 phase nor the expression of mKO2-CDT1.

V. Neuroactive drugs and ion channel blockers

ZK 93423 (ZK) is a non-benzodiazepine, β-carbonile GABA$_A$ agonist commonly used as an anxiolytic, anticonvulsant, and muscle relaxant. No study has addressed any link between ZK and the GI tract, except for the development of hyperphagia which might be associated with the enteroendocrine cells and the gut-brain axis. However, GABA-mediated stimulation has been associated with S-phase arrest and decreased cell proliferation. The result from our screening indicated that ZK treatment led to a decrease in the total cell count, the RFI of H2B-GFP, the percentage of cells in G1 phase, and the RFI of mKO2-CDT1.

Ouabain (OUA) is a cardiotonic steroid hormone isolated from *Strophanthus gratus*. It is a potent inhibitor of the Na$^+$/K$^+$-ATPase membrane pump and has been commonly used as an anti-arrythmia drug for the treatment of congestive heart failure and chronic atrial fibrillation. OUA has shown pro-apoptotic properties and the proposed mechanism of action has pointed to a mitochondria-mediated

pathway. In this scenario, OUA treatment led to the activation of caspases 3 and 9, ATP depletion and release of cytochrome c into the cytoplasm, resulting in cell death. Alternatively, the antineoplastic activity of OUA has been linked to a ROS-dependent mechanism, and a downregulation of cell adhesion molecules which, in a model of spheroids, has shown to inhibit the tumour growth. Our study found that, similar to ZK, OUA treatment led to a decrease in the total cell count, the RFI of H2B-GFP, the percentage of cells in G1 phase, and the RFI of mKO2-CDT1.

DNQX also known as **FG-9041**, is a competitive antagonist of ionotropic glutamate receptors AMPA and kainate. No association with the GI tract nor potential link with the cell cycle has been reported. In our study, DNQX led to a decrease in the RFI of mKO2-CDT1.

Dantrolene (DTL) also known for its bioactive form **dantrium**, is a hydantoin derivative used as a muscle relaxant in cases of malignant hyperthermia. DTL reduces the intracellular concentration of Ca^{2+} by binding to the ryanodine receptor 1. Interestingly, some evidence has suggested a potential link between DTL and the upregulation of the anti-apoptotic protein BCL2. Regardless, the results from our screening only found an increase in the percentage of cells expressing H2B-GFP, following DTL treatment, but no effect was detected in the other parameters analyzed in this work.

Linopirdine (LPD) is neuroactive drug that inhibits the voltage-gated potassium channels (KCNQ) and triggers the release of acetylcholine. HTS results showed an increase in the percentage of cells expressing H2B-GFP; no effect was detected in the total cell count, RFI of H2B-GFP, percentage of cells in G1 or the RFI of mKO2-CDT1.

BMY 14802 (BMY) and **LY 344864 (LY)** are agonists for the serotonin receptor. LY has been studied for the treatment of migraines; whereas BMY is an antipsychotic drug used in the treatment of psychosis, schizophrenia, and due to its dual activity as an antagonist of the sigma receptor 1 (σ1) has been proposed to control L-DOPA-induced dyskinesia. The information obtained from the databases did not register any direct link between these compounds and alterations in the cell cycle or the GI tract. The results from our study found that BMY treatment provoked an increase in the percentage of cells expressing H2B-GFP, while LY led to a decrease in the total cell count.

VI. Other signalling pathway effectors

Dasatinib (DAS) is a chemotherapeutic dual tyrosine kinase (TK) inhibitor with selectivity for BCR-ABL and members of the SRC family. It has been extensively used for the treatment of chronic myeloid leukaemia which has shown resistance against other TK inhibitors. Other first line chemotherapeutic drugs have focused on the inhibition of BCR-ABL TK, leading to the development of resistance;

however, the dual activity of DAS against BCR-ABL and SRC TKs has offered a new alternative for the treatment of resistant cancers. SRC TKs are involved in proliferation, differentiation, and migration, thereby suggesting a correlation with the malignancy of breast and colon cancer and highlighting the importance of DAS as a chemotherapeutic option. In our study DAS treatment showed a decrease in the total cell count, the RFI of H2B-GFP, the percentage of cells in G1 phase, and the RFI of mKO2-CDT1; additionally, the percentage of cells expressing H2B-GFP was increased.

Methotrexate (MTX), also known as aminopterin, is a chemotherapeutic antimetabolite used in the treatment of different cancers. Also, it has been repurposed as an immunosuppressant for the treatment of rheumatoid arthritis and psoriasis. Its mechanism of action is through the inhibition of dihydrofolate reductase, thymidylate synthase, and other enzymes involved in the synthesis of nucleotides; this results in the inhibition of DNA and RNA synthesis. Screening results showed MTX led to a decrease in the total cell count, and the RFI of both H2B-GFP, and mKO2-CDT1; also, the percentage of cells in G1 phase was increased.

DAPT is an inhibitor of NOTCH signalling which has shown to reduce the levels of β-amyloid aggregates in mouse models of Alzheimer. Its molecular mechanism of action consists of inhibiting gamma secretase from cleaving the intracellular domain of the NOTCH receptor, thereby hampering the signalling cascade. NOTCH signalling regulates the normal proliferation and self-renewal of stem cell populations; however, it has also been associated with the hyperproliferation of cancer cells; therefore, in light of this delicate balance, compounds like DAPT might be suitable candidates for the modulation of the activity of NOTCH signalling pathway. Interestingly, in spite of targeting different pathways, FUCCI-CaCo-2 cells treated with DAPT showed similar results as the ones observed with MTX: a decrease in the total cell count, and the RFI of both fluorescent reporters; although, in this case the percentage of cells expressing H2B-GFP was increased, rather than cells in G1 phase.

Valproic acid (VA), is a synthetic short-chain fatty acid which has been associated with several signalling pathways through different molecular mechanisms: inhibition of histone deacetylases, NOTCH signalling activator, inhibition of nitric oxide synthase, and increased production of GABA. In this work, VA treatment provoked a decrease in the percentage of cells expressing H2B-GFP and the percentage of cells in G1 phase; no effect was detected in the total cell count or the RFI of either fluorescent reporter.

(R)-CR8 also known as **CR8**, a potent inhibitor of cyclin-dependent kinases (CDKs) 1/2/3/5/7/9 with potential pro apoptotic propertied. It is also known for being a stronger synthetic derivative of roscovitine/seliciclib. Its effect with different CDKs results in a broad spectrum of alterations over the

cell cycle and its progression. Roscovitine and CR8, have been studied as potential new therapies against cancer, given that a common feature in several malignancies is the overexpression of CDKs. HTS results showed a decrease in the total cell count, the RFI of H2B-GFP, and the RFI of mKO2-CDT1; no effect was observed with either the percentage of H2B-GFP$^+$ cells, or cells in G1 phase.

BIBU 1361 (BIBU) is a selective EGFR inhibitor, although little information is recorded about this compound and merely a handful of publications report its use. Given the role EGF signalling in the growth, proliferation, and migration of cancer cells, BIBU appeared to be a suitable candidate to induce cell cycle arrest and inhibit EGF-related downstream signalling pathways such as MAPK. In our study, BIBU treatment resulted in a decrease in the percentage of cells in G1 phase, but no effect was detected in the total cell count, the RFI of mKO2-CDT1, or the presence and expression of H2B-GFP.

VII.   Others (MMOA not defined)

Nicotinamide (NAM) is the bioactive form of vitamin B3 and a precursor of the coenzyme nicotinamide adenine dinucleotide (NAD). NAM is a neuroprotective agent, and its deficiency has been associated with pellagra and neurodegeneration. It is not normally produced by humans and therefore the essential requirements of NAM are obtained through the diet or other supplements. Upon absorption, NAM is rapidly converted into NAD$^+$, thus it is rarely found in high enough concentrations to affect any other pathways. On itself it has not been linked to a specific signalling pathway, although it is known to inhibit poly (ADP-ribose) polymerase (PARP) and sirtuin 1 (SIRT1). Given the role of SIRT1 in longevity, it has been speculated NAM might play a role in shortening cellular lifespan. Additionally, PARP inhibition impedes the repair of DNA strand breaks caused by chemo- and/or radiotherapy to cancerous cells, thus it has been proposed as a sensitizing compound to improve the efficacy of cancer treatments. In our study, FUCCI-CaCo-2 cells treated with NAM showed a decrease in the total cell count, the RFI of H2B-GFP, the percentage of cells in G1 phase, and the RFI of mKO2-CDT1; no effect was detected in the percentage of cells expressing H2B-GFP.

Taurodeoxycholic acid (TDCA) is a bile acid with detergent properties, normally produced in humans as part of the digestive process for the emulsification of lipids. It has not been conclusively linked to any signalling pathway, although some evidence suggests a potential role in stimulating mucin secretion in the intestinal epithelium. HTS results showed TDCA treatment led to a decrease in the RFI of mKO2-CDT1; no effect was observed in other parameters.

Based on the results presented in **Table 5.1**, candidate compounds were sorted according to their effect over the parameters analyzed (**Figure 5.9**). No apparent direct pattern was identified between the MMOA of all the compounds and their effect on the expression of the cell cycle reporter.
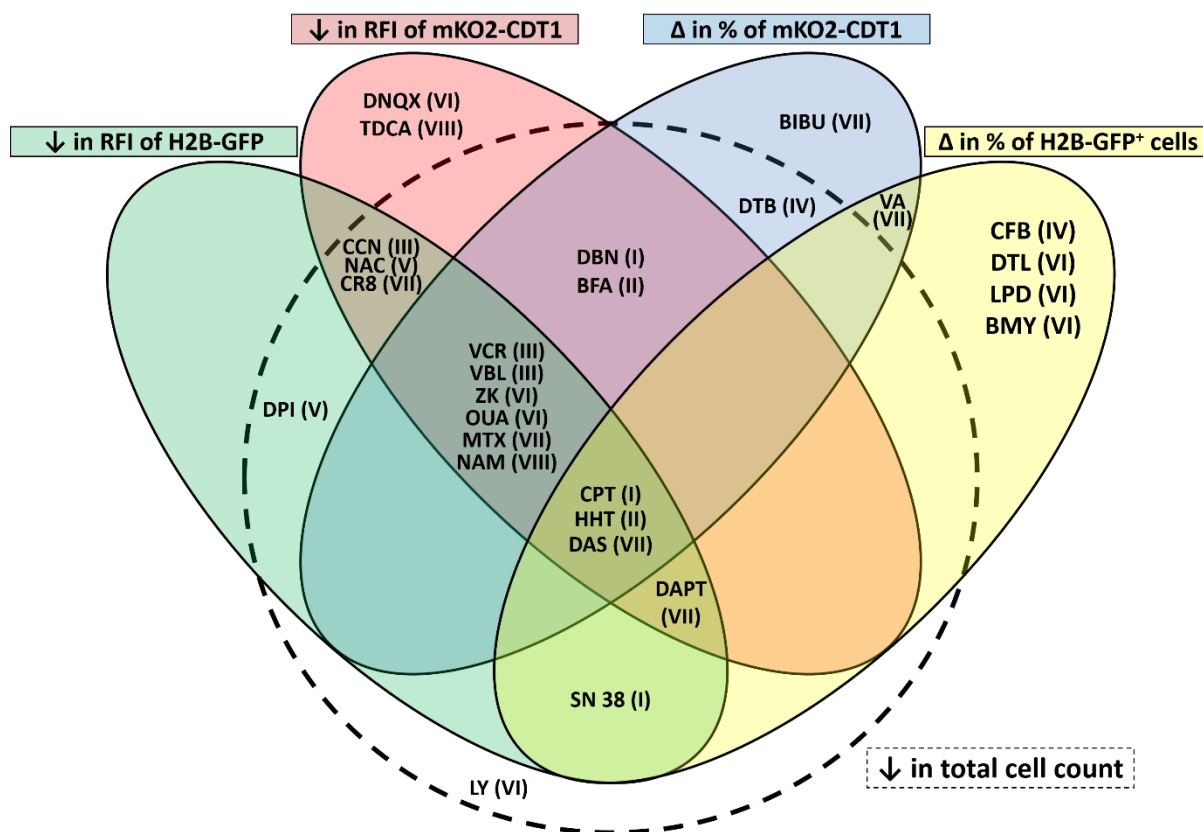
Figure 5.9 Venn diagram of HTS hits sorted based on their effect over the expression of the FUCCI reporter. Small-molecule HTS assessed 1536 compounds on a model of FUCCI-CaCo-2 cells. The screening identified 27 compounds which exerted a statistically significant effect (z-score = ±2.5 standard deviations from the median) in at least one of the following parameters: total cell count (dashed line); percentage of H2B-GFP+ cells (yellow); RFI of H2B-GFP (green); percentage of mKO2-CDT1+ cells (blue); or RFI of mKO2-CDT1 (red). Roman numerals in parenthesis indicate the group classification based on the molecular mechanism of action (MMOA): (I) DNA topoisomerase inhibitors; (II) Protein inhibitors; (III) Antimicrotubule agents; (IV) Nucleoside analogues; (V) Antioxidants; (VI) Neuroactive drugs and ion channel blockers; (VII) Other signalling pathway effectors; (VIII) Others (MMOA not defined).
(↓) Decrease; (Δ) Variations, either increase or decrease; (BIBU) BIBU 1361; (BFA) Brefeldin A; (BMY) BMY 14802; (CCN) Colchicine; (CFB) Clofarabine; (CPT) Camptothecin; (DAS) Dasatinib; (DBN) Daunorubicin; (DPI) Diphenyleneiodonium;(DTB) Decitabine; (DTL) Dantrolene; (HHT) Homoharringtonine; (LPD) Linopirdine; (LY) LY 344864; (MTX) Methotrexate; (NAC) N-acetyl-L-cysteine; (NAM) Nicotinamide; (OUA) Ouabain; (TDCA) Taurodeoxycholic acid; (VA) Valproic acid; (VBL) Vinblastine; (VCR) Vincristine; (ZK) ZK 93423.

Nevertheless, 2 main cluster of hits were identified in the study: compounds with and without an effect on the cell count. From the 19 compounds which provoked a decrease in the total cell count (dotted line), 13 showed a concomitant decrease (↓) in the RFI of H2B-GFP (green) and mKO2-CDT1 (red). This particular pattern might be explained by different mechanisms: (i) rapid turnover of proteins; (ii) rapid transition through G1 resulting in low protein expression, particularly of the reporters, as they may be deemed unessential; or (iii) the drugs altered the cellular physiology in such way that has an impact in the emission of fluorescence, e.g., hypoxia or low pH could affect these parameters.

Moreover, from this subset of 13 compounds with reduction in both reporters: 3 drugs (CCN, NAC, and CR8) did not affect any other parameter; 6 compounds (VBL, VCR, ZK, OUA, MTX, and NAM) also had an effect in the percentage of cells expressing mKO2-CDT1 (blue), supporting the idea of a shortening of G1, early transition into S phase, or induction of cell cycle arrest in a different phase; only DAPT increased the percentage of H2B-GFP$^+$ cells (yellow); and 3 other compounds (CPT, HHT, and DAS) affected all the parameters of the study, but in different forms.

Aside from these cluster of compounds, SN38 showed a reduction in both the RFI and the percentage of cells expressing H2B-GFP; these, alongside with the reduction in the total cell count, might suggest an overall reduction in the cell population due to the cytotoxicity of the drug. DBN and BFA, decreased the RFI and the percentage of mKO2-CDT1$^+$ cells, suggesting a direct effect in the G1 phase, likely due to a shortening of this, or cell cycle arrest in a different phase. Finally, DPI produced a marginal reduction (z = -2.54) in the percentage of H2B-GFP$^+$ cells, and LY only showed a slight reduction in the cell count (z = -2.90) with no effect in the rest of the parameters, in both cases this might suggest either a decrease in proliferation or mild cytotoxicity.

The remaining 8 compounds with no effect in the total cell count, only affected a single parameter of the screening. In addition to this, the z-scores of these hits indicate a relatively low statistical significance (z < 3.5) compared to the rest of the compounds. Overall, these compounds showed little or no association with the intestinal system or the cell cycle, and in some cases, the information about their use, field of application, or cellular function is considerably scarce. Therefore, it is possible that the score of these hits was an artefact of the experiment with no biological relevance for the purpose of this study.

TDCA (z = -2.56) and DNQX (z = -2.51) only showed a marginal decrease in the RFI of mKO2-CDT1. Three candidates from group VI, (DTL, LPD, and BMY) produced a decrease in the percentage of H2B-GFP$^+$ cells, while only 1 compound from group IV (CFB) caused a decrease in this parameter. The EGFR

inhibitor BIBU (z = -2.91) produced a slight decrease in the percentage mKO2-CDT1$^+$ cells, putatively cells in G1 phase. Considering that inhibition of EGF signalling usually leads to G1 arrest, these results might be an indicative of cell cycle arrest in a different phase. Only 1 compound, VA, showed an effect in two parameters: a decrease in the percentage of H2B-GFP$^+$ cells and mKO2-CDT1$^+$ cells. Considering that the reduction of these subpopulations is not accompanied with an overall reduction in the cell count, the results could be owed to the silencing of the reporters.

Aside from this, 6 compounds (HHT, DAS, DAPT, DTL, LPD, and BMY) caused an increase in the percentage of H2B-GFP$^+$ cells; however, H2B-GFP is expected to be expressed in the entire population, alongside with the DAPI (All nuclei) channel. We cannot provide a broad explanation that justifies this result in all these different compounds. A potential reason for these variations could be associated with the segmentation of the binary mask, and the different grayscale threshold used for the GFP channel. In this scenario, the drugs could have caused a significant formation of apoptotic vacuoles or nuclear debris, which could have led to the detection of additional structures. This resulted in more 'cells' being detected in the GFP channel, which do not match with the cells detected on the DAPI channel.

5.3 Discussion

In our study, we sought to identify compounds which may exert an effect on the G1 phase of the cell cycle using a FUCCI reporter. G1, constitutes a window in the cell cycle in which changes in the structure of chromatin generate a permissive state that allows for its interaction with signalling cues from the microenvironment (Dalton, 2015). This leads to the input of mitogenic, antiproliferative, pro apoptotic or differentiation signals (Sherr, 1996; Singh *et al.*, 2013). In normal ISCs, a short G1 phase has been implicated with the maintenance of stemness, whereas G1 lengthening increases the likelihood of accumulating and responding to differentiation signals (Pauklin *et al.*, 2016; Carroll *et al.*, 2018). In CSCs, a short G1 phase has been associated with the insensitivity towards antiproliferative signals, and lower quality control by the cell to detect DNA mutations. Conversely, induction of G1 arrest facilitates the response to the DNA repair machinery and pro apoptotic signals, thereby hindering the spread of the malignancy (Sherr, 1996; Hanahan & Weinberg, 2000; Massagué, 2004).

A previous study described the use of cell-cycle-arrest patterns to identify FDA-approved drugs with previously unknown antineoplastic potential, to be repurposed for cancer treatment (Lo *et al.*, 2017*a*). This supports our strategy of using the proportion of cells in G1 phase, and the RFI of the reporter, as a hallmark for the identification of cell cycle modulators. We expected to identify novel compounds that stop the proliferation and induce the cell death of malignant cells; alternatively, we sought for compounds which may promote the regeneration of the ISC population, thus ameliorating the adverse effects from chemotherapy regimens.

The results from screening identified 10 drugs (CPT, SN38, DBN, HHT, VBL, VCR, DTB, CFB, DAS, and MTX) commonly used as antineoplastic agents. Notably, with the exception of CPT and its derivative SN38, most of these compounds have been indicated for the treatment of haematological malignancies, breast, lung, or testicular cancer, but not CRC (Sun *et al.*, 2017; WHO, 2019). From this set of compounds only CFB did not have an effect in the total cell count, whereas DBN, HHT, VBL, DAS, and MTX showed an overall reduction in the number of FUCCI-CaCo-2 cells. In addition to the cluster of recognized chemotherapeutic agents, the assay identified another cluster of compounds (BFA, CCN, BIBU, CR8, DAPT, and VA) with potential antineoplastic activity, but which have not been approved for this application. The members of this group do not share a common MMOA, though all of them target a specific signalling pathway involved in cell proliferation. We analyzed the candidates from both of these clusters and compared them with previous reports from the literature. Our research regrouped these compounds into three subsets based on their most likely effect on the cell cycle: (i) S or G2/M arrest; (ii) G1 arrest; and (iii) Effects unrelated to induction of cell cycle arrest.

Based on this classification nine compounds were found likely to induce cell cycle arrest at either G0, S or G2/M phase: CPT and its derivative SN38 (Xie *et al.*, 2000; Li *et al.*, 2017; Jayasooriya *et al.*, 2018; Du *et al.*, 2018), DBN (Chikayama *et al.*, 1998; Mansilla *et al.*, 2003), VBL and VCR (Kothari *et al.*, 2016), MTX (Tsurusawa *et al.*, 1990; Richardson *et al.*, 1994), DTB (Lavelle *et al.*, 2003; Shin *et al.*, 2013), BIBU (Ghildiyal *et al.*, 2013), CR8 (Bettayeb *et al.*, 2008), DAPT (Rasul *et al.*, 2009; Wang *et al.*, 2014*a*), and CCN (Fleisig & Wong, 2012; Strömberg *et al.*, 2015; Wu *et al.*, 2016). Even though these compounds did not exhibit a similar pattern of variations in the parameters analyzed, the common denominator was the cell cycle arrest in any phase other than G1. Therefore, the decrease in the percentage of putative G1 cells and in the RFI of mKO2-CDT1 could be explained by the arrest and accumulation of cells in G0, S or G2/M phase. This could have also affected the synthesis of proteins, thereby explaining the decrease in the RFI of the reporters. Finally, the reduction in the total cell count and the percentage of H2B-GFP^{+} cells could be explained by apoptotic induction caused by prolonged cell cycle arrest or through mechanisms intrinsic to the specific candidate.

Three compounds were allocated into the second subset, in which the effects are attributed to G1 arrest: HHT (Baaske & Heinstein, 1977; Slichenmyer & Von Hoff, 1990; Franco *et al.*, 2020), DAS (Johnson *et al.*, 2005; Guerrouahen *et al.*, 2010; Inge *et al.*, 2013), and BFA (Rajamahanty *et al.*, 2010). In this instance, the increase in the percentage of mKO2-CDT1^{+} cells could indicate G1 arrest. However, a decrease in the expression of mKO2-CDT1 could also be explained by prolonged G1 arrest that resulted in the degradation of licensing factors such as CDT1 (Carroll *et al.*, 2018). Additionally, the concomitant decrease in the RFI of both reporters could be attributed to a generalized inhibition in the synthesis of new proteins. Ultimately, the decrease in the cell number could be explained by apoptotic induction from the treatments.

Only for VA the effects observed in the expression of the reporters could not be attributed to cell cycle arrest, thereby falling within the third subset classification. VA is a NOTCH activator which has been used to maintain the self-renewal capacity of LGR5^{+} ISCs (Yin *et al.*, 2014). This evidence suggests that the decrease of the G1 subpopulation, seen in our study, could be justified by the induction of cell proliferation.

The variations and discrepancies in the pattern in which these compounds affected the parameters analyzed could be explained by the specific behaviour of the candidates. The specific MMOA of each compound did not fall within the scope of this preliminary study but following the validation of the candidates a deeper analysis could be conducted. Overall, these results provide preliminary evidence that justifies additional study of these compounds into its specific use for the treatment of CRC or for the modulation of the cell cycle of ISCs.

The screening also identified a cluster of compounds with no previous reported function or association with either the intestinal epithelium or the cell cycle. Group VI consisted mostly of neuroactive compounds indicated for the treatment of psychiatric and neurodegenerative conditions, and ion channel inhibitors used for the modulation of cardiac and skeletal muscle contractions. A deeper look into the specific molecular mechanism of action has suggested potential applications in the regulation of the cell cycle, to induce cell cycle arrest and hinder the hyperproliferation of CSCs.

The most remarkable members of this group were ZK and OUA, both of which led to a significant reduction in the total cell number, a simultaneous decrease in the fluorescence of both reporters, and a decrease in the population of putative cells in G1 phase (mKO2-CDT1$^+$). ZK is a GABA$_A$ agonist mostly studied for its effects as an anxiolytic and muscle relaxant (Klockgether *et al.*, 1985; Dodd *et al.*, 1987), though with no mention of any effect in the GI tract, cell cycle or the treatment of cancer. Still, GABA$_A$ agonists have been reported to reduce cell proliferation, arrest the cells in S phase, or in the G1/G0 checkpoint, the latter is likely due to the cells entering a quiescent state (G0) (Andäng *et al.*, 2008; Wang *et al.*, 2019). On the other hand, OUA is a Na$^+$/K$^+$ ATPase inhibitor commonly used for the treatment of arrythmias; though, previous studies have shown OUA can induce cell cycle arrest in S/G2, and ultimately push the cells toward G0 (Hiyoshi *et al.*, 2012; Schneider *et al.*, 2018). The exact mechanism by which these drugs induce cell cycle arrest, has not been defined. It has been postulated that the change in the ion homeostasis may trigger the DNA-damage response, resulting in cell cycle arrest, apoptosis, or quiescence. It has also been hypothesized that GABA receptors and Na$^+$/K$^+$ transporters may act as transducers of some signalling cascade which reacts to the drugs and leads to the observed outcome (Andäng *et al.*, 2008; Hiyoshi *et al.*, 2012). Aside from these, ion channel blockers have been postulated to modify the intracellular pH (Marakhova *et al.*, 2019). Particularly, low intracellular pH has been associated with aggregation of fluorescent proteins, thereby reducing the amount of active reporters, which could explain the decrease in the fluorescence of both reporters in our study (Krasowska *et al.*, 2010). Overall, this might justify the results found in our study for both candidates and opens the possibility for further works to explore their application as antitumoral drugs.

In addition to this results, two uncategorized compounds, NAC and NAM, were identified to produce a significant effect in the expression of the reporters. NAC (antioxidant) and NAM (vitamin B3) are commonly used as supplements with no strict therapeutic purpose. However, our revision has identified potential health benefits for the maintenance, protection, self-renewal, and proliferation of the ISC population of organoids (Sato *et al.*, 2011*b*). Previous works have found that NAC and NAM can induce apoptosis and arrest the cells at G1 (Liu *et al.*, 1999*b*, 2017; Kim *et al.*, 2001; Wang *et al.*,

2018). Apoptotic induction explains the decrease in the total cell count observed in the results of our screening. However, it is not entirely clear if the reduction in the RFI of the reporters, and in the case of NAM a decrease in the percentage of mKO2-CDT1+ cell, could have been caused by a prolonged G1 arrest, followed by the degradation of the fluorescent proteins.

Finally, we identified a cluster of assorted compounds from different groups (CFB, DPI, DNQX, DTL, LPD, BMY, LY, and TDCA), which had little or no effect in the total cell count. This cluster was characterized for showing marginal levels of statistical significance (z < 3.5). None of the compounds had any effect in the putative G1 population (mKO2-CDT1$^+$ cells). Also, except for DPI, the members of this cluster just affected a single parameter from the study. Furthermore, given the low significance of the results and the lack of association with the cell cycle, cancer treatment, and/or the intestinal tract, it remains possible some of these hits are false positives which were caused by an artefact of the assay. Due to the aforementioned criteria, these compounds were not discussed in this work, as the effects observed in the screening do not provide a solid and relevant basis for analysis. Also, in light of the results from the screening, it appeared unlikely these compounds could be repurposed for chemotherapeutic applications or to promote the proliferation of ISCs.

In this project, we opted for using a model of FUCCI-CaCo-2 cells cultured as a bidimensional monolayer to perform a preliminary small-molecules HTS. This was a more feasible alternative, due to the high cost of using an organoids model for an experiment of this scale. Nevertheless, the candidate compounds identified in this work are expected to later be validated in a model of HIO.

CaCo-2 remains as the gold standard for pharmaceutical companies to evaluate the absorption, processing, and effect of new drugs over the intestinal epithelium (Tan *et al.*, 2018; Keemink & Bergström, 2018). Moreover, studies have found CaCo-2 cells have a significantly high expression of LGR5 (Uchida *et al.*, 2010), making it an ideal system for preliminary screenings on the LGR5$^+$ population, either for the study of ISCs or CSCs. Therefore, this model was better suited to identify and reduce the number of compounds to be tested in a three-dimensional model of the intestinal epithelium. In this regard, the main three-dimensional models developed for the study of the normal intestinal epithelium and CRC, are spheroids and organoids.

The spheroids model is an avascular representation of a tumour, consisting of dense three-dimensional cellular aggregate. Spheroids self-assemble with layers of cells that generate a gradient of nutrients, oxygen, and pH; this results in the formation of a necrotic core with limited availability of nutrients, low pH, and a hypoxic microenvironment (Mehta *et al.*, 2012; Katt *et al.*, 2016). Its configuration makes ideal for the study of tumoral growth in the absence of vascularization, to assess

the penetration and distribution of a drug within a solid tumour, the development of therapeutic resistance against chemotherapy, and to study the cancer stem cell model to describe the growth of a tumour (Herheliuk *et al.*, 2019; Nunes *et al.*, 2019; Zanoni *et al.*, 2020; Gilazieva *et al.*, 2020). However, in terms of practical implementation, the conditions of the necrotic core (low pH and hypoxia) considerably limit the use of reporters based on fluorescent proteins (Coralli *et al.*, 2001). Alternatively, previous studies have reported the use of semisolid ECMs, such as Matrigel, to induce the self-assembly of CaCo-2 cells into cyst-like three-dimensional structures. This form of CaCo-2 spheroids exhibits polarized cells organized for the formation of an inner luminal compartment and an outer basolateral compartment (Cerchiari *et al.*, 2015; Lee *et al.*, 2018; Samy *et al.*, 2019). This system is an improvement to traditional bidimensional monolayers and disorganized cellular aggregates; although, the use of Matrigel for the preparation of the cyst spheroids diminishes the main feature of CaCo-2 models which is their simplicity of preparation and low cost. Additionally, this system still carries the disadvantage of being derived from a cancerous cell line and is only comprised of a single cell type.

In contrast, organoids are self-organizing three-dimensional structures that exhibit the main anatomical features of a specific tissue. This model exhibits a heterogeneous cell population, allowing for the study of interactions between different cell types (Aurora & Spence, 2016; Fatehullah *et al.*, 2016; Yin *et al.*, 2016; Fong *et al.*, 2020). Furthermore, it is particularly important to highlight the interaction with the mesenchymal compartment in our model of HIOs. Previous works have addressed the role of the intestinal subepithelial myofibroblasts in maintaining the stemness and regulating the proliferation and self-renewal of the ISC population (Lei *et al.*, 2014; Pastuła & Marcinkiewicz, 2019). Also, in cases of CRC, the mesenchymal compartment and cancer-associated fibroblasts have been implicated in the development of resistance against immunotherapy (Garvey *et al.*, 2020).

For the purpose of this study, a model of spheroids is not particularly relevant, nor is it comparable with a model of intestinal organoids as it does not allow for the observation of the behaviour of an organized tissue. Conversely, organoids allow for a more detailed assessment of the interactions between the ISCs and other cell types of the intestinal epithelium or the mesenchymal compartment. Arguably, this model is better suited to recapitulate the physiology of the normal intestinal epithelium, and it may provide a more accurate screening system to assess the effect that different compounds exert over the cell cycle on normal ISCs. Alternatively, models of CRC patient-derived tumour organoids have been developed to study these effects over the cell cycle of cancer cells. However, the production of organoids is significantly more expensive, and is better suited as a system to validate the results from a preliminary screening conducted in a cheaper model.

Nevertheless, there are important caveats to consider regarding the validation of the compounds identified in this screen and the expected behaviour of the putative ISC population in a model of organoids. First, given the limitations encountered with the detection of the ISC marker LGR5 (See Chapter 4), it is still unclear how extensive is the LGR5$^+$ ISC population in our model of HIOs. Based on previous reports from a similar model, the LGR5 is relatively widespread at least prior to day 35 of the organoid growth (Watson *et al.*, 2014). Regardless, it is possible that the results from our model of FUCCI-CaCo-2 would not be as significant in a model of HIOs. A possible explanation is that CaCo-2 cells have reported a significant overexpression of proliferative LGR5$^+$ cells (Uchida *et al.*, 2010), whereas in a model of HIOs the population of LGR5+ ISC could be considerably smaller (Finkbeiner *et al.*, 2015*b*). Second, the presence of the mesenchymal compartment may interfere with the interaction of the candidate compounds and the intestinal epithelium. Previous reports have suggested that mesenchymal cells may counteract the effects of the drugs by overexpressing a specific growth factor, ligand, or agonist, thereby attenuating the effects of the drug in the ISCs (Garvey *et al.*, 2020). Third, in the monolayer model the apical compartment of CaCo-2 cells is exposed to the medium and the drugs. This orientation ensures the interaction of the drugs with the receptors involved in their absorption or signalling function. Conversely, in our model of HIOs, even after surpassing the barrier from the mesenchymal cells, the drugs are in direct contact with the basolateral compartment of the cells, rather than the apical section. This may hinder the absorption of the compounds or it functional interaction with the target receptor, resulting in an attenuated or completely absent effect of the drugs within the cells (Negoro *et al.*, 2016; Klunder *et al.*, 2017; Mochel *et al.*, 2018; Youhanna & Lauschke, 2020). The inaccessibility to the luminal compartment of the organoids is an issue which has been extensively highlighted in the literature, and has led to the development of alternative models (Altay *et al.*, 2019; Kondo *et al.*, 2020). Particularly, a recent study developed a protocol to invert the polarity of the cells in a model of mouse enteroids. The inverted enteroids exposed the apical compartment outward in contact with the medium, and the basolateral compartment inward to the centre of the organoid (Co *et al.*, 2019). Alternatively, the models of gut-on-a-chip, such as the one developed in this project, are a suitable option to overcome this limitation and conduct the validation of the compounds identified in this study (Naumovska *et al.*, 2020).

To conclude, we have performed a small-molecule HTS on FUCCI-CaCo-2 cells given the convenience, low cost, and robustness of these model to perform large-scale assays. We sought compounds with an effect over the G1 phase of the cell cycle, as it has been associated with the proliferation, differentiation, and cell death of ISCs and CSCs. Our assay identified 19 compounds which showed a significant reduction in the cell number and evidence of arrest in any phase of the cell cycle. Nine candidates were recognized chemotherapeutic agents, from which 2 (CPT and SN38) have already

been indicated for the treatment of CRC, and 7 (DAS, DBN, DTB, HHT, MTX, VBL, and VCR) are used in the treatment of other forms of cancer. A subset of 4 compounds (BFA, CCN, DAPT, and CR8) are not officially described as chemotherapeutic agents, though they are involved in signalling pathways associated with inhibiting cell proliferation, inducing cell cycle arrest, or triggering apoptosis. Interestingly, some of the hits included compounds with no previous association with the GI tract, the cell cycle, or the treatment of cancer, such as: ZK (GABA$_A$ agonist), OUA (ion channel blocker), NAC (antioxidant), and NAM (member of the vitamin B complex). Finally, ten other compounds showed lower values of statistical significance, and given the lack of association with the intestinal epithelium or the cell cycle, we have determined these might not be relevant for the purposes of our study. It remains possible in some of these cases the effects could have been artefacts from the experiment and no real hits. Future works shall address the validation of the findings from this study in our model of HIOs. Overall, neither of the candidate compounds showed evidence of increasing the cell number or lengthening the G1 phase. Therefore, none of the candidates could be repurposed to promote cell proliferation and contribute to the regeneration of the ISC population. Also, it discards the possibility of being used as cell cycle modulators to control and facilitate the differentiation of ISCs. Nevertheless, these results provide preliminary evidence to conduct further experiments to support the repurposing of these compounds in the treatment of CRC.

6.1 Establishment and optimization of a protocol for the generation of human intestinal organoids

Current works addressing the use of intestinal organoids still derive from three main models (Miura & Suzuki, 2018; Antfolk & Jensen, 2020): Clevers' model of enteroids, derived from intestinal crypt cells (Sato *et al.*, 2009, 2011*b*); Wells' model of intestinal organoids, generated from a stepwise differentiation process of PSCs into intestinal tissue (Spence *et al.*, 2011; McCracken *et al.*, 2011); and Jensen's model of foetal enterospheres obtained from dissociated foetal intestinal epithelial cells (Fordham *et al.*, 2013). However, these models are not without limitations and over the years have been continuously upgraded and the culture conditions have been modified to: improve the overall efficiency of the differentiation protocol (Sato *et al.*, 2011*b*; Watson *et al.*, 2014; Fujii *et al.*, 2018; Takahashi *et al.*, 2018); induce the development and differentiation of all the cell types of the intestinal epithelium (Yin *et al.*, 2014; Chen *et al.*, 2017; Sinagoga *et al.*, 2018); develop organoid cultures in suspension to rescind the use of Matrigel (Takahashi *et al.*, 2018); improve and automate the selection of organoid-forming units (Arora *et al.*, 2017; Fong *et al.*, 2020; Kim *et al.*, 2020); and integrate multisystemic interactions with the microbiome, and the vascular, immune, and nervous system (Min *et al.*, 2020; Holloway *et al.*, 2020; Son *et al.*, 2020).

In the present study we report the successful generation of HIOs derived from iPSCs. Results from our characterization experiments showed comparable similarities between our model of iPSC-derived organoids and the model of PSC-derived organoids reported by Wells' group (McCracken *et al.*, 2011; Finkbeiner *et al.*, 2015*b*). Our model of HIOs consisted of spherical hollow structures comprised by an inner layer of CDX2$^+$ intestinal epithelium and an outer layer of COL1A1$^+$ mesenchyme. Gene expression analysis indicated the presence of a subpopulation of proliferative cells responsible for the renewal of the epithelium. Also, it showed evidence of a differentiation toward the absorptive lineage, while the secretory population was practically absent, and provided further confirmation of a mesenchymal population.

Furthermore, our protocol built upon the work from Wells' group (McCracken *et al.*, 2011), and modified the culture conditions to reduce the time and cost required for the differentiation of the organoids. These modifications compile advantages previously reported by individual studies, but which, to the extent of our knowledge, had never been incorporated together into a single differentiation protocol for the generation of intestinal organoids. The advantages of our new optimized protocol SRSF v.4, are: (i) the use of laminin-521, an economic, chemically defined, xeno-free ECM for the culture of iPSCs (Rodin *et al.*, 2014; Albalushi *et al.*, 2018); (ii) a reduction in the time required for the differentiation of the definitive endoderm (Siller *et al.*, 2015); (iii) the use of small

molecules and in-house-produced recombinant growth factors, instead of expensive commercial recombinant proteins (Ootani *et al.*, 2009; Watson *et al.*, 2014); and (iv) the culture of the organoids in suspension during the final stage of intestinal growth and differentiation, which reduces the volume of medium required, and in consequence the cost of production (Takahashi *et al.*, 2018).

Our new protocol SRSF v.4 represents an important contribution to the field as it provides an alternative for the generation of HIOs derived from iPSCs at a lower cost. Additionally, by removing the BMM Matrigel matrix during the suspension culture of the organoids we expect to facilitate the direct physical manipulation of the organoid, and to ease the integration and interaction with other systems. Similar to Wells' model, we anticipate our model could be applied to: (i) investigate the elements involved in the maturation of the foetal intestine into its mature state; (ii) model the infection of different microorganisms; (iii) identify compounds which may induce the differentiation of specific populations; (iv) study the crosstalk between the mesenchyme and the intestinal stem cell niche; (v) study the regenerative response of the intestinal epithelium after injury; (vi) evaluate the chemo- and radio sensitivity of the normal intestinal epithelium; (vii) study the factors associated with the onset of inflammatory diseases and their degenerative progression; and (viii) induce the formation or integration of components from the vascular, immune, or nervous system.

6.2 Development of a novel model of gut-on-a-chip generated from *in situ* differentiation of iPSCs

Since their first publication, organoid models have taken widespread popularity due to exhibiting three dimensional features that other existing models had not been capable to replicate. However, these still are significantly expensive to be implemented in HTS, present considerable limitations to access to the luminal compartment, and the existing organoid models which have attempted to incorporate other multisystemic interactions, are still in the early stages of development (Zanoni *et al.*, 2020).

Alternative models have proposed the use of dissociated organoids cells to generate cultures of normal intestinal epithelium on a Transwell system; even though this model provides access to the luminal compartment, it completely sacrifices the three-dimensional microarchitecture (Foulke-Abel *et al.*, 2014). Another study reported the generation of inverted organoids, in which the apical compartment of the cells is in contact with the medium, while the basolateral portion is oriented towards the centre of the organoid. This system maintains the three-dimensional configuration, and provides access to the luminal compartment; however, access to the basolateral compartment is still necessary to assess the absorption and metabolism of luminal compounds (Co *et al.*, 2019).

Consequently, the model of gut-on-a-chip represents a suitable solution to overcome these limitations. Different microfluidic chip designs have been generated to optimize the culture conditions and to incorporate multisystemic interactions into the model (Bein *et al.*, 2018). Perhaps the most commonly referred model is the one developed by Ingber's group. This system consists of two microchannels separated by a polymer porous membrane and coupled to a vacuum pump to emulate the mechanical stress from the perfusion of medium through the lumen and the basolateral compartment (Huh *et al.*, 2012).

Alternatively, Mimetas OrganoPlate system consists of microfluidic chips with 3 microchannels separated by phaseguides. The phaseguides are a proprietary design responsible for the control of the fluid dynamics within the channel and the liquid-air interface between adjacent channels. This design generates a virtual separation between the content of the channels and allows for the co culture of two different tissues (e.g., epithelium and endothelium) supported by an ECM (Vulto *et al.*, 2011).

Both systems have previously reported the generation of models of gut-on-a-chip using CaCo-2 cells (Kim *et al.*, 2012; Trietsch *et al.*, 2017); however, since these are derived from a cancer cell, certain application may not be recommended for this model, for instance those which may be affected by its genomic instability, or its mutational profile (Bein *et al.*, 2018).

Recent studies have reported the development of new gut-on-a-chip models generated with Ingber's microfluidic chip and intestinal epithelial cells obtained from dissociated biopsy-derived enteroids. This model leaps the limitations of using colorectal cancer cell lines, however the availability of source material could considerably limit its applications (Kasendra *et al.*, 2018, 2020).

Therefore, to capitalize from our newly developed protocol SRSF v.4 we pursued a collaboration with Mimetas and applied it into the *in situ* differentiation of iPSCs in an OrganoPlate microfluidics chip. The result was the development of a new model of gut-on-a-chip comprised by a tubular structure of iPSC-derived normal intestinal epithelium expressing a major marker of the intestinal lineage, CDX2. Further characterization performed by Mimetas, revealed the formation of an impermeable epithelial barrier and the expression of markers of enterocytes, Paneth, and enteroendocrine cells.

Our new model provides significant advantages, such as: (i) sufficient availability of source material, since iPSCs can be sampled once from a patient and expanded indefinitely *in vitro*; (ii) access to the intestinal lumen and the basolateral compartment; (iii) possibility of integrating multisystemic interactions, such as vascularization and microbiota; (iv) the mechanical strain exerted by the perfusion of the medium could contribute to the maturation of the intestinal epithelium; and (v) the configuration of the OrganoPlates allow for an easy integration into high-throughput experiments.

Based on its characteristics and the applications of previous similar models we are confident our new gut-on-a-chip model can be applied to: model inflammatory response; perform drug screening studies evaluating permeability, cytotoxicity, and/or activation of specific markers in the epithelium (differentiation, apoptosis, proliferation, inflammation); evaluate the interaction with commensal and pathogenic microbiota; and assess multisystemic interactions with endothelial, immune or nerve cells. Furthermore, the combination of the high-throughput format of OrganoPlates along with the use of iPSC-derived intestinal epithelium tubules, holds the potential for future applications in personalized medicine.

The results from our collaboration with Mimetas led to the publication of a new model of gut-on-a-chip generated with our protocol SRSF v.4 (Naumovska *et al.*, 2020). This represents a significant contribution since to the extent of our revision, this is the first model to describe the formation of normal intestinal epithelium derived from iPSCs differentiated *in situ* in a microfluidic chip. Finally, these provides additional evidence to support the fact that our new protocol SRSF v.4 represents a robust alternative suitable for the generation three-dimensional models of normal intestinal epithelium derived from the differentiation of iPSCs.

6.3 Assessment of commercial anti human LGR5 monoclonal antibodies and generation of an LGR5-GFP reporter cell line

In light of the versatility and potential applications of our models of HIOs and gut-on-a-chip, we sought to develop them further by incorporating a fluorescent reporter tagging the intestinal stem cell marker LGR5. The development of a robust three-dimensional model of the intestinal epithelium integrated with a fluorescent reporter system for the study of the stem cell population in real time would significantly facilitate its implementation in HTS experiments.

Originally, we considered the use of immunostaining with anti LGR5 antibodies directed to the ISC population. However, we were unable to obtain a robust and reproducible fluorescent output from the immunostaining of control intestinal cell lines using commercial anti human LGR5 monoclonal antibodies (clone OTI2A1). Furthermore, the studies addressing the use of anti human LGR5 antibodies present important caveats, mainly the use of samples overexpressing LGR5 and detection techniques which enhance the signal output (Becker *et al.*, 2008; Takeda *et al.*, 2011; Kemper *et al.*, 2012). Aside from being unable to provide fluorescence images, antibody staining is considerably expensive and not recommended for high-throughput applications; therefore, the generation of a LGR5 reporter cell line appeared to be the best option.

In 2014, both Clevers' and Wells' group reported the generation of a hES cell line expressing an LGR5-GFP reporter, and described the generation of HIOs derived from these reporter cell lines (Forster *et al.*, 2014; Watson *et al.*, 2014). Clevers' reporter was only used for sorting teratoma-derived LGR5 cells, and no information was provided about its performance for fluorescence microscopy (Forster *et al.*, 2014). Wells' reporter was later mentioned in follow up works by the same group, however after analysing in detail the methods of this work, the signal from the LGR-EGFP reporter was enhanced through secondary staining with anti GFP antibodies. Additionally, it is possible that the maturation process which requires the transplant of the organoids into the kidney capsule of mice, could have had some effect in enhancing the signal of the reporter (Tsai *et al.*, 2016; Múnera *et al.*, 2017; Liu *et al.*, 2019*b*).

Later, Sato's group used CRISPR/Cas9 to introduce an LGR5-GFP reporter into CRC organoids (Shimokawa *et al.*, 2017). The evidence showed the fluorescence of the reporter; however, it is important to highlight that LGR5 has been found overexpressed in CRC cells (Becker *et al.*, 2008; Takeda *et al.*, 2011; Ihemelandu *et al.*, 2019). Thus, the intensity of the signal might not be comparable in a model of normal intestinal epithelium. In a later work, the authors generated a rainbow LGR5 reporter to track the ISC population in colonic organoids xenografted into mice. The results appeared to show the expression of the reporter, however based on the description of the materials and

215

methods, it is possible the signal was enhanced with antibody staining targeted against the fluorescent proteins (Sugimoto *et al.*, 2018). In another study, the authors replaced the GFP reporter for a tdTomato, in this instance there is no apparent evidence that the signal was enhanced. Thus, it is possible that the combination of LGR5-tdTomato is compatible with fluorescence microscopy studies (Fujii *et al.*, 2018). Nevertheless, in this work the reporter was transfected directly into the organoids, therefore there are still no studies demonstrating the generation of an LGR5 reporter stem cell line.

Furthermore, in spite of the apparent reported success of these LGR5 reporters, recent studies have continued working in identifying new molecular markers for the ISC population. A recent study reported the generation of the stem cell ASCL2 reporter (STAR), these construct was transfected into intestinal and colonic organoids and the expression of the reporter appeared confined to the CBC, colocalizing with LGR5 (Oost *et al.*, 2018; Heinz *et al.*, 2020). Further validations studies are still required but STAR appears to be a suitable candidate to replace or complement the use of LGR5.

This evidence supported our decision to generate an LGR5 reporter iPS cell line for the generation of HIOs. It is important to highlight that several of the aforementioned studies were published during the development of this project, and therefore the decision to generate our reporter cell line responded to a yet unmet need at the time. Additionally, based on our analysis of these works, our reporter system addressed a different venue, since our objective was to generate organoids from cells already carrying the LGR5-GFP reporter. We expected this system will provide a deeper insight into the first appearance of the ISC population and its development along with the differentiation of the organoids.

We successfully generated the LGR5-GFP reporter cassette, however after several attempts we were unable to achieve its integration into the genome of iPSCs or CaCo-2 cells. We suspect this could be an artifact from the human LGR5 gene in particular, given that the existing LGR5 reporters also present issues in detecting the fluorescence of the reporter without enhancing treatments. Furthermore, the existing antibodies have also been unable to provide fluorescence images of non-cancerous human LGR5$^+$ ISCs.

In spite of its consistent limitations, no publication has directly addressed the caveats of LGR5 as a marker, or with the commercial antibodies and reporter cell lines. Our work has provided direct evidence of the lack of functionality of commercial anti human LGR5 monoclonal antibodies (clone OTI2A1), for immunofluorescence applications. Additionally, the results from our experimental work and the literature revision have raised significant concerns with the existing LGR5-GFP reporters. Finally, we have presented evidence of ongoing studies focused on development and validation a new ISC reporter based on the expression of ASCL2.

6.4 Evaluation of high-throughput applications of HIOs and preliminary screening in CaCo-2 cells

In spite of the modification we have performed to the differentiation protocol for the generation of HIOs, these still are significantly expensive for their implementation in HTS experiments (Zanoni *et al.*, 2020). Other modelling systems such as the gut on a chip could be relatively expensive and time consuming to set up, depending on the cell type used for the preparation of the intestinal epithelium (Bein *et al.*, 2018; Naumovska *et al.*, 2020). Spheroid models are more economic; however, they are mostly indicated for cytotoxicity and chemoresistance assays in solid tumours. Also, spheroids do not develop a polarized intestinal epithelium, and the necrotic core could affect the expression of fluorescent reporters (Nunes *et al.*, 2019; Gilazieva *et al.*, 2020). The model of intestinal epithelium using CaCo-2 cells, has been the gold standard for screening assays in the early stages of drug discovery. This is an economic and simple model which can provide information regarding the absorption, intestinal metabolism, and potential cytotoxicity of new compounds (Tan *et al.*, 2018; Keemink & Bergström, 2018). In the context of HTS studies, CaCo-2 models can reduce the number of compounds by discarding those which exhibit high cytotoxicity or low therapeutic effect; the remaining candidates can be validated in more sophisticated models.

The initial approach of our study was to use the LGR5-GFP reporter for the detection of compounds affecting the behaviour of the ISC population, i.e., proliferation, differentiation, and variations in the fluorescence intensity and number of cells expressing the reporter. However, this was no longer possible given the results from the development of the reporter cell line. Alternatively, previous works have related the length of the G1 phase with the potential of stem cells to undergo differentiation, and cancer cells to ignore antiproliferative signals (Pauklin *et al.*, 2016; Carroll *et al.*, 2018). Therefore, we opted for using the FUCCI reporter, which provides information regarding the duration, percentage, and potential arrest of cells going through the G1 phase of the cell cycle (Sakaue-Sawano *et al.*, 2008; Calder *et al.*, 2013).

Our model of FUCCI-CaCo-2 cells is an economic, robust, easy-to-prepare model for high-throughput drug screening searching for compounds with an impact in the cell cycle of the intestinal epithelium. In this study we use it to perform a preliminary HTS to identify a small subset of candidate compounds, which can later be validated in a model of organoids.

The results from our preliminary HTS experiment identified 27 compounds with an effect in any of the parameters analyzed. Significantly, ten were known antineoplastic agents, from which only two are indicated against CRC. Other compounds targeted a variety of different pathways, but in general these are not currently indicated for the treatment of cancer. Unexpectedly, a group of neuroactive drugs and ion channel blockers showed significant results in the parameters analyzed, though these

compounds had no previous reported relationship with the control of cell proliferation or cell cycle. Thus, the results from our study can set the foundation for further repurposing studies exploring the use of these compounds in the treatment of CRC. Alternatively, due to their effect in controlling the transition of G1/S, some of these candidates can be studied for their role in regulating the balance between self-renewal and differentiation in ISCs.

The candidates identified in this study represent a significant contribution by providing new alternatives for drug repurposing in the field of cancer research. Additionally, some of these compounds can regulate the transitions of the cell cycle, thereby providing an alternative to modulate the length of G1, and in consequence the differentiation window in ISCs. Following the validation of these hits in other intestinal cell lines and in organoids, some of these compounds can develop into new venues of research exploring in detail their mechanism of action in the regulation of the cell cycle, the control of cell proliferation, and/or their potential role in regulating the differentiation of ISCs.

In this study we have successfully established the protocol described by Wells' group, for the generation of HIOs from iPSCs. This model showed important limitations, such as the absence of a representative secretory lineage, and an elevated cost of production, which rendered it incompatible with high-throughput studies. Consequently, we performed additional modifications to the culture conditions resulting in an important reduction in the time and cost for the production of the organoids. Furthermore, we used our optimized protocol to differentiate iPSCs on a microfluidics chip, resulting in the generation of a new model of gut-on-a-chip. Next, we sought to develop a cell line of iPSCs expressing an LGR5-GFP reporter, however we were unable to successfully integrate the reporter construct into the genome of the host. In spite of these results, we have provided solid evidence of our experimental approach and have encountered anecdotal reports from other research groups which have attempted to generate reporter cell lines with human LGR5 and had no success. This suggested an inherent problem with the use and detection of LGR5 in fluorescence-based techniques on non-cancerous human ISCs. Interestingly, this issue has not been properly discussed in the literature; therefore, we recommend a thorough re-evaluation of the capabilities and limitations of LGR5 as a reliable marker under the aforementioned conditions. Finally, we performed a preliminary small-molecule high-throughput screening on FUCCI-CaCo-2 cells, instead of LGR-GFP HIOs, due to the outcome from the reporter cell line, and the time and funding limitations of the project. The results of the screening identified 27 compounds with a potential effect over the G1 phase of the cell cycle. Given the role that G1 plays in the lineage specification of ISC and the malignant transformation in intestinal CSCs, these compounds could potentially serve in regulating the self-renewal and differentiation of the ISCs or to exert some control in the events prior to the transformation of ISCs into CSCs. Future work would be needed to validate these results through secondary screening, with different intestinal cell lines, and with HIOs.

Appendix 1. Solutions and buffers

Genomic DNA extraction

Nuclei lysis solution

10 mM	EDTA
0.8%	SDS
50 mM	Tris-HCl, pH 8.0
	dH$_2$O

TBE buffer [10x]$_{stock}$

445 mM	Boric acid
10 mM	EDTA
445 mM	Tris base
	dH$_2$O

TE buffer

1 mM	EDTA, pH 8.0
10 mM	Tris-HCl
	dH$_2$O

Adjust to pH 7.4.

Immunostaining

Fixing solution

3.7%	Formaldehyde
	PBS
	PBS

Hank's Balanced Salt Solution [10x]$_{stock}$

13 mM	Calcium chloride
55 mM	D-glucose
5 mM	Magnesium chloride anhydrous
4 mM	Magnesium sulphate anhydrous
54 mM	Potassium chloride
4 mM	Potassium phosphate monobasic
42 mM	Sodium bicarbonate
1369 mM	Sodium chloride
3 mM	Sodium phosphate dibasic

Adjust to pH 6.5, autoclave and store at 4°C.

Immunofluorescence blocking buffer

3%	BSA
	PBS

Immunofluorescence washing buffer

1%	BSA

Permeabilization solution

0.1%	Triton X-100
	PBS

Organoid immunostaining

HCE buffer [10x]_{stock}

HCE buffer [10x]$_{stock}$

25 mM	Calcium chloride
50 mM	EDTA
1 M	HEPES buffer pH 7.42

Organoids blocking solution

1%	BSA
1x	IF buffer

Organoids immunofluorescence buffer/IF buffer

1x	PBS
0.2%	Triton X-100
0.05%	Tween-20

Organoids permeabilization solution

1x	PBS
0.5%	Triton X-100

Plasmid isolation

Alkaline lysis solution I

10 mM	EDTA, pH 8.0
50 mM	Glucose
25 mM	Tris-HCl, pH 8.0
	dH$_2$O

Autoclave and store at 4°C

Alkaline lysis solution II

1%	SDS
200 mM	Sodium hydroxide
	dH$_2$O

Alkaline lysis solution III

2 M	Glacial acetic acid
3 M	Potassium acetate
	dH$_2$O

Store at 4°C.

Protein purification

Elution buffer [10x]_{stock}

2 M   Glycine
                dH_2O
Adjust to pH 2.85.

Storage buffer

2.7 mM   Potassium chloride
150 mM   Sodium chloride
10 mM   Sodium phosphate monobasic
                dH_2O
Adjust to pH 7.4 and add 20% ethanol.

Wash/binding buffer [5x]_{stock}

500 mM   Sodium phosphate dibasic
750 mM   Sodium chloride
                dH_2O
Adjust to pH 7.4.

SDS-PAGE/Western blot

Coomassie blue staining solution

10%   Acetic acid
0.1%   Coomassie brilliant blue R-250
50%   Methanol
            dH_2O
Filter the solution through a Whatman No. 1 filter.

Destaining solution

10%   Acetic acid
40%   Methanol
50% dH_2O

SDS-PAGE running buffer [10x]_{stock}

2 M   Glycine
1%   SDS
250 mM   Tris base
            dH_2O
Adjust to pH 8.3.

TBST/western blot washing buffer [10x]_{stock}

1.5 M   Sodium chloride
200 mM   Tris-HCl, pH 7.5
1%   Tween-20
            dH_2O

Western blot blocking buffer

5%   BSA
            TBST buffer

Appendix 2. SYBR Green RT-qPCR primer design

Gene	Primer	Size (nt)	Sense	% GC	T_m (°C)	ΔG hairpin	Temp	ΔG homo	ΔG hetero	Amplicon nt
ATOH1	TGAAGTGAAGGAGTTGGGAGAC	22	Fwd	50.0	60.7	0.57	13.6	-1.94	-4.75	115
	GTAGACGGGATGCTCTCTCG	20	Rev	60.0	60.0	-1.19	38.5	-3.61		
BMI1	CTTTCATTGTCTTTTCCGCC	20	Fwd	45.0	59.7	2.25	-22.0	-3.61	-4.64	122
	CAGGTGGGGATTTAGCTCAG	20	Rev	55.0	59.7	0.83	13.5	-6.34		
CDH1	GAACGCATTGCCACATACAC	20	Fwd	50.0	60.0	0.61	14.3	-5.09	-6.21	118
	ATTCGGGCTTGTTGTCATTC	20	Rev	45.0	59.9	0.8	11.5	-3.61		
CHGA	GTCCTGGCTCTTCTGCTCTG	20	Fwd	60.0	60.3	-0.49	31.2	-3.14	-4.64	114
	TGTGTCGGAGATGACCTCAA	20	Rev	50.0	60.3	-1.96	46.4	-3.61		
DEFA5	CCTTTGCAGGAAATGGACTC	20	Fwd	50.0	59.7	-0.73	36.8	-7.05	-5.09	98
	GGACTCACGGGTAGCACAAC	20	Rev	60.0	60.6	0.32	18.6	-3.61		
FOXA2	CGACTGGAGCGCTACTATGC	20	Fwd	57.1	60.2	-0.68	33.5	-6.34	-5.09	90
	TACGTGTTCATGCCGTTCAT	20	Rev	45.0	60.0	-0.74	34.8	-6.3		
HES1	AACCAAAGACAGCATCTGAGC	21	Fwd	47.6	59.5	-1.22	41.8	-3.55	-5.13	114
	GAGCATCCAAAATCAGTGTTTTC	23	Rev	39.1	60.0	0.33	21.0	-5.83		
HPRT1	TGGCGTCGTGATTAGTGATG	20	Fwd	50.0	60.7	0.55	9.5	-3.61	-5.02	88
	CACCCTTTCCAAATCCTCAG	20	Rev	50.0	59.5	1.58	-3.8	-3.89		
LGR5	CAGCGTCTTCACCTCCTACC	20	Fwd	60.0	59.9	1.22	3.2	-3.61	-4.64	128
	TGGGAATGTATGTCAGAGCG	20	Rev	50.0	59.7	0.38	19.3	3.61		
MKI67	TGGGTCTGTTATTGATGAGCC	21	Fwd	47.6	60.0	-1.45	37.5	-3.14	-5.02	109
	TGACTTCCTTCCATTCTGAAGAC	23	Rev	43.5	59.7	-1.82	41.5	-5.12		
MUC2	GACACCATCTACCTCACCCG	20	Fwd	60.0	60.4	0.73	11.6	-3.61	-4.67	103
	TGTAGGCATCGCTCTTCTCA	20	Rev	50.0	59.7	0.1	23.5	-3.61		
NANOG	GATTTGTGGGCCTGAAGAAA	20	Fwd	45.0	60.1	1.71	-0.9	-9.28	-4.67	93
	ATGGAGGAGGGAAGAGGAGA	20	Rev	50.0	57.8	-	-	-1.47		
OCT4	GTGGAGGAAGCTGACAACAA	20	Fwd	50.0	58.9	0.27	19.1	-6.34	-3.52	97
	GGTTCTCGATACTGGTTCGC	20	Rev	55.0	59.7	-0.36	29.3	-6.76		
SOX17	CAGAATCCAGACCTGCACAA	20	Fwd	50.0	59.8	0.21	21.8	-7.05	-5.13	101
	TCTGCCTCCTCCACGAAG	18	Rev	61.1	60.1	1.55	-3.3	-3.61		
VIL1	CCCTGGAGCAGCTAGTGAAC	20	Fwd	60.0	60.0	-0.18	28.3	-6.34	-6.69	157
	AGGTTTTGTTGCTTCCATCG	20	Rev	45.0	60.1	-0.01	25.1	-3.61		
VIM	CTTCAGAGAGAGGAAGCCGA	20	Fwd	55.0	59.8	-0.29	28.3	-5.12	-6.59	97
	ATTCCACTTTGCGTTCAAGG	20	Rev	45.0	60.1	0.19	23.0	-3.9		

Appendix 3. Taqman RT-qPCR primer design

Gene	NCBI Accession	UPL #	Primer	Size (nt)	Sense	% GC	T$_m$ (°C)	Transcript amplicon (nt)
ACTA2	>NM_001141945.2	78	CCTATCCCCGGGACTAAGAC	20	Fwd	60.0	59.8	74
			AGGCAGTGCTGTCCTCTTCT	20	Rev	55.0	59.2	
ATOH1	>NM_005172.1	70	GCCTTGTCCGAGCTGCTA	18	Fwd	61.1	60.2	78
			GTGGTCGCTTTTGCAGGA	18	Rev	55.6	61.0	
B2M	>NM_004048.2	42	TTCTGGCCTGGAGGCTATC	19	Fwd	57.9	60.3	86
			TCAGGAAATTTGACTTTCCATTC	23	Rev	34.8	59.5	
BMI1	>NM_005180.8	63	TTCTTTGACCAGAACAGATTGG	22	Fwd	40.9	59.2	112
			GCATCACAGTCATTGCTGCT	20	Rev	50.0	60.0	
CDX2	>NM_001265.5	34	ATCACCATCCGGAGGAAAG	19	Fwd	52.6	59.9	82
			TGCGGTTCTGAAACCAGATT	20	Rev	45.0	60.6	
CHGA	>NM_001275.3	17	CAAACCGCAGACCAGAGG	18	Fwd	61.1	60.4	61
			TCCAGCTCTGCTTCAATGG	19	Rev	53.0	60.1	
DEFA5	>NM_021010.2	60	TGAGGCTACAACCCAGAAGC	20	Fwd	55.0	60.4	108
			GCTCTTGCCTGAGAACCTGA	20	Rev	55.0	60.7	
FOXA2	>NM_021784.4	42	GGTGATTGCTGGTCGTTTG	19	Fwd	52.6	60.1	68
			AGCATACTGGAAGCCGAGTG	20	Rev	55.0	60.4	
GATA4	>NM_001308093.1	17	GGAAGCCCAAGAACCTGAAT	20	Fwd	50.0	60.4	98
			GTTGCTGGAGTTGCTGGAA	19	Rev	52.6	60.0	
HES1	>NM_005524.3	60	GAAGCACCTCCGGAACCT	18	Fwd	61.1	60.2	111
			GTCACCTCGTTCATGCACTC	20	Rev	55.0	59.3	
HPRT1	>NM_000194.2	73	TGACCTTGATTTATTTTGCATACC	24	Fwd	33.3	59.3	102
			CGAGCAAGACGTTCAGTCCT	20	Rev	55.0	60.6	
LGR5	>NM_003667.3	78	ACCAGACTATGCCTTTGGAAAC	22	Fwd	45.5	59.5	76
			TCCCAGGGAGTGGATTCTATT	21	Rev	47.6	59.8	
LYZ	>NM_000239.2	68	CCGCTACTGGTGTAATGATGG	21	Fwd	52.4	60.4	92
			CATCAGCGATGTTATCTTGCAG	22	Rev	45.5	60.8	
MUC2	>NM_002457.4	61	CCAGCTCATCAAGGACAGC	19	Fwd	57.9	59.5	78
			AACACGCAGGCATCGTAGTA	20	Rev	50.0	59.4	
NANOG	>NM_024865.3	87	TCTCCAACATCCTGAACCTCA	21	Fwd	47.6	60.6	106
			TTGCTATTCTTCGGCCAGTT	20	Rev	45.0	59.8	
SOX17	>NM_022454.3	61	ACGCCGAGTTGAGCAAGA	18	Fwd	55.6	60.7	82
			TCTGCCTCCTCCACGAAG	18	Rev	61.1	60.1	
VIL1	>NM_007127.2	87	TTGCCACAATTCCCTGAGAT	20	Fwd	45.0	60.5	71
			CTTGGTCATGGTGAGTGAGC	20	Rev	55.0	59.3	

Appendix 4. Breakdown of the protocols used in the optimization of the SRSF protocol

Cell line	ECM for stem cell stage	ECM for 3D culture	Pluripotent stage (D0)	Definitive endoderm stage (D1–D3)	Hindgut stage (D4–D7)	Growth and differentiation (D7–D10)	End product	Reference
H1 or H9 hESCs	hESC-qualified Matrigel	Intestinal/basement membrane Matrigel	mTeSR1; 10 µM Y-27632	RPMI 1640 basal medium + 1% P/S + 2 mM L-Gln. D1: 100 ng/mL Activin A. D2: 100 ng/mL Activin A, 0.2% dFBS. D3: 100 ng/mL Activin A, 2% dFBS	RPMI 1640 basal medium + 1% P/S + 2 mM L-Gln. D4–D6: 2% dFBS, 500 ng/mL FGF4, 500 ng/mL WNT3A	Intestinal growth and differentiation (D8->): Advanced DMEM-F12 basal medium + 1% P/S + 2 mM L-Gin; 15 mM HEPES, 1x B27, 100 ng/mL NOG, 500 ng/mL RSPO1, 100 ng/mL EGF	Intestinal organoid	McCracken et al, 2011
H1 or H9 hESCs	hESC-qualified Matrigel	Intestinal/basement membrane Matrigel	mTeSR1; 10 µM Y-27632	RPMI 1640 basal medium + 1% P/S + 2 mM L-Gln. D1: 100 ng/mL Activin A, 50 ng/mL BMP4. D2: 100 ng/mL Activin A, 0.2% dFBS. D3: 100 ng/mL Activin A, 2% dFBS	Foregut stage: RPMI 1640 basal medium + 1% P/S + 2 mM L-Gln. D4–D6: 2% dFBS, 2 µM CHIR 99021, 500 ng/mL FGF4, 200 ng/mL NOG; 2% dFBS, 2 µM CHIR 99021, 2 µM Retinoic acid, 500 ng/mL FGF4, 200 ng/mL NOG	Gastric growth and differentiation (D7–D10): Advanced DMEM-F12 basal medium + 1% P/S + 2 mM L-Gln; 10 mM HEPES, 1x N2, 2 µM Retinoic acid, 100 ng/mL NOG, 100 ng/mL EGF; D10->: 10 mM HEPES, 1x N2, 1x B27, 100 ng/mL EGF	Gastric organoid	McCracken et al, 2014
LGR5+ cells from crypt isolates	Matrigel, growth factor reduced, phenol free	Matrigel, growth factor reduced, phenol free	Stem cell expansion stage (D0): Advanced DMEM-F12 basal medium + 1% P/S + 2 mM Glutamax; 10 mM HEPES, 1x B27, 1x N2, 1 mM N-acetylcysteine, 10 mM Gastrin, 10 mM Nicotinamide, 100 ng/mL NOG, 1 µg/mL RSPO1, 100 ng/mL WNT3A, 50 ng/mL EGF, 500 nM A-83-01 (TGF β inhibitor), 10 µM SB202190 (p38 inhibitor), 10 µM Y-27632	Advanced DMEM-F12 basal medium + 1% P/S + 2 mM Glutamax; 10 mM HEPES, 1x B27, 1x N2, 1 mM N-acetylcysteine, 10 mM Gastrin, 10 mM Nicotinamide, 100 ng/mL NOG, 1 µg/mL RSPO1, 100 ng/mL WNT3A, 50 ng/mL EGF, 500 nM A-83-01 (TGF β inhibitor), 10 µM SB202190 (p38 inhibitor)	Intestinal growth and differentiation (D7 -> 26 months): Advanced DMEM-F12 basal medium + 1% P/S + 2 mM Glutamax	Advanced DMEM-F12 basal medium + 1% P/S + 2 mM Glutamax; 10 mM HEPES, 1x B27, 1x N2, 1 mM N-acetylcysteine, 10 mM Gastrin, 100 ng/mL NOG, 10 nM Gastrin, 1 µg/mL RSPO1, 50 ng/mL EGF, 500 nM A-83-01 (TGF β inhibitor)	Intestinal enteroid	Sato et al, 2011a,b
H1 and 207 hESCs, and Detroit 551 hiPSCs	-		E8 medium	RPMI 1640 Glutamax basal medium + 1% P/S; 1x B27, 3 µM CHIR 99021	Hepatocyte progenitors (D4–D6): Knockout DMEM + 1% P/S + 2 mM Glutamax; 1x NEAA, 20% Knockout serum replacement, 100 µM 2-mercaptoethanol, 1% DMSO	Hepatocyte-like cells differentiation (D8–D17): Leibovitz L15 media + 1% P/S + 2 mM Glutamax; 8.3% Tryptose phosphate broth, 10 µM Hydrocortisone 21-hemisuccinate, 50 µg/mL Sodium L-acorbate, 100 nM Dexamethasone, 0.58% Insulin-transferrin-selenium, 100 nM Dihexa	Monolayer of hepatocyte-like cells	Siller et al, 2015
miFF1 hiPSCs	laminin-521	Intestinal/basement membrane Matrigel	mTeSR1; 10 µM Y-27632	RPMI 1640 basal medium + 1% P/S + 2 mM L-Gln; 1x Non-essential amino acids, 1x B27, 2 µM CHIR 99021, 100 ng/mL Activin A	Hindgut stage: RPMI 1640 basal medium + 1% P/S + 2 mM L-Gln; 1x Non-essential amino acids, 2% dFBS, 2 µM CHIR 99021, 500 ng/mL FGF4, 100 ng/mL NOG	Intestinal growth and differentiation (D8->): Advanced DMEM-F12 basal medium + 1% P/S + 2 mM L-Gin; 15 mM HEPES, 1x B27, 100 ng/mL NOG, 500 ng/mL RSPO1, 100 ng/mL EGF	Intestinal organoid	SRSF protocol v.1
miFF1 hiPSCs	v.2.1 - Laminin-521; v.2.2 - Vitronectin (VTN-N); v.2.3 - 50% Laminin-521 + 50% Vitronectin (VTN-N)	Intestinal/basement membrane Matrigel	mTeSR1; 10 µM Y-27632	RPMI 1640 basal medium + 1% P/S + 2 mM L-Gln; 1x Non-essential amino acids, 1x B27, 2 µM CHIR 99021, 100 ng/mL Activin A	Hindgut stage: RPMI 1640 basal medium + 1% P/S + 2 mM L-Gln; 1x Non-essential amino acids, 2% dFBS, 2 µM CHIR 99021, 500 ng/mL FGF4, 100 ng/mL NOG	Intestinal growth and differentiation (D8->): Advanced DMEM-F12 basal medium + 1% P/S + 2 mM L-Gin; 15 mM HEPES, 1x B27, 100 ng/mL NOG, 500 ng/mL rmRSPO1, 100 ng/mL EGF	Intestinal organoid	SRSF protocol v.2
miFF1 hiPSCs	v.3.1 - Laminin-521; v.3.2 - Vitronectin (VTN-N); v.3.3 - 50% Laminin-521 + 50% Vitronectin (VTN-N)	Intestinal/basement membrane Matrigel	mTeSR1; 10 µM Y-27632	RPMI 1640 basal medium + 1% P/S + 2 mM L-Gln; 1x NEAA, 1x B27, 2 µM CHIR 99021, 100 ng/mL Activin A	Hindgut stage: RPMI 1640 basal medium + 1% P/S + 2 mM L-Gln; 1x NEAA, 2% dFBS, 2 µM CHIR 99021, 500 ng/mL FGF4, 100 ng/mL NOG	Intestinal growth and differentiation (D8->): Advanced DMEM-F12 basal medium + 1% P/S + 2 mM L-Gin; 15 mM HEPES, 1x B27, 100 ng/mL NOG, 500 ng/mL rmRSPO1, 100 ng/mL EGF	Intestinal organoid	SRSF protocol v.3
miFF1 hiPSCs	laminin-521	Intestinal/basement membrane Matrigel	mTeSR1; 10 µM Y-27632	RPMI 1640 basal medium + 1% P/S + 2 mM L-Gln; 1x NEAA, 1x B27, 3 µM CHIR 99021	Hindgut stage: RPMI 1640 basal medium + 1% P/S + 2 mM L-Gln; 1x NEAA, 2% dFBS, 2 µM CHIR 99021, 500 ng/mL FGF4, 100 ng/mL NOG	Intestinal growth and differentiation (D7->): Advanced DMEM-F12 basal medium + 1% P/S + 2 mM L-Gin; 15 mM HEPES, 1x B27, 100 ng/mL NOG, 500 ng/mL rmRSPO1, 100 ng/mL EGF	Intestinal organoid	SRSF protocol v.4

Table A.1 Protocols consulted to optimize the differentiation of the definitive endoderm and for the generation of HIOs.

Appendix 5. Breakdown of the data from the biological replicates assessed in the HTS
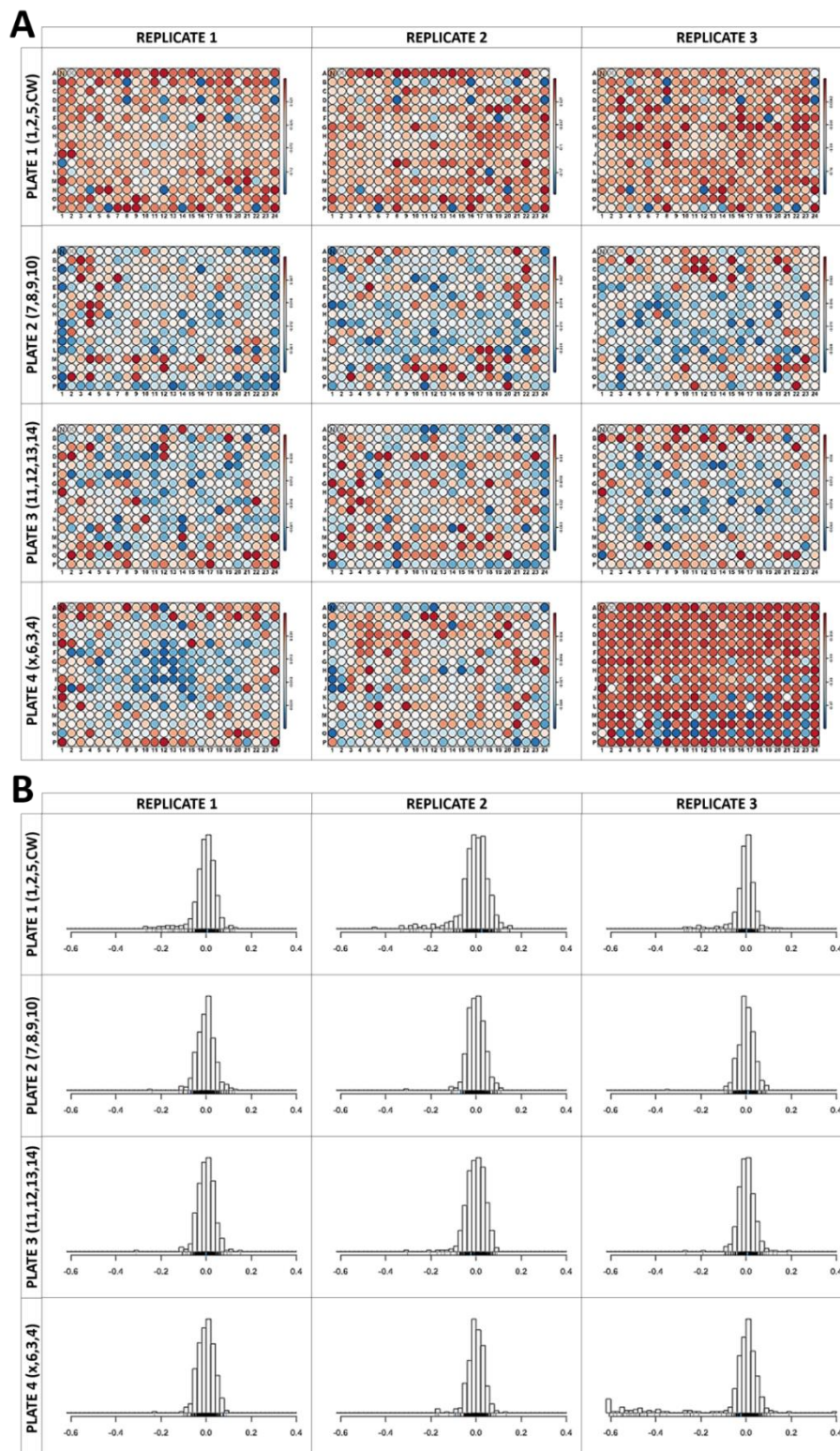
Figure A.1 Breakdown of the data from the biological replicates in Experiment 1
Experiment 1 from the HTS measured the percentage of cells in G1 phase, based on the expression of the reporter mKO2-CDT1. (A) Heat map from the plates of each biological replicate showing the distribution of the hits and their scoring intensity across the plate; (B) Histogram of the data of each biological replicate indicating the presence of a normal distribution of the data, and the outliers representing potential hits.
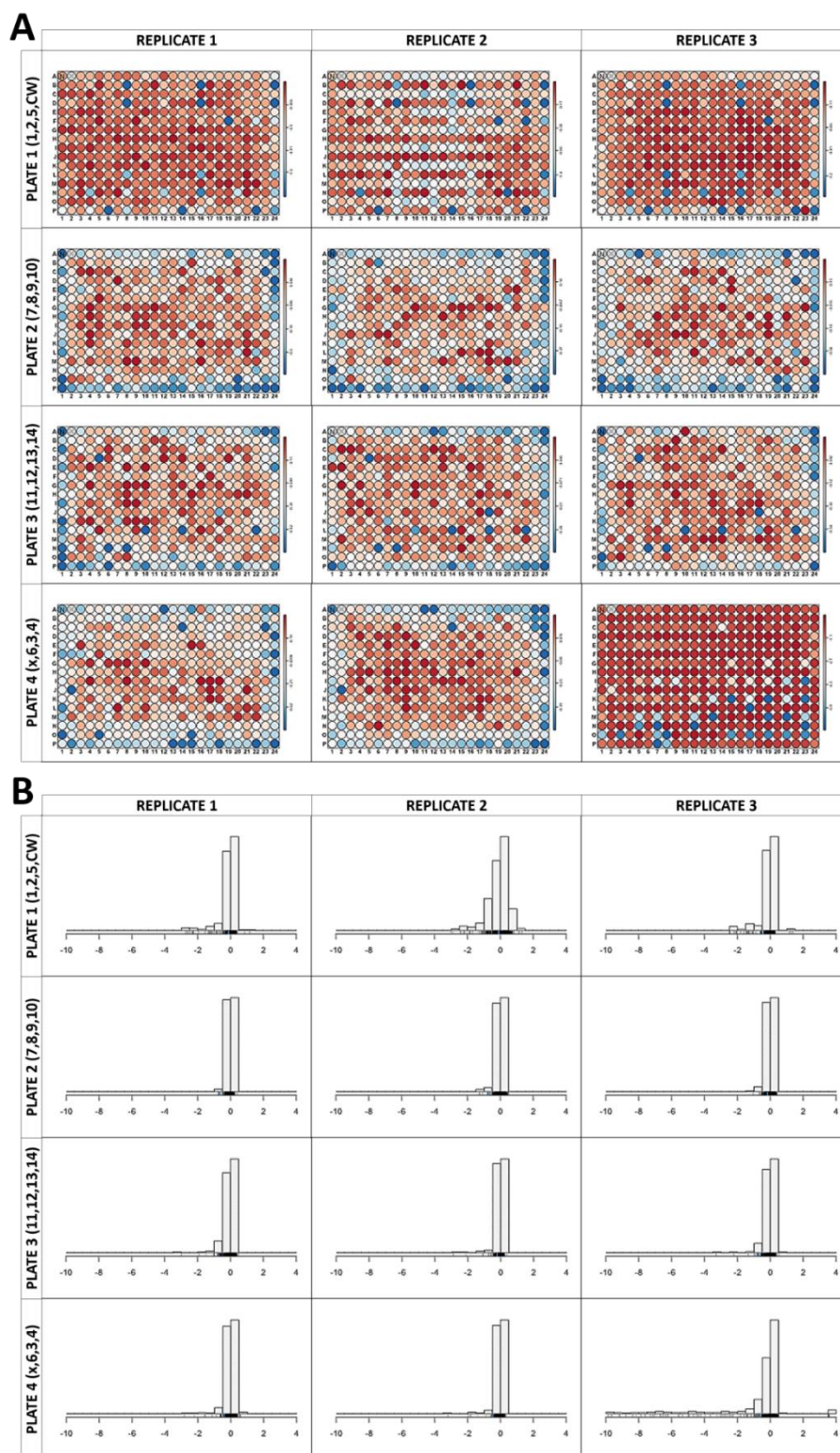
Figure A.2 Breakdown of the data from the biological replicates in Experiment 2
Experiment 2 from the HTS measured the RFI from the reporter mKO2-CDT1. (A) Heat map from the plates of each biological replicate showing the distribution of the hits and their scoring intensity across the plate; (B) Histogram of the data of each biological replicate indicating the presence of a normal distribution of the data, and the outliers representing potential hits.
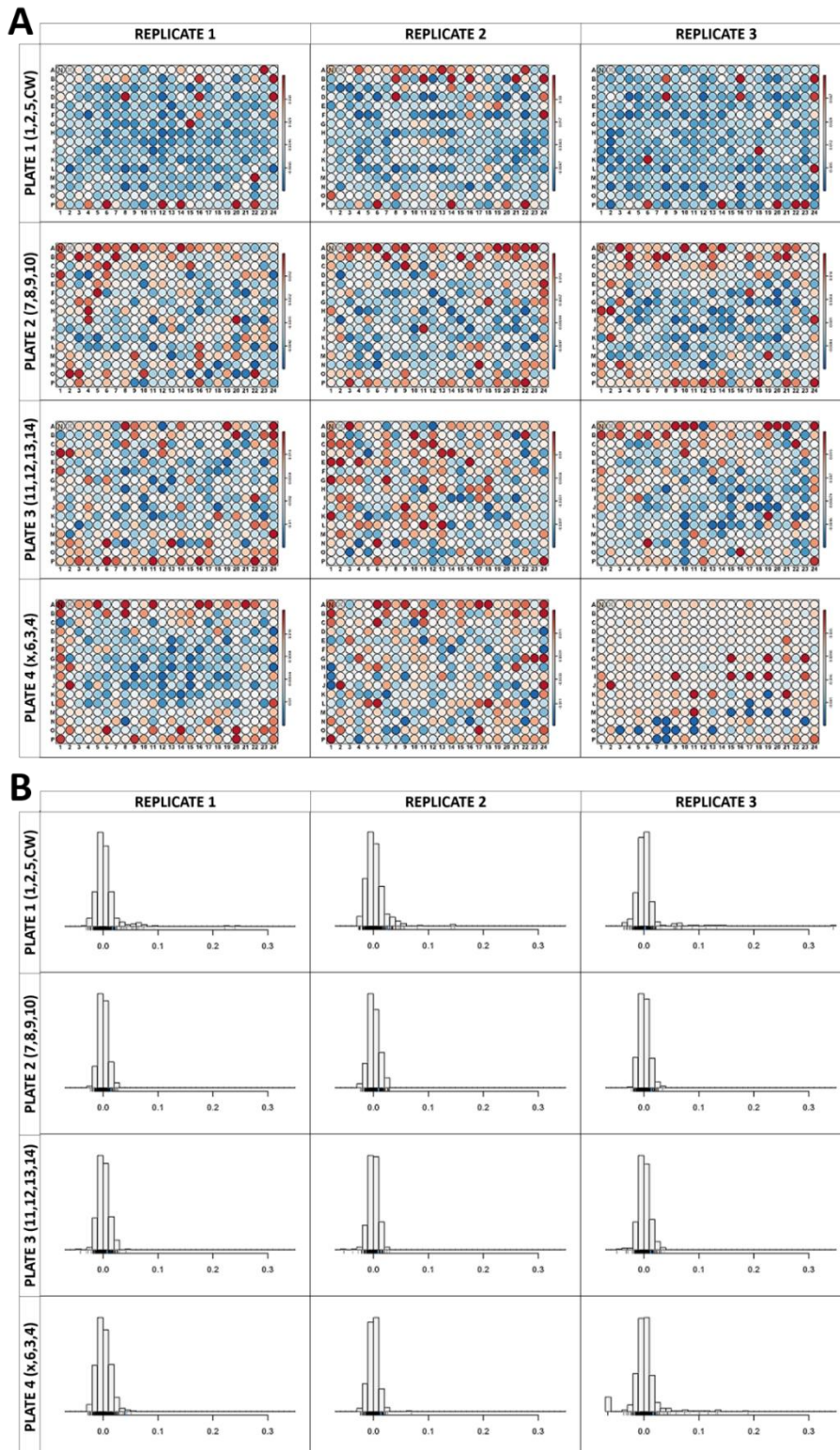
Figure A.3 Breakdown of the data from the biological replicates in Experiment 3
Experiment 3 from the HTS measured the percentage of cells expressing the reporter H2B-GFP. (A) Heat map from the plates of each biological replicate showing the distribution of the hits and their scoring intensity across the plate; (B) Histogram of the data of each biological replicate indicating the presence of a normal distribution of the data, and the outliers representing potential hits.
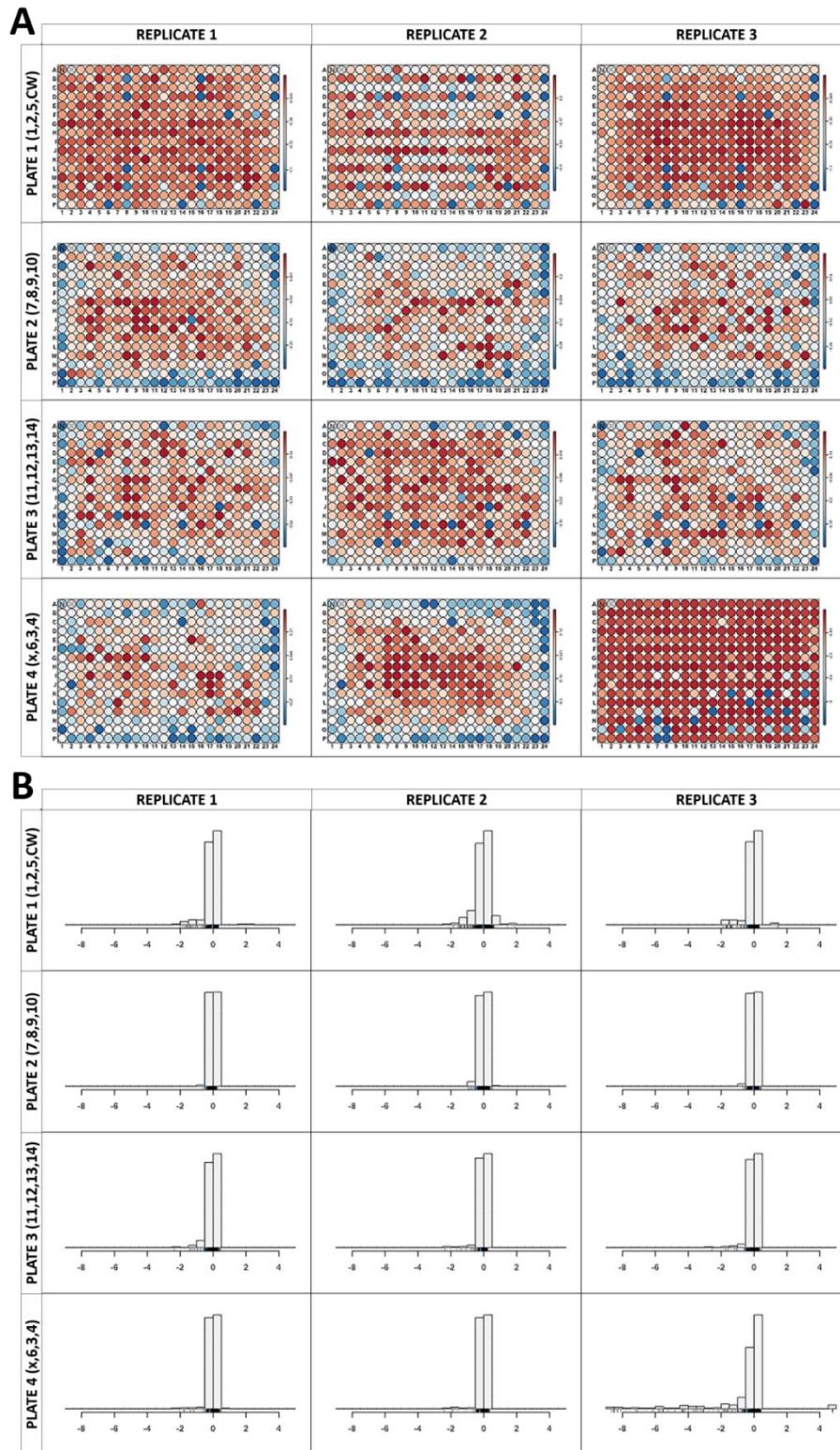
Figure A.4 Breakdown of the data from the biological replicates in Experiment 4
Experiment 4 from the HTS measured the RFI from the reporter H2B-GFP. (A) Heat map from the plates of each biological replicate showing the distribution of the hits and their scoring intensity across the plate; (B) Histogram of the data of each biological replicate indicating the presence of a normal distribution of the data, and the outliers representing potential hits.

REFERENCES

Agrawal S, Woźniak M, Łuc M, Makuch S, Pielka E, Agrawal AK, Wietrzyk J, Banach J, Gamian A, Pizon M & Ziółkowski P (2019). Insulin enhancement of the antitumor activity of chemotherapeutic agents in colorectal cancer is linked with downregulating PIK3CA and GRB2. *Sci Rep* **9,** 16647.

Ahmed D, Eide PW, Eilertsen IA, Danielsen SA, Eknæs M, Hektoen M, Lind GE & Lothe RA (2013). Epigenetic and genetic features of 24 colon cancer cell lines. *Oncogenesis* **2,** e71.

Ahmed M & Ffrench-Constant C (2016). Extracellular Matrix Regulation of Stem Cell Behavior. *Curr Stem Cell Reports* **2,** 197–206.

Aigelsreiter A, Janig E, Stumptner C, Fuchsbichler A, Zatloukal K & Denk H (2007). How a Cell Deals with Abnormal Proteins Pathogenetic Mechanisms in Protein Aggregation Diseases. *Pathobiology* **74,** 145–158.

Albalushi H, Kurek M, Karlsson L, Landreh L, Kjartansdóttir KR, Söder O, Hovatta O & Stukenborg JB (2018). Laminin 521 stabilizes the pluripotency expression pattern of human embryonic stem cells initially derived on feeder cells. *Stem Cells Int* **2018,** 7127042.

Allaire JM, Morampudi V, Crowley SM, Stahl M, Yu H, Bhullar K, Knodler LA, Bressler B, Jacobson K & Vallance BA (2018). Frontline defenders: Goblet cell mediators dictate host-microbe interactions in the intestinal tract during health and disease. *Am J Physiol - Gastrointest Liver Physiol* **314,** G360–G377.

Altay G, Larrañaga E, Tosi S, Barriga FM, Batlle E, Fernández-Majada V & Martínez E (2019). Self-organized intestinal epithelial monolayers in crypt and villus-like domains show effective barrier function. *Sci Rep* **9,** 10140.

Andäng M, Hjerling-Leffler J, Moliner A, Lundgren TK, Castelo-Branco G, Nanou E, Pozas E, Bryja V, Halliez S, Nishimaru H, Wilbertz J, Arenas E, Koltzenburg M, Charnay P, Manira A El, Ibañez CF & Ernfors P (2008). Histone H2AX-dependent GABA(A) receptor regulation of stem cell proliferation. *Nature* **451,** 460–464.

Anderson JM, Van Itallie CM, Peterson MD, Stevenson BR, Carew EA & Mooseker MS (1989). ZO-1 mRNA and protein expression during tight junction assembly in Caco- 2 cells. *J Cell Biol* **109,** 1047–1056.

Andoh A, Bamba S, Brittan M, Fujiyama Y & Wright NA (2007). Role of intestinal subepithelial myofibroblasts in inflammation and regenerative response in the gut. *Pharmacol Ther* **114,** 94–

106.

Andrews PW, Banting G, Damjanov I, Arnaud D & Avner P (1984). Three monoclonal antibodies defining distinct differentiation antigens associated with different high molecular weight polypeptides on the surface of human embryonal carcinoma cells. *Hybridoma* **3,** 347–361.

Andrews PW, Bronson DL, Benham F, Strickland S & Knowles BB (1980). A comparative study of eight cell lines derived from human testicular teratocarcinoma. *Int J Cancer* **26,** 269–280.

Andrews PW, Goodfellow PN, Shevinsky LH, Bronson DL & Knowles BB (1982). Cell-surface antigens of a clonal human embryonal carcinoma cell line: morphological and antigenic differentiation in culture. *Int J Cancer* **29,** 523–531.

Ansari AM, Ahmed AK, Matsangos AE, Lay F, Born LJ, Marti G, Harmon JW & Sun Z (2016). Cellular GFP Toxicity and Immunogenicity: Potential Confounders in in Vivo Cell Tracking Experiments. *Stem Cell Rev Reports* **12,** 553–559.

Antfolk M & Jensen KB (2020). A bioengineering perspective on modelling the intestinal epithelial physiology in vitro. *Nat Commun* **11,** 6244.

Arora N, Alsous JI, Guggenheim JW, Mak M, Munera J, Wells JM, Kamm RD, Asada HH, Shvartsman SY & Griffith LG (2017). A process engineering approach to increase organoid yield. *Development* **144,** 1128–1136.

Artursson P (1990). Epithelial transport of drugs in cell culture. I: A model for studying the passive diffusion of drugs over intestinal absorbtive (Caco-2) cells. *J Pharm Sci* **79,** 476–482.

Artursson P & Karlsson J (1991). Correlation between oral drug absorption in humans and apparent drug permeability coefficients in human intestinal epithelial (Caco-2) cells. *Biochem Biophys Res Commun* **175,** 880–885.

Artursson P, Palm K & Luthman K (2001). Caco-2 monolayers in experimental and theoretical predictions of drug transport. *Adv Drug Deliv Rev* **64,** 280–289.

Attene-Ramos MS, Nava GM, Muellner MG, Wagner ED, Plewa MJ & Gaskins HR (2010). DNA damage and toxicogenomic analyses of hydrogen sulfide in human intestinal epithelial FHs 74 int cells. *Environ Mol Mutagen* **51,** 304–314.

Auclair BA, Benoit YD, Rivard N, Mishina Y & Perreault N (2007). Bone Morphogenetic Protein Signaling Is Essential for Terminal Differentiation of the Intestinal Secretory Cell Lineage. *Gastroenterology*

133, 887–896.

Aurora M & Spence JR (2016). hPSC-derived lung and intestinal organoids as models of human fetal tissue. *Dev Biol* **420,** 230–238.

Baaske DM & Heinstein P (1977). Cytotoxicity and cell cycle specificity of homoharringtonine. *Antimicrob Agents Chemother* **12,** 298–300.

Badder LM et al. (2020). 3D imaging of colorectal cancer organoids identifies responses to Tankyrase inhibitors. *PLoS One* **15,** e0235319.

Baens M, Noels H, Broeckx V, Hagens S, Fevery S, Billiau AD, Vankelecom H & Marynen P (2006). The dark side of EGFP: Defective polyubiquitination. *PLoS One* **1,** e54.

Baker A-M, Graham TA, Elia G, Wright NA & Rodriguez-Justo M (2015). Characterization of LGR5 stem cells in colorectal adenomas and carcinomas. *Sci Rep* **5,** 8654.

Baker AM, Cereser B, Melton S, Fletcher AG, Rodriguez-Justo M, Tadrous PJ, Humphries A, Elia G, McDonald SAC, Wright NA, Simons BD, Jansen M & Graham TA (2014). Quantification of crypt and stem cell evolution in the normal and neoplastic human colon. *Cell Rep* **8,** 940–947.

Baptista AP, Olivier BJ, Goverse G, Greuter M, Knippenberg M, Kusser K, Domingues RG, Veiga-Fernandes H, Luster AD, Lugering A, Randall TD, Cupedo T & Mebius RE (2013). Colonic patch and colonic SILT development are independent and differentially regulated events. *Mucosal Immunol* **6,** 511–521.

Barker N (2014). Adult intestinal stem cells: critical drivers of epithelial homeostasis and regeneration. *Nat Rev Mol Cell Biol* **15,** 19–33.

Barker N, Bartfeld S & Clevers H (2010). Tissue-resident adult stem cell populations of rapidly self-renewing organs. *Cell Stem Cell* **7,** 656–670.

Barker N, van Es JH, Kuipers J, Kujala P, van den Born M, Cozijnsen M, Haegebarth A, Korving J, Begthel H, Peters PJ & Clevers H (2007). Identification of stem cells in small intestine and colon by marker gene Lgr5. *Nature* **449,** 1003–1007.

Barker N, Van Oudenaarden A & Clevers H (2012). Identifying the stem cell of the intestinal crypt: Strategies and pitfalls. *Cell Stem Cell* **11,** 452–460.

Basak O, Van De Born M, Korving J, Beumer J, Van Der Elst S, Van Es JH & Clevers H (2014). Mapping

early fate determination in Lgr5 + crypt stem cells using a novel Ki67-RFP allele. *EMBO J* **33,** 2057–2068.

Becker KA, Ghule PN, Therrien JA, Lian JB, Stein JL, Van Wijnen AJ & Stein GS (2006). Self-renewal of human embryonic stem cells is supported by a shortened G1 cell cycle phase. *J Cell Physiol* **209,** 883–893.

Becker L, Huang Q & Mashimo H (2008). Immunostaining of Lgr5, an intestinal stem cell marker, in normal and premalignant human gastrointestinal tissue. *ScientificWorldJournal* **8,** 1168–1176.

Bein A, Shin W, Jalili-Firoozinezhad S, Park MH, Sontheimer-Phelps A, Tovaglieri A, Chalkiadaki A, Kim HJ & Ingber DE (2018). Microfluidic Organ-on-a-Chip Models of Human Intestine. *Cell Mol Gastroenterol Hepatol* **5,** 659–668.

Benlloch S, Payá A, Alenda C, Bessa X, Andreu M, Jover R, Castells A, Llor X, Aranda FI & Massutí B (2006). Detection of BRAF V600E mutation in colorectal cancer: Comparison of automatic sequencing and real-time chemistry methodology. *J Mol Diagnostics* **8,** 540–543.

Bennett KM, Parnell EA, Sanscartier C, Parks S, Chen G, Nair MG & Lo DD (2016). Induction of Colonic M Cells during Intestinal Inflammation. *Am J Pathol* **186,** 1166–1179.

Bettayeb K, Oumata N, Echalier A, Ferandin Y, Endicott JA, Galons H & Meijer L (2008). CR8, a potent and selective, roscovitine-derived inhibitor of cyclin-dependent kinases. *Oncogene* **27,** 5797–5807.

Bezençon C, Fürholz A, Raymond F, Mansourian R, Métairon S, Le Coutre J & Damak S (2008). Murine intestinal cells expressing Trpm5 are mostly brush cells and express markers of neuronal and inflammatory cells. *J Comp Neurol* **509,** 514–525.

Bian J, Dannappel M, Wan C & Firestein R (2020). Transcriptional Regulation of Wnt/β-Catenin Pathway in Colorectal Cancer. *Cells* **9,** 2125.

Birchenough GMH, Johansson ME V, Gustafsson JK, Bergström JH & Hansson GC (2015). New developments in goblet cell mucus secretion and function. *Mucosal Immunol* **8,** 712–719.

Bjerknes M & Cheng H (2006). Neurogenin 3 and the enteroendocrine cell lineage in the adult mouse small intestinal epithelium. *Dev Biol* **300,** 722–735.

Boisvert EM, Means RE, Michaud M, Thomson JJ, Madri JA & Katz SG (2020). A static self-directed method for generating brain organoids from human embryonic stem cells. *J Vis Exp* **2020,**

e60379.

Bond CE & Whitehall VLJ (2018). How the BRAF V600E Mutation Defines a Distinct Subgroup of Colorectal Cancer: Molecular and Clinical Implications. *Gastroenterol Res Pract* **2018,** 9250757.

Bondow BJ, Faber ML, Wojta KJ, Walker EM & Battle MA (2012). E-cadherin is required for intestinal morphogenesis in the mouse. *Dev Biol* **371,** 1–12.

Borggrefe T & Oswald F (2009). The Notch signaling pathway: Transcriptional regulation at Notch target genes. *Cell Mol Life Sci* **66,** 1631–1646.

Borghesi C, Taussig MJ & Nicoletti C (1999). Rapid appearance of M cells after microbial challenge is restricted at the periphery of the follicle-associated epithelium of Peyer's patch. *Lab Investig* **79,** 1393–1401.

De Bosscher K, Hill CS & Nicolás FJ (2004). Molecular and functional consequences of Smad4 C-terminal missense mutations in colorectal tumour cells. *Biochem J* **379,** 209–216.

Bourgeois MA & Oaks JL (2013). Laboratory Diagnosis of Viral Infections. In *Equine Infectious Diseases*, 2nd edn., ed. Sellon DC & Long MT, pp. 132-140.e2. W. B. Saunders.

Braam SR, Zeinstra L, Litjens S, Ward-van Oostwaard D, van den Brink S, van Laake L, Lebrin F, Kats P, Hochstenbach R, Passier R, Sonnenberg A & Mummery CL (2008). Recombinant Vitronectin Is a Functionally Defined Substrate That Supports Human Embryonic Stem Cell Self-Renewal via αVβ5 Integrin. *Stem Cells* **26,** 2257–2265.

Brafman DA, Phung C, Kumar N & Willert K (2013). Regulation of endodermal differentiation of human embryonic stem cells through integrin-ECM interactions. *Cell Death Differ* **20,** 369–381.

Bronson DL, Andrews PW, Solter D, Cervenka J, Lange PH & Fraley EE (1980). Cell line derived from a metastasis of a human testicular germ cell tumor. *Cancer Res* **40,** 2500–2506.

Brüning A & Jückstock J (2015). Misfolded proteins: From little villains to little helpers in the fight against cancer. *Front Oncol* **5,** 47.

de Bruyn JR, van den Brink GR, Steenkamer J, Buskens CJ, Bemelman WA, Meisner S, Muncan V, te Velde AA, D'Haens GR & Wildenberg ME (2018). Fibrostenotic Phenotype of Myofibroblasts in Crohn's Disease is Dependent on Tissue Stiffness and Reversed by LOX Inhibition. *J Crohn's Colitis* **12,** 849–859.

Buckley AM, Petersen J, Roe AJ, Douce GR & Christie JM (2015). LOV-based reporters for fluorescence imaging. *Curr Opin Chem Biol* **27,** 39–45.

Cabin R & Mitchell R (2000). To Bonferroni or Not to Bonferroni: When and How Are the Questions on JSTOR. *Bull Ecol Soc Am* **81,** 246–248.

Calder A (2011). *A lengthened G1 phase indicates differentiation status across multiple lineages in human embryonic stem cells* (thesis). McMaster University.

Calder A, Roth-Albin I, Bhatia S, Pilquil C, Lee JH, Bhatia M, Levadoux-Martin M, McNicol J, Russell J, Collins T & Draper JS (2013). Lengthened G1 Phase Indicates Differentiation Status in Human Embryonic Stem Cells. *Stem Cells Dev* **22,** 279–295.

Cameron K, Tan R, Schmidt-Heck W, Campos G, Lyall MJ, Wang Y, Lucendo-Villarin B, Szkolnicka D, Bates N, Kimber SJ, Hengstler JG, Godoy P, Forbes SJ & Hay DC (2015). Recombinant Laminins Drive the Differentiation and Self-Organization of hESC-Derived Hepatocytes. *Stem Cell Reports* **5,** 1250–1262.

Carroll TD, Newton IP, Chen Y, Blow JJ & Näthke I (2018). Lgr5+ intestinal stem cells reside in an unlicensed G1 phase. *J Cell Biol* **217,** 1667–1685.

Carulli AJ, Samuelson LC & Schnell S (2014). Unraveling intestinal stem cell behavior with models of crypt dynamics. *Integr Biol* **6,** 243.

Cerchiari A, Garbe JC, Todhunter ME, Jee NY, Pinney JR, LaBarge MA, Desai TA & Gartner ZJ (2015). Formation of Spatially and Geometrically Controlled Three-Dimensional Tissues in Soft Gels by Sacrificial Micromolding. *Tissue Eng - Part C Methods* **21,** 541–547.

Chatterjee A, Guo J, Lee HS & Schultz PG (2013). A genetically encoded fluorescent probe in mammalian cells. *J Am Chem Soc* **135,** 12540–12543.

Chen K, Srinivasan T, Tung K, Belmonte JM, Wang L, Murthy PKL, Choi J, Rakhilin N, King S, Varanko AK, Witherspoon M, Nishimura N, Glazier JA, Lipkin SM, Bu P & Shen X (2017). A Notch positive feedback in the intestinal stem cell niche is essential for stem cell self-renewal. *Mol Syst Biol* **13,** 927.

Chen W, Dong J, Haiech J, Kilhoffer MC & Zeniou M (2016). Cancer stem cell quiescence and plasticity as major challenges in cancer therapy. *Stem Cells Int* **2016,** 1740936.

Chen XM, Elisia I & Kitts DD (2010). Defining conditions for the co-culture of Caco-2 and HT29-MTX

cells using Taguchi design. *J Pharmacol Toxicol Methods* **61,** 334–342.

Chen Y, Lin Y, Davis KM, Wang Q, Rnjak-Kovacina J, Li C, Isberg RR, Kumamoto CA, Mecsas J & Kaplan DL (2015). Robust bioengineered 3D functional human intestinal epithelium. *Sci Rep* **5,** 13708.

Cheng H & Leblond CP (1974). Origin, differentiation and renewal of the four main epithelial cell types in the mouse small intestine V. Unitarian theory of the origin of the four epithelial cell types. *Am J Anat* **141,** 537–561.

Cheng H, Merzel J & Leblond CP (1969). Renewal of Paneth cells in the small intestine of the mouse. *Am J Anat* **126,** 507–525.

Chiang T-WW, le Sage C, Larrieu D, Demir M & Jackson SP (2016). CRISPR-Cas9D10A nickase-based genotypic and phenotypic screening to enhance genome editing. *Sci Rep* **6,** 24356.

Chikayama S, Kimura S, Kobayashi Y, Abe T, Maekawa T & Kondo M (1998). Effects of daunorubicin on cell growth, cell cycle and induction of apoptosis in HL-60 cells. *Haematol* **29,** 115–121.

Clevers H (2013). The intestinal crypt, a prototype stem cell compartment. *Cell* **154,** 274–284.

Clevers H (2016). Modeling Development and Disease with Organoids. *Cell* **165,** 1586–1597.

Clevers H & Nusse R (2012). Wnt/β-catenin signaling and disease. *Cell* **149,** 1192–1205.

Clevers HC & Bevins CL (2013). Paneth Cells: Maestros of the Small Intestinal Crypts. *Annu Rev Physiol* **75,** 289–311.

ClinicalTrials.gov (2016). Identifier: NCT02726334, A Phase I, Dose Escalation Study of BNC101 in Patients With Metastatic Colorectal Cancer. Available at: https://clinicaltrials.gov/ct2/show/NCT02726334 [Accessed November 17, 2020].

ClinicalTrials.gov (2018). Identifier: NCT03526835, A Study of Bispecific Antibody MCLA-158 in Patients With Advanced Solid Tumors. Available at: https://clinicaltrials.gov/ct2/show/NCT03526835 [Accessed November 17, 2020].

Co JY, Margalef-Català M, Li X, Mah AT, Kuo CJ, Monack DM & Amieva MR (2019). Controlling Epithelial Polarity: A Human Enteroid Model for Host-Pathogen Interactions. *Cell Rep* **26,** 2509-2520.e4.

Coker EA, Mitsopoulos C, Tym JE, Komianou A, Kannas C, Di Micco P, Villasclaras Fernandez E, Ozer B, Antolin AA, Workman P & Al-Lazikani B (2019). canSAR: Update to the cancer translational research and drug discovery knowledgebase. *Nucleic Acids Res* **47,** D917–D922.

Coralli C, Cemazar M, Kanthou C, Tozer GM & Dachs GU (2001). Limitations of the Reporter Green Fluorescent Protein under Simulated Tumor Conditions. *Cancer Res* **61,** 4784–4790.

Corr SC, Gahan CCGM & Hill C (2008). M-cells: Origin, morphology and role in mucosal immunity and microbial pathogenesis. *FEMS Immunol Med Microbiol* **52,** 2–12.

Creamer B, Shorter RG & Bamforth J (1961). The turnover and shedding of epithelial cells. *Gut* **2,** 110–118.

D'Amour KA, Agulnick AD, Eliazer S, Kelly OG, Kroon E & Baetge EE (2005). Efficient differentiation of human embryonic stem cells to definitive endoderm. *Nat Biotechnol* **23,** 1534–1541.

Dabiri Y, Abu el Maaty MA, Chan HY, Wölker J, Ott I, Wölfl S & Cheng X (2019). p53-Dependent Anti-Proliferative and Pro-Apoptotic Effects of a Gold(I) N-Heterocyclic Carbene (NHC) Complex in Colorectal Cancer Cells. *Front Oncol* **9,** 438.

Dalton S (2015). Linking the Cell Cycle to Cell Fate Decisions. *Trends Cell Biol* **25,** 592–600.

Date S & Sato T (2015). Mini-Gut Organoids: Reconstitution of the Stem Cell Niche. *Annu Rev Cell Dev Biol* **31,** 269–289.

Davila M & Bresalier RS (2008). Gastrointestinal complications of oncologic therapy. *Nat Clin Pract Gastroenterol Hepatol* **5,** 682–696.

Demagny H & De Robertis EM (2016). Point mutations in the tumor suppressor Smad4/DPC4 enhance its phosphorylation by GSK3 and reversibly inactivate TGF-β signaling. *Mol Cell Oncol* **3,** e1025181.

Demitrack ES & Samuelson LC (2016). Notch regulation of gastrointestinal stem cells. *J Physiol* **594,** 4791–4803.

Desmarais JA, Unger C, Damjanov I, Meuth M & Andrews P (2016). Apoptosis and failure of checkpoint kinase 1 activation in human induced pluripotent stem cells under replication stress. *Stem Cell Res Ther* **7,** 17.

Dillon A & Lo DD (2019). M cells: Intelligent engineering of mucosal immune surveillance. *Front Immunol* **10,** 1499.

DiMasi JA, Grabowski HG & Hansen RW (2016). Innovation in the pharmaceutical industry: New estimates of R&D costs. *J Health Econ* **47,** 20–33.

Dodd RH, Ouannes C, Potier M-C, Prado de Carvalho L, Rossiei J & Potier P (1987). Synthesis of β-carboline-benzodiazepine hybrid molecules: Use of the known structural requirements for benzodiazepine and β-carboline binding in designing a novel, high-affinity ligand for the benzodiazepine receptor. *J Med Chem* **30,** 1248–1254.

Dohi T, Rennert PD, Fujihashi K, Kiyono H, Shirai Y, Kawamura YI, Browning JL & McGhee JR (2001). Elimination of Colonic Patches with Lymphotoxin β Receptor-Ig Prevents Th2 Cell-Type Colitis. *J Immunol* **167,** 2781–2790.

Domansky K, Leslie DC, McKinney J, Fraser JP, Sliz JD, Hamkins-Indik T, Hamilton GA, Bahinski A & Ingber DE (2013). Clear castable polyurethane elastomer for fabrication of microfluidic devices. *Lab Chip* **13,** 3956.

Drost J, van Jaarsveld RH, Ponsioen B, Zimberlin C, van Boxtel R, Buijs A, Sachs N, Overmeer RM, Offerhaus GJ, Begthel H, Korving J, van de Wetering M, Schwank G, Logtenberg M, Cuppen E, Snippert HJ, Medema JP, Kops GJPL & Clevers H (2015). Sequential cancer mutations in cultured human intestinal stem cells. *Nature* **521,** 43–47.

Du H, Huang Y, Hou X, Quan X, Jiang J, Wei X, Liu Y, Li H, Wang P, Zhan M, Ai X, Lu L, Yuan S & Sun L (2018). Two novel camptothecin derivatives inhibit colorectal cancer proliferation via induction of cell cycle arrest and apoptosis in vitro and in vivo. *Eur J Pharm Sci* **123,** 546–559.

Du J, Zu Y, Li J, Du S, Xu Y, Zhang L, Jiang L, Wang Z, Chien S & Yang C (2016). Extracellular matrix stiffness dictates Wnt expression through integrin pathway. *Sci Rep* **6,** 20395.

Du Y, Li X, Niu Q, Mo X, Qui M, Ma T, Kuo CJ & Fu H (2020). Development of a miniaturized 3D organoid culture platform for ultra-high-throughput screening ed. Yao X. *J Mol Cell Biol* **12,** 630–643.

van Duinen V, Trietsch SJ, Joore J, Vulto P & Hankemeier T (2015). Microfluidic 3D cell culture: From tools to tissue models. *Curr Opin Biotechnol* **35,** 118–126.

Elisia I & Kitts DD (2013). Modulation of NF-κB and Nrf2 control of inflammatory responses in FHs 74 Int cell line is tocopherol isoform-specific. *Am J Physiol - Gastrointest Liver Physiol* **305,** G940-9.

Elmore SA (2006). Enhanced Histopathology of Mucosa-Associated Lymphoid Tissue. *Toxicol Pathol* **34,** 687–696.

Elphick DA & Mahida YR (2005). Paneth cells: Their role in innate immunity and inflammatory disease. *Gut* **54,** 1802–1809.

Enver T, Soneji S, Joshi C, Brown J, Iborra F, Orntoft T, Thykjaer T, Maltby E, Smith K, Abu Dawud R, Jones M, Matin M, Gokhale P, Draper J & Andrews PW (2005). Cellular differentiation hierarchies in normal and culture-adapted human embryonic stem cells. *Hum Mol Genet* **14,** 3129–3140.

van Es JH, Sato T, van de Wetering M, Lyubimova A, Yee Nee AN, Gregorieff A, Sasaki N, Zeinstra L, van den Born M, Korving J, Martens ACM, Barker N, van Oudenaarden A & Clevers H (2012). Dll1+ secretory progenitor cells revert to stem cells upon crypt damage. *Nat Cell Biol* **14,** 1099–1104.

Fan XS, Wu HY, Yu HP, Zhou Q, Zhang YF & Huang Q (2010). Expression of Lgr5 in human colorectal carcinogenesis and its potential correlation with β-catenin. *Int J Colorectal Dis* **25,** 583–590.

Fang Y & Eglen RM (2017). Three-Dimensional Cell Cultures in Drug Discovery and Development. *SLAS Discov* **22,** 456–472.

Fatehullah A, Tan SH & Barker N (2016). Organoids as an in vitro model of human development and disease. *Nat Cell Biol* **18,** 246–254.

Finkbeiner SR, Freeman JJ, Wieck MM, El-Nachef W, Altheim CH, Tsai Y-H, Huang S, Dyal R, White ES, Grikscheit TC, Teitelbaum DH & Spence JR (2015*a*). Generation of tissue-engineered small intestine using embryonic stem cell-derived human intestinal organoids. *Biol Open* **4,** 1462–1472.

Finkbeiner SR, Hill DR, Altheim CH, Dedhia PH, Taylor MJ, Tsai YH, Chin AM, Mahe MM, Watson CL, Freeman JJ, Nattiv R, Thomson M, Klein OD, Shroyer NF, Helmrath MA, Teitelbaum DH, Dempsey PJ & Spence JR (2015*b*). Transcriptome-wide Analysis Reveals Hallmarks of Human Intestine Development and Maturation In Vitro and In Vivo. *Stem Cell Reports* **4,** 1140–1155.

Finkbeiner SR, Zeng XL, Utama B, Atmar RL, Shroyer NF & Estes MK (2012). Stem cell-derived human intestinal organoids as an infection model for rotaviruses. *MBio* **3,** 1–6.

Finzi G, Cornaggia M, Capella C, Fiocca R, Bosi F, Solcia E & Samloff IM (1993). Cathepsin E in follicle associated epithelium of intestine and tonsils: localization to M cells and possible role in antigen processing. *Histochemistry* **99,** 201–211.

Fleisig H & Wong J (2012). Measuring cell cycle progression kinetics with metabolic labeling and flow cytometry. *J Vis Exp*e4045.

van der Flier LG, van Gijn ME, Hatzis P, Kujala P, Haegebarth A, Stange DE, Begthel H, van den Born M, Guryev V, Oving I, van Es JH, Barker N, Peters PJ, van de Wetering M & Clevers H (2009*a*). Transcription Factor Achaete Scute-Like 2 Controls Intestinal Stem Cell Fate. *Cell* **136,** 903–912.

van der Flier LG, Haegebarth A, Stange DE, van de Wetering M & Clevers H (2009*b*). OLFM4 Is a Robust Marker for Stem Cells in Human Intestine and Marks a Subset of Colorectal Cancer Cells. *Gastroenterology* **137,** 15–17.

Fogh J, Fogh JM & Orfeo T (1977*a*). One hundred and twenty seven cultured human tumor cell lines producing tumors in nude mice. *J Natl Cancer Inst* **59,** 221–226.

Fogh J & Trempe G (1975). New Human Tumor Cell Lines. In *Human Tumor Cells in Vitro*, 1st edn., ed. Fogh J, pp. 115–159. Plenum Press, New York.

Fogh J, Wright WC & Loveless JD (1977*b*). Absence of HeLa cell contamination in 169 cell lines derived from human tumors. *J Natl Cancer Inst* **58,** 209–214.

Fong EJ, Strelez C & Mumenthaler SM (2020). A Perspective on Expanding Our Understanding of Cancer Treatments by Integrating Approaches from the Biological and Physical Sciences. *SLAS Discov* **25,** 672–683.

Forbester JL, Goulding D, Vallier L, Hannan N, Hale C, Pickard D, Mukhopadhyay S & Dougan G (2015). Interaction of salmonella enterica serovar Typhimurium with intestinal organoids derived from human induced pluripotent stem cells. *Infect Immun* **83,** 2926–2934.

Fordham RP, Yui S, Hannan NRF, Soendergaard C, Madgwick A, Schweiger PJ, Nielsen OH, Vallier L, Pedersen RA, Nakamura T, Watanabe M & Jensen KB (2013). Transplantation of expanded fetal intestinal progenitors contributes to colon regeneration after injury. *Cell Stem Cell* **13,** 734–744.

Forster R, Chiba K, Schaeffer L, Regalado SG, Lai CS, Gao Q, Kiani S, Farin HF, Clevers H, Cost GJ, Chan A, Rebar EJ, Urnov FD, Gregory PD, Pachter L, Jaenisch R & Hockemeyer D (2014). Human intestinal tissue with adult stem cell properties derived from pluripotent stem cells. *Stem Cell Reports* **2,** 838–852.

Foulke-Abel J, In J, Kovbasnjuk O, Zachos NC, Ettayebi K, Blutt SE, Hyser JM, Zeng XL, Crawford SE, Broughman JR, Estes MK & Donowitz M (2014). Human enteroids as an ex-vivo model of host–pathogen interactions in the gastrointestinal tract. *Exp Biol Med* **239,** 1124–1134.

Franco DP, de Biazi BI, Zanetti TA, Marques LA, de Lima LVA, Lepri SR & Mantovani MS (2020). Apoptotic and cell cycle response to homoharringtonine and harringtonine in wild and mutant p53 hepatocarcinoma cells. *Hum Exp Toxicol* **39,** 1405–1416.

Fucile S, Palma E, Martínez-Torres A, Miledi R & Eusebi F (2002). The single-channel properties of

human acetylcholine α7 receptors are altered by fusing α7 to the green fluorescent protein. *Proc Natl Acad Sci U S A* **99,** 3956–3961.

Fujii M, Matano M, Toshimitsu K, Takano A, Mikami Y, Nishikori S, Sugimoto S & Sato T (2018). Human Intestinal Organoids Maintain Self-Renewal Capacity and Cellular Diversity in Niche-Inspired Culture Condition. *Cell Stem Cell* **23,** 787–793.

Fujimura Y, Hosobe M & Kihara T (1992). Ultrastructural study of M cells from colonic lymphoid nodules obtained by colonoscopic biopsy. *Dig Dis Sci* **37,** 1089–1098.

Fujimura Y & Iida M (2001). A new marker for cup cells in the rabbit small intestine: Expression of vimentin intermediate filament protein. *Med Electron Microsc* **34,** 223–229.

Gagnon M, Zihler Berner A, Chervet N, Chassard C & Lacroix C (2013). Comparison of the Caco-2, HT-29 and the mucus-secreting HT29-MTX intestinal cell models to investigate Salmonella adhesion and invasion. *J Microbiol Methods* **94,** 274–279.

Gamboa JM & Leong KW (2013). In vitro and in vivo models for the study of oral delivery of nanoparticles. *Adv Drug Deliv Rev* **65,** 800–810.

Gao N, White P & Kaestner KH (2009). Establishment of Intestinal Identity and Epithelial-Mesenchymal Signaling by Cdx2. *Dev Cell* **16,** 588–599.

Garvey CM, Lau R, Sanchez A, Sun RX, Fong EJ, Doche ME, Chen O, Jusuf A, Lenz HJ, Larson B & Mumenthaler SM (2020). Anti-EGFR therapy induces EGF secretion by cancer-associated fibroblasts to confer colorectal cancer chemoresistance. *Cancers (Basel)* **12,** 1393.

Gasparri F & Galvani A (2010). Image-based high-content reporter assays: Limitations and advantages. *Drug Discov Today Technol* **7,** e21–e30.

Gattazzo F, Urciuolo A & Bonaldo P (2014). Extracellular matrix: a dynamic microenvironment for stem cell niche. *Biochim Biophys Acta* **1840,** 2506–2519.

Gebert A, Hach G & Bartels H (1992). Co-localization of vimentin and cytokeratins in M-cells of rabbit gut-associated lymphoid tissue (GALT). *Cell Tissue Res* **269,** 331–340.

Gebert A, Rothkötter HJ & Pabst R (1996). M cells in payer's patches of the intestine. *Int Rev Cytol* **167,** 91–159.

Geibel JP (2005). Secretion and absorption by colonic crypts. *Annu Rev Physiol* **67,** 471–490.

Gerbe F, Brulin B, Makrini L, Legraverend C & Jay P (2009). DCAMKL-1 Expression Identifies Tuft Cells Rather Than Stem Cells in the Adult Mouse Intestinal Epithelium. *Gastroenterology* **137,** 2179–2180.

Gerbe F, Sidot E, Smyth DJ, Ohmoto M, Matsumoto I, Dardalhon V, Cesses P, Garnier L, Pouzolles M, Brulin B, Bruschi M, Harcus Y, Zimmermann VS, Taylor N, Maizels RM & Jay P (2016). Intestinal epithelial tuft cells initiate type 2 mucosal immunity to helminth parasites. *Nature* **529,** 226–230.

Ghildiyal R, Dixit D & Sen E (2013). EGFR inhibitor BIBU induces apoptosis and defective autophagy in glioma cells. *Mol Carcinog* **52,** 970–982.

Gilazieva Z, Ponomarev A, Rutland C, Rizvanov A & Solovyeva V (2020). Promising applications of tumor spheroids and organoids for personalized medicine. *Cancers (Basel)* **12,** 1–19.

Goding JW (1996). Immunofluorescence. In *Monoclonal Antibodies*, 3rd edn., pp. 352–399. Academic Press.

Gonsalves FC, Klein K, Carson BB, Katz S, Ekas LA, Evans S, Nagourney R, Cardozo T, Brown AMC & Das Gupta R (2011). An RNAi-based chemical genetic screen identifies three small-molecule inhibitors of the Wnt/wingless signaling pathway. *Proc Natl Acad Sci U S A* **108,** 5954–5963.

Goto H, Yang B, Petersen D, Pepper KA, Alfaro PA, Kohn DB & Reynolds CP (2003). Transduction of green fluorescent protein increased oxidative stress and enhanced sensitivity to cytotoxic drugs in neuroblastoma cell lines. *Mol Cancer Ther* **2,** 911–917.

Goto N, Ueo T, Fukuda A, Kawada K, Sakai Y, Miyoshi H, Taketo MM, Chiba T & Seno H (2017). Tumor and Stem Cell Biology Distinct Roles of HES1 in Normal Stem Cells and Tumor Stem-like Cells of the Intestine. *Cancer Res* **77,** 3442–3454.

Goto T, Kaida A & Miura M (2015). Visualizing cell-cycle kinetics after hypoxia/reoxygenation in HeLa cells expressing fluorescent ubiquitination-based cell cycle indicator (Fucci). *Exp Cell Res* **339,** 389–396.

Van de Graaf KM (1986). Anatomy and physiology of the gastrointestinal tract. *Pediatr Infect Dis* **5,** S11-16.

Gracz AD & Magness ST (2014). Defining hierarchies of stemness in the intestine: evidence from biomarkers and regulatory pathways. *Am J Physiol - Gastrointest Liver Physiol* **307,** G260-73.

Grapin-Botton A & Melton DA (2000). Endoderm development: From patterning to organogenesis.

Trends Genet **16,** 124–130.

Gregorieff A, Pinto D, Begthel H, Destrée O, Kielman M & Clevers H (2005). Expression pattern of Wnt signaling components in the adult intestine. *Gastroenterology* **129,** 626–638.

Guerrouahen BS, Futami M, Vaklavas C, Kanerva J, Whichard ZL, Nwawka K, Blanchard EG, Lee FY, Robinson LJ, Arceci R, Kornblau SM, Wieder E, Cayre YE & Corey SJ (2010). Dasatinib inhibits the growth of molecularly heterogeneous myeloid leukemias. *Clin Cancer Res* **16,** 1149–1158.

Gunawardene AR, Corfe BM & Staton CA (2011). Classification and functions of enteroendocrine cells of the lower gastrointestinal tract. *Int J Exp Pathol* **92,** 219–231.

Halldorsson S, Lucumi E, Gómez-Sjöberg R & Fleming RMT (2015). Advantages and challenges of microfluidic cell culture in polydimethylsiloxane devices. *Biosens Bioelectron* **63,** 218–231.

Hanahan D & Weinberg RA (2000). The hallmarks of cancer. *Cell* **100,** 57–70.

Hanson MR & Köhler RH (2001). GFP imaging: Methodology and application to investigate cellular compartmentation in plants. In *Journal of Experimental Botany*, pp. 529–539. Oxford University Press.

Hansson EM, Lendahl U & Chapman G (2004). Notch signaling in development and disease. *Semin Cancer Biol* **14,** 320–328.

Hao HX, Xie Y, Zhang Y, Zhang O, Oster E, Avello M, Lei H, Mickanin C, Liu D, Ruffner H, Mao X, Ma Q, Zamponi R, Bouwmeester T, Finan PM, Kirschner MW, Porter JA, Serluca FC & Cong F (2012). ZNRF3 promotes Wnt receptor turnover in an R-spondin-sensitive manner. *Nature* **485,** 195–202.

Hao Y et al. (2016). Oncogenic PIK3CA mutations reprogram glutamine metabolism in colorectal cancer. *Nat Commun* **7,** 11971.

He X, Tan C, Wang F, Wang Y, Zhou R, Cui D, You W, Zhao H, Ren J & Feng B (2016). Knock-in of large reporter genes in human cells via CRISPR/Cas9-induced homology-dependent and independent DNA repair. *Nucleic Acids Res* **44,** e85.

Van Der Heijden M & Vermeulen L (2019). Stem cells in homeostasis and cancer of the gut. *Mol Cancer* **18,** 66.

Heinz MC, Oost KC & Snippert HJG (2020). Introducing the Stem Cell ASCL2 Reporter STAR into Intestinal Organoids. *STAR Protoc* **1,** 100126.

Henderson JK, Draper JS, Baillie HS, Fishel S, Thomson JA, Moore H & Andrews PW (2002). Preimplantation human embryos and embryonic stem cells show comparable expression of stage-specific embryonic antigens. *Stem Cell* **20,** 329–337.

Herheliuk T, Perepelytsina O, Ugnivenko A, Ostapchenko L & Sydorenko M (2019). Investigation of multicellular tumor spheroids enriched for a cancer stem cell phenotype. *Stem Cell Investig* **6,** 21.

Herr R, Halbach S, Heizmann M, Busch H, Boerries M & Brummer T (2018). BRAF inhibition upregulates a variety of receptor tyrosine kinases and their downstream effector Gab2 in colorectal cancer cell lines. *Oncogene* **37,** 1576–1593.

Hidalgo IJ, Raub TJ & Borchardt RT (1989). Characterization of the Human Colon Carcinoma Cell Line (Caco-2) as a Model System for Intestinal Epithelial Permeability. *Gastroenterology* **96,** 736–749.

Hilgers a R, Conradi R a & Burton PS (1990). Caco-2 cell monolayers as a model for drug transport across the intestinal mucosa. *Pharm Res* **7,** 902–910.

Hiyoshi H, Abdelhady S, Segerström L, Sveinbjörnsson B, Nuriya M, Lundgren TK, Desfrere L, Miyakawa A, Yasui M, Kogner P, Johnsen JI, Andäng M & Uhlén P (2012). Quiescence and γH2AX in neuroblastoma are regulated by ouabain/Na,K-ATPase. *Br J Cancer* **106,** 1807–1815.

Hodin RA, Shei A & Meng S (1997). Transcriptional activation of the human villin gene during enterocyte differentiation. *J Gastrointest Surg* **1,** 433–438.

Hofman F (2002). Immunohistochemistry. In *Current Protocols in Immunology*. John Wiley & Sons, Inc., Hoboken, NJ, USA.

Holloway EM, Wu JH, Czerwinski M, Sweet CW, Wu A, Tsai YH, Huang S, Stoddard AE, Capeling MM, Glass I & Spence JR (2020). Differentiation of Human Intestinal Organoids with Endogenous Vascular Endothelial Cells. *Dev Cell* **54,** 516-528.e7.

Honda-Uezono A, Kaida A, Michi Y, Harada K, Hayashi Y, Hayashi Y & Miura M (2012). Unusual expression of red fluorescence at M phase induced by anti-microtubule agents in HeLa cells expressing the fluorescent ubiquitination-based cell cycle indicator (Fucci). *Biochem Biophys Res Commun* **428,** 224–229.

Hou Q, Ye L, Liu H, Huang L, Yang Q, Turner J & Yu Q (2018). Lactobacillus accelerates ISCs regeneration to protect the integrity of intestinal mucosa through activation of STAT3 signaling pathway

induced by LPLs secretion of IL-22. *Cell Death Differ* **25,** 1657–1670.

Howitt MR, Lavoie S, Michaud M, Blum AM, Tran S V., Weinstock J V., Gallini CA, Redding K, Margolskee RF, Osborne LC, Artis D & Garrett WS (2016). Tuft cells, taste-chemosensory cells, orchestrate parasite type 2 immunity in the gut. *Science (80-)* **351,** 1329–1333.

Hsi LC, Angerman-Stewart J & Eling TE (1999). Introduction of full-length APC modulates cyclooxygenase-2 expression in HT-29 human colorectal carcinoma cells at the translational level. *Carcinogenesis* **20,** 2045–2049.

Hsu PD, Scott DA, Weinstein JA, Ran FA, Konermann S, Agarwala V, Li Y, Fine EJ, Wu X, Shalem O, Cradick TJ, Marraffini LA, Bao G & Zhang F (2013). DNA targeting specificity of RNA-guided Cas9 nucleases. *Nat Biotechnol* **31,** 827–832.

Hsu SY, Liang S-G & Hsueh AJW (1998). Characterization of Two LGR Genes Homologous to Gonadotropin and Thyrotropin Receptors with Extracellular Leucine-Rich Repeats and a G Protein-Coupled, Seven-Transmembrane Region. *Mol Endocrinol* **12,** 1830–1845.

Hubatsch I, Ragnarsson EGE & Artursson P (2007). Determination of drug permeability and prediction of drug absorption in Caco-2 monolayers. *Nat Protoc* **2,** 2111–2119.

Huh D, Torisawa Y, Hamilton GA, Kim HJ & Ingber DE (2012). Microengineered physiological biomimicry: Organs-on-Chips. *Lab Chip* **12,** 2156.

Ichiba H, Kusuda S, Itagane Y, Fujita K & Issiki G (1992). Measurement of growth promoting activity in human milk using a fetal small intestinal cell line. *Neonatology* **61,** 47–53.

Ihemelandu C, Naeem A, Parasido E, Berry D, Chaldekas K, Harris BT, Rodriguez O & Albanese C (2019). Clinicopathologic and prognostic significance of LGR5, a cancer stem cell marker in patients with colorectal cancer. *Color Cancer* **8,** CRC11.

Ilyas M, Tomlinson IPM, Rowan A, Pignatelli M & Bodmer WF (1997). β-Catenin mutations in cell lines established from human colorectal cancers. *Proc Natl Acad Sci U S A* **94,** 10330–10334.

Imai H, Kato S, Sakamoto Y, Kakudo Y, Shimodaira H & Ishioka C (2014). High throughput RNAi screening identifies ID1 as a synthetic sick/lethal gene interacting with the common TP53 mutation R175H. *Oncol Rep* **31,** 1043–1050.

Inge LJ, Fowler AJ, Paquette KM, Richer AL, Tran N & Bremner RM (2013). Dasatinib, a small molecule inhibitor of the Src kinase, reduces the growth and activates apoptosis in pre-neoplastic Barrett's

esophagus cell lines: Evidence for a noninvasive treatment of high-grade dysplasia. *J Thorac Cardiovasc Surg* **145,** 531–538.

Ishizuya-Oka A (2005). Epithelial-Connective Tissue Cross-Talk Is Essential for Regeneration of Intestinal Epithelium. *J Nippon Med Sch* **72,** 13–18.

Jabaji Z, Brinkley GJ, Khalil HA, Sears CM, Lei NY, Lewis M, Stelzner M, Martín MG & Dunn JCY (2014). Type I collagen as an extracellular matrix for the in vitro growth of human small intestinal epithelium. *PLoS One* **9,** 1–9.

Jadhav U, Saxena M, O'Neill NK, Saadatpour A, Yuan GC, Herbert Z, Murata K & Shivdasani RA (2017). Dynamic Reorganization of Chromatin Accessibility Signatures during Dedifferentiation of Secretory Precursors into Lgr5+ Intestinal Stem Cells. *Cell Stem Cell* **21,** 65-77.e5.

Jaladanki RN & Wang J-Y (2010). *Regulation of gastrointestinal mucosal growth*ed. Granger DN & Granger JP. Morgan & Claypool Life Sciences, San Rafael CA.

Jayasooriya RGPT, Dilshara MG, Molagoda IMN, Park C, Park SR, Lee S, Choi YH & Kim GY (2018). Camptothecin induces G2/M phase arrest through the ATM-Chk2- Cdc25C axis as a result of autophagy-induced cytoprotection: Implications of reactive oxygen species. *Oncotarget* **9,** 21744–21757.

Jepson MA, Mason CM, Bennett MK, Simmons NL & Hirst BH (1992). Co-expression of vimentin and cytokeratins in M cells of rabbit intestinal lymphoid follicle-associated epithelium. *Histochem J* **24,** 33–39.

Jesch ED, Seo JM, Carr TP & Lee JY (2009). Sitosterol reduces messenger RNA and protein expression levels of Niemann-Pick C1-like 1 in FHs 74 Int cells. *Nutr Res* **29,** 859–866.

Jia Z, Wignall A, Prestidge C & Thierry B (2021). An ex vivo investigation of the intestinal uptake and translocation of nanoparticles targeted to Peyer's patches microfold cells. *Int J Pharm* **594,** 120167.

Jin YH, Joo H, Lee K, Kim H, Didier R, Yang Y, Shin H & Lee C (2019). Streamlined procedure for gene knockouts using all-in-one adenoviral CRISPR-Cas9. *Sci Rep* **9,** 277.

Johnson FM, Saigal B, Talpaz M & Donato NJ (2005). Dasatinib (BMS-354825) tyrosine kinase inhibitor suppresses invasion and induces cell cycle arrest and apoptosis of head and neck squamous cell carcinoma and non-small cell lung cancer cells. *Clin Cancer Res* **11,** 6924–6932.

Jose SS, De Zuani M, Tidu F, Hortová Kohoutková M, Pazzagli L, Forte G, Spaccapelo R, Zelante T & Frič J (2020). Comparison of two human organoid models of lung and intestinal inflammation reveals Toll-like receptor signalling activation and monocyte recruitment. *Clin Transl Immunol* **9,** e1131.

Jung C, Hugot J-P & Barreau F (2010). Peyer's Patches: The Immune Sensors of the Intestine. *Int J Inflam* **2010,** 1–12.

Jung KB, Lee H, Son YS, Lee MO, Kim YD, Oh SJ, Kwon O, Cho S, Cho HS, Kim DS, Oh JH, Zilbauer M, Min JK, Jung CR, Kim J & Son MY (2018). Interleukin-2 induces the in vitro maturation of human pluripotent stem cell-derived intestinal organoids. *Nat Commun* **9,** 3039.

Kaida A & Miura M (2012*a*). Visualizing the effect of hypoxia on fluorescence kinetics in living HeLa cells using the fluorescent ubiquitination-based cell cycle indicator (Fucci). *Exp Cell Res* **318,** 288–297.

Kaida A & Miura M (2012*b*). Differential dependence on oxygen tension during the maturation process between monomeric Kusabira Orange 2 and monomeric Azami Green expressed in HeLa cells. *Biochem Biophys Res Commun* **421,** 855–859.

Kaida A, Sawai N, Sakaguchi K & Miura M (2011). Fluorescence kinetics in HeLa cells after treatment with cell cycle arrest inducers visualized with Fucci (fluorescent ubiquitination-based cell cycle indicator). *Cell Biol Int* **35,** 359–363.

Kaji K, Norrby K, Paca A, Mileikovsky M, Mohseni P & Woltjen K (2009). Virus-free induction of pluripotency and subsequent excision of reprogramming factors. *Nature* **458,** 771–775.

Kanninen LK, Harjumäki R, Peltoniemi P, Bogacheva MS, Salmi T, Porola P, Niklander J, Smutný T, Urtti A, Yliperttula ML & Lou YR (2016). Laminin-511 and laminin-521-based matrices for efficient hepatic specification of human pluripotent stem cells. *Biomaterials* **103,** 86–100.

Karim BO & Huso DL (2013). Mouse models for colorectal cancer. *Am J Cancer Res* **3,** 240–250.

Karve SS, Pradhan S, Ward D V. & Weiss AA (2017). Intestinal organoids model human responses to infection by commensal and Shiga toxin producing Escherichia coli. *PLoS One* **12,** e0178966.

Kasendra M, Luc R, Yin J, Manatakis D V., Kulkarni G, Lucchesi C, Sliz J, Apostolou A, Sunuwar L, Obrigewitch J, Jang KJ, Hamilton GA, Donowitz M & Karalis K (2020). Duodenum intestine-chip for preclinical drug assessment in a human relevant model. *Elife* **9,** e50135.

Kasendra M, Tovaglieri A, Sontheimer-Phelps A, Jalili-Firoozinezhad S, Bein A, Chalkiadaki A, Scholl W,

Zhang C, Rickner H, Richmond CA, Li H, Breault DT & Ingber DE (2018). Development of a primary human Small Intestine-on-a-Chip using biopsy-derived organoids. *Sci Rep* **8,** 2871.

Katt ME, Placone AL, Wong AD, Xu ZS & Searson PC (2016). In vitro tumor models: Advantages, disadvantages, variables, and selecting the right platform. *Front Bioeng Biotechnol* **4,** 12.

Kawai K, Viars C, Arden K, Tarin D, Urquidi V & Goodison S (2002). Comprehensive karyotyping of the HT-29 colon adenocarcinoma cell line. *Genes Chromosom Cancer* **34,** 1–8.

Kazanjian A & Shroyer NF (2011). NOTCH signaling and ATOH1 in colorectal cancers. *Curr Colorectal Cancer Rep* **7,** 121–127.

Keemink J & Bergström CAS (2018). Caco-2 Cell Conditions Enabling Studies of Drug Absorption from Digestible Lipid-Based Formulations. *Pharm Res* **35,** 74.

Kemper K, Prasetyanti PR, De Lau W, Rodermond H, Clevers H & Medema JP (2012). Monoclonal antibodies against Lgr5 identify human colorectal cancer stem cells. *Stem Cells* **30,** 2378–2386.

Kernéis S, Bogdanova A, Kraehenbuhl JP & Pringault E (1997). Conversion by Peyer's patch lymphocytes of human enterocytes into M cells that transport bacteria. *Science (80-)* **277,** 949–952.

Kessler M, Hoffmann K, Brinkmann V, Thieck O, Jackisch S, Toelle B, Berger H, Mollenkopf H-J, Mangler M, Sehouli J, Fotopoulou C & Meyer TF (2015). The Notch and Wnt pathways regulate stemness and differentiation in human fallopian tube organoids. *Nat Commun* **6,** 8989.

Kikuchi K & Hoshino D (2020). Sensitization of HT29 colorectal cancer cells to vemurafenib in three-dimensional collagen cultures. *Cell Biol Int* **44,** 621–629.

Kim HJ, Huh D, Hamilton G & Ingber DE (2012). Human gut-on-a-chip inhabited by microbial flora that experiences intestinal peristalsis-like motions and flow. *Lab Chip* **12,** 2165.

Kim HJ & Ingber DE (2013). Gut-on-a-Chip microenvironment induces human intestinal cells to undergo villus differentiation. *Integr Biol* **5,** 1130.

Kim HJ, Li H, Collins JJ & Ingber DE (2016). Contributions of microbiome and mechanical deformation to intestinal bacterial overgrowth and inflammation in a human gut-on-a-chip. *Proc Natl Acad Sci* **113,** E7-15.

Kim K et al. (2010). Epigenetic memory in induced pluripotent stem cells. *Nature* **467,** 285–290.

Kim KY, Rhim TY, Choi I & Kim SS (2001). N-Acetylcysteine Induces Cell Cycle Arrest in Hepatic Stellate Cells through Its Reducing Activity. *J Biol Chem* **276,** 40591–40598.

Kim S, Choung S, Sun RX, Ung N, Hashemi N, Fong EJ, Lau R, Spiller E, Gasho J, Foo J & Mumenthaler SM (2020). Comparison of Cell and Organoid-Level Analysis of Patient-Derived 3D Organoids to Evaluate Tumor Cell Growth Dynamics and Drug Response. *SLAS Discov* **25,** 744–754.

Kim S, Kim D, Cho SW, Kim J & Kim JS (2014). Highly efficient RNA-guided genome editing in human cells via delivery of purified Cas9 ribonucleoproteins. *Genome Res* **24,** 1012–1019.

Klockgether T, Pardowitz I, Schwarz M, Sontag K & Turski L (1985). Evaluation of the muscle relaxant properties of a novel β-carboline, ZK 93423 in rats and cats. *Br J Pharmacol* **86,** 357–366.

Klunder LJ, Faber KN, Dijkstra G & Van Ijzendoorn SCD (2017). Mechanisms of cell polarity – Controlled epithelial homeostasis and immunity in the intestine. *Cold Spring Harb Perspect Biol* **9,** a027888.

Kondo S, Mizuno S, Hashita T, Iwao T & Matsunaga T (2020). Establishment of a novel culture method for maintaining intestinal stem cells derived from human induced pluripotent stem cells. *Biol Open* **9,** bio049064.

Koo B-K, Spit M, Jordens I, Low TY, Stange DE, van de Wetering M, van Es JH, Mohammed S, Heck AJR, Maurice MM & Clevers H (2012). Tumour suppressor RNF43 is a stem-cell E3 ligase that induces endocytosis of Wnt receptors. *Nature* **488,** 665–669.

Koo B-K, Stange DE, Sato T, Karthaus W, Farin HF, Huch M, van Es JH & Clevers H (2011). Controlled gene expression in primary Lgr5 organoid cultures. *Nat Methods* **9,** 81–83.

Koo BK & Clevers H (2014). Stem cells marked by the r-spondin receptor LGR5. *Gastroenterology* **147,** 289–302.

Kosinski C, Li VSW, Chan ASY, Zhang J, Ho C, Tsui WY, Chan TL, Mifflin RC, Powell DW, Yuen ST, Leung SY & Chen X (2007). Gene expression patterns of human colon tops and basal crypts and BMP antagonists as intestinal stem cell niche factors. *Proc Natl Acad Sci* **104,** 15418–15423.

Kothari A, Hittelman WN & Chambers TC (2016). Cell cycle-dependent mechanisms underlie vincristine-induced death of primary acute lymphoblastic leukemia cells. *Cancer Res* **76,** 3553–3561.

Krasowska J, Olasek M, Bzowska A, Clark PL & Wielgus-Kutrowska B (2010). The comparison of aggregation and folding of enhanced green fluorescent protein (EGFP) by spectroscopic studies.

Spectroscopy **24,** 343–348.

Krausova M & Korinek V (2014). Wnt signaling in adult intestinal stem cells and cancer. *Cell Signal* **26,** 570–579.

Ku CS, Rasmussen HE, Park Y, Jesch ED & Lee J (2011). Unsaturated fatty acids repress the expression of ATP-binding cassette transporter A1 in HepG2 and FHs 74 Int cells. *Nutr Res* **31,** 278–285.

Lai EC (2004). Notch signaling: Control of cell communication and cell fate. *Development* **131,** 965–973.

Laperle A, Masters KS & Palecek SP (2015). Influence of substrate composition on human embryonic stem cell differentiation and extracellular matrix production in embryoid bodies. *Biotechnol Prog* **31,** 212–219.

Latorre R, Sternini C, De Giorgio R & Greenwood-Van Meerveld B (2016). Enteroendocrine cells: A review of their role in brain-gut communication. *Neurogastroenterol Motil* **28,** 620–630.

de Lau W, Barker N, Low TY, Koo B-K, Li VSW, Teunissen H, Kujala P, Haegebarth A, Peters PJ, van de Wetering M, Stange DE, van Es J, Guardavaccaro D, Schasfoort RBM, Mohri Y, Nishimori K, Mohammed S, Heck AJR & Clevers H (2011). Lgr5 homologues associate with Wnt receptors and mediate R-spondin signalling. *Nature* **476,** 293–297.

de Lau W, Peng WC, Gros P & Clevers H (2014). The R-spondin/Lgr5/Rnf43 module: regulator of Wnt signal strength. *Genes Dev* **28,** 305–316.

Lavelle D, DeSimone J, Hankewych M, Kousnetzova T & Chen YH (2003). Decitabine induces cell cycle arrest at the G1 phase via p21 WAF1 and the G2/M phase via the p38 MAP kinase pathway. *Leuk Res* **27,** 999–1007.

Lee CS, Ryan EJ & Doherty GA (2014). Gastro-intestinal toxicity of chemotherapeutics in colorectal cancer: The role of inflammation. *World J Gastroenterol* **20,** 3751–3761.

Lee JM, Park DY, Yang L, Kim EJ, Ahrberg CD, Lee KB & Chung BG (2018). Generation of uniform-sized multicellular tumor spheroids using hydrogel microwells for advanced drug screening. *Sci Rep* **8,** 17145.

Lei NY, Jabaji Z, Wang J, Joshi VS, Brinkley GJ, Khalil H, Wang F, Jaroszewicz A, Pellegrini M, Li L, Lewis M, Stelzner M, Dunn JCY & Martìn MG (2014). Intestinal subepithelial myofibroblasts support the growth of intestinal epithelial stem cells. *PLoS One* **9,** e84651.

Leibowitz BJ, Yang L, Wei L, Buchanan ME, Rachid M, Parise RA, Beumer JH, Eiseman JL, Schoen RE, Zhang L & Yu J (2018). Targeting p53-dependent stem cell loss for intestinal chemoprotection. *Sci Transl Med* **10,** 7610.

Lelouard H, Sahuquet A, Reggio H & Montcourrier P (2001). Rabbit M cells and dome enterocytes are distinct cell lineages. *J Cell Sci* **114,** 2077–2083.

Lennernäs H, Palm K, Fagerholm U & Artursson P (1996). Comparison between active and passive drug transport in human intestinal epithelial (Caco-2) cells in vitro and human jejunum in vivo. *Int J Pharm* **127,** 103–107.

Lepourcelet M, Chen YNP, France DS, Wang H, Crews P, Petersen F, Bruseo C, Wood AW & Shivdasani RA (2004). Small-molecule antagonists of the oncogenic Tcf/β-catenin protein complex. *Cancer Cell* **5,** 91–102.

Leslie JL, Huang S, Opp JS, Nagy MS, Kobayashi M, Young VB & Spence JR (2015). Persistence and toxin production by Clostridium difficile within human intestinal organoids result in disruption of epithelial paracellular barrier function. *Infect Immun* **83,** 138–145.

Lesuffleur T, Barbat A, Dussaulx E & Zweibaum A (1990). Growth Adaptation to Methotrexate of HT-29 Human Colon Carcinoma Cells Is Associated with Their Ability to Differentiate into Columnar Absorptive and Mucus-secreting Cells. *Cancer Res* **50,** 6334–6343.

Lewis SL & Tam PPL (2006). Definitive endoderm of the mouse embryo: Formation, cell fates, and morphogenetic function. *Dev Dyn* **235,** 2315–2329.

Li F, Jiang T, Li Q & Ling X (2017). Camptothecin (CPT) and its derivatives are known to target topoisomerase I (Top1) as their mechanism of action: Did we miss something in CPT analogue molecular targets for treating human disease such as cancer? *Am J Cancer Res* **7,** 2350–2394.

Li H, Zhang J, Tong JHM, Chan AWH, Yu J, Kang W & To KF (2019). Targeting the oncogenic p53 mutants in colorectal cancer and other solid tumors. *Int J Mol Sci* **20,** 5999.

Li S, Xue H, Long B, Sun L, Truong T & Liu Y (2015). Efficient generation of hiPSC neural lineage specific knockin reporters using the CRISPR/Cas9 and Cas9 double nickase system. *J Vis Exp*e52539.

Li VC, Ballabeni A & Kirschner MW (2012). Gap 1 phase length and mouse embryonic stem cell self-renewal. *Proc Natl Acad Sci U S A* **109,** 12550–12555.

Li Y, Liu Y, Liu B, Wang J, Wei S, Qi Z, Wang S, Fu W & Chen YG (2018). A growth factor-free culture

system underscores the coordination between Wnt and BMP signaling in Lgr5+ intestinal stem cell maintenance. *Cell Discov* **4,** 49.

Liang X, Potter J, Kumar S, Zou Y, Quintanilla R, Sridharan M, Carte J, Chen W, Roark N, Ranganathan S, Ravinder N & Chesnut JD (2015). Rapid and highly efficient mammalian cell engineering via Cas9 protein transfection. *J Biotechnol* **208,** 44–53.

Lim ML, Jungebluth P, Sjöqvist S, Nikdin H, Kjartansdóttir KR, Unger C, Vassliev I & Macchiarini P (2013). Decellularized Feeders: An Optimized Method for Culturing Pluripotent Cells. *Stem Cells Transl Med* **2,** 975–982.

Lindemans CA et al. (2015). Interleukin-22 promotes intestinal-stem-cell-mediated epithelial regeneration. *Nature* **528,** 560–564.

Lino CA, Harper JC, Carney JP & Timlin JA (2018). Delivering crispr: A review of the challenges and approaches. *Drug Deliv* **25,** 1234–1257.

Liu B, Yu Z, Chen C, Kling DE & Newburg DS (2012). Human milk mucin 1 and mucin 4 inhibit Salmonella enterica serovar Typhimurium invasion of human intestinal epithelial cells in vitro. *J Nutr* **142,** 1504–1509.

Liu H, Jan M, Chou C, Chen P & Ke N (1999*a*). Is Green Fluorescent Protein Toxic to the Living Cells? *Biochem Biophys Res Commun* **260,** 712–717.

Liu M, Wikonkal NM & Brash DE (1999*b*). Induction of cyclin-dependent kinase inhibitors and G 1 prolongation by the chemopreventive agent N-acetylcysteine. *Carcinogenesis* **20,** 1869–1872.

Liu R, Li H, Cai J, Wei Q & Han X (2019*a*). Lgr5 + intestinal stem cell sorting and organoid culture. *Anim Model Exp Med* **2,** 132–135.

Liu R, Moriggl R, Zhang D, Li H, Karns R, Ruan H Bin, Niu H, Mayhew C, Watson C, Bangar H, Cha S wook, Haslam D, Zhang T, Gilbert S, Li N, Helmrath M, Wells J, Denson L & Han X (2019*b*). Constitutive STAT5 activation regulates Paneth and Paneth-like cells to control Clostridium difficile colitis. *Life Sci Alliance* **2,** e201900296.

Liu Y & Bodmer WF (2006). Analysis of P53 mutations and their expression in 56 colorectal cancer cell lines. *Proc Natl Acad Sci U S A* **103,** 976–981.

Liu Y & Chen Y-G (2018). 2D- and 3D-Based Intestinal Stem Cell Cultures for Personalized Medicine. *Cells* **7,** 225.

Liu Y, Liu K, Wang N & Zhang H (2017). N-acetylcysteine induces apoptosis via the mitochondria-dependent pathway but not via endoplasmic reticulum stress in H9c2 cells. *Mol Med Rep* **16,** 6626–6633.

Lo YC, Senese S, France B, Gholkar AA, Damoiseaux R & Torres JZ (2017*a*). Computational Cell Cycle Profiling of Cancer Cells for Prioritizing FDA-Approved Drugs with Repurposing Potential. *Sci Rep* **7,** 11261.

Lo YH, Chung E, Li Z, Wan YW, Mahe MM, Chen MS, Noah TK, Bell KN, Yalamanchili HK, Klisch TJ, Liu Z, Park JS & Shroyer NF (2017*b*). Transcriptional Regulation by ATOH1 and its Target SPDEF in the Intestine. *Cell Mol Gastroenterol Hepatol* **3,** 51–71.

Lochner M (2011). Tertiary lymphoid tissues in the colon: Friend and foe. *Gut Microbes* **2,** 193–197.

Lopez-Garcia C, Klein AM, Simons BD & Winton DJ (2010). Intestinal Stem Cell Replacement Follows a Pattern of Neutral Drift. *Science (80-)* **330,** 822–825.

Lotze J, Reinhardt U, Seitz O & Beck-Sickinger AG (2016). Peptide-tags for site-specific protein labelling: In vitro and in vivo. *Mol Biosyst* **12,** 1731–1745.

Mabbott NA, Donaldson DS, Ohno H, Williams IR & Mahajan A (2013). Microfold (M) cells: Important immunosurveillance posts in the intestinal epithelium. *Mucosal Immunol* **6,** 666–677.

Madara JL (1982). Cup Cells: Structure and Distribution of a Unique Class of Epithelial Cells in Guinea Pig, Rabbit, and Monkey Small Intestine. *Gastroenterology* **83,** 981–994.

Madara JL (1991). Functional morphology of epithelium of the small intestine. *Handb Physiol* **4,** 83–120.

Madara JL & Carlson SL (1985). Cup cells: Further structural characterization of the brush border and the suggestion that they may serve as an attachment site for an unidentified bacillus in guinea pig ileum. *Gastroenterology* **89,** 1374–1386.

Mahoney ZX, Stappenbeck TS & Miner JH (2008). Laminin 5 influences the architecture of the mouse small intestine mucosa. *J Cell Sci* **121,** 2493–2502.

Majumder S, Crabtree JS, Golde TE, Minter LM, Osborne BA & Miele L (2020). Targeting Notch in oncology: the path forward. *Nat Rev Drug Discov*.

Manghwar H, Lindsey K, Zhang X & Jin S (2019). CRISPR/Cas System: Recent Advances and Future

Prospects for Genome Editing. *Trends Plant Sci* **24,** 1102–1125.

Mansilla S, Piña B & Portugal J (2003). Daunorubicin-induced variations in gene transcription: Commitment to proliferation arrest, senescence and apoptosis. *Biochem J* **372,** 703–711.

Marakhova I, Domnina A, Shatrova A, Borodkina A, Burova E, Pugovkina N, Zemelko V & Nikolsky N (2019). Proliferation-related changes in K+ content in human mesenchymal stem cells. *Sci Rep* **9,** 346.

Mariadason JM, Bordonaro M, Aslam F, Shi L, Kuraguchi M, Velcich A & Augenlicht LH (2001). Down-regulation of beta-catenin TCF signaling is linked to colonic epithelial cell differentiation. *Cancer Res* **61,** 3465–3471.

Martin CR, Osadchiy V, Kalani A & Mayer EA (2018). The Brain-Gut-Microbiome Axis. *Cell Mol Gastroenterol Hepatol* **6,** 133–148.

Marx U et al. (2016). Biology-inspired microphysiological system approaches to solve the prediction dilemma of substance testing. *ALTEX* **33,** 272–321.

Massagué J (2004). G1 cell-cycle control and cancer. *Nature* **432,** 298–306.

Matano M, Date S, Shimokawa M, Takano A, Fujii M, Ohta Y, Watanabe T, Kanai T & Sato T (2015). Modeling colorectal cancer using CRISPR-Cas9–mediated engineering of human intestinal organoids. *Nat Med* **21,** 256–262.

Mathew S, Jaramillo M, Zhang X, Zhang L, Soto-Gutiérrez A & Banerjee I (2012). Analysis of alternative signaling pathways of endoderm induction of human embryonic stem cells identifies context specific differences. *BMC Syst Biol* **6,** 154.

Mathew S, Sundararaj S & Banerjee I (2015). Network Analysis Identifies Crosstalk Interactions Governing TGF-β Signaling Dynamics during Endoderm Differentiation of Human Embryonic Stem Cells. *Processes* **3,** 286–308.

May R, Qu D, Weygant N, Chandrakesan P, Ali N, Lightfoot SA, Li L, Sureban SM & Houchen CW (2014). Brief report: Dclk1 deletion in tuft cells results in impaired epithelial repair after radiation injury. *Stem Cells* **32,** 822–827.

McConnell RE, Higginbotham JN, Shifrin DA, Tabb DL, Coffey RJ & Tyska MJ (2009). The enterocyte microvillus is a vesicle-generating organelle. *J Cell Biol* **185,** 1285–1298.

McCracken KW, Catá EM, Crawford CM, Sinagoga KL, Schumacher M, Rockich BE, Tsai Y-H, Mayhew CN, Spence JR, Zavros Y & Wells JM (2014). Modelling human development and disease in pluripotent stem-cell-derived gastric organoids. *Nature* **516,** 400–404.

McCracken KW, Howell JC, Wells JM & Spence JR (2011). Generating human intestinal tissue from pluripotent stem cells in vitro. *Nat Protoc* **6,** 1920–1928.

Mehta G, Hsiao AY, Ingram M, Luker GD & Takayama S (2012). Opportunities and challenges for use of tumor spheroids as models to test drug delivery and efficacy. *J Control Release* **164,** 192–204.

Meridian Bioscience (2020*a*). BIOTAQ™ DNA Polymerase and Mixes. Available at: https://www.bioline.com/mwdownloads/download/link/id/1125//m/e/meridian_research_bio taq_dna_polymerase.pdf [Accessed November 20, 2020].

Meridian Bioscience (2020*b*). PCR Enzymes and Kits: Enzymes, optimized PCR mixes and other reagents for human, animal, plant and environmental applications. Available at: https://www.bioline.com/media/wysiwyg/support/product_guides/GBL0919_PCR_Enzymes_U Sbooklet_Digital.pdf [Accessed November 20, 2020].

Miller AJ, Dye BR, Ferrer-Torres D, Hill DR, Overeem AW, Shea LD & Spence JR (2019). Generation of lung organoids from human pluripotent stem cells in vitro. *Nat Protoc* **14,** 518–540.

Min S, Kim S & Cho SW (2020). Gastrointestinal tract modeling using organoids engineered with cellular and microbiota niches. *Exp Mol Med* **52,** 227–237.

Miranda Pessoa R, Gustavo Lima W, Duarte Vital K, Nascimento Cardoso V & Antunes Fernandes SO (2018). Repurposing the Thalidomide to the Treatment of Irinotecan-Induced Intestinal Mucositis: An Old Drug to a New Use. *Glob J Pharm Pharm Sci* **6,** 555682.

Miura S & Suzuki A (2017). Generation of Mouse and Human Organoid-Forming Intestinal Progenitor Cells by Direct Lineage Reprogramming. *Cell Stem Cell* **21,** 456–471.

Miura S & Suzuki A (2018). Brief summary of the current protocols for generating intestinal organoids. *Dev Growth Differ* **60,** 387–392.

Mochel JP, Jergens AE, Kingsbury D, Kim HJ, Martín MG & Allenspach K (2018). Intestinal Stem Cells to Advance Drug Development, Precision, and Regenerative Medicine: A Paradigm Shift in Translational Research. *AAPS J* **20,** 1–9.

von Moltke J (2018). Intestinal Tuft Cells. In *Physiology of the Gastrointestinal Tract*, 6th edn., ed. Said

HM, pp. 721–733. Academic Press.

Montgomery RK & Breault DT (2008). Small intestinal stem cell markers. *J Anat* **213,** 52–58.

Montgomery RK, Carlone DL, Richmond CA, Farilla L, Kranendonk MEG, Henderson DE, Baffour-Awuah NY, Ambruzs DM, Fogli LK, Algra S & Breault DT (2011). Mouse telomerase reverse transcriptase (mTert) expression marks slowly cycling intestinal stem cells. *Proc Natl Acad Sci* **108,** 179–184.

Moreno EL, Hachi S, Hemmer K, Trietsch SJ, Baumuratov AS, Hankemeier T, Vulto P, Schwamborn JC & Fleming RMT (2015). Differentiation of neuroepithelial stem cells into functional dopaminergic neurons in 3D microfluidic cell culture. *Lab Chip* **15,** 2419–2428.

Morgan RG, Mortensson E & Williams AC (2018). Targeting LGR5 in Colorectal Cancer: Therapeutic gold or too plastic? *Br J Cancer* **118,** 1410–1418.

Morin PJ, Vogelstein B & Kinzler KW (1996). Apoptosis and APC in colorectal tumorigenesis. *Proc Natl Acad Sci U S A* **93,** 7950–7954.

Mörkl S, Butler MI, Holl A, Cryan JF & Dinan TG (2020). Probiotics and the Microbiota-Gut-Brain Axis: Focus on Psychiatry. *Curr Nutr Rep* **9,** 171–182.

Mosca A, Leclerc M & Hugot JP (2016). Gut microbiota diversity and human diseases: Should we reintroduce key predators in our ecosystem? *Front Microbiol* **7,** 455.

Mulvaney J & Dabdoub A (2012). Atoh1, an essential transcription factor in neurogenesis and intestinal and inner ear development: function, regulation, and context dependency. *J Assoc Res Otolaryngol* **13,** 281–293.

Múnera JO, Sundaram N, Rankin SA, Hill D, Watson C, Mahe M, Vallance JE, Shroyer NF, Sinagoga KL, Zarzoso-Lacoste A, Hudson JR, Howell JC, Chatuvedi P, Spence JR, Shannon JM, Zorn AM, Helmrath MA & Wells JM (2017). Differentiation of Human Pluripotent Stem Cells into Colonic Organoids via Transient Activation of BMP Signaling. *Cell Stem Cell* **21,** 51-64.e6.

Múnera JO & Wells JM (2017). Generation of gastrointestinal organoids from human pluripotent stem cells. In *Organ Regeneration*, ed. Tsuji T, pp. 167–177. Humana Press Inc.

Muñoz J, Stange DE, Schepers AG, van de Wetering M, Koo B-K, Itzkovitz S, Volckmann R, Kung KS, Koster J, Radulescu S, Myant K, Versteeg R, Sansom OJ, van Es JH, Barker N, van Oudenaarden A, Mohammed S, Heck AJR & Clevers H (2012). The Lgr5 intestinal stem cell signature: robust expression of proposed quiescent '+4' cell markers. *EMBO J* **31,** 3079–3091.

Murata K, Jadhav U, Madha S, van Es J, Dean J, Cavazza A, Wucherpfennig K, Michor F, Clevers H & Shivdasani RA (2020). Ascl2-Dependent Cell Dedifferentiation Drives Regeneration of Ablated Intestinal Stem Cells. *Cell Stem Cell* **26,** 377-390.e6.

Nakagawa S (2004). A farewell to Bonferroni: the problems of low statistical power and publication bias. *Behav Ecol* **15,** 1044–1045.

Nam MO, Hahn S, Jee JH, Hwang TS, Yoon H, Lee DH, Kwon MS & Yoo J (2018). Effects of a small molecule R-spondin-1 substitute RS-246204 on a mouse intestinal organoid culture. *Oncotarget* **9,** 6356–6368.

Nass SJ, Rothenberg ML, Pentz R, Hricak H, Abernethy A, Anderson K, Gee AW, Harvey RD, Piantadosi S, Bertagnolli MM, Schrag D & Schilsky RL (2018). Accelerating anticancer drug development — opportunities and trade-offs. *Nat Rev Clin Oncol* **15,** 777–786.

Naumovska E, Aalderink G, Wong Valencia C, Kosim K, Nicolas A, Brown S, Vulto P, Erdmann KS & Kurek D (2020). Direct On-Chip Differentiation of Intestinal Tubules from Induced Pluripotent Stem Cells. *Int J Mol Sci* **21,** 4964.

Navabi N, McGuckin MA & Lindén SK (2013). Gastrointestinal cell lines form polarized epithelia with an adherent mucus layer when cultured in semi-wet interfaces with mechanical stimulation. *PLoS One* **8,** e68761.

Negoro R, Takayama K, Nagamoto Y, Sakurai F, Tachibana M & Mizuguchi H (2016). Modeling of drug-mediated CYP3A4 induction by using human iPS cell-derived enterocyte-like cells. *Biochem Biophys Res Commun* **472,** 631–636.

Ninomiya H, Takahashi S, Tanegashima K, Yokota C & Asashima M (1999). Endoderm differentiation and inductive effect of activin-treated ectoderm in Xenopus. *Dev Growth Differ* **41,** 391–400.

Noah TK, Donahue B & Shroyer NF (2011). Intestinal development and differentiation. *Exp Cell Res* **317,** 2702–2710.

Noah TK & Shroyer NF (2013). Notch in the Intestine: Regulation of Homeostasis and Pathogenesis. *Annu Rev Physiol* **75,** 263–288.

Noel G, Baetz NW, Staab JF, Donowitz M, Kovbasnjuk O, Pasetti MF & Zachos NC (2017). A primary human macrophage-enteroid co-culture model to investigate mucosal gut physiology and host-pathogen interactions. *Sci Rep* **7,** 45270.

Novellasdemunt L, Antas P & Li VSW (2015). Targeting Wnt signaling in colorectal cancer. A review in the theme: Cell signaling: Proteins, pathways and mechanisms. *Am J Physiol - Cell Physiol* **309,** C511–C521.

Nowak-Sliwinska P, Scapozza L & Altaba AR i. (2019). Drug repurposing in oncology: Compounds, pathways, phenotypes and computational approaches for colorectal cancer. *Biochim Biophys Acta - Rev Cancer* **1871,** 434–454.

Nowrouzi A, Sertorio MG, Akbarpour M, Knoll M, Krunic D, Kuhar M, Schwager C, Brons S, Debus J, Wells SI, Wells JM & Abdollahi A (2020). Personalized Assessment of Normal Tissue Radiosensitivity via Transcriptome Response to Photon, Proton and Carbon Irradiation in Patient-Derived Human Intestinal Organoids. *Cancers (Basel)* **12,** 469.

Nunes AS, Barros AS, Costa EC, Moreira AF & Correia IJ (2019). 3D tumor spheroids as in vitro models to mimic in vivo human solid tumors resistance to therapeutic drugs. *Biotechnol Bioeng* **116,** 206–226.

Nusse R, Fuerer C, Ching W, Harnish K, Logan C, Zeng A, Ten Berge D & Kalani Y (2008). Wnt signaling and stem cell control. *Cell Res* **18,** 523–527.

O'Hurley G, Sjöstedt E, Rahman A, Li B, Kampf C, Pontén F, Gallagher WM & Lindskog C (2014). Garbage in, garbage out: A critical evaluation of strategies used for validation of immunohistochemical biomarkers. *Mol Oncol* **8,** 783–798.

O'Rourke KP, Dow LE & Lowe SW (2016). Immunofluorescent staining of mouse intestinal stem cells. *Bio-protocol* **6,** e1732.

Ohno H (2016). Intestinal M cells. *J Biochem* **159,** 151–160.

Okuyama K, Kaida A, Hayashi Y, Hayashi Y, Harada K & Miura M (2015). KPU-300, a novel benzophenone diketopiperazine-typeanti-microtubule agent with a 2-pyridyl structure, is a potent radiosensitizer that synchronizes the cell cycle in early M Phase. *PLoS One* **10,** e0145995.

Oost KC, van Voorthuijsen L, Fumagalli A, Lindeboom RGH, Sprangers J, Omerzu M, Rodriguez-Colman MJ, Heinz MC, Verlaan-Klink I, Maurice MM, Burgering BMT, van Rheenen J, Vermeulen M & Snippert HJG (2018). Specific Labeling of Stem Cell Activity in Human Colorectal Organoids Using an ASCL2-Responsive Minigene. *Cell Rep* **22,** 1600–1614.

Ootani A, Li X, Sangiorgi E, Ho QT, Ueno H, Toda S, Sugihara H, Fujimoto K, Weissman IL, Capecchi MR

& Kuo CJ (2009). Sustained in vitro intestinal epithelial culture within a Wnt-dependent stem cell niche. *Nat Med* **15,** 701–706.

Ouahoud S, Hardwick JCH & Hawinkels LJAC (2020). Extracellular BMP antagonists, multifaceted orchestrators in the tumor and its microenvironment. *Int J Mol Sci* **21,** 3888.

Owen RL, Piazza AJ & Ermak TH (1991). Ultrastructural and cytoarchitectural features of lymphoreticular organs in the colon and rectum of adult BALB/c mice. *Am J Anat* **190,** 10–18.

Owens RB, Smith HS, Nelson-Rees WA & Springer EL (1976). Epithelial cell cultures from normal and cancerous human tissues. *J Natl Cancer Inst* **56,** 843–849.

Papp B & Plath K (2011). Reprogramming to pluripotency: Stepwise resetting of the epigenetic landscape. *Cell Res* **21,** 486–501.

Pastuła A & Marcinkiewicz J (2019). Cellular Interactions in the Intestinal Stem Cell Niche. *Arch Immunol Ther Exp (Warsz)* **67,** 19–26.

Pauklin S, Madrigal P, Bertero A & Vallier L (2016). Initiation of stem cell differentiation involves cell cycle-dependent regulation of developmental genes by Cyclin D. *Genes Dev* **30,** 421–433.

Pauklin S & Vallier L (2013). The cell-cycle state of stem cells determines cell fate propensity. *Cell* **155,** 135–147.

Pelaseyed T, Bergström JH, Gustafsson JK, Ermund A, Birchenough GMH, Schütte A, van der Post S, Svensson F, Rodríguez-Piñeiro AM, Nyström EEL, Wising C, Johansson ME V & Hansson GC (2014). The mucus and mucins of the goblet cells and enterocytes provide the first defense line of the gastrointestinal tract and interact with the immune system. *Immunol Rev* **260,** 8–20.

Perneger T V. (1998). What's wrong with Bonferroni adjustments. *Br Med J* **316,** 1236–1238.

Poling HM, Wu D, Brown N, Baker M, Hausfeld TA, Huynh N, Chaffron S, Dunn JCY, Hogan SP, Wells JM, Helmrath MA & Mahe MM (2018). Mechanically induced development and maturation of human intestinal organoids in vivo. *Nat Biomed Eng* **2,** 429–442.

Polo JM, Liu S, Figueroa ME, Kulalert W, Eminli S, Tan KY, Apostolou E, Stadtfeld M, Li Y, Shioda T, Natesan S, Wagers AJ, Melnick A, Evans T & Hochedlinger K (2010). Cell type of origin influences the molecular and functional properties of mouse induced pluripotent stem cells. *Nat Biotechnol* **28,** 848–855.

Potten CS (1977). Extreme sensitivity of some intestinal crypt cells to X and γ irradiation. *Nature* **269,** 518–521.

Potten CS, Chadwick C, Ijiri K, Tsubouchi S & Hanson WR (1984). The recruitability and cell-cycle state of intestinal stem cells. *Int J Cell Cloning* **2,** 126–140.

Powell DW, Adegboyega PA, Di Mari JF & Mifflin RC (2005). Epithelial cells and their neighbors I. Role of intestinal myofibroblasts in development, repair, and cancer. *Am J Physiol - Gastrointest Liver Physiol* **289,** G2-7.

Pradhan S, Karve SS, Weiss AA, Hawkins J, Poling HM, Helmrath MA, Wells JM & McCauley HA (2020). Tissue Responses to Shiga Toxin in Human Intestinal Organoids. *Cell Mol Gastroenterol Hepatol* **10,** 171–190.

Purow B (2012). Notch inhibition as a promising new approach to cancer therapy. *Adv Exp Med Biol* **727,** 305–319.

Pursglove SE & Mackay JP (2005). CSL: A notch above the rest. *Int J Biochem Cell Biol* **37,** 2472–2477.

Qi Z, Li Y, Zhao B, Xu C, Liu Y, Li H, Zhang B, Wang X, Yang X, Xie W, Li B, Han JDJ & Chen YG (2017). BMP restricts stemness of intestinal Lgr5 + stem cells by directly suppressing their signature genes. *Nat Commun* **8,** 13824.

Qu S, Yan L, Fang B, Ye S, Li P, Ge S, Wu J, Qu D & Song H (2017). Generation of enhanced definitive endoderm from human embryonic stem cells under an albumin/insulin-free and chemically defined condition. *Life Sci* **175,** 37–46.

Quyn AJ, Appleton PL, Carey FA, Steele RJC, Barker N, Clevers H, Ridgway RA, Sansom OJ & Näthke IS (2010). Spindle Orientation Bias in Gut Epithelial Stem Cell Compartments Is Lost in Precancerous Tissue. *Cell Stem Cell* **6,** 175–181.

Rajamahanty S, Alonzo C, Aynehchi S, Choudhury M & Konno S (2010). Growth inhibition of androgen-responsive prostate cancer cells with brefeldin A targeting cell cycle and androgen receptor. *J Biomed Sci* **17,** 1–8.

Ramirez C & Gebert A (2003). Vimentin-positive Cells in the Epithelium of Rabbit Ileal Villi Represent Cup Cells but Not M-cells. *J Histochem Cytochem* **51,** 1533–1544.

Ran FA, Hsu PD, Lin CY, Gootenberg JS, Konermann S, Trevino AE, Scott DA, Inoue A, Matoba S, Zhang Y & Zhang F (2013). Double nicking by RNA-guided CRISPR cas9 for enhanced genome editing

specificity. *Cell* **154,** 1380–1389.

Ranga A, Gjorevski N & Lutolf MP (2014). Drug discovery through stem cell-based organoid models. *Adv Drug Deliv Rev* **69–70,** 19–28.

Rangel-Huerta E & Maldonado E (2017). Transit-Amplifying Cells in the Fast Lane from Stem Cells towards Differentiation. *Stem Cells Int* **2017,** 7602951.

Rasul S, Balasubramanian R, Filipovi A, Slade MJ, Yagüe E & Coombes RC (2009). Inhibition of γ-secretase induces G2M arrest and triggers apoptosis in breast cancer cells. *Br J Cancer* **100,** 1879–1888.

Rayner E, Durin M-A, Thomas R, Moralli D, O'Cathail SM, Tomlinson I, Green CM & Lewis A (2019). CRISPR-Cas9 Causes Chromosomal Instability and Rearrangements in Cancer Cell Lines, Detectable by Cytogenetic Methods. *Cris J* **2,** 406–416.

Reboldi A & Cyster JG (2016). Peyer's patches: Organizing B-cell responses at the intestinal frontier. *Immunol Rev* **271,** 230–245.

Richardson VB, Littlefield LG, Sayer AM & Peterson PT (1994). Cell-cycle-stage specificity of the methotrexate block as resolved by X-ray-induced chromosome damage. *Cytogenet Genome Res* **66,** 126–128.

Richmond CA, Rickner H, Shah MS, Ediger T, Deary L, Zhou F, Tovaglieri A, Carlone DL & Breault DT (2018). JAK/STAT-1 Signaling Is Required for Reserve Intestinal Stem Cell Activation during Intestinal Regeneration Following Acute Inflammation. *Stem Cell Reports* **10,** 17–26.

Ridlon JM, Kang DJ, Hylemon PB & Bajaj JS (2014). Bile acids and the gut microbiome. *Curr Opin Gastroenterol* **30,** 332–338.

Rios D, Wood MB, Li J, Chassaing B, Gewirtz AT & Williams IR (2016). Antigen sampling by intestinal M cells is the principal pathway initiating mucosal IgA production to commensal enteric bacteria. *Mucosal Immunol* **9,** 907–916.

Rizk P & Barker N (2012). Gut stem cells in tissue renewal and disease: Methods, markers, and myths. *Wiley Interdiscip Rev Syst Biol Med* **4,** 475–496.

Roccio M, Schmitter D, Knobloch M, Okawa Y, Sage D & Lutolf MP (2013). Predicting stem cell fate changes by differential cell cycle progression patterns. *Development* **140,** 459–470.

Rodansky ES, Johnson LA, Huang S, Spence JR & Higgins PDR (2015). Intestinal organoids: A model of intestinal fibrosis for evaluating anti-fibrotic drugs. *Exp Mol Pathol* **98,** 346–351.

Rodin S, Antonsson L, Hovatta O & Tryggvason K (2014). Monolayer culturing and cloning of human pluripotent stem cells on laminin-521-based matrices under xeno-free and chemically defined conditions. *Nat Protoc* **9,** 2354–2368.

Rojas-Fernandez A, Herhaus L, Macartney T, Lachaud C, Hay RT & Sapkota GP (2015). Rapid generation of endogenously driven transcriptional reporters in cells through CRISPR/Cas9. *Sci Rep* **5,** 9811.

Roma C, Rachiglio AM, Pasquale R, Fenizia F, Iannaccone A, Tatangelo F, Antinolfi G, Parrella P, Graziano P, Sabatino L, Colantuoni V, Botti G, Maiello E & Normanno N (2016). BRAF V600E mutation in metastatic colorectal cancer: Methods of detection and correlation with clinical and pathologic features. *Cancer Biol Ther* **17,** 840–848.

Roth S, Franken P, Sacchetti A, Kremer A & Anderson K (2012). Paneth Cells in Intestinal Homeostasis and Tissue Injury. *PLoS One* **7,** e38965.

Rothenberg ME, Nusse Y, Kalisky T, Lee JJ, Dalerba P, Scheeren F, Lobo N, Kulkarni S, Sim S, Qian D, Beachy PA, Pasricha PJ, Quake SR & Clarke MF (2012). Identification of a cKit+ colonic crypt base secretory cell that supports Lgr5+ stem cells in mice. *Gastroenterology* **142,** 1195–1205.

Rouch JD, Scott A, Lei NY, Solorzano-Vargas RS, Wang J, Hanson EM, Kobayashi M, Lewis M, Stelzner MG, Dunn JCY, Eckmann L & Martín MG (2016). Development of functional microfold (M) cells from intestinal stem cells in primary human enteroids. *PLoS One* **11,** e0148216.

Roy A, Tesauro C, Frøhlich R, Hede MS, Nielsen MJ, Kjeldsen E, Bonven B, Stougaard M, Gromova I & Knudsen BR (2014). Decreased Camptothecin Sensitivity of the Stem-Cell-Like Fraction of Caco2 Cells Correlates with an Altered Phosphorylation Pattern of Topoisomerase I ed. Leng F. *PLoS One* **9,** e99628.

Ryu SM, Hur JW & Kim K (2019). Evolution of CRISPR towards accurate and efficient mammal genome engineering. *BMB Rep* **52,** 475–481.

Sachs N & Clevers H (2014). Organoid cultures for the analysis of cancer phenotypes. *Curr Opin Genet Dev* **24,** 68–73.

Sachs N, Tsukamoto Y, Kujala P, Peters PJ & Clevers H (2017). Intestinal epithelial organoids fuse to form self-organizing tubes in floating collagen gels. *Development* **144,** 1107–1112.

Sakaue-Sawano A, Kobayashi T, Ohtawa K & Miyawaki A (2011). Drug-induced cell cycle modulation leading to cell-cycle arrest, nuclear mis-segregation, or endoreplication. *BMC Cell Biol* **12,** 2.

Sakaue-Sawano A, Kurokawa H, Morimura T, Hanyu A, Hama H, Osawa H, Kashiwagi S, Fukami K, Miyata T, Miyoshi H, Imamura T, Ogawa M, Masai H & Miyawaki A (2008). Visualizing Spatiotemporal Dynamics of Multicellular Cell-Cycle Progression. *Cell* **132,** 487–498.

Samuels Y, Diaz LA, Schmidt-Kittler O, Cummins JM, DeLong L, Cheong I, Rago C, Huso DL, Lengauer C, Kinzler KW, Vogelstein B & Velculescu VE (2005). Mutant PIK3CA promotes cell growth and invasion of human cancer cells. *Cancer Cell* **7,** 561–573.

Samy KE, Levy ES, Phong K, Demaree B, Abate AR & Desai TA (2019). Human intestinal spheroids cultured using Sacrificial Micromolding as a model system for studying drug transport. *Sci Rep* **9,** 9936.

San Roman AK, Jayewickreme CD, Murtaugh LC & Shivdasani RA (2014). Wnt secretion from epithelial cells and subepithelial myofibroblasts is not required in the mouse intestinal stem cell niche in vivo. *Stem Cell Reports* **2,** 127–134.

San Roman AK, Tovaglieri A, Breault DT & Shivdasani RA (2015). Distinct processes and transcriptional targets underlie CDX2 requirements in intestinal stem cells and differentiated villus cells. *Stem Cell Reports* **5,** 673–681.

Sangiorgi E & Capecchi MR (2008). Bmi1 is expressed in vivo in intestinal stem cells. *Nat Genet* **40,** 915–920.

Sasaki N, Sachs N, Wiebrands K, Ellenbroek SIJ, Fumagalli A, Lyubimova A, Begthel H, Van Born M Den, Van Es JH, Karthaus WR, Li VSW, López-Iglesias C, Peters PJ, Van Rheenen J, Van Oudenaarden A & Clevers H (2016). Reg4+ deep crypt secretory cells function as epithelial niche for Lgr5+ stem cells in colon. *Proc Natl Acad Sci U S A* **113,** E5399–E5407.

Sato T, van Es JH, Snippert HJ, Stange DE, Vries RG, van den Born M, Barker N, Shroyer NF, van de Wetering M & Clevers H (2011*a*). Paneth cells constitute the niche for Lgr5 stem cells in intestinal crypts. *Nature* **469,** 415–418.

Sato T, Stange DE, Ferrante M, Vries RGJ, Van Es JH, Van Den Brink S, Van Houdt WJ, Pronk A, Van Gorp J, Siersema PD & Clevers H (2011*b*). Long-term expansion of epithelial organoids from human colon, adenoma, adenocarcinoma, and Barrett's epithelium. *Gastroenterology* **141,** 1762–1772.

Sato T, Vries RG, Snippert HJ, van de Wetering M, Barker N, Stange DE, van Es JH, Abo A, Kujala P, Peters PJ & Clevers H (2009). Single Lgr5 stem cells build crypt&-villus structures in vitro without a mesenchymal niche. *Nature* **459,** 262–265.

Scheper AG, Snippert HJ, Stange DE, Born M van den, Es JH van, Wetering M van de & Clevers H (2012). Lineage Tracing Reveals Lgr5+ Stem Cell Activity in Mouse Intestinal Adenomas. *Science (80-)* **337,** 730–735.

Schneider C, O'Leary CE & Locksley RM (2019). Regulation of immune responses by tuft cells. *Nat Rev Immunol* **19,** 584–593.

Schneider MR, Dahlhoff M, Horst D, Hirschi B, Trülzsch K, Müller-Höcker J, Vogelmann R, Allgäuer M, Gerhard M, Steininger S, Wolf E & Kolligs FT (2010). A key role for E-cadherin in intestinal homeostasis and paneth cell maturation. *PLoS One* **5,** e14325.

Schneider NFZ, Cerella C, Lee JY, Mazumder A, Kim KR, de Carvalho A, Munkert J, Pádua RM, Kreis W, Kim KW, Christov C, Dicato M, Kim HJ, Han BW, Braga FC, Simões CMO & Diederich M (2018). Cardiac glycoside glucoevatromonoside induces cancer type-specific cell death. *Front Pharmacol* **9,** 70.

Schonhoff SE, Giel-Moloney M & Leiter AB (2004). Minireview: Development and differentiation of gut endocrine cells. *Endocrinology* **145,** 2639–2644.

Schuijers J, Junker JP, Mokry M, Hatzis P, Koo BK, Sasselli V, Van Der Flier LG, Cuppen E, Van Oudenaarden A & Clevers H (2015). Ascl2 acts as an R-spondin/wnt-responsive switch to control stemness in intestinal crypts. *Cell Stem Cell* **16,** 158–170.

Sei Y, Feng J, Chow CC & Wank SA (2019). Asymmetric cell division-dominant neutral drift model for normal intestinal stem cell homeostasis. *Am J Physiol Liver Physiol* **316,** G64–G74.

Senger S, Ingano L, Freire R, Anselmo A, Zhu W, Sadreyev R, Walker WA & Fasano A (2018). Human Fetal-Derived Enterospheres Provide Insights on Intestinal Development and a Novel Model to Study Necrotizing Enterocolitis (NEC). *Cell Mol Gastroenterol Hepatol* **5,** 549–568.

Sevin E, Dehouck L, Fabulas-da Costa A, Cecchelli R, Dehouck MP, Lundquist S & Culot M (2013). Accelerated Caco-2 cell permeability model for drug discovery. *J Pharmacol Toxicol Methods* **68,** 334–339.

Shaik JP, Alanazi IO, Pathan AAK, Parine NR, Almadi MA, Azzam NA, Aljebreen AM, Alharbi O, Alanazi

MS & Khan Z (2020). Frequent Activation of Notch Signaling Pathway in Colorectal Cancers and Its Implication in Patient Survival Outcome. *J Oncol* **2020,** 6768942.

Sherr CJ (1996). Cancer cell cycles. *Science (80-)* **274,** 1672–1677.

Sherwood RI, Maehr R, Mazzoni EO & Melton DA (2011). Wnt signaling specifies and patterns intestinal endoderm. *Mech Dev* **128,** 387–400.

Shevinsky LH, Knowles BB, Damjanov I & Solter D (1982). Monoclonal antibody to murine embryos defines a stage-specific embryonic antigen expressed on mouse embryos and human teratocarcinoma cells. *Cell* **30,** 697–705.

Shimokawa M, Ohta Y, Nishikori S, Matano M, Takano A, Fujii M, Date S, Sugimoto S, Kanai T & Sato T (2017). Visualization and targeting of LGR5 + human colon cancer stem cells. *Nature* **545,** 187–192.

Shin DY, Sung Kang H, Kim GY, Kim WJ, Yoo YH & Choi YH (2013). Decitabine, a DNA methyltransferases inhibitor, induces cell cycle arrest at G2/M phase through p53-independent pathway in human cancer cells. *Biomed Pharmacother* **67,** 305–311.

Shroyer NF, Helmrath MA, Wang VY-C, Antalffy B, Henning SJ & Zoghbi HY (2007). Intestine-specific ablation of mouse atonal homolog 1 (Math1) reveals a role in cellular homeostasis. *Gastroenterology* **132,** 2478–2488.

Siller R, Greenhough S, Naumovska E & Sullivan GJ (2015). Small-molecule-driven hepatocyte differentiation of human pluripotent stem cells. *Stem Cell Reports* **4,** 939–952.

Da Silva C, Wagner C, Bonnardel J, Gorvel JP & Lelouard H (2017). The Peyer's patch mononuclear phagocyte system at steady state and during infection. *Front Immunol* **8,** 1254.

Simmini S, Bialecka M, Huch M, Kester L, van de Wetering M, Sato T, Beck F, van Oudenaarden A, Clevers H & Deschamps J (2014). Transformation of intestinal stem cells into gastric stem cells on loss of transcription factor Cdx2. *Nat Commun* **5,** 5728.

Sinagoga KL, McCauley HA, Muńera JO, Reynolds NA, Enriquez JR, Watson C, Yang HC, Helmrath MA & Wells JM (2018). Deriving functional human enteroendocrine cells from pluripotent stem cells. *Dev* **145,** dev165795.

Sinagoga KL & Wells JM (2015). Generating human intestinal tissues from pluripotent stem cells to study development and disease. *EMBO J* **34,** 1149–1163.

Singh AM, Chappell J, Trost R, Lin L, Wang T, Tang J, Wu H, Zhao S, Jin P & Dalton S (2013). Cell-cycle control of developmentally regulated transcription factors accounts for heterogeneity in human pluripotent cells. *Stem Cell Reports* **1,** 532–544.

Slichenmyer WJ & Von Hoff DD (1990). New natural products in cancer chemotherapy. *J Clin Pharmacol* **30,** 770–788.

Smith HS (1979). In vitro properties of epithelial cell lines established from human carcinomas and nonmalignant tissue. *J Natl Cancer Inst* **62,** 225–230.

Smith HS, Springer EL & Hackett AJ (1979). Nuclear ultrastructure of epithelial cell lines derived from human carcinomas and nonmalignant tissues. *Cancer Res* **39,** 332–344.

Snippert HJ, van der Flier LG, Sato T, van Es JH, van den Born M, Kroon-Veenboer C, Barker N, Klein AM, van Rheenen J, Simons BD & Clevers H (2010). Intestinal crypt homeostasis results from neutral competition between symmetrically dividing Lgr5 stem cells. *Cell* **143,** 134–144.

Snippert HJ, Schepers AG, Van Es JH, Simons BD & Clevers H (2014). Biased competition between Lgr5 intestinal stem cells driven by oncogenic mutation induces clonal expansion. *EMBO Rep* **15,** 62–69.

Snoeck V, Goddeeris B & Cox E (2005). The role of enterocytes in the intestinal barrier function and antigen uptake. *Microbes Infect* **7,** 997–1004.

Soboleski MR, Oaks J & Halford WP (2005). Green fluorescent protein is a quantitative reporter of gene expression in individual eukaryotic cells. *FASEB J* **19,** 1–20.

Solter D & Knowles BB (1978). Monoclonal antibody defining a stage-specific mouse embryonic antigen (SSEA-1). *Proc Natl Acad Sci* **75,** 5565–5569.

Sommer F & Bäckhed F (2013). The gut microbiota — masters of host development and physiology. *Nat Rev Microbiol* **11,** 227–238.

Son YS, Ki SJ, Thanavel R, Kim J, Lee M, Kim J, Jung C, Han T, Cho H, Ryu C, Kim S, Park D & Son M (2020). Maturation of human intestinal organoids in vitro facilitates colonization by commensal lactobacilli by reinforcing the mucus layer. *FASEB J* **34,** 9899–9910.

Sottoriva A, Kang H, Ma Z, Graham TA, Salomon MP, Zhao J, Marjoram P, Siegmund K, Press MF, Shibata D & Curtis C (2015). A Big Bang model of human colorectal tumor growth. *Nat Genet* **47,** 209–216.

Soufi A & Dalton S (2016). Cycling through developmental decisions: How cell cycle dynamics control pluripotency, differentiation and reprogramming. *Development* **143,** 4301–4311.

Spence JR, Mayhew CN, Rankin SA, Kuhar MF, Vallance JE, Tolle K, Hoskins EE, Kalinichenko V V., Wells SI, Zorn AM, Shroyer NF & Wells JM (2011). Directed differentiation of human pluripotent stem cells into intestinal tissue in vitro. *Nature* **470,** 105–109.

Spencer J, Finn T & Isaacson PG (1986). Human Peyer's patches: an immunohistochemical study. *Gut* **27,** 405–410.

Steele SP, Melchor SJ & Petri WA (2016). Tuft Cells: New Players in Colitis. *Trends Mol Med* **22,** 921–924.

Steff AM, Fortin M, Arguin C & Hugo P (2001). Detection of a decrease in green fluorescent protein fluorescence for the monitoring of cell death: An assay amenable to high-throughput screening technologies. *Cytometry* **45,** 237–243.

Stiemsma LT & Michels KB (2018). The Role of the microbiome in the developmental origins of health and disease. *Pediatrics* **141,** e20172437.

Stringer EJ, Duluc I, Saandi T, Davidson I, Bialecka M, Sato T, Barker N, Clevers H, Pritchard CA, Winton DJ, Wright NA, Freund J-N, Deschamps J & Beck F (2012). Cdx2 determines the fate of postnatal intestinal endoderm. *Development* **139,** 465–474.

Strömberg T, Feng X, Delforoush M, Berglund M, Lin Y, Axelson M, Larsson O, Georgii-Hemming P, Lennartsson J & Enblad G (2015). Picropodophyllin inhibits proliferation and survival of diffuse large B-cell lymphoma cells. *Med Oncol* **32,** 188.

Sugimoto S, Ohta Y, Fujii M, Matano M, Shimokawa M, Nanki K, Date S, Nishikori S, Nakazato Y, Nakamura T, Kanai T & Sato T (2018). Reconstruction of the Human Colon Epithelium In Vivo. *Cell Stem Cell* **22,** 171-176.e5.

Sulzbacher S, Schroeder IS, Truong TT & Wobus AM (2009). Activin a-induced differentiation of embryonic stem cells into endoderm and pancreatic progenitors-the influence of differentiation factors and culture conditions. *Stem Cell Rev Reports* **5,** 159–173.

Sun J, Wei Q, Zhou Y, Wang J, Liu Q & Xu H (2017). A systematic analysis of FDA-approved anticancer drugs. *BMC Syst Biol* **11,** 87.

Sun Y, Jiang W, Lu W, Song M, Liu K, Chen P, Chang A, Ling J, Chiao PJ, Hu Y & Huang P (2018).

Identification of cisplatin sensitizers through high-throughput combinatorial screening. *Int J Oncol* **53,** 1237–1246.

Szabó A & Merks RMH (2013). Cellular Potts Modeling of Tumor Growth, Tumor Invasion, and Tumor Evolution. *Front Oncol* **3,** 87.

Taha MF, Javeri A, Majidizadeh T & Valojerdi MR (2016). Both BMP4 and serum have significant roles in differentiation of embryonic stem cells to primitive and definitive endoderm. *Cytotechnology* **68,** 1315–1324.

Takahashi T & Shiraishi A (2020). Stem cell signaling pathways in the small intestine. *Int J Mol Sci* **21,** 2032.

Takahashi Y, Sato S, Kurashima Y, Yamamoto T, Kurokawa S, Yuki Y, Takemura N, Uematsu S, Lai CY, Otsu M, Matsuno H, Osawa H, Mizushima T, Nishimura J, Hayashi M, Yamaguchi T & Kiyono H (2018). A Refined Culture System for Human Induced Pluripotent Stem Cell-Derived Intestinal Epithelial Organoids. *Stem Cell Reports* **10,** 314–328.

Takeda K, Kinoshita I, Shimizu Y, Matsuno Y, Shichinohe T & Dosaka-Akita H (2011). Expression of LGR5, an Intestinal Stem Cell Marker, During Each Stage of Colorectal Tumorigenesis. *Anticancer Res* **31,** 263–270.

Takeda T, Sakata M, Minekawa R, Yamamoto T, Hayashi M, Tasaka K & Murata Y (2004). Human milk induces fetal small intestinal cell proliferation - involvement of a different tyrosine kinase signaling pathway from epidermal growth factor receptor. *J Endocrinol* **181,** 449–457.

Takeuchi H, Nakatsuji N & Suemori H (2015). Endodermal differentiation of human pluripotent stem cells to insulin-producing cells in 3D culture. *Sci Rep* **4,** 4488.

Tam PPL, Hogan BLM, Tessier-lavigne MT, Jessell T & Dodd J (1993). Regionalisation of the mouse embryonic ectoderm: allocation of prospective ectodermal tissues during gastrulation. *Development* **107,** 55–67.

Tan H-Y, Trier S, Rahbek UL, Dufva M, rg Kutter JP & Andresen TL (2018). A multi-chamber microfluidic intestinal barrier model using Caco-2 cells for drug transport studies. *PLoS One* **13,** e0197101.

Taylor-Weiner H, Ravi N & Engler AJ (2015). Traction forces mediated by integrin signaling are necessary for definitive endoderm specification. *J Cell Sci* **128,** 1961–1968.

Taylor-Weiner H, Schwarzbauer JE & Engler AJ (2013). Defined extracellular matrix components are

necessary for definitive endoderm induction. *Stem Cells* **31,** 2084–2094.

Teller IC, Auclair J, Herring E, Gauthier R, Ménard D & Beaulieu JF (2007). Laminins in the developing and adult human small intestine: Relation with the functional absorptive unit. *Dev Dyn* **236,** 1980–1990.

Teo AKK, Ali Y, Wong KY, Chipperfield H, Sadasivam A, Poobalan Y, Tan EK, Wang ST, Abraham S, Tsuneyoshi N, Stanton LW & Dunn NR (2012). Activin and BMP4 synergistically promote formation of definitive endoderm in human embryonic stem cells. *Stem Cells* **30,** 631–642.

Teo AKK, Valdez IA, Dirice E & Kulkarni RN (2014). Comparable generation of activin-induced definitive endoderm via additive Wnt or BMP signaling in absence of serum. *Stem Cell Reports* **3,** 5–14.

Thant AA, Wu Y, Lee J, Mishra DK, Garcia H, Koeffler HP & Vadgama J V (2008). Role of caspases in 5-FU and selenium-induced growth inhibition of colorectal cancer cells. *Anticancer Res* **28,** 3579–3592.

Thirumaran R, Prendergast GC & Gilman PB (2007). Cytotoxic Chemotherapy in Clinical Treatment of Cancer. In *Cancer Immunotherapy*, ed. Prendergast GC & Jaffee EM, pp. 101–116. Academic Press.

Thomson JA, Itskovitz-Eldor J, Shapiro SS, Waknitz MA, Swiergiel JJ, Marshall VS & Jone JM (1998). Embryonic stem cell lines derived from human blastocysts. *Science (80-)* **282,** 1145–1147.

Ting H-A & von Moltke J (2019). The Immune Function of Tuft Cells at Gut Mucosal Surfaces and Beyond. *J Immunol* **202,** 1321–1329.

Toivonen S, Lundin K, Balboa D, Ustinov J, Tamminen K, Palgi J, Trokovic R, Tuuri T & Otonkoski T (2013). Activin A and Wnt-dependent specification of human definitive endoderm cells. *Exp Cell Res* **319,** 2535–2544.

Totaro A, Castellan M, Battilana G, Zanconato F, Azzolin L, Giulitti S, Cordenonsi M & Piccolo S (2017). YAP/TAZ link cell mechanics to Notch signalling to control epidermal stem cell fate. *Nat Commun* **8,** 15206.

Trier JS (1963). Studies On Small Intestinal Crypt Epithelium: I. The Fine Structure of the Crypt Epithelium of the Proximal Small Intestine of Fasting Humans. *J Cell Biol* **18,** 599–620.

Trietsch SJ, Israëls GD, Joore J, Hankemeier T & Vulto P (2013). Microfluidic titer plate for stratified 3D cell culture. *Lab Chip* **13,** 3548.

Trietsch SJ, Naumovska E, Kurek D, Setyawati MC, Vormann MK, Wilschut KJ, Lanz HL, Nicolas A, Ng CP, Joore J, Kustermann S, Roth A, Hankemeier T, Moisan A & Vulto P (2017). Membrane-free culture and real-time barrier integrity assessment of perfused intestinal epithelium tubes. *Nat Commun* **8,** 262.

Tsai YH, Hill DR, Kumar N, Huang S, Chin AM, Dye BR, Nagy MS, Verzi MP & Spence JR (2016). LGR4 and LGR5 Function Redundantly During Human Endoderm Differentiation. *Cell Mol Gastroenterol Hepatol* **2,** 648-662.e8.

Tsurusawa M, Niwa M, Katano N & Fujimoto T (1990). Methotrexate Cytotoxicity as Related to Irreversible S Phase Arrest in Mouse L1210 Leukemia Cells. *Japanese J Cancer Res* **81,** 85–90.

Uchida H, Yamazaki K, Fukuma M, Yamada T, Hayashida T, Hasegawa H, Kitajima M, Kitagawa Y & Sakamoto M (2010). Overexpression of leucine-rich repeat-containing G protein-coupled receptor 5 in colorectal cancer. *Cancer Sci* **101,** 1731–1737.

Uddin F, Rudin CM & Sen T (2020). CRISPR Gene Therapy: Applications, Limitations, and Implications for the Future. *Front Oncol* **10,** 1387.

Ueo T, Imayoshi I, Kobayashi T, Ohtsuka T, Seno H, Nakase H, Chiba T & Kageyama R (2012). The role of Hes genes in intestinal development, homeostasis and tumor formation. *Development* **139,** 1071–1082.

VanDussen KL, Carulli AJ, Keeley TM, Patel SR, Puthoff BJ, Magness ST, Tran IT, Maillard I, Siebel C, Kolterud Å, Grosse AS, Gumucio DL, Ernst SA, Tsai Y-H, Dempsey PJ & Samuelson LC (2012). Notch signaling modulates proliferation and differentiation of intestinal crypt base columnar stem cells. *Development* **139,** 488–497.

VanDussen KL & Samuelson LC (2010). Mouse atonal homolog 1 directs intestinal progenitors to secretory cell rather than absorptive cell fate. *Dev Biol* **346,** 215–223.

Veeman MT, Slusarski DC, Kaykas A, Louie SH & Moon RT (2003). Zebrafish prickle, a modulator of noncanonical Wnt/Fz signaling, regulates gastrulation movements. *Curr Biol* **13,** 680–685.

Vermeulen L, Morrissey E, Van Der Heijden M, Nicholson AM, Sottoriva A, Buczacki S, Kemp R, Tavaré S & Winton DJ (2013). Defining stem cell dynamics in models of intestinal tumor initiation. *Science (80-)* **342,** 995–998.

Verzi MP, Shin H, Roman KS, Liu XS & Shivdasani A (2013). Intestinal Master Transcription Factor CDX2

Controls Chromatin. *Mol Cell Biol* **33,** 281–292.

Vieira GC, Chockalingam S, Melegh Z, Greenhough A, Malik S, Szemes M, Park JH, Kaidi A, Zhou L, Catchpoole D, Morgan R, Bates DO, Gabb PD & Malik K (2015). LGR5 regulates pro-survival MEK/ERK and proliferative Wnt/β-catenin signalling in neuroblastoma. *Oncotarget* **6,** 40053–40067.

Vivarelli S, Salemi R, Candido S, Falzone L, Santagati M, Stefani S, Torino F, Banna GL, Tonini G & Libra M (2019). Gut microbiota and cancer: From pathogenesis to therapy. *Cancers (Basel)* **11,** 38.

Vollaire J, Machuca-Gayet I, Lavaud J, Bellanger A, Bouazza L, El Moghrabi S, Treilleux I, Coll J-L, Peyruchaud O, Josserand V & Cohen PA (2019). The Bone Morphogenetic Protein Signaling Inhibitor LDN-193189 Enhances Metastasis Development in Mice. *Front Pharmacol* **10,** 667.

van der Vorst MJDL, Neefjes ECW, Konings IRHM & Verheul HMW (2015). Prophylactic treatment for delayed chemotherapy-induced nausea and vomiting after non-AC based moderately emetogenic chemotherapy: a systematic review of randomized controlled trials. *Support Care Cancer* **23,** 2499–2506.

Vulto P, Podszun S, Meyer P, Hermann C, Manz A & Urban GA (2011). Phaseguides: a paradigm shift in microfluidic priming and emptying. *Lab Chip* **11,** 1596.

Wang H, Luo X, Yao L, Lehman DM & Wang P (2015). Improvement of Cell Survival During Human Pluripotent Stem Cell Definitive Endoderm Differentiation. *Stem Cells Dev* **24,** 2536–2546.

Wang J, Chen WD & Wang YD (2020). The Relationship Between Gut Microbiota and Inflammatory Diseases: The Role of Macrophages. *Front Microbiol* **11,** 1065.

Wang M, Ma X, Wang J, Wang L & Wang Y (2014*a*). Pretreatment with the γ-secretase inhibitor DAPT sensitizes drug-resistant ovarian cancer cells to cisplatin by downregulation of Notch signaling. *Int J Oncol* **44,** 1401–1409.

Wang P, McKnight KD, Wong DJ, Rodriguez RT, Sugiyama T, Gu X, Ghodasara A, Qu K, Chang HY & Kim SK (2012). A Molecular Signature for Purified Definitive Endoderm Guides Differentiation and Isolation of Endoderm from Mouse and Human Embryonic Stem Cells. *Stem Cells Dev* **21,** 2273–2287.

Wang Q, Wei F, Lv G, Li C, Liu T, Hadjipanayis CG, Zhang G, Hao C & Bellail AC (2013). The association of TP53 mutations with the resistance of colorectal carcinoma to the insulin-like growth factor-

1 receptor inhibitor picropodophyllin. *BMC Cancer* **13,** 521.

Wang RN et al. (2014*b*). Bone Morphogenetic Protein (BMP) signaling in development and human diseases. *Genes Dis* **1,** 87–105.

Wang S, Du L, Peng G & Li W (2019). GABA inhibits proliferation and self-renewal of mouse retinal progenitor cell. *Cell Death Discov* **5,** 80.

Wang Y, Ryu HS & Jang JJ (2018). Nicotinamide suppresses cell growth by G1-phase arrest and induces apoptosis in intrahepatic cholangiocarcinoma. *Mol Cell Toxicol* **14,** 43–51.

Watson CL, Mahe MM, Múnera J, Howell JC, Sundaram N, Poling HM, Schweitzer JI, Vallance JE, Mayhew CN, Sun Y, Grabowski G, Finkbeiner SR, Spence JR, Shroyer NF, Wells JM & Helmrath MA (2014). An in vivo model of human small intestine using pluripotent stem cells. *Nat Med* **20,** 1310–1314.

Watts TL & Fasano A (2000). Modulation of Intestinal Permeability: A Novel and Innovative Approach for the Oral Delivery of Drugs, Macromolecules and Antigens. *Biotechnol Genet Eng Rev* **17,** 433– 454.

Wells JM & Melton DA (1999). Vertebrate endoderm development. *Annu Rev Cell Dev Biol* **15,** 393– 410.

Wells JM & Spence JR (2014). How to make an intestine. *Development* **141,** 752–760.

Van De Wetering M et al. (2015). Prospective derivation of a living organoid biobank of colorectal cancer patients. *Cell* **161,** 933–945.

Whissell G, Montagni E, Martinelli P, Hernando-Momblona X, Sevillano M, Jung P, Cortina C, Calon A, Abuli A, Castells A, Castellvi-Bel S, Nacht AS, Sancho E, Stephan-Otto Attolini C, Vicent GP, Real FX & Batlle E (2014). The transcription factor GATA6 enables self-renewal of colon adenoma stem cells by repressing BMP gene expression. *Nat Cell Biol* **16,** 695–707.

White T, van der Ende J & Nichols TE (2019). Beyond Bonferroni revisited: concerns over inflated false positive research findings in the fields of conservation genetics, biology, and medicine. *Conserv Genet* **20,** 927–937.

WHO (2019). World Health Organization Model List of Essential Medicines. Available at: https://apps.who.int/iris/bitstream/handle/10665/325771/WHO-MVP-EMP-IAU-2019.06-eng.pdf [Accessed December 17, 2020].

Wiles M V. & Johansson BM (1999). Embryonic stem cell development in a chemically defined medium. *Exp Cell Res* **247,** 241–248.

Williams IR & Owen RL (2015). M Cells: Specialized Antigen Sampling Cells in the Follicle-Associated Epithelium. In *Mucosal Immunology*, 4th edn., ed. Mestecky J, Russell MW, Cheroutre H, Strober W, Kelsall BL & Lambrecht BN, pp. 211–229. Academic Press.

Williams JM, Duckworth CA, Burkitt MD, Watson AJM, Campbell BJ & Pritchard DM (2015). Epithelial Cell Shedding and Barrier Function: A Matter of Life and Death at the Small Intestinal Villus Tip. *Vet Pathol* **52,** 445–455.

Wilmer MJ, Ng CP, Lanz HL, Vulto P, Suter-Dick L & Masereeuw R (2016). Kidney-on-a-Chip Technology for Drug-Induced Nephrotoxicity Screening. *Trends Biotechnol* **34,** 156–170.

Wilson G, Hassan IF, Dix CJ, Williamson I, Shah R & Mackay M (1990). Transport and permeability properties of human CaCo-2 cells: An in vitro model of the intestinal epithelial barrier. *J Control Release* **11,** 25–40.

Winton DJ & Ponder BAJ (1990). Stem-cell organization in mouse small intestine. *Proc R Soc B Biol Sci* **241,** 13–18.

Wong JCY, Gao SY, Lees JG, Best MB, Wang R & Tuch BE (2010). Definitive endoderm derived from human embryonic stem cells highly express the integrin receptors αV and β5. *Cell Adh Migr* **4,** 39–45.

Wong JMW, De Souza R, Kendall CWC, Emam A & Jenkins DJA (2006). Colonic health: Fermentation and short chain fatty acids. *J Clin Gastroenterol* **40,** 235–243.

Workman MJ, Gleeson JP, Troisi EJ, Estrada HQ, Kerns SJ, Hinojosa CD, Hamilton GA, Targan SR, Svendsen CN & Barrett RJ (2018). Enhanced Utilization of Induced Pluripotent Stem Cell-Derived Human Intestinal Organoids Using Microengineered Chips. *Cell Mol Gastroenterol Hepatol* **5,** 669–677.

Workman MJ, Mahe MM, Trisno S, Poling HM, Watson CL, Sundaram N, Chang CF, Schiesser J, Aubert P, Stanley EG, Elefanty AG, Miyaoka Y, Mandegar MA, Conklin BR, Neunlist M, Brugmann SA, Helmrath MA & Wells JM (2017). Engineered human pluripotent-stem-cell-derived intestinal tissues with a functional enteric nervous system. *Nat Med* **23,** 49–59.

Worthington JJ, Reimann F & Gribble FM (2018). Enteroendocrine cells-sensory sentinels of the

intestinal environment and orchestrators of mucosal immunity. *Mucosal Immunol* **11,** 3–20.

Wright A, Andrews N, Bardsley K, Nielsen JE, Avery K, Pewsey E, Jones M, Harley D, Nielsen AR, Moore H, Gokhale P, Rajpert-De Meyts E, Andrews PW, Walsh J & Harrison NJ (2011). Mapping the stem cell state: Eight novel human embryonic stem and embryonal carcinoma cell antibodies. *Int J Androl* **34,** 175–188.

Wu HC, Chen YS, Shien JH, Shen PC & Lee LH (2016). Characterization of functionally active interleukin-18/eGFP fusion protein expression during cell cycle phases in recombinant chicken DF1 Cells. *Biotechnol Prog* **32,** 581–591.

Xie X, Sasai K, Shibuya K, Tachiiri S, Nihei K, Ohnishi T & Hiraoka M (2000). P53 status plays no role in radiosensitizing effects of SN-38, a camptothecin derivative. *Cancer Chemother Pharmacol* **45,** 362–368.

Xie Y, Kang R & Tang D (2017). Assessment of Posttranslational Modifications of ATG proteins. In *Methods in Enzymology*, ed. Galluzzi L, Bravo-San Pedro JM & Kroemer G, pp. 171–188. Academic Press.

Yamazaki M, Kato A, Zaitsu Y, Watanabe T, Iimori M, Funahashi S, Kitao H, Saeki H, Oki E & Suzuki M (2015). Intensive immunofluorescence staining methods for low expression protein: Detection of intestinal stem cell marker LGR5. *Acta Histochem Cytochem* **48,** 159–164.

Yan K, Chia L & Li X (2012). The intestinal stem cell markers Bmi1 and Lgr5 identify two functionally distinct populations. *Proc Natl Acad Sci* **109,** 466–471.

Yang QM for secretory cell lineage commitment in the mouse intestine., Bermingham NA, Finegold MJ & Zoghbi HY (2001). Requirement of Math1 for secretory cell lineage commitment in the mouse intestine. *Science (80-)* **294,** 2155–2158.

Yang Y, Zhao Y, Yu A, Sun D & Yu LX (2017). Oral drug absorption: Evaluation and prediction. In *Developing Solid Oral Dosage Forms: Pharmaceutical Theory and Practice*, 2nd edn., ed. Qiu Y, Zhang GGZ, Mantri R V., Chen Y & Yu L, pp. 331–354. Academic Press.

Ye L, Tao K, Yu Y & Wang G (2010). Reduction of G0 phase cells of colon cancer caco-2 cells may enhance 5-fluorouracil efficacy. *J Biomed Res* **24,** 64–68.

Yi J, Bergstrom K, Fu J, Shan X, McDaniel JM, McGee S, Qu D, Houchen CW, Liu X & Xia L (2019). Dclk1 in tuft cells promotes inflammation-driven epithelial restitution and mitigates chronic colitis. *Cell*

Death Differ **26,** 1656–1669.

Yin X, Farin HF, van Es JH, Clevers H, Langer R & Karp JM (2014). Niche-independent high-purity cultures of Lgr5+ intestinal stem cells and their progeny. *Nat Methods* **11,** 106–112.

Yin X, Mead BE, Safaee H, Langer R, Karp JM & Levy O (2016). Engineering Stem Cell Organoids. *Cell Stem Cell* **18,** 25–38.

Ying L, Mills JA, French DL & Gadue P (2015). OCT4 coordinates with WNT signaling to pre-pattern chromatin at the SOX17 locus during human ES cell differentiation into definitive endoderm. *Stem Cell Reports* **5,** 490–498.

Yokoyama Y, Watanabe T, Tamura Y, Hashizume Y, Miyazono K & Ehata S (2017). Autocrine BMP-4 signaling is a therapeutic target in colorectal cancer. *Cancer Res* **77,** 4026–4038.

Yoshida S, Miwa H, Kawachi T, Kume S & Takahashi K (2020). Generation of intestinal organoids derived from human pluripotent stem cells for drug testing. *Sci Rep* **10,** 1–11.

Youhanna S & Lauschke VM (2020). The Past, Present and Future of Intestinal In Vitro Cell Systems for Drug Absorption Studies. *J Pharm Sci* **110,** 50–65.

Yu J (2013). Intestinal stem cell injury and protection during cancer therapy. *Transl Cancer Res* **2,** 384–396.

Yu JSL, Ramasamy TS, Murphy N, Holt MK, Czapiewski R, Wei S-K & Cui W (2015). PI3K/mTORC2 regulates TGF-β/Activin signalling by modulating Smad2/3 activity via linker phosphorylation. *Nat Commun* **6,** 7212.

Yui S, Nakamura T, Sato T, Nemoto Y, Mizutani T, Zheng X, Ichinose S, Nagaishi T, Okamoto R, Tsuchiya K, Clevers H & Watanabe M (2012). Functional engraftment of colon epithelium expanded in vitro from a single adult Lgr5+ stem cell. *Nat Med* **18,** 618–623.

Zanoni M, Cortesi M, Zamagni A, Arienti C, Pignatta S & Tesei A (2020). Modeling neoplastic disease with spheroids and organoids. *J Hematol Oncol* **13,** 97.

Zebisch M, Xu Y, Krastev C, MacDonald BT, Chen M, Gilbert RJC, He X & Jones EY (2013). Structural and molecular basis of ZNRF3/RNF43 transmembrane ubiquitin ligase inhibition by the Wnt agonist R-spondin. *Nat Commun* **4,** 2787.

Zecchini V, Domaschenz R, Winton D & Jones P (2005). Notch signaling regulates the differentiation of

post-mitotic intestinal epithelial cells. *Genes Dev* **19,** 1686–1691.

Zeng H, Umar S, Rust B, Lazarova D & Bordonaro M (2019). Secondary bile acids and short chain fatty acids in the colon: A focus on colonic microbiome, cell proliferation, inflammation, and cancer. *Int J Mol Sci* **20,** 1214.

Zhang L, Ye Y, Long X, Xiao P, Ren X & Yu J (2016). BMP signaling and its paradoxical effects in tumorigenesis and dissemination. *Oncotarget* **7,** 78206–78218.

Zhang XH, Tee LY, Wang XG, Huang QS & Yang SH (2015). Off-target effects in CRISPR/Cas9-mediated genome engineering. *Mol Ther - Nucleic Acids* **4,** e264.

Zhao Y et al. (2019). P53-R273H mutation enhances colorectal cancer stemness through regulating specific lncRNAs. *J Exp Clin Cancer Res* **38,** 379.

Ziskin JL, Dunlap D, Yaylaoglu M, Fodor IK, Forrest WF, Patel R, Ge N, Hutchins GG, Pine JK, Quirke P, Koeppen H & Jubb AM (2013). In situ validation of an intestinal stem cell signature in colorectal cancer. *Gut* **62,** 1012–1023.

Zitvogel L, Galluzzi L, Viaud S, Vétizou M, Daillère R, Merad M & Kroemer G (2015). Cancer and the gut microbiota: An unexpected link. *Sci Transl Med* **7,** 271ps1.